PERFORMANCE OF A PILOT-SCALE, STEAM-BLOWN, PRESSURIZED FLUIDIZED BED BIOMASS GASIFIER

by

Daniel Joseph Sweeney

A dissertation submitted to the faculty of
The University of Utah
in partial fulfillment of the requirements of the degree of

Doctor of Philosophy

Department of Mechanical Engineering

The University of Utah

December 2012

The University of Utah Graduate School

STATEMENT OF DISSERTATION APPROVAL

The dissertation of **Daniel Joseph Sweeney**

has been approved by the following supervisory committee members:

Kevin Whitty	, Chair	**June 12, 2012** Date Approved
Eric Eddings	, Member	**June 12, 2012** Date Approved
Patrick McMurtry	, Member	**June 12, 2012** Date Approved
Eric Pardyjak	, Member	**June 12, 2012** Date Approved
Kent Udell	, Member	**June 13, 2012** Date Approved

and by **Timothy Ameel** , Chair of

the Department of **Mechanical Engineering**

and by Charles A. Wight, Dean of The Graduate School.

ABSTRACT

With the discovery of vast fossil resources, and the subsequent development of the fossil fuel and petrochemical industry, the role of biomass-based products has declined. However, concerns about the finite and decreasing amount of fossil and mineral resources, in addition to health and climate impacts of fossil resource use, have elevated interest in innovative methods for converting renewable biomass resources into products that fit our modern lifestyle.

Thermal conversion through gasification is an appealing method for utilizing biomass due to its operability using a wide variety of feedstocks at a wide range of scales, the product has a variety of uses (e.g., transportation fuel production, electricity production, chemicals synthesis), and in many cases, results in significantly lower greenhouse gas emissions. In spite of the advantages of gasification, several technical hurdles have hindered its commercial development.

A number of studies have focused on laboratory-scale and atmospheric biomass gasification. However, few studies have reported on pilot-scale, woody biomass gasification under pressurized conditions. The purpose of this research is an assessment of the performance of a pilot-scale, steam-blown, pressurized fluidized bed biomass gasifier. The 200 kW_{th} fluidized bed gasifier is capable of operation using solid feedstocks at feedrates up to 65 lb/hr, bed temperatures up to 1600°F, and pressures up to 8 atm. Gasifier performance was assessed under various temperatures, pressure, and feedstock (untreated woody biomass, dark and medium torrefied biomass) conditions by measuring product gas yield and composition, residue (e.g., tar and char) production, and mass and energy conversion efficiencies.

Elevated temperature and pressure, and feedstock pretreatment were shown to have a significant influence on gasifier operability, tar production, carbon conversion, and process efficiency. High-pressure and temperature gasification of dark torrefied biomass yielded the lowest tar concentration (1.6 g/Nm^3). High-temperature and low-pressure conditions achieved the highest carbon conversion and cold gas efficiencies of 91 and 94%, respectively.

In addition, a relatively new method for monitoring hydrodynamic conditions in fluidized bed reactors using high-frequency bed pressure fluctuation measurement was demonstrated. This method proved capable of being used as a fluidized bed diagnostic method under reactive conditions.

CONTENTS

APPENDICES

CHAPTER 1

INTRODUCTION

1.1. Biomass as an energy feedstock

Since mankind's earliest existence, branches, twigs, bark, peat, grasses, plant and animal waste, leaves, moss, and various other forms of what we now classify as "biomass" were a source of energy in the form of heat and light. In essence, biomass was mankind's first fuel. In more recent history, the role of biomass has been expanded to uses in the production of charcoal, paper, steam, weapons, tools, sports equipment, and building materials. Biomass, a renewable source of materials and energy when harvested such that an ecosystem's biomass inventory does not decrease, has experienced a sharp decrease in its utilization due to the discovery and development of worldwide fossil and mineral resources. However, concerns about the finite and decreasing amount of fossil and mineral resources, in addition to the health and climate impacts of fossil resource use, have caused a growth in interest and innovative methods for converting renewable biomass resources into products that fit our modern lifestyle.

With worldwide energy consumption projected to increase by 9.8 quadrillion Btu (quads) per year on an average annual basis from 505 quads in 2008 to 770 quads in 2035, it is imperative that resources exist to meet global energy needs. In the United States, petroleum consumption has increased by over 25% during the past 30 years; however, the amount of domestic petroleum production has decreased by approximately 30% and the amount of imported petroleum has increased by nearly 300% since 1970 (*1*). Utilization of biomass and waste materials has the potential to make a significant contribution to domestic energy supply. An annual, sustainable supply of approximately 1.3 billion dry tons of biomass, primarily derived from forest and agricultural resources, is available for energy and fuels production in the United States (*2*). This amounts to approximately one-third of the total petroleum consumption in the United States. In addition, most biomass-derived energy results in substantially lower greenhouse gas emissions compared to fossil-derived energy (*3*).

1.2. Gasification background

Gasification is the process of converting a carbonaceous feedstock to synthesis gas (syngas), a valuable gaseous fuel primarily comprising hydrogen (H_2), carbon monoxide (CO), methane (CH_4), and carbon dioxide (CO_2). A reactive environment at moderate temperature (>700°C, 1300°F), and in cases elevated pressure (up to 70 atm), in reducing (oxygen-starved) conditions is necessary to convert the carbonaceous feedstock to synthesis gas. Typical gasification feedstocks include coal, petroleum coke (petcoke), wood, agricultural residues (e.g., corn stover, sugar cane bagasse), municipal solid waste (MSW), peat, and energy crops (e.g., switchgrass, miscanthus, jatropha).

In general, the gasification can be separated into four processes: drying, devolatilization, char and volatile oxidation, and gasification.

The drying process occurs rapidly as the fuel particle is introduced into the high-temperature, reactive environment. As heat is supplied to the particle by the high-temperature conditions in the reactor, moisture in the particle vaporizes. Typically, a low moisture content (MC) fuel is desirable because vaporization of moisture in the fuel particle requires relatively large amounts of energy (2250 kJ/kg, 1000 Btu/lb, 10%+ of the fuel heating value).

Following the drying of the fuel material, the volatile components vaporize in a process known as devolatilization. This complex, rapid progression of physical and chemical processes occurs between 150°C and 700°C and is heavily dependent on the rate of heat transfer to, the size of, and the porosity of the fuel particle. The composition of the gases produced from devolatilization depends on the gasifier temperature, pressure, and the gas composition in the environment surrounding the particle. For biomass particles in a fluidized bed gasifier at 1300°F, devolatilization occurs within times on the order of 2-3 seconds (*4*). For a pulverized coal particle, the devolatilization time is on the order of 200-300 milliseconds (*5*). Following devolatilization, the particle is reduced to char, a solid residue mainly containing carbon and noncombustible ash.

After devolatilization of the fuel particle, a portion of the volatile gases and char reacts with the oxidant in the reactor in a series of exothermic reactions. This process is critical for gasification as it provides some, or all in the case of autothermal gasification, of the heat required to drive the endothermic gasification reactions. In the case of steam gasification, the water-gas shift reaction is utilized to produce increased amounts of hydrogen.

The endothermic reactions that are driven by the reactive conditions in the gasifier yield combustible gases, including hydrogen, carbon monoxide, and methane. Depending on the desired product gas composition, conditions in the gasifier can be tailored to produce specific gas species. The primary chemical reactions that encompass the overall gasification process are listed in Table 1.

Table 1. Primary gasification reactions (*5–7*)

Reaction	Formula	Heat of reaction (MJ/kmol)
R1. Char gasification	$C + \frac{1}{2}O_2 \rightarrow CO$	-111
R2. Char oxidation	$C + O_2 \rightarrow CO_2$	-394
R3. Carbon monoxide oxidation	$CO + \frac{1}{2}O_2 \rightarrow CO_2$	-238
R4. Hydrogen oxidation	$H_2 + \frac{1}{2}O_2 \rightarrow H_2O$	-243
R5. Water-gas	$C + H_2O \rightarrow CO + H_2$	+131
R6. Methanation	$C + 2H_2 \rightarrow CH_4$	-75
R7. Methane reforming	$CH_4 + H_2O \leftrightarrow CO + 3H_2$	+206
R8. Methane oxidation	$CH_4 + 2O_2 \rightarrow CO_2 + H_2O$	-803
R9. Water-gas shift	$CO + H_2O \leftrightarrow CO_2 + H_2$	-41
R10. Carbon dioxide gasification	$C + CO_2 \leftrightarrow 2CO$	+172
R11. Methane reforming	$CH_4 + 2H_2O \leftrightarrow CO_2 + 4H_2$	-165
R12. Steam hydrocarbon reforming[1]	$C_xH_y + aH_2O \leftrightarrow bCH_4 + cCO_2$	

[1] "x" and "y" refer to the number of moles of carbon and hydrogen, respectively, in the hydrocarbon reactant. "a", "b", and "c" refer to the number of moles of steam, methane, and carbon dioxide, respectively.

CHAPTER 2

LITERATURE REVIEW

2.1. Tar reduction methods

When a carbonaceous material is heated, the molecular bonds that hold the material structure together fracture, resulting in the release of long chain molecules during the devolatilization process. The smallest molecules are light gases (e.g., hydrogen, carbon monoxide, and methane). The larger molecules are referred to as "tars," which are long chain hydrocarbon molecules that resemble the original fuel material. Operationally, "tar" species in gasification product gas are important because they can condense in significant quantities at relatively high temperature (<700°F) (*8*). Formally, gasifier tars are defined as all organic products with a boiling temperature above that of benzene (*9*). The accumulation of condensed "tars" on components in the gasification system can lead to clogging, corrosion, slagging, and catalyst deactivation (*10*).

Due to the importance of tar reduction on the commercial success of biomass gasification, a number of methods have been proposed and tested to produce low-tar synthesis gas. In general, tar content is reduced in two ways: chemical methods and physical methods. Chemical methods destroy tar by converting it into smaller hydrocarbons, thus retaining most of the tar energy content in the synthesis gas. Physical methods remove tar from the synthesis gas stream. Arena et al. (*11*) classify chemical and physical methods for tar reduction into two categories: primary methods and secondary methods. Primary methods attempt to reduce tar content by tuning conditions in the gasifier (e.g., temperature, pressure, stoichiometric ratio, gas residence time, bed material, etc.) to yield a low tar content synthesis gas. Secondary methods utilize downstream processes such as filters, scrubbers, catalytic and thermal crackers, cyclones, and separators to achieve tar contents adequate for downstream processes. While primary methods are generally less effective than secondary methods, secondary methods are generally more expensive, and can shift the problem of tar in synthesis gas to disposal of the material used to remove the tars. Bergman et al. (*12*) illustrates the expectation that both primary and secondary methods will be needed for synthesis gas cleanup (Figure 1). However, as primary methods are better understood (with respect to feedstock flexibility, scale-up, production of waste-streams, decrease in gasifier efficiency, complex gasifier design, and narrow operating windows), they can potentially play a larger role in overall synthesis gas tar cleanup.

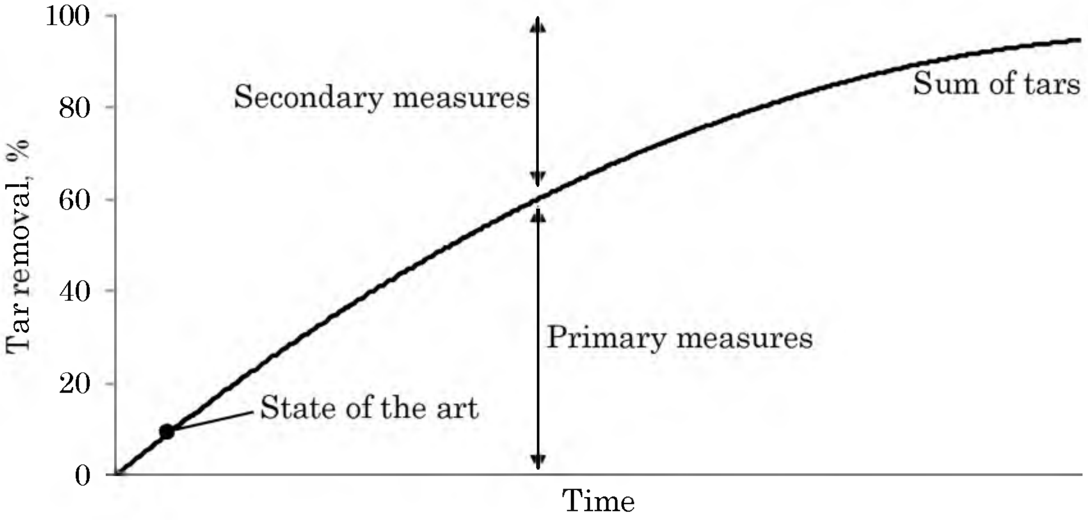

Figure 1. Need for primary and secondary tar removal measures with technology development vs. time

2.1.1. Primary methods

Primary methods for tar reduction attempt to reduce the tar content of the gasifier product gas within the gasifier. These methods are attractive because they avoid the cost and operational complexity of using downstream gas cleaning equipment. However, due to the variability of conditions within the gasifier, it is difficult to tune operating parameters to maximize tar reduction in the gasifier, while still maintaining the desired synthesis gas composition. The following sections present various primary tar reduction methods and cite literature in which those methods have been tested and reported.

2.1.1.1. Temperature

The primary reactions in gasification are endothermic, so availability of thermal energy plays an important role in biomass gasification. In general, higher temperatures promote thermal cracking of hydrocarbon chains into smaller molecules. Ideally, these thermally driven reactions continue until all volatile components of the biomass are broken down to simple, combustible gaseous molecules (hydrogen and carbon monoxide). In reality, some tar content remains in the product gas. Additionally, large amounts of energy input are required to drive thermal tar decomposition, which reduces the efficiency of the conversion process.

In general, hydrocarbon reforming with steam (R12) is favored at high temperature due to the endothermic nature of these reactions. However, the equilibrium yield of the shift reaction decreases with temperature, resulting in increased carbon monoxide concentration at the expense of hydrogen and carbon dioxide. Overall, the synthesis gas yield increases with temperature.

Of critical importance to the generation of volatile and tar species in the product gas is the heating rate of the feedstock particles, which determines the amount of time required for devolatilization. Introduction of the fuel particle into a high temperature reactor environment results in rapid devolatilization, which allows for the subsequent gas-phase reactions to occur, producing the final product gas. For high-temperature gasification (>1000°C), the devolatilization and gas-phase gasification reactions can occur simultaneously, resulting in a cleaner synthesis gas (*5*). For example, entrained flow gasification of pulverized coal at high temperature requires short residence times (10-200 milliseconds) for conversion (*13*).

Many studies have shown that increased reactor temperature results in decreased synthesis gas tar content. In a laboratory scale study investigating tar content from pine wood chips, Corella et al. (*14*) observed a 25% decrease in exit gas tar content with a temperature increase from 660°C to 810°C. In a similar study, Gil et al. (*15*) observe a 75% decrease in exit gas tar content and a 5% increase in hydrogen yield for a temperature increase from 800°C to 850°C. Studying similar conditions as Corella et al. (*14*) and Gil et al. (*15*), Narvaez et al. (*16*) observe a 75% decrease in tar content with a temperature change from 700°C to 800°C. Gasifying biomass in a circulating fluidized bed reactor, Lin et al. (*17*) report a tar content decrease from 15 g/Nm^3 to 0.54 g/Nm^3 for an average bed temperature increase from 700°C to 820°C. Fagbemi et al. (*18*) found that tar content in biomass pyrolysis gas increases until 600°C, after which the tar content decreases significantly. In a pilot-scale fluidized bed gasification experiment using pine chips as a feedstock, Gil et al. (*19*) increased the gasifier temperature autothermally by injecting oxygen in order to promote exothermic oxidation reactions. At low gasification ratios (GR, ratio of fluidizing agent flow rate-to-feed injection rate, similar to steam-to-biomass ratio), the temperature had a substantial effect on tar content in the exit gas. However, at higher GR values, the bed temperature did not have a significant effect on exit gas tar content, indicating that the added oxidizer in the blast flow had a larger effect on reducing tar content than the temperature.

While synthesis gas tar content generally decreases with increasing gasifier temperature, as shown from the previously mentioned studies, increased gasifier temperature can also result in the formation of more complex tertiary tars that can be more problematic for end-use devices than primary and secondary tars. Evans and Milne (*20*) performed biomass gasification experiments and measured the tar composition using molecular-beam mass-spectrometry (MBMS) while varying the reaction severity (temperature and residence time). While the overall tar yield decreased with reaction severity, the ratio of tertiary to secondary tars increased. In a similar experiment for air-blown, pressurized fluidized bed gasification of woody biomass, Simell et al. (*21*) observed increases in the concentration of heavy PAH tar species with the fluidized bed temperature. Mayerhofer et al. (*22*) measured tar yield and composition during wood pellet steam gasification in a laboratory scale, top-fed, bubbling fluidized bed and measured a 38% decrease in total tar but a 13% increase in tertiary tars (naphthalene) for a bed temperature increase from 750 to 840°C. Evans and

Milne (*23*) point out the dilemma that is encountered when optimizing efficiency and reaction rate through high-temperature operation and heavy tar formation. While the benefit of high-temperature operation is reduced overall tar concentration, the formation of refractory tertiary tars presents challenges for cleanup processes and end-use devices. Furthermore, heavy tertiary products are likely to mature to higher molecular weight species and onward to soot, which can be a serious operational concern.

As indicated from these findings, there is a good deal of variation in the amount of tar reduction due to reactor temperature increase. Some of this variation can be accounted for in the differences in type and scale of reactor. However, it is likely that a good deal of this variation comes from the method utilized for tar sampling and the definition of "tar" used. Many of these studies were performed prior to serious discussion about tar protocols and subsequent development of standard tar measurement methods at the IEA Bioenergy meeting in 1998. Therefore, a tar definition and tar sampling methods were not consistent across studies. This reinforces the need for adhering to current standards and also reporting any variation from the standard, as emphasized by Milne et al. (*23*).

2.1.1.2. Pressure

High-pressure gasification has recently gained attention due in large part to the increased interest in integrated gasification, combined cycle (IGCC) power plants and catalytic fuels synthesis process, both of which require high pressures. High-pressure gasification experiments are difficult to perform due to the added cost of high-pressure equipment, particularly in solids feeding for biomass gasification. Therefore, relatively little work has been done in investigating the effect of pressure on tar content. In addition to the cost of running high-pressure experiments, sampling tar in a high-pressure environment offers additional difficulties primarily related to constructing a high-temperature, high-pressure sampling probe and filter assembly. The European Committee for Standardization (CEN) (*24*) tar sampling protocol technical report outlines a method for sampling condensable hydrocarbons using a high-temperature, high-pressure probe and filter assembly which requires robust construction with specialty materials and a careful measurement procedure.

For gasification in general, operation at elevated pressure has a significant effect on the composition and yield of products. The forward methanation (R6 in Table 1) and methane reforming reactions (R7) are enhanced at high pressure while the water-gas (R5) and carbon dioxide gasification (R10) reactions are suppressed, resulting in a higher methane, carbon dioxide and steam content and lower hydrogen and carbon monoxide content. Due to the higher methane content, the heating value of the product gas per unit volume increases with pressure(*5*).

In general, steam reforming of a hydrocarbon (R12 in Table 1) species is favored at higher pressure, as these reactions involve a decrease in volume in the forward direction (*6*). However, due to the complexity of biomass gasifier tars and the pathways to their formation, a variety of products can be formed, depending on gasifier pressure. Evans and Milne (*25*) identify the potential pathways for the pyrolysis of biomass at low and high pressure. Low pressure biomass conversion results in the formation of light gaseous products (e.g., synthesis gas) and primary oxygenated vapors, which go on to form light hydrocarbons, aromatics, and oxygenates and onward again to polynuclear aromatics, synthesis gas, and soot. High pressure biomass conversion, on the other hand, primarily results in the formation of primary hydrocarbon liquids, which can go on to form condensed oils and coke (solid carbon residue) or reform to lighter gaseous hydrocarbons and ultimately synthesis gas if reaction conditions are adequate (e.g., high temperature, long residence time).

In addition to the pressure effect on product formation pathway, the devolatilization process in general has some dependence on pressure, although much less than temperature. For an atmospheric combustion process and a pressurized gasification process, the weight loss due to devolatilization can be on the order of 10% less at typical gasifier pressures of 30 bar (*5*). This is due in part to lower diffusivity of evolved species from the fuel particle and also to recondensation of volatile components on char particles at elevated pressure conditions.

Knight (*26*) investigated the effect of pressure on tar yield for gasification of woodchips and found that there was a 25% decrease in total tar content with a pressure increase from 8 to 24 bar. However, the PAH content increased by approximately 50%, indicating that the formation of secondary and tertiary tars likely increases at high temperature and high pressure. Brage et al. (*27*) measured a 40% increase in tar concentration for an increase in pressure from 0.4 to 1.5 MPa in a top-fed laboratory-scale fluidized bed gasifier operating between 700 and 900°C. Condensable hydrocarbons (C_6 and larger) were measured in the product gas stream from commercial scale air gasification of bagasse and found to decrease from 2.3 to 0.8% (by weight) with a pressure increase from 2.9 to 4.2 bar and indicate benzene and naphthalene as the principal components (*28*). In a study similar to the work reported in this thesis, Mayerhofer et al. (*22*) measured tar yield and concentration during biomass gasification at atmospheric and elevated pressure (0.25 MPa). At lower bed temperature (750°C), tar yield increases by nearly 50% with increasing pressure and constant steam-to-biomass ratio

(1.2). Larger tar species accounted for most of the increase, especially in the case of naphthalene, which increased by nearly 200% from atmospheric to elevated pressure. These results were consistent at higher bed temperature (800°C) and lower steam-to-biomass ratio (0.8). Inconsistencies in total tar reductions as reported from the literature arise from inconsistency in the definition of tar used and also due to differences in pressure effect on conversion of different classes of tars.

2.1.1.3. Reactive gas

Depending on the desired product gas composition, a variety of gases may be used for the reactive flow in biomass gasification. The relationship of fluidizing agent to tar destruction has been widely studied. The introduction of an oxidizer (e.g., air, oxygen) results in exothermic reactions, which convert hydrocarbons (including tars) molecules to smaller hydrocarbons and carbon dioxide. Heat produced from exothermic reactions also helps to drive endothermic gasification reactions and the thermal cracking of heavy hydrocarbons. Disadvantages of using oxygenated fluidizing agents is the loss of product gas heating value due to increased carbon dioxide content, and nitrogen content if air is used, and the additional cost of producing oxygen.

Steam, as well as the combination of steam and air/oxygen, gasification is receiving increased attention due to improved conversion efficiency and energy content of the product gas. Herguido et al. (*29*) used pure steam as the fluidizing agent and reported the effects of the steam-to-biomass ratio (SB) on the product distribution. The use of steam yielded high concentrations of hydrogen in the product gas (up to 60% by volume) as well as a decrease in total tar content from approximately 8% (by volume) of the total product gas at SB = 0.5, to <1% at SB = 2.5 due to the tar reforming reaction. However, the heating value of the product gas decreased due to increased concentration of carbon dioxide and decreased concentration of carbon monoxide from the water-gas shift reaction (R9 in Table 1).

A disadvantage of steam gasification is that steam gasification is endothermic, so it requires heat addition from an external source, or through the addition of oxygen.

2.1.1.4. Fluidizing velocity

The residence time of the gas in the gasifier can be controlled by either changing the geometry of the gasifier or by modulating the superficial gas velocity (SGV, velocity of reactive gas flow through the gasifier). Increased gas residence time provides more time for reactions to occur in the gasifier. With respect to tar composition, increased residence time can be beneficial in that there is more time for primary tars to react, producing desirable gaseous species. However, there is also potential for increased concentrations of secondary and tertiary tars (*23*).

Results from literature vary somewhat, with some experiments showing that there is very little or no tar content dependence on gas residence time to others showing significant reduction in tar content and increased value of product gas with gas residence time. Bridgwater (*30*) addressed increased bed and freeboard residence times as a partial solution for exit gas tar reduction. Arena et al. (*11*) report a 50% decrease in exit gas tar content and a 15% increase in lower heating value (LHV) for a decrease in superficial gas velocity from 0.7 m/s to 0.5 m/s for air gasification of polyethylene waste. Kinoshita et al. (*28*) suggest that residence time has no effect on the amount of tar in the product gas but does have significant effects on the composition of the tar, shifting from large quantities of oxygenated primary tars for short residence times to multiple ring aromatic (secondary and tertiary) tars for longer residence times. Corella et al. (*14*) evaluated the effects of a variety of operating parameters on tar reduction for gasification of pine woodchips and found that gas residence time had very little influence on exit gas tar content. However, for this experiment, the feedstock was injected at the top of the gasifier, which likely flawed the results because the biomass devolatilized as it entered the reactor. Therefore, tar formed as the fuel devolatilized likely exited the reactor without ever reaching the gasifier bed.

2.1.1.5. Stoichiometric ratio

The stoichiometric ratio (SR, ratio of oxygen to fuel) has been shown to have a strong influence on reducing tar content. As the SR is increased, there is more oxygen available to react with volatiles being released from the feedstock during devolatilization. In addition, increased oxygen content can also result in increased gasifier temperature driving thermal decomposition of hydrocarbons. However, increased SR also results in increased production of carbon dioxide, which reduces the LHV of the product gas.

Much of the tar data related to SR show drastic reductions with increasing SR. Arena et al. (*11*) observed a 50% (by weight) decrease in tar content and a 25% decrease in product gas LHV for an SR increase from 0.2 to 0.3. Lv et al. (*31*) found that there are two stages of gasification based on SR:

- $0.19 < SR < 0.23$: increase in gas yield and LHV and a decrease in tar content
- $0.23 < SR < 0.27$: decrease in LHV and decrease in tar content

Narvaez et al. (*16*) reported tar content as low as 2 g/Nm^3 with an SR = 0.35. However, the resulting hydrogen and carbon monoxide concentrations were low at 10 and 15% (by volume), respectively.

2.1.1.6. Feedstock characteristics

To some degree, the biomass feedstock has an effect on the amount of tar in the product gas. However, for a particular feedstock, careful selection of the gasifier operating parameters can greatly reduce tar content. For cellulosic biomass feedstocks, the amount of tar in the exit gas is related to the content of cellulose, hemicellulose, and lignin in the feedstock. Kosstrin (*32*) reported the maximum tar yields for different types of biomass and residues: wood (35%, by weight), paper (60%), and sawdust (30%). In agreement with the results reported by Kosstrin (*32*), Hanaoka et al. (*33*) and Sadakata et al. (*34*) found that feedstocks with higher cellulose and hemicelluloses content generate product gases with higher tar content.

In addition to the lignocellulosic composition of the feedstock, van Paasen (*35*) studied other biomass properties, including ash content and moisture content. They found that ash content had a negligible effect on tar concentration. However, a 35% increase in moisture content reduced the total tar concentration from 14 to 8 g/Nm^3 on a dry basis. They also noted significant variation in the total tar concentration but very little change in tar composition with changing lignocellulosic composition.

2.1.1.7. Feedstock pretreatment

A method for improving feedstock characteristic to better suit the particular thermal conversion process is to prepare the feedstock in a pretreatment process. One such process is torrefaction, a mild pyrolysis process which drives off moisture and some portion of the volatile matter in the feedstock, thus producing a dry, energy dense fuel material.

Couhert et al. (*36*) carried out gasification experiments using torrefied beech wood in an entrained flow gasifier. From this study, it was confirmed that torrefaction reduces the oxygen-to-carbon ratio in the feedstock and the quality of the synthesis gas produced is improved. Synthesis gas produced from torrefied wood gasification was shown to produce 7% (by volume) more hydrogen, 20% more carbon monoxide, and approximately the same concentration of carbon dioxide as produced with the raw wood feedstock. Qin et al. (*37*) propose a process which combines torrefaction of agricultural residues with co-gasification of the treated residues with coal in an entrained flow gasifier. They point out several advantages of such an arrangement, including utilization of the torrefaction product gas and liquids as an energy input to the pyrolysis reactor and improved gasification of moist biomass feedstocks.

Many positive and negative effects of torrefaction on gasification have been pointed out through the previous studies. According to Prins et al. (*38*), the integration of torrefaction and gasification results in higher overall energy efficiency than stand-alone biomass gasification. Some other advantages of using torrefied feedstock are better fluidization quality in fluidized bed gasifiers, less problems with feedstock storage (e.g., molding), improved feeding qualities, and the ease of producing a ground feedstock (*36*, *38*, *39*). The disadvantages of using torrefied feedstock are the decreased net efficiency of the gasifier, decreased synthesis gas yield, increased heat load on the gasifier, and increased char residue production (*38*–*40*).

2.1.1.8. Bed material

An increasingly promising method for improved performance in fluidized bed gasification of biomass is the use of bed additives, which promote catalytic reduction of tar content. Catalytic bed materials have been shown to be very effective at reducing tar levels to or near maximum allowable levels for end-use devices (engines, compressors, turbines, fuel cells, etc.). However, there is still a need for additional research regarding bed additives in order to increase selectivity, resistivity to deactivation due to fouling and sintering, particle strength and lifetime, and to decrease cost.

Two catalytic materials that have been widely studied for tar reduction are olivine and dolomite. Arena et al. (*11*) studied the effects of activated olivine as a bed material in a pilot-scale, bubbling fluidized bed gasifier using waste polyethylene as a feedstock, and considered olivine addition to the bed to be the most effective primary method for tar reduction. The use of inert quartz sand yielded on average about 100 g/Nm^3 of tar in the exit gas. Initial tests with olivine yielded tar reductions to about 14 g/Nm^3, and after increasing the temperature to 850-900°C, the tar content was reportedly nearly eliminated (not measurable) and the synthesis gas yield increased from 80 Nm^3/h to 120 Nm^3/h. Olivine is attractive as a bed additive because it is a naturally occurring mineral which does not require large amounts of processing before use as a bed additive in gasification. The use of dolomite, also a naturally occurring ore, has been studied as a bed additive and has been shown to decrease tar content while also increasing product gas yield. Gil et al. (*15*) report that the use of 30% (by volume) dolomite in the bed results in a reduction of total tar content to 1 g/Nm^3. Experiments have shown that dolomite does have some problems with softening at high temperature and breaking during use in a fluidized bed, both rendering the catalyst inactive.

2.1.2. Secondary methods

Secondary methods for tar reduction in gasification consist mainly of hot gas cleaning downstream of the gasifier. These methods include thermal cracking, catalytic cracking, cyclones, ceramic filters, fabric, electrostatic filters, and scrubbers. In general, these methods are effective at removing a large amount of the tar content in the synthesis gas. However, they are not always economically viable and can also be very complex if very low tar content is required. The focus of the proposed research work relates mostly to primary methods. Therefore, secondary methods will be reviewed briefly.

2.1.2.1. Thermal cracking

Thermal cracking units are effective at using large amounts of energy (heat) to convert heavy hydrocarbons to lighter hydrocarbons. Typically, for thermal tar decomposition, a cracking unit temperature of at least 1250°C is needed (*41*). In their 1995 review, Bridgwater concluded that thermal cracking of biomass product gas is difficult due to the need for direct contact with a hot surface, and as a result, has a large energy cost (*30*).

2.1.2.2. Catalytic cracking

Catalytic cracking units have the same effects as catalysts added to a fluidized bed gasifier. The advantages of using an external vessel (or external vessels) for catalytic tar reforming are that the catalysts can be used in a fixed bed configuration (some catalyst particles easily erode and break in a fluidized bed), a downstream vessel can be maintained at a different temperature (methanation, steam reforming, and catalytic cracking are more effective at temperatures other than the gasification temperature), sulfur species formed from gasification can deactivate catalyst particles, and fluidization conditions can be adjusted for the specific catalyst particle (*42*). Studies have investigated the use of secondary catalyst beds using dolomites (*42–45*), pure calcite (*44*, *46*), pure magnesite (*44*), nickel-based catalysts (*47*, *48*), and olivine (*43*, *49*, *50*). The major disadvantage to catalytic conversion outside the gasifier is the added equipment cost. However, if a particular catalyst particle requires specific conditions, this cost can easily be outweighed by the benefit of using a selective catalyst.

2.1.2.3. Mechanical methods

Han et al. (*51*) use the term "mechanism methods" (also "mechanical methods") for tar reduction by means of physical removal of tars from the exit gas stream. These methods include a particle filter, water scrubber, venturi scrubber, cyclone, electrostatic precipitator (ESP) (*35*, *52*), oil-based gas washer (*12*), and rotational particle separators. Mechanical methods are effective at removing particulate and tars from the exit gas with up to 99% (by weight) tar removal reported. A major disadvantage of mechanical methods is that the energy stored in the tar molecules is wasted as it becomes a process waste stream. This produces another problem in that the tar waste stream requires special handling and disposal as some hydrocarbon species are detrimental to human health and the environment. These methods are also generally expensive and maintenance intensive and can present various upsets in process operation such as large pressure drops.

2.2. Characterization of fluidization quality

The use of high-frequency measurements in flow fields is well established. In the study of turbulent flow fields, high-frequency measurement of the velocity components allows for the decomposition of the mass and momentum conservation equations and a model formulation for the Reynold's stress term allowing for a closed solution to the "turbulent closure problem." Applications of high-frequency flow field measurement range from aerodynamic studies on scaled wind tunnel models using hot wire anemometers to atmospheric boundary layer studies using sonic anemometers.

High-frequency pressure measurements are of interest in a wide variety of applications. While pressure, a scalar, does not provide the amount of detailed information about a flow field as the velocity field measurement can provide, the major advantage of its use for flow field diagnostics is the relative simplicity of its measurement. Acoustic measurements in combustion systems have been shown to provide information regarding flame stability, and have also been used in combustion control (*53*).

Reactive environments involving high velocities and rapid mixing (e.g., combustion and gasification) present a difficult challenge for *in situ* measurement of any kind. In many cases, exotic materials (e.g., metal alloys, ceramics) or complicated liquid or gas probe designs are required in order to withstand the conditions in high-temperature reactive environments (*54*). In addition, due to the relatively small length scales and short time scales of motion in these types of reactive processes (*55*), conventional measurement methods (e.g., bi-metallic junction temperature measurement) are not suitable for capturing the details of phenomena in a reactive environment.

The application of high-frequency pressure measurement in fluidized beds has been researched fairly extensively over the past 20 years, mostly through the use of small-scale, cold-flow fluidized bed experimental investigations. In general, tests are conducted using gas-solid, cold-flow fluidized beds which are equipped with a pressure transducer and data acquisition system capable of sampling data at relatively high frequencies (200-1000 Hz). The transducers are specially built for fast response pressure analysis, generally utilizing precision piezo-electric measurement in small volumes (*56*).

In general, a time-series signal can be analyzed by one of the three types of analysis: time domain, frequency domain, and state-space. While a large amount of research has been reported in literature related to the application of these analyses to fluidized bed systems, Johnsson et al. (*57*) report that it is difficult to draw universal conclusions from data in the literature due to the wide variability of experimental conditions (e.g., geometry, particle characteristics, analytical technique, etc.). For example, two foundational papers in the area by Yerushami and Avidan (*58*), and Bi and Fan (*59*) come to different conclusions about characteristics of flow measurements that indicate transition to turbulent fluidization. In an effort to standardize measurement and analysis techniques for time-series pressure fluctuations, Johnsson et al. (*57*) and van Ommen et al. (*56*) have published broad reviews of the subject, including recommended practices, especially for signal analysis procedures.

Time domain analysis is generally the simplest analysis method, and should be the first method used for analysis of the pressure fluctuation signal. Computation of the central moments of the signal can reveal information related to the probability distribution of the signal. The standard deviation has been reported to indicate transition from bubbling to turbulent transition (*60*). However, this is disputed as over-predicting turbulent transition (*61*). Higher order moments (e.g., variance, skewness, and kurtosis) of the pressure signal have been reported by only a few researchers in literature (*57*). The value of the information contained in higher order moments and probability density function (PDF) of the pressure signal is disputed as all of the information in the time scale is lost. In order to preserve the time scale information, the PDF of the pressure *increments* ($\Delta p = p(t + \Delta t) - p(t)$) is computed rather than the PDF of the original pressure signal. For varying increments Δt, Gheorgui et al. (*62*) showed that non-Gaussian PDFs were observed in lower velocity flow regimes, which could indicate turbulent flow characteristics for these regimes.

Frequency domain analysis is another common method for analyzing pressure measurements made in fluidized beds. In general, frequency analysis is carried out using a Fourier transform of the signal and subsequently applying spectral or wavelet methods to the signal. Spectral analysis is generally applied to estimate the dominant frequencies present in the signal and relating those to physical transport phenomena in the fluidized bed (*63*). To determine dominant frequencies, van Ommen et al. (*64*) state that sampling frequencies of about 20 Hz are required since most spectral information is contained in frequencies of 10 Hz or less. Spectral analysis has also been applied to validate scale-up of fluidized beds by comparing spectra from model and full-scale units (*65*). In addition to determination of the dominant frequencies, characteristics of the power spectrum fall-off at high frequency resemble characteristics of turbulent flow (*56*). However, Bai et al. (*66*) attribute the spectrum fall-off to bubble size distributions in bubbling fluidized beds, which generally exhibit a power-law in the tail of the distribution, which could account for the fall-off in the power spectrum.

A limited amount of work has been done to investigate the use of pressure fluctuation measurement and analysis on the diagnostics of fluidized bed reactors. Most reported pressure fluctuation measurements for diagnostic purposes focus on prediction and prevention of fluidized bed agglomeration, a significant problem. Van Ommen et al. (*67*) applied pressure fluctuation measurement to an industrial fluidized bed and found that the standard deviation of the pressure fluctuation signal could be used to detect defluidization. Gheorghui et al. (*68*) showed that the shape of the PDF of pressure increments is sensitive to agglomeration in biomass gasification. Lin et al. (*69*) investigated the formation of organic pollutants from fluidized bed incineration and found a correlation between polycyclic aromatic hydrocarbon (PAH) formation and fluidizing velocity using pressure signal diagnostics.

A potential shortcoming of local diagnostic measurement is the limited region of detectability. In the case of fluidized bed diagnostics, different sections of the bed may exhibit different hydrodynamic characteristics. For example, plugging of a single bubble cap or sparger vane will generate a local dead zone in the bed, which can become a risk for particle agglomeration. In order to assess the range of detectability for local pressure fluctuation measurement in fluidized beds, van Ommen et al. (*64*) investigated the spacing of multiple probes in the bed and the ability of adjacent probes to resolve bubble flow in the proximity of those probes. From experiments and modeling of bubble formation and flow, it was determined that pressure waves can be detected from a radial distance of approximately 0.5 m. from their origin for fluidized beds in the bubbling regime. Therefore, for shallow beds of approximately 1 m. in height, a single pressure probe can be used for diagnostic monitoring and should be located at an axial distance of 30-40% of the bed height from the distributor plate.

In addition to the work of van Ommen on determining the detectable region for a single pressure probe in a fluidized bed, Brown et al. (*70*) investigated problems associated with pressure probe placement at the wall of the bed. Static pressure fluctuations were measured at the wall and center of the bed in several cold-flow fluidized beds of different diameter. Power spectrums of both pressure signals were identical, indicating that pressure measurements from the wall and bed interior both detected pressure wave phenomena in the bed. Furthermore, this result supports the contended theory that global transport phenomena are responsible for pressure fluctuations in bubbling fluidized beds rather than local, random phenomena (e.g., bubbles). If the passage of bubbles by the static pressure probe were responsible for all or part of the pressure fluctuations in the bed, an internally positioned probe would produce a different pressure fluctuation signal since the majority of bubbles rise to the bed surface through the center of the bed. Furthermore, Brown et al. (*71*) strengthened this argument by performing cold-flow fluidized bed experiments with distributor plates containing different numbers of holes. These experiments again showed no power spectra dependence on the number of distributor plate holes which produce different bubble structures at different formation frequencies.

CHAPTER 3

OBJECTIVES AND APPROACHES

The primary objective of this research is to assess the effectiveness of primary methods for tar reduction during pilot-scale, fluidized bed gasification of woody biomass and residues. In addition, the effect of primary method implementation on gasifier performance and operability will be assessed using well-established metrics. The goal of this research is to identify operating conditions or windows that are suitable for operation of the pilot-scale gasifier and transferrable to pressurized steam gasification of biomass and residues in general. In addition to quantitative assessment of product and residue composition and yields, and system efficiency measurement, qualitative observations regarding the operation of the gasifier in general and under challenging conditions is provided. These data and observations will be a valuable addition to existing knowledge, and can be of use in the design of biomass gasification systems and relevant policy decisions.

This project focuses on answering the following questions:

1. Are primary methods for tar reduction effective at reducing tar content in synthesis gas produced from woody biomass gasification to end-use device requirements?
2. What are the associated impacts on gasifier performance and operability from the implementation of primary methods for tar reduction?
3. Is the measurement and analysis of in-bed, local pressure fluctuations a suitable method for assessing the hydrodynamic conditions in a fluidized bed gasifier?

In order to answer these research questions, experimental and physical modeling approaches were utilized and are briefly summarized:

- Experimental research was performed using a 200 kW_{th}, fluidized bed gasifier upgraded for use with solid feedstocks and hot-synthesis gas filtration under pressurized conditions. This system was used to assess primary methods for tar reduction, and measurement of fluidized bed hydrodynamics from local pressure fluctuations.
- Tar sampling and analysis was conducted using the conventional cold-trapping method and solid phase extraction (SPE) method. Measured tar yields and composition for varying gasifier operating conditions were utilized to develop conclusions regarding the effectiveness of primary methods for tar reduction.

- Local bed pressure is measured at high frequency to resolve details regarding flow conditions in the fluidized bed. A scaled, cold-flow model of the gasifier was utilized for measurement method validation and controlled studies. The apparatus was installed on the pilot-scale, fluidized bed gasifier and sampled pressure measurements during several gasifier experimental campaigns. The measured pressure signal was decomposed into its mean and fluctuating components, and statistical and spectral analyses were used to identify important flow features detected by the probe.

CHAPTER 4

MATERIALS AND METHODS

The proposed research project was carried out using experimental facilities at the University of Utah, in particular the Industrial Combustion and Gasification Research Center (ICGRF). The ICGRF is well equipped with experimental and analytical equipment for use in experimental research involving reactive processes. The following is a description of the equipment and methods that were utilized to complete the objectives of this research.

4.1. Biomass gasification system

The ICGRF at the University of Utah includes all feed, product gas handling, and analytical systems required for synthesis gas characterization. The entire gasification system (Figure 2) is integrated into a distributed controls system (DCS), which allows for safe operation by an experienced operator. The DCS also includes safety systems which will automatically shut down and purge the gasification system in the case of an undesirable event (e.g., power failure or loss of cooling water). Important measurements (e.g., temperatures, pressures, flow rates, gas composition) throughout the

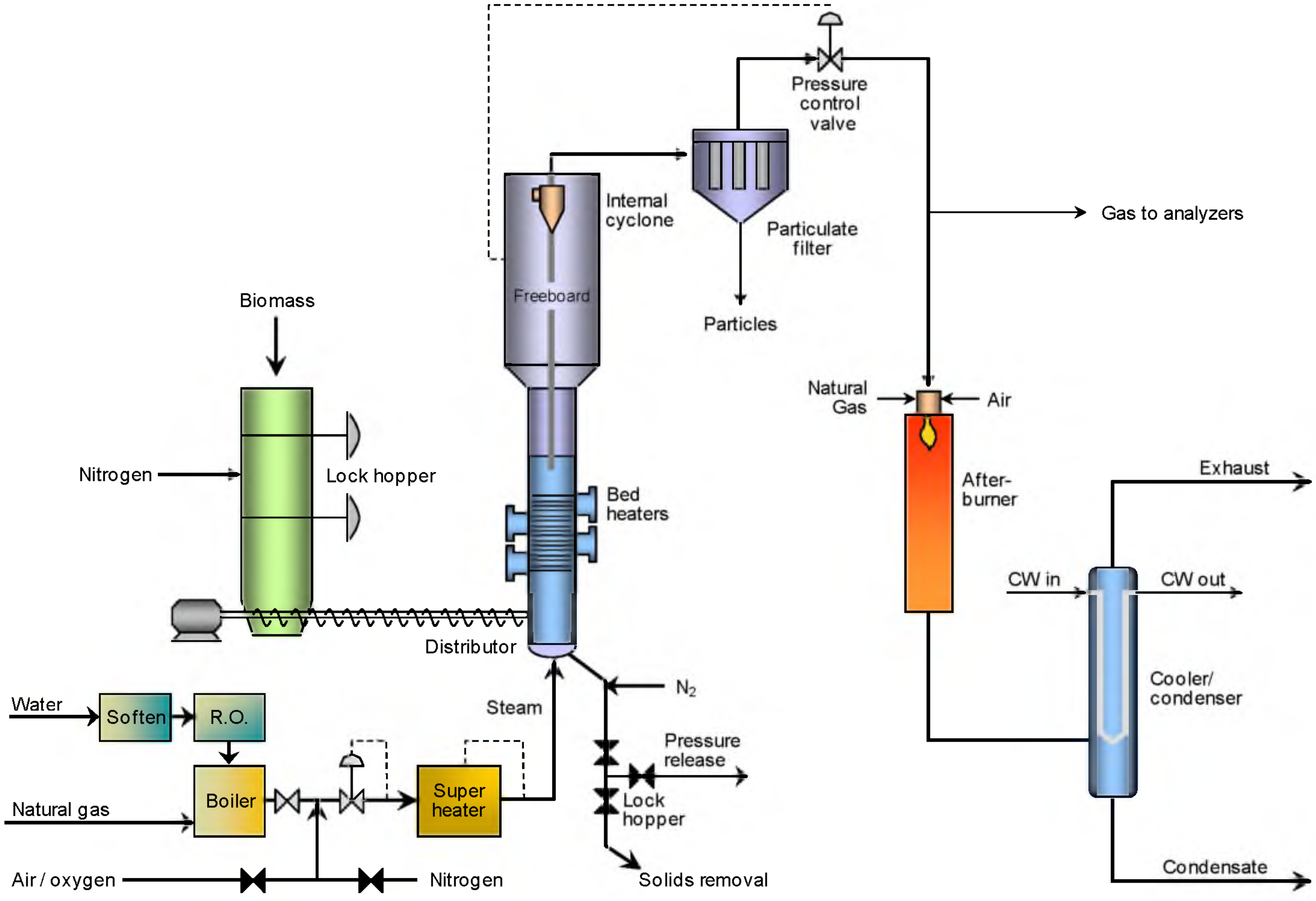

Figure 2. University of Utah biomass gasification system schematic

system are monitored and continuously recorded throughout an experimental campaign. Typical operating parameters, as determined by design of the system and limitations due to individual components, for the gasification system are displayed in Table 2.

The experimental work for this research will be carried out using a 200 kW, steam-blown, bubbling fluidized bed gasifier housed in the ICGRF (Figure 3). The gasifier is a refractory-lined pressure vessel capable of operating at temperatures up to 870°C (1600°F) and pressures up to 7 bar (100 psig). The fluidized bed section is 1.5 m (59 in.) in height and 25 cm (10 in.) in diameter. The freeboard section above the bed is 3 m (10 ft.) in height and expands from 25 cm (10 in.) to 36 cm (14 in) in diameter at the half-height to reduce gas velocity and limit particle entrainment. An internal cyclone is positioned within the reactor at the top of the freeboard to return particulate matter to the bed via a dipleg.

Steam is supplied to the gasifier by a 116 kW (396,000 Btu/hr) water-tube boiler that is capable of delivering up to 286 lb/hr of saturated steam. Prior to entering the gasifier, the steam is superheated by a 35 kW (119,400 Btu/hr) electrical resistance process heater. Inside the fluidized bed, additional heat can be supplied by four bundles of 20 each, Inconel® 800HT, electrical resistance cartridge heaters (Figure 3) capable of providing a total of 32 kW (109,200 Btu/hr) of heat to drive endothermic gasification reactions

Table 2. Fluidized bed biomass gasification system specifications

Specification	Typical		Maximum	
Reactor operating pressure	200 kPa	29.0 psia	689 kPa	100.0 psia
Reactor operating temperature	760°C	1400 °F	870°C	1600°F
Biomass feedrate	20 kg/hr	44 lb/hr	30 kg/hr	66 lb/hr
Steam feed rate	18 kg/hr	40 lb/hr	130 kg/hr	286 lb/hr
Superficial gas velocity	0.3 m/s	1.0 ft/s	1.52 m/s	5.00 ft/s
Bed diameter	0.25 m	10.0 inch	-	-
Bed height	1.50 m	59.0 inch	1.65 m	65.0 inch
Mass of bed solids	91 kg	200 lb	100 kg	220 lb

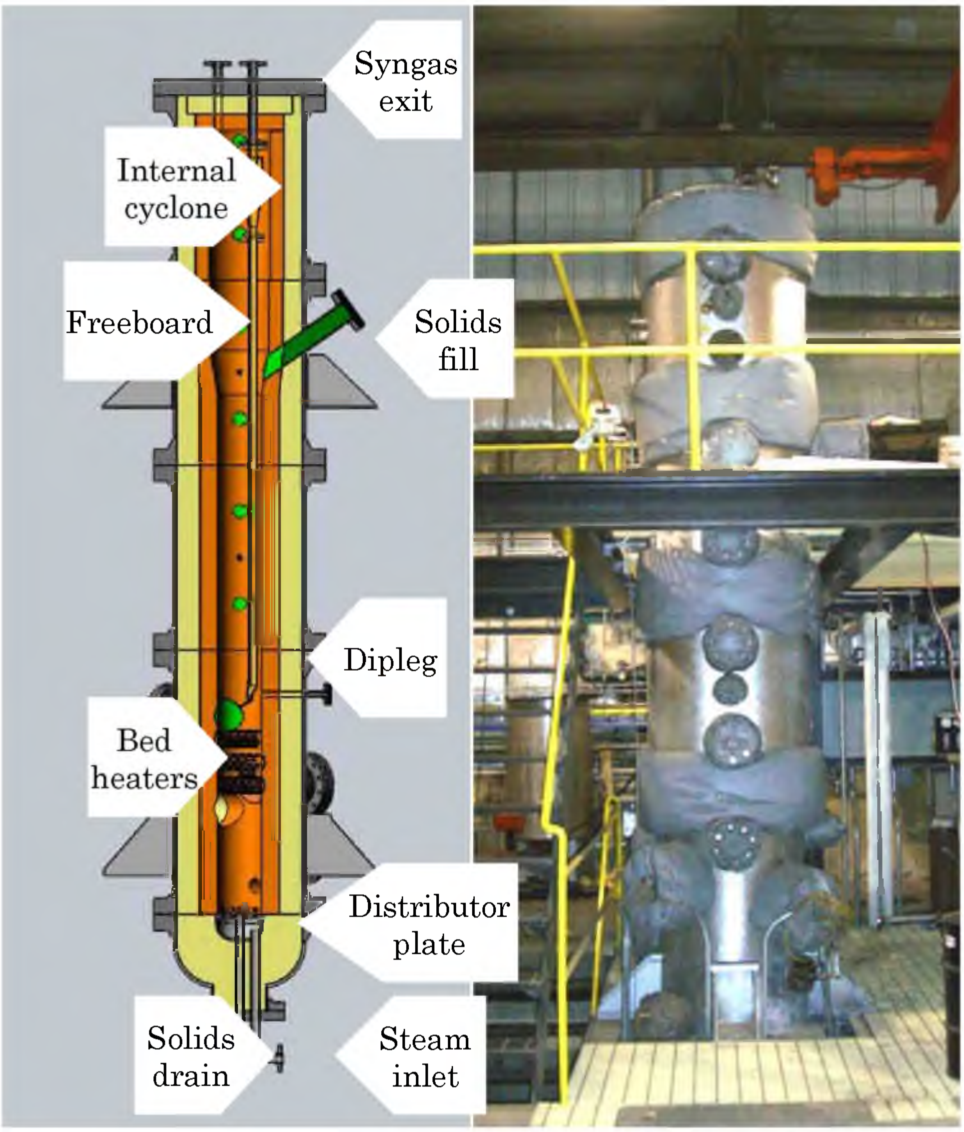

Figure 3. Fluidized bed gasifier annotated solid model cross-section (left) and actual fluidized bed reactor (right)

in the bed. The bed heaters can be automatically controlled to maintain a user-supplied bed temperature set point. Additional reactant gases (e.g., air, oxygen, carbon monoxide) can be added to the gasifier at various locations (e.g., inlet, bed, freeboard). Temperature and pressure are measured at various locations along the height of the reactor. Automatic (controlled by the fluidized bed pressure drop) or manually operated removal of bed solids can be achieved at any time by a nitrogen purged lock-hopper at the bottom of the gasifier.

Product gas exits the gasifier and is expanded to atmospheric pressure through a pressure control valve after which it is combusted in a 117 kW (400,000 Btu/hr), natural gas fired thermal oxidizer ("Afterburner" in Figure 2) to burn combustible species and destroy any condensable hydrocarbons and environmentally harmful species in the product gas. Prior to entering the thermal oxidizer, a slip-stream of product gas is sampled to monitor and record product gas composition using a continuous emissions analyzer (hydrogen, carbon monoxide, carbon dioxide, and methane) and micro-GC (18 species in the product gas). The flue gas from the afterburner is cooled and condensate is removed in a water-cooled shell-and-tube heat exchanger. The dry flue gas from the heat exchanger is exhausted from the facility through the flue gas handling system and induced draft blower.

In order to accommodate feeding of solid feedstocks, a pressurized feeder (Figure 4) was added to the gasification system, which is capable of feeding bulk solid feedstocks at feedrates up to 65 lb/hr. All components of the feeder are rated to operate at pressures up to 21 atm to match the pressure rating of the rest of the fluidized bed gasification system.

Feedstock material is introduced into pressurized conditions through a 1 ft^3 lock-hopper, which is sealed by "c-ball" valves with inflatable nitrile seals. Feedstock is transferred from the lock-hopper to the feed bin, which has a capacity of 3 ft^3. The feed bin is nitrogen purged to prevent backflow of hot

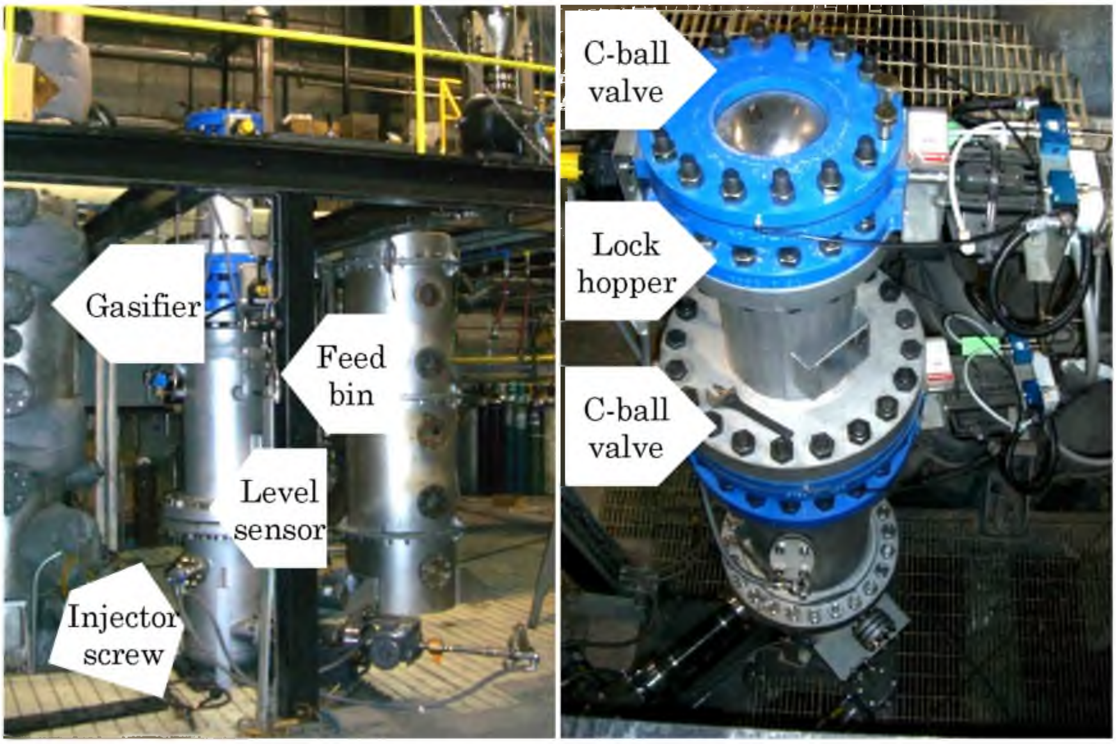

Figure 4. Pressurized solids feeder

reactor gas and bed solids into the feed vessel. A tuning fork level sensor in the feed bin controls an automated sequence to add fuel. Four variable frequency drive (VFD) controlled metering screws at the bottom of the feed bin meter fuel into the 6 ft. long, water cooled, AISI316, injector screw, which delivers feedstock into the gasifier near the bottom of the fluidized bed.

Due to the nature of solid fuel conversion processes, a substantial amount of particulate is generally present in the product gas. For most applications, the particulate content needs to be filtered or scrubbed out of the product gases to meet environmental regulations and prevent damage to downstream equipment. In the case of fluidized bed biomass gasification, a substantial amount of particulate entrainment is expected due to the presence of bed fines, char (carbon residue), and ash (feedstock inorganic content). For this system, an internal cyclone separates particulate from the exit gas stream and returns it to the bed through a dipleg (Figure 3). However, bed fines, char, and ash can still entrain in the gas flow exiting the cyclone. In order to remove entrained particulate from the product gas and protect downstream equipment (e.g., valves, flow meters, pressure transducers), a high-temperature particulate filter was installed downstream of the gasifier (Figure 5). The filter consists of seven, 30 in. long, Fecralloy®, metal fiber filter elements that are capable of removing 99% of particulate 10 micron in size and larger. The particulate filter vessel is constructed of AISI316L steel

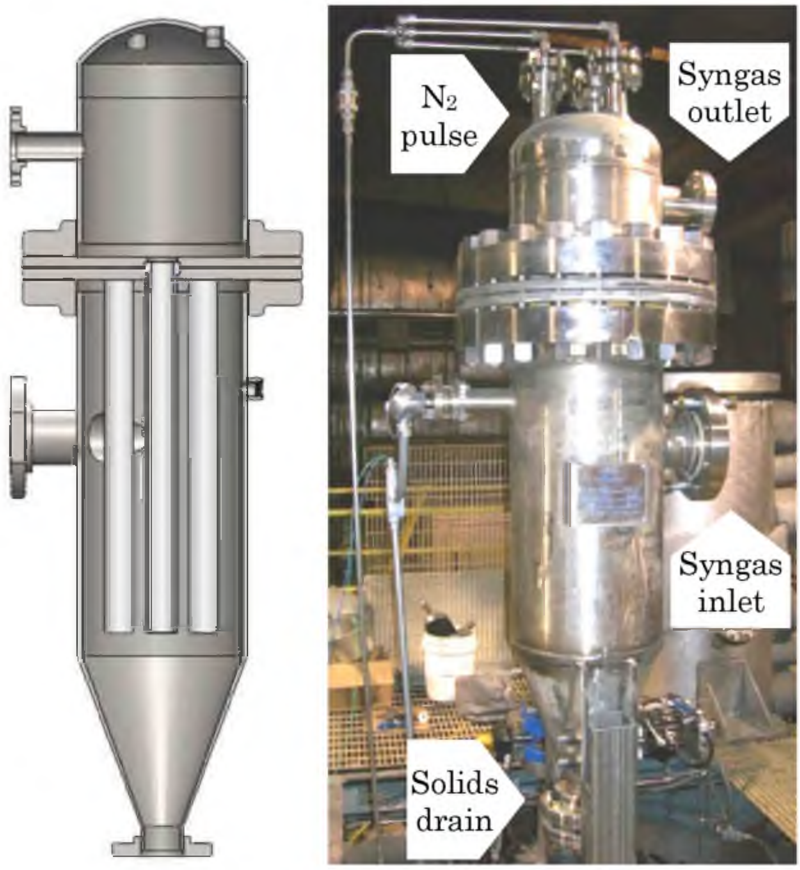

Figure 5. High-temperature particulate filter solid model (left) and installed (right)

and is rated for 1100°F at 500 psig. All flanges on the filter vessel are class 600# rated.

As particulate material is captured in the filter media, a "cake" of captured particles builds up on the surface of the filter elements, causing an increase in filter pressure drop and subsequent increase in gasifier pressure. In order to reduce the filter pressure drop, a nitrogen back-flush system pulses the filter elements with high pressure nitrogen to break loose the filter cake. During operation, particulate collected in the filter are removed via a lock-hopper at the conical bottom section of the filter vessel. This material will be weighed and carbon content will be determined by mass difference after a carbon burnout test of a representative filter sample. Accurate accounting of the solid carbon content exiting the gasifier allows for closure of a carbon balance on the system.

4.2. Biomass feedstock

A woody biomass feedstock for this research was prepared by the Department of Forest Biomaterials at North Carolina State University (NCSU). NCSU has facilities for chipping, sieving, and drying raw biomass materials. For this research, NCSU provided a loblolly pine material of size < 1 cm (0.375 in.) that was dried to <15% moisture content by weight. An elemental analysis of the feedstocks utilized in this research is provided by NCSU and is displayed in Table 3. The raw material was utilized for the primary methods test campaign and the TB (medium torrefied) and TC (dark torrefied) were utilized for the torrefied biomass campaign.

4.3. Synthesis gas sampling and analysis

Synthesis gas produced from these experiments was analyzed to determine yield and composition, which provided necessary data for

Table 3. Loblolly pine wood chip, torrefied material (TA-TC), and lignite (for comparison) compositions, dry basis (*calculated by difference)

	MC	Proximate analysis, wt%			Ultimate analysis, wt%				O/C Ratio	Heating Value (HHV), MJ/Kg
		VM	FC	Ash	C	H	N	O		
Raw	7.69	84.6	14.8	0.6	50.5	6.26	0.09	42.6	0.63	20.0 (18.2)
TA	6.32	78.6	20.8	0.6	55.0	5.94	0.11	38.3	0.52	22.7 (20.8)
TB	5.43	76.4	22.8	0.8	57.3	5.79	0.14	36.0	0.47	24.0 (22.1)
TC	4.03	59.9	38.6	1.4	65.8	4.87	0.28	27.6	0.31	26.3 (25.2)
Lignite	36.1	41.5	43.1	15.4	61.9	4.29	0.98	16.4	0.20	24.3

evaluating the performance of the gasifier. A wet gas slipstream is drawn from the main synthesis gas flow downstream of the particulate filter. The wet sample gas is cooled in a continuously flowing impinger, in which steam and tar components will condense. The cool, relatively dry gas is then routed through a refrigerated heat exchanger to further condense any low dew point tars and moisture remaining in the sample gas stream. The gas then passes through a series of three coalescing filters and an additional refrigerated sample conditioner before being analyzed using continuous emissions monitors (CEMs) for instantaneous hydrogen, carbon monoxide, methane, and carbon dioxide concentration measurement. Gas is also analyzed using a gas chromatograph, which measures concentrations of 18 gas species found in synthesis gas.

4.4. Tar sampling and analysis

As an objective of this research project is to understand the effectiveness of methods for reducing tar content in biomass-derived synthesis gas, the tar measurement method is of critical importance. The cold-trapping, or impinger train, method according to the International Energy Agency protocol (*24*) is most common. However, due to the time and materials required for the cold-trapping method, an alternate method was proposed using a solid phase adsorption (SPA) technique. For this research project, both methods were utilized initially to ensure consistency between the two. Due to the large amount of labor and equipment required for the cold-trapping method, the SPA method was used to extract most tar samples for this research. However, both methods will be introduced and discussed.

4.4.1. Cold-trapping method

The cold-trapping method, also known as the impinger train method, was developed under the IEA Tar Sampling Protocol (*72*). A diagram displaying the cold-trapping setup is displayed in Figure 6. An identical sampling train was utilized in previous research using the ICGRF fluidized bed gasifier (*73*). The sample train can be divided into three main modules: the particulate collection module, the condensable collection module, and the volume

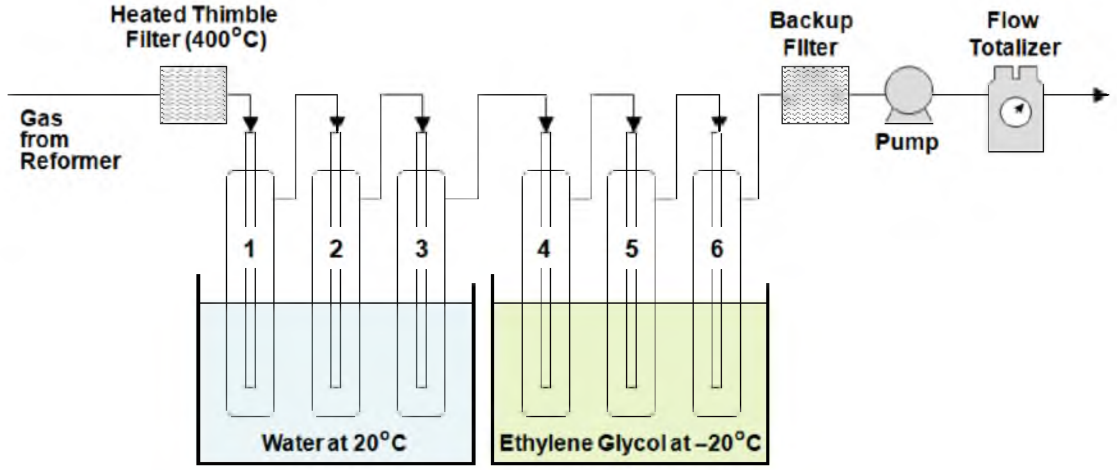

Figure 6. IEA protocol cold-trapping method setup

measurement module.

The particulate collection module consists of a heated slip-stream sample line leading to a thimble filter (3 x10 cm) housed in a heated filter housing. The thimble filter removes any particulate (e.g., bed material, ash, char) entrained in the sample flow in order to avoid particulate contamination of the impinger samples. The temperature of the sample line and thimble filter is regulated by electrical heat trace, which is controlled by a temperature controller using a surface thermocouple fixed to the sample tube and filter housing. Typically, a sample line and filter temperature of 350°C (660°F) is maintained to avoid tar condensation.

The condensable collection module consists of three subsections. The first submodule is the moisture collection section, which consists of three impingers. The first impinger is filled with glass beads, the second with water, and the third with isopropyl alcohol (IPA). These three impingers are immersed in a water bath regulated at 20°C (68°F). The second submodule is the section where tars and volatile organic compounds (VOCs) are absorbed in IPA and consists of three impingers. The first two impingers are filled with IPA only and the third impinger is filled with IPA and glass beads. These impingers are immersed in a bath of ethylene glycol that is maintained at approximately -20°C (-4°F).

The sampling module controls and measures the flow of dry, tar-free synthesis gas through the sample train. Flow is controlled using a critical orifice and a sample pump if the gasifier pressure is not sufficiently high. A dry gas meter is installed at the end of the sample train to measure the total volume of gas flow through the sample train during the sample period. Typically, tars are collected for 200 L of dry synthesis gas flow.

Following tar sampling, approximately 2 L of a mixture of water, IPA, and tar remain in the impinger bottles. In order to measure the total tar content in the sample (equal to the total tar content per 200 L of synthesis gas), separation of the tar component from the mixture is carried out using a separatory funnel and rotary evaporator. The separatory funnel is used to separate the initial water-solvent mixture. Most of the organic material is dissolved in the solvent. However, some tar is dissolved in the water phase. Therefore, several liquid-liquid extractions are carried out to separate any dissolved organics in the water phase. Following extraction of the solvent-tar mixture, a rotary evaporator is used to separate the IPA from the tar. In order to do this, the solvent-tar mixture is submerged in a water bath at 40°C and the IPA is boiled using the rotary evaporator. The evaporated IPA is then condensed, and added back to the separatory funnel to wash the funnel and capture any organic material still present in the water phase. The solvent phase is then extracted again and IPA is boiled and extracted using the rotary evaporator. This process is repeated several times until the rate of condensation of the IPA in the rotary evaporator is approximately one drop per minute. The final tar concentration is determined after the final IPA extraction.

Dilute tar samples are prepared by mixing 150 mL of solvent to 3 mL of concentrated tar sample. The sample is then stored in an amber bottle at approximately 4°C to prevent further reaction. The dilute tar samples (approximately 2.7% by volume of tar) are analyzed for their composition using a gas-chromatograph connected to a flame ionization detector (GC-FID). The GC-FID is used to determine concentrations of specific compounds in the tar-solvent mixture.

4.4.2. Solid phase adsorption (SPA) method

In addition to the cold-trapping method described above, an alternate method has been developed by the Royal Institute of Technology, Sweden (KTH) based on solid phase adsorption (SPA) of tars in the vapor phase onto an amino phase sorbent. This method is intended as an alternative to the cold-trapping method with much shorter sampling time required. The SPA method is described in detail in Brage et al. (*74*) and has been utilized by several groups working on biomass gasification (*75–79*). The majority of the tar samples collected for this research was collected using the SPA method.

Sampling of tars using the SPA method requires very little equipment preparation compared to the cold-trapping method. Just as in the cold-trapping method, the synthesis gas slipstream sample line should be heated to approximately 370°C (700°F) to avoid tar condensation in the sample line. In addition, the sample line pressure should be reduced (<5 psig) using a high-temperature needle valve upstream of the tar sample point. At the sample point, a 0.25 in. cross fitting is installed, with synthesis gas inlet and outlet, thermocouple, and Viton® septum installed at the fitting. The thermocouple is used to ensure adequate gas temperature during sampling and the Viton® septum allows pressure-sealed access for the sample syringe.

The sample apparatus consists of a stainless-steel needle (0.8 mm ID x 10 cm), attached to a SPA cartridge, containing 500 mg of coconut shell charcoal particles (for drying of the filtrate) and a 500 mg amino phase column. The cartridge is attached to a 100 mL gas-tight syringe which is used to draw the sample into the adsorption cartridge.

Prior to extracting a tar sample, the pressure and temperature in the sample line are checked to ensure that conditions are adequate for sampling (<5 psig and 370°C). If flow through the sample line has been lost (due to blockage of flow at the needle valve), it is likely that water and tar has condensed in the line and needs to be flushed out for some time prior to sampling. If conditions are sufficient for sampling, with the complete cartridge sampling apparatus assembled, the needle is inserted through the Viton® septum into the sample line so that the entire needle is immersed in the hot gas flow. The needle is then allowed to thermally equilibrate with the hot sample gas for several seconds before extracting the sample. The sample is extracted manually by slowly retracting the syringe plunger until 20 mL of gas occupies the syringe. Due to the cooling of the sample, the gas will tend to compress, thus causing a force opposite the force applied by the sample taker. Therefore, after 30 mL of sample has been drawn into the syringe, force should remain applied to the plunger to maintain the 30 mL sample volume. After extraction of the sample is complete, the needle is drawn out from the septum and the sample cartridge is removed from the sample assembly and placed in a sealed test tube. The total sample extraction time is approximately 15 minutes.

Desorption of the sample from the sample cartridge, containing the charcoal and SPE column, is done by washing the cartridges with solvents to elute the sample. Three gravity-fed washes are used for this purpose, each followed by a pressurized wash. Dichloromethane (DCM) is used as the solvent for the first wash. One milliliter is dripped through the sample cartridge. When most of the eluent has passed through the adsorbent, pressure is applied to elute the remaining solvent through. This step is repeated, bringing the total volume of the sample to 2 milliliters. The second wash follows the same procedure using a 1:1 mixture of dichloromethane and isopropyl alcohol. These two solvents are used to remove tars of different polarities from the cartridge. Finally, the cartridge is washed with two milliliters of pure isopropyl alcohol.

The prepared samples are then analyzed using a HP 5890 GC-FID. The method settings used are specified in Table 4. The chromatograms obtained allow for the calculation of the mass of tar in the GC sample. From this information, the concentration of tar in a standard volume of dry synthesis gas is determined.

Figure 7 displays the chromatogram for a tar sample extracted at steady the tar sample is eluted from the SPA column with a solvent, in this case,

Table 4. GC-FID parameters tar sample analysis

Parameter	Value	Parameter	Value
Initial temperature	40°C	Carrier gas	He
Initial time	5 min	Carrier gas velocity	35 cm/s
Heating rate 1	2°C/min	Head pressure	16 kPa
Final temperature 1	160°C	Split ratio	splitless
Heating rate 2	10°C/min	Column	HP-5
Final temperature 2	290°C	Column length	30 m
Final time	15 min	Column diameter	0.25 mm
Detector temperature	300°C	Injection temperature	300°C
Run time	93 min	Injection volume	7 μL

Figure 7. GC-FID chromatogram including solvent peak (far left) for tar sample extracted during test PM4 (tar concentration = 53.0 g/Nm^3). Abscissa is retention time (0-100 minutes) and ordinate is FID response intensity (0-600 millivolts).

dichloromethane (DCM). The area under each peak is computed by integration of the signal with time. The ratio of the area under a single peak to the total area of all peaks detected is the mass concentration of the chemical species represented by the peak. In GC-FID, peak locations (retention time) can be correlated to a particular chemical species by calibrating the instrument with external or internal standards. An external standard is typically a mixture of species at known concentrations that can be analyzed by GC-FID to identify retention times and peak areas for each of the species in the mixture. An internal standard is mixture of chemical species that are added to a real sample in a known quantity whose peaks can be identified and used to calibrate the concentration of those species in the actual sample.

The large peak on the left-hand side of the chromatogram is the solvent peak, in this case, DCM. The solvent fraction of a sample mixture is typically very large, on the order of <99% by weight. The actual sample species, which are represented by the small peaks appearing to the right of the solvent peak, are a very small fraction of the injected sample.

From left-to-right, the peaks represent species that are separated and eluted from the column as the column temperature increases based on the GC method. The retention time, or time that a particular analyte takes to travel through the column to the detector, of a particular species depends mostly on the boiling point (BP) of that species. Therefore, the boiling point of the sample species increases from left-to-right. For the case of tars, light, or low molecular weight species with low boiling points generally have short retention times and appear early in the analysis sequence. Heavy, or high molecular weight species have long retention times and appear later in the analysis sequence. Tar samples typically contain a wide range of species from very low molecular weight species such as benzene (MW=78.1 g/mol, BP=80°C), to high molecular weight species such as pyrene (MW=202.3 g/mol, BP=404°C). Heavier tar species typically cannot be measured using GC-FID because a typical GC column suitable for use with tar analysis (e.g., HP5) cannot withstand temperatures higher than approximately 325°C.

4.5. Gasifier performance evaluation

In accordance with the objectives of this research, the performance of the pilot-scale biomass gasification system will be evaluated in conjunction with the effectiveness of primary methods for tar reduction. In order to thoroughly evaluate the performance of the biomass gasification system under the operating conditions of interest, a set of efficiency metrics are applied, which consider the efficiency of the gasifier in converting both input mass and energy into a desirable synthesis gas product. While certain primary methods may promote low tar production, this is typically accomplished at the expense of increased energy input or decreased synthesis gas production. Therefore, the reduction of tar should be balanced with the cost of cleaner synthesis gas. The following are descriptions of the metrics which are used to evaluate the performance of the biomass gasification system.

4.5.1. System material balance

Due to the wide range of products that are produced during gasification, which are produced in all three phases, the closure of a material balance is challenging. Ultimately, an elemental input should be selected and accounted for throughout the process. In that case, carbon, hydrogen, oxygen, nitrogen, and sulfur are eligible candidates for closing a system mass balance as these elements are found in the reactants. Due to difficulty in precisely controlling the steam mass flow rate, hydrogen and oxygen cannot be used. Sulfur cannot be used because it reacts to form hydrogen sulfide, which is difficult to sample and measure because it is soluble in water and therefore needs to remain hot to be accurately measured. Carbon and nitrogen are the remaining potential elements to account for in closing the system mass balance. Carbon reacts to form gaseous, solid, and condensable hydrocarbon (tar) species during gasification. Accurate accounting of these products is difficult and tedious. Therefore, use of carbon should be avoided.

Nitrogen is supplied to the system in trace amounts through the feedstock (0.1-0.3% by mass) and through purge flows. In addition, nitrogen is mostly inert in a reducing environment. Therefore, elemental nitrogen input (N_2) typically remains unreacted and exits the system as gaseous nitrogen, which is easily detectable by gas chromatograph (GC). Alternatively, an inert gas can be doped into the system, but this can become expensive, especially under pressurized conditions when high volumes of gas flow are necessary.

For this research, nitrogen is used to close the system mass balance. Nitrogen input is carefully accounted for by closely controlling purge nitrogen input. The biomass nitrogen content, which is small in comparison to the purge input, is assumed to be constant for a given material. Nitrogen gas mass input is equal to nitrogen gas mass outflow (Equation 1). The concentration of nitrogen in the sample gas stream is measured by GC. The concentrations of each gas in the sample flow allow for determination of the synthesis gas molecular weight. Knowledge of the synthesis gas molecular weight then allows for the determination of the species mass fraction (Equation 2). The mass flow rate of a species in the product gas can then be computed based on the ratio of its mass fraction (y_i) with that of nitrogen (y_{N_2}), the ratio of the species molecular weight (MW_i) with that of nitrogen (MW_{N_2}), and the nitrogen mass flow rate ($\dot{m}_{N_2}$).

$$\dot{m}_{N_2,in} = \dot{m}_{N_2,out} = \dot{m}_{N_2} \tag{1}$$

$$\dot{m}_i = \dot{m}_{N_2} \cdot \frac{y_i MW_i}{y_{N_2} MW_{N_2}} \tag{2}$$

4.5.2. Carbon conversion efficiency

In order meet the fuel requirements of modern end-use devices, an economical process is required to convert the original feedstock to an appropriate energy carrier. In most cases, this process requires reactive conditions to convert feedstock at a large enough scale for economic viability. The purpose of such a process is to convert feedstock mass to product mass that is within the quality tolerance of the end-use device. In the case of biomass gasification, carbon, hydrogen, and oxygen in the feedstock are converted to synthesis gas, secondary products (e.g., carbon dioxide, methane, and higher gaseous hydrocarbons), and undesirable products (e.g., sulfur species, tars). Ideally, 100% of the feedstock mass is converted to synthesis gas, or a desired mixture of synthesis gas and secondary products.

The carbon conversion efficiency (CCE) is a common measure of the ability of a process to convert reactant carbon to a desirable product. In the case of photosynthetic biomass production, glucose is the desirable product formed from the reaction of adsorbed carbon dioxide and water. In the case of gasification of hydrocarbon feedstock, carbon monoxide, methane, and in some cases, larger hydrocarbon species are the desirable products formed from the reaction of the feedstock and the gasifier reactant input (e.g., air, oxygen, steam).

For this research, the CCE is a measure of the conversion efficiency of fuel carbon to synthesis gas carbon (Equation 4). Fuel carbon content is determined from an ultimate analysis of the dried feedstock according to ASTM Standard D3176-09 (*80*). Synthesis gas carbon content is determined by first measuring the composition of the product gas using an online gas chromatograph. In order to determine the mass flow of each product gas component, the nitrogen (N_2) input into the system is assumed to remain in elemental form with the mass inflow of N_2 equal to the mass outflow of N_2. Therefore, for a known fuel and purge nitrogen input, the mass outflow of nitrogen can be used to determine the mass flow of each product gas component relative to the nitrogen concentration, as described in the previous section. While some amount of nitrogen reacts to form ammonia (NH_3) and other nitrogen-containing species, formation of these species has been linked mostly to fuel-bound nitrogen (*81*). For this research, the mass flow rate of fuel-bound nitrogen is at most 1% (0.05-0.1 lb/hr) of the total nitrogen mass inflow. Therefore, error associated with conversion of elemental nitrogen to other nitrogen species is considered insignificant with regard to the determination of the product gas mass flow rate as discussed in a previous section. Carbon mass flow in the product gas can be determined by summing the contributions of each carbon containing component in the product gas (Equation 5).

$$\dot{m}_{g,out} = \sum_{i} \dot{m}_i \tag{3}$$

$$CCE = \frac{\dot{m}_{C,syngas}}{\dot{m}_{C,fuel}} \tag{4}$$

$$\dot{m}_{C,syngas} = \dot{m}_{syngas} \sum_{i} \chi_i n_{C,i} \frac{MW_C}{MW_i} \tag{5}$$

4.5.3. Cold gas efficiency

In addition to the conversion of feedstock mass to product mass, several indicators are used to determine the energy efficiency of a gasification process. The cold gas efficiency (CGE, Equation 7) accounts for the energy input from the feedstock, which is calculated using the fuel lower heating value (LHV_{fuel}, Equation 6) and mass flow rate ($\dot{m}_{fuel}$). The output energy is assumed to be only the energy in the synthesis gas at standard conditions, given by the synthesis gas lower heating value (LHV_{syngas}) multiplied by the synthesis gas mass flow rate ($\dot{m}_{syngas}$). Typical CGE values for fluidized bed gasifiers are 70-90% (*6*).

$$LHV_{syngas} = \sum_{i} \chi_i LHV_i \tag{6}$$

$$CGE = \frac{LHV_{syngas}\dot{m}_{syngas}}{LHV_{fuel}\dot{m}_{fuel}} \tag{7}$$

4.5.4. Hot gas efficiency

The hot gas efficiency (HGE, Equation 11), like the cold gas efficiency, accounts for the feedstock energy content as an input and synthesis gas chemical energy as an output, but also accounts for thermal inputs ($\dot{W}_{elec}$, $\dot{W}_{boiler}$, Equation 9 and 10) to the system and sensible energy output, or enthalpy (h_{syngas}, Equation 8), of the product gas. The electrical energy input includes electrical energy consumed in the steam superheater ($\dot{W}_{elec,SH}$) and the sum of the four bed heater bundles ($\dot{W}_{elec,BHi}$). The enthalpy of synthesis

$$h_{syngas} = \sum_{i} C_{p,i}\chi_i(T_{outlet} - T_o) \tag{8}$$

$$\dot{W}_{elec} = \sum_{i} \dot{W}_{elec,BHi} + \dot{W}_{elec,SH} \tag{9}$$

$$\dot{W}_{boiler} = \dot{m}_{steam}\left(h_{g,sat} - h_{f,o}\right) \tag{10}$$

$$HGE = \frac{\dot{m}_{syngas}\left(LHV_{syngas} + h_{syngas}\right)}{LHV_{fuel}\dot{m}_{fuel} + \dot{W}_{boiler} + \dot{W}_{elec}} \tag{11}$$

gas (Equation 8) is computed by summing the energy content for each synthesis gas component at the outlet of the gasifier (T_{outlet}) using the specific heat of that component ($C_{p,i}$) and standard reference temperature (T_o). The hot gas efficiency cannot exceed 100% in accordance with the Second Law of Thermodynamics due to entropy generation, heat loss from the system, and chemical and sensible energy in the residue products (e.g., char, ash, and tar). A diagram of the HGE energy balance is displayed in Figure 8.

4.5.5. Net gasification effectiveness

While the cold and hot gas efficiencies account for the efficiency in converting feedstock energy to synthesis gas energy, these indicators do not account for other forms of energy input and products. Other energy inputs include electrical energy ($\dot{W}_{elec}$, Equation 9) from the bed heaters ($\dot{W}_{elec,BHi}$) and the steam superheater ($\dot{W}_{elec,SH}$), and thermal energy from the natural gas boiler to produce the saturated steam ($\dot{W}_{boiler}$, Equation 10). Additional energy carrier outputs include the tar component ($\dot{m}_{tar}HV_{tar}$), which has a heating value of approximately 40 MJ/kg, and the char component ($\dot{m}_{char}HV_{char}$), which has a heating value of approximately 32 MJ/kg (*82*).

In order to account for these additional energy inputs and outputs, several additional performance metrics are defined in this section. The net

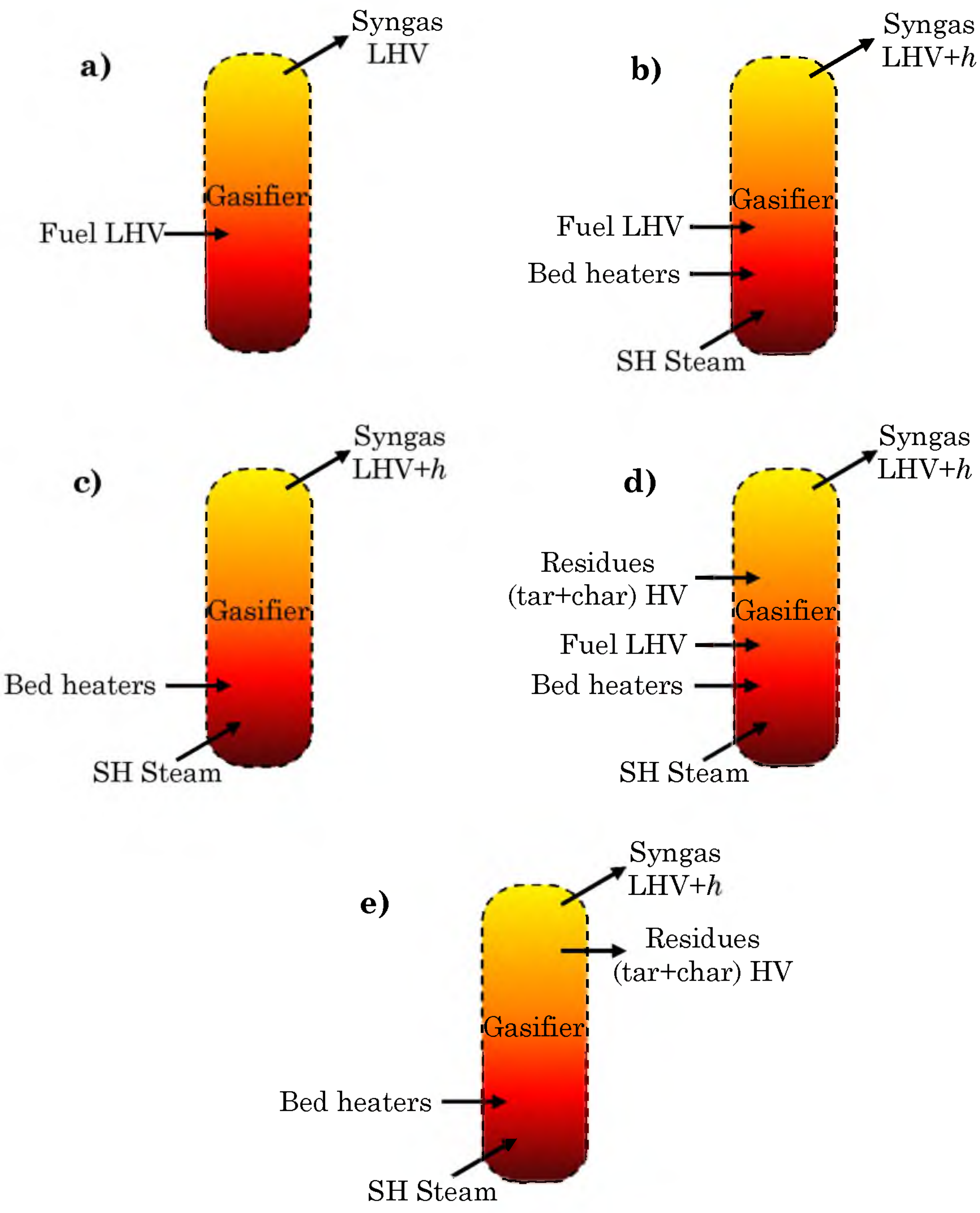

Figure 8. Gasification energy performance metric diagrams: a) cold gas efficiency (CGE); b) hot gas efficiency (HGE); c) NGE1 effectiveness; d) NGE2 effectiveness; e) NGE3 effectiveness

gasification effectiveness (NGE) like the CGE and HGE is a comparison between energy outputs and inputs, but can have a value greater than unity depending on the definition used. Three NGE definitions are described below. Diagrams of the NGE energy balances are displayed in Figure 8.

The NGE1 net gasification effectiveness (Equation 12) accounts for the heat inputs ($\dot{W}_{elec} + \dot{W}_{boiler}$, Equation 9 and 10) to the gasification system and assumes that the fuel has no energy cost to the process. The assumed energy output is the chemical and sensible energy in the synthesis gas ($\dot{m}_{syngas}(LHV_{syngas} + h_{syngas})$). NGE1 is the maximum possible energy conversion efficiency without recovery of residues and should be significantly higher than unity for a properly functioning system.

$$NGE1 = \frac{\dot{m}_{syngas}(LHV_{syngas} + h_{syngas})}{\dot{W}_{elec} + \dot{W}_{boiler}} \tag{12}$$

The NGE2 net effectiveness (Equation 13) is similar to the HGE but accounts for recycle of residues produced from the gasification process (e.g., char and tar). The char component ($\dot{m}_{char}HV_{char}$) for this calculation is considered to be the char that exits the gasifier with the product gas and is captured and collected for recycle back to the system. Char can be directly combusted to produce heat for the gasifier, or can be recycled back into the reactor for further conversion. The tar component remains in the hot synthesis gas that exits the gasifier and can be removed in a quench column or scrubber. The tar component can be separated and directly combusted for heat or steam generation ($\dot{m}_{tar}HV_{tar}$). For this research, the char elutriation rate for each experiment was both measured from the particulate filter filtrate and was calculated based on carbon conservation. The tar production rate was measured using the tar sampling methods previously described. For NGE2, these residues appear as inputs that offset other energy inputs (e.g., electric bed heater, boiler). With residue recovery, the NGE2 net effectiveness is typically higher than the HGE, but will not be significantly higher for gasifier operating conditions that do not produce large amounts of residues.

$$NGE2 = \frac{\dot{m}_{syngas}\left(LHV_{syngas} + h_{syngas}\right)}{\dot{W}_{elec} + \dot{W}_{boiler} + LHV_{fuel}\dot{m}_{fuel} - \dot{m}_{tar}HV_{tar} - \dot{m}_{char}HV_{char}} \qquad (13)$$

The NGE3 net effectiveness (Equation 14) is similar to the NGE1 net effectiveness but, like NGE2, considers energy recovery from residues. However, unlike NGE2, the NGE3 net effectiveness assumes that the char and tar have fuel value that is not recycled back into the gasifier, but collected as a process energy output. The reason for this is that accounting for the residues as a system energy offset in the denominator would result in a negative efficiency value for conditions that required very little heat energy input but produced large amounts of residues (e.g., low temperature gasification). NGE3 represents the maximum possible conversion effectiveness for a given reactor operating condition since it assumes that the fuel has no energy cost. NGE3 is typically the highest of the net effectiveness values with typical values much greater than unity.

$$NGE3 = \frac{\dot{m}_{syngas}\left(LHV_{syngas} + h_{syngas}\right) + \dot{m}_{tar}HV_{tar} + \dot{m}_{char}HV_{char}}{\dot{W}_{elec} + \dot{W}_{boiler}} \qquad (14)$$

4.6. Chemical equilibrium modeling

An equilibrium model was used to determine chemical equilibrium molar composition of synthesis gas for each of the operating conditions investigated. The software GasEq was utilized to compute the equilibrium compositions. The basis of the calculation is molar conservation and minimization of the Gibb's free energy at constant temperature and pressure. Gasifier operating conditions and moles of each reactant are defined by the user. This requires a stoichiometric calculation to determine the moles of each element in the feedstock and the moles of steam. Two separate equilibrium cases were run at each operating condition. One case at the actual stoichiometric ratio (SR) was based on the steam gasification reaction: $C_xH_yO_z + aH_2O \rightarrow bH_2 + cCO$. The second case assumes an SR=1 for steam gasification and is used for comparison with the actual measured gas composition and the actual equilibrium composition.

4.7. High-frequency pressure measurement and analysis

Measurement of high-frequency pressure fluctuations has been shown to be an effective method for monitoring conditions in gas-solid fluidized beds. While measurement of the bed temperature profile and bed pressure drop can provide useful "global" information, high-frequency pressure fluctuation data may provide details about local transport phenomena, which give an indication of the quality of fluidization, the fluidization regime, and any disturbances in the fluidizing conditions. While this research field is well established, the application of fluidization diagnostics using pressure fluctuation measurement in real reactors is relatively limited to only a few test cases. The measurements made on the fluidized bed gasifier that are presented in this research are a unique addition to the limited amount of data that exists for pressure fluctuation measurement and analysis in real conditions.

4.7.1. Measurement device

In order to measure high-frequency pressure fluctuations, a Validyne DP15 variable reluctance, differential pressure transducer (+/- 35 in H_2O, +/-

0.25% full-scale accuracy, 3 kHz maximum sampling frequency) and Validyne CD15 sine wave carrier demodulator, which supplies the transducer with the required 5 kHz excitation signal and converts the transducer output (+/- 35 mV/V) to a +/- 10 VDC signal, were used. Figure 9 displays the actual differential pressure transducer and a cross-section schematic of the data acquisition system (National Instruments SCXI-1000) capable of sampling at frequencies up to 333 kHz. From a survey of literature related to pressure fluctuation analysis in gas-solid fluidized beds, a sample frequency of 200 Hz has been selected (*83*).

4.7.2. Signal processing

The high-frequency pressure transducer used for fluidized bed monitoring in this research outputs a +/- 10 VDC signal that is proportional to the

Figure 9. Validyne DP15 differential pressure transducer

magnitude of the differential pressure across the high and low ports on the transducer. The signal is sampled at 200 Hz using a National Instruments (NI) LabView-based data acquisition program. The data acquisition software allows for the user to specify the sample length or to sample continuously until prompted to stop. The data files were saved in a propriety NI format (.tdms). A Matlab script was developed to convert the NI data file to a .mat file. The raw data in the .mat file can then be analyzed using a Matlab script developed for this research (Appendix B).

For the cold-flow experiments, a set sample length of 6 minutes was specified. This was plenty of sample time and allowed for the original sample to be divided into three ensemble sets. Statistical and spectral analyses were performed on each ensemble set. The three sets were then averaged, resulting in an ensemble averaged dataset for the experiment.

Sampling and analysis for the fluidized bed gasifier tests were not as straightforward. During the gasification tests, the data acquisition software sampled the pressure transducer continuously. The sampling routine was restarted each day, giving one pressure data file for each day. Each of these files easily reached ten to twenty million data points, which made the analysis of the fluidized bed gasifier data more challenging. Specific pieces of the data had to be extracted from the original data file and analyzed individually. Therefore, finding and extracting a single sample period was quite tedious.

After a pressure signal sample period was selected and ready for analysis, a Matlab script was used to perform the series of calculations used to interpret the hydrodynamic conditions in the bed during that measurement period. This routine was the same for both the cold-flow, fluidized bed data and the fluidized bed gasifier data. Built in Matlab functions were utilized whenever possible. The analysis code is included in the Appendix B of this thesis. The series of calculations that were performed are described as follows:

- Decomposition of the signal into its mean and fluctuating components
- Calculation of the first four central moments of each signal component (mean, variance, skewness, and kurtosis)
- Calculation of the normalized autocorrelation function for the fluctuating pressure component
- Calculation of the normalized probability density function (PDF) of the mean and fluctuating pressure components
- Calculation of the covariance power spectral density (PSD) by computing the fast Fourier transform (FFT) of the signal

4.7.3. Cold-flow fluidized bed

Initial experiments using the differential pressure transducer were carried out using a 2/3 scale cold-flow model of the pilot-scale fluidized bed reactor at the ICGRF (Figure 10). The cold-flow fluidized bed has previously been used for studies investigating fluidization regimes of various bed materials and bubble frequency measurement using optical methods (*84*).

For this testing, a pressure tap was installed on the wall of the bed at the

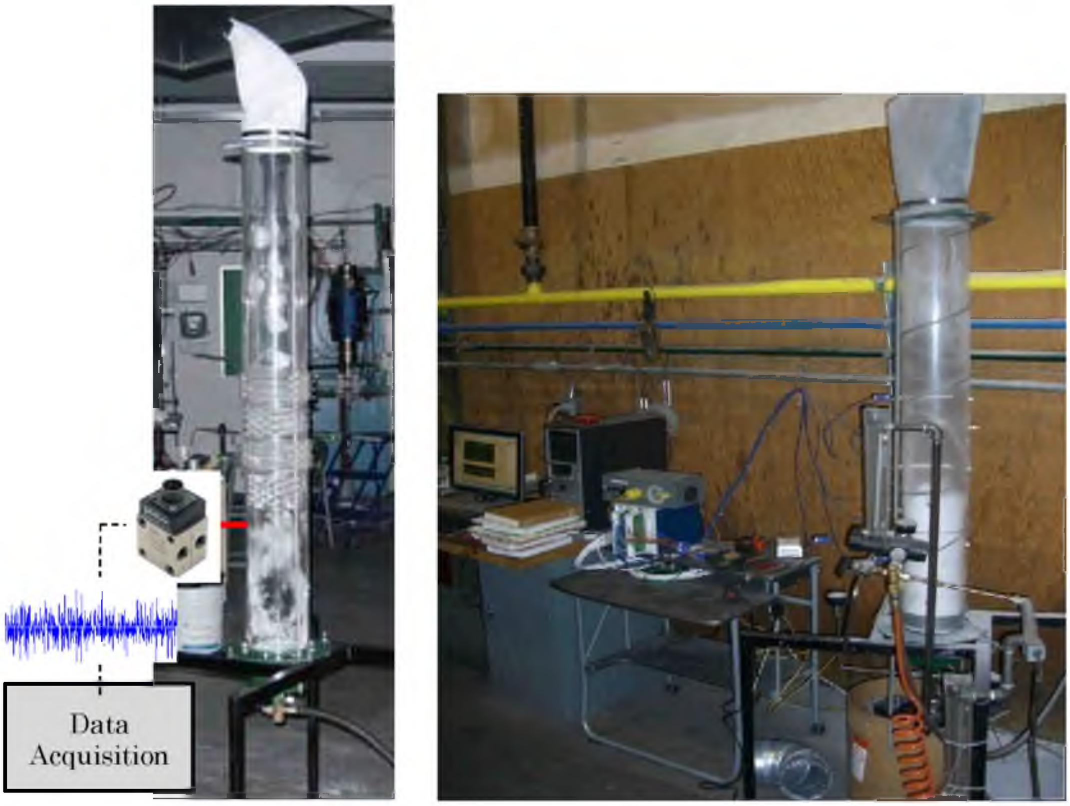

Figure 10. Cold-flow fluidized bed apparatus and pressure transducer assembly diagram

equivalent scaled location (13 in. from distributor plate) of the pressure tap on the pilot-scale unit (20 in. from distributor plate). This location is within the bed section on both units at an adequate height above the distributor plate to capture flow of developed bubbles that originate at the distributor plate. The transducer is installed at the pressure bed wall pressure tap with minimal tubing to reduce the dampening effects due to excess volume upstream of the transducer. The positive transducer tap is connected to the bed wall tap and the low-pressure transducer was left open to atmosphere.

4.7.4. Fluidized bed gasifier

For use of the transducer on the fluidized bed gasifier, a new diaphragm was installed which allows differential pressure measurements up to +/- 140 in. H_2O (Figure 11). The pressure transducer was installed in the fluidized bed gasifier by a tube connection on an access flange in the bed region below the bed heaters. The tube protrudes through the access flange and the refractory plug attached to the inside of the flange, up to the inside wall of the reactor bed section (Figure 3). Since the gasifier operates at elevated pressure, it is necessary to connect the low-pressure side of the transducer to a downstream location on the gasifier. The low-pressure transducer tap was plumbed upward to a purged tubing section that provides a pressure tap in the freeboard section of the reactor, which is consistently lower in pressure

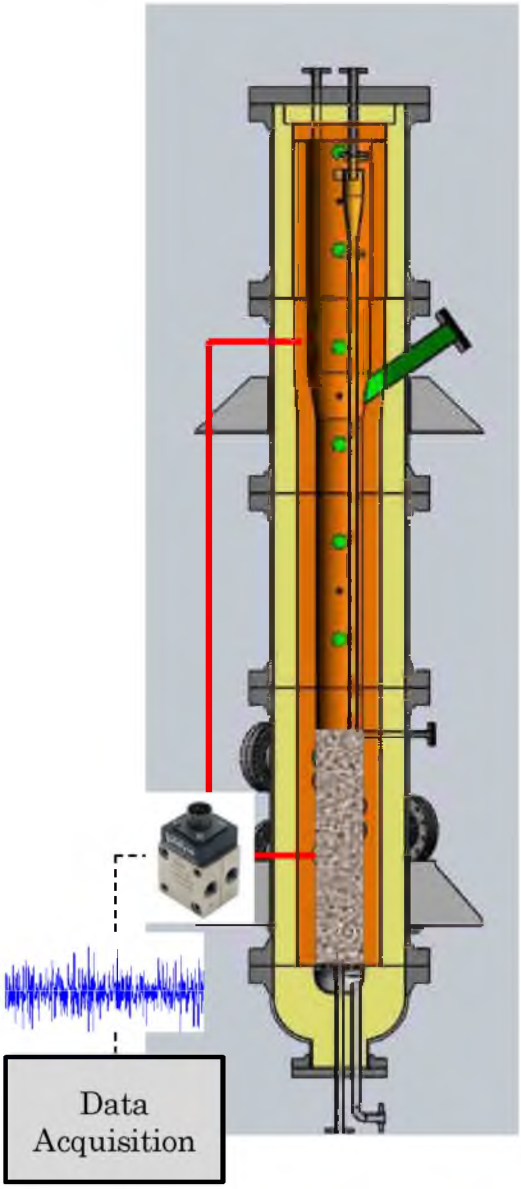

Figure 11. Fluidized bed gasifier and pressure transducer diagram.

than the bed tap location.

4.8. Experimental conditions

In following with the objective of this research to study the effects of gasifier operating conditions and feedstock pretreatment on tar formation and gasifier performance, a series of experiments was designed to provide an adequate amount of information to make judgments about primary method effectiveness while remaining within the budget constraints of the project. Therefore, three variables were studied, two of which directly affect the reactive conditions in the gasifier and the third of which relates to the feedstock properties.

First, the fluidized bed temperature has been shown to have a significant effect on the yield and composition of tars formed during biomass gasification. In general, a higher bed temperature results in better overall fuel conversion to synthesis gas as more energy is available to drive the endothermic gasification reactions. However, increases in reactor temperature have also been shown to result in polymerization of tar species, forming more refractory tar species that are less tolerable in end-use devices (*23*).

Second, gasifier pressure is a process parameter that is less well characterized than conditions that effect reaction severity (e.g., temperature, gas-phase residence time). In general, gasifier operation at elevated pressure results in an overall reduction of tar but a relative increase in concentration of secondary and tertiary tars compared to low-pressure operation. While the tar reduction benefits alone may not warrant it, operation at elevated pressure is desirable in many advanced gasification systems due to reactor volume reduction and elimination of the need for downstream synthesis gas compression. A unique characteristic of the experimental apparatus used for this research is the ability of the gasification system to operate at elevated pressure (up to 20 atm) using solid feedstocks.

Finally, the effect of feedstock pretreatment on tar production is investigated in this research. A variety of feedstock pretreatment methods exist, ranging from physical pretreatment processes including size reduction or pelletizing, to chemical pretreatments including pyrolysis and torrefaction. For this research, torrefaction was considered as a feedstock pretreatment which could potentially improve synthesis gas quality through higher hydrogen and carbon monoxide and lower tar concentrations. Torrefaction is a mild pyrolysis process in which the fuel material is exposed to slightly elevated temperature in the absence of oxygen, resulting in a reduction of the volatile matter, an increase in the carbon content, and a subsequent increase in the energy density of the feedstock. As a result of the reduced volatile matter in the feedstock, the potential for tar formation decreases and the synthesis gas quality improves with higher hydrogen and carbon monoxide concentrations. For this research, medium and dark torrefied material was prepared and gasified in the pilot-scale biomass gasification system.

The experimental matrix for both the primary methods and torrefied biomass campaigns is presented in Table 5. Eleven primary methods tests were completed in total. The first test was a shakedown test, the results of which are not discussed. The primary methods experiments do not follow a consistent logical structure. Rather, it was determined each day which experiment would be run based on the day-to-day operability of the gasifier. On certain days, challenges were faced in preparing the gasifier for operation. Therefore, a less severe condition would be selected for that day. For example, it is not uncommon for disruptions to occur during steam standby operation overnight, which cause the bed to cool, or a large temperature disparity to occur in the bed. The test codes (e.g., PM1, PM2) follow the primary methods tests chronologically. An additional test matrix is supplied in Appendix C, which can be removed and used as a reference while reading the remainder of the document. The six torrefied biomass gasification tests were split into two sets. The first (T1-T3), investigated gasification of medium torrefied material under several different conditions. The second set (T4-T6), investigated gasification of dark torrefied material at the same

Table 5. Primary methods experimental design

Test #	Description	Target temp., °F	Target pressure, psig	Biomass type	Target biomass feedrate, lb/hr
PM1	Low press shakedown	-	5	Raw wood	45
PM2	High temp, low press	1450	5	Raw wood	45
PM3	Med temp, low press	1250	5	Raw wood	45
PM4	Low temp, low press	1050	5	Raw wood	45
PM5	High temp, med press	1450	30	Raw wood	45
PM6	Med temp, med press	1250	30	Raw wood	45
PM7	High temp, high press	1450	60	Raw wood	45
PM8	Med temp, high press	1250	60	Raw wood	45
PM9	Low temp, high press	1050	60	Raw wood	45
PM10	Low temp, Med press	1050	30	Raw wood	45
PM11	Duplicate: High temp, med press	1450	30	Raw wood	45
T1	Med torr, high temp, high feed	1450	5	Med torr	45
T2	Med torr, high temp, low feed	1450	5	Med torr	30
T3	Med torr, med temp, low feed	1250	5	Med torr	30
T4	Dark torr, high temp, high feed	1450	5	Dark torr	45
T5	Dark torr, high temp, low feed	1450	5	Dark torr	30
T6	Dark torr, med temp, low feed	1250	5	Dark torr	30

conditions tested in the first set. Again, these tests are numbered based on chronological order.

CHAPTER 5

RESULTS: PRIMARY METHODS FOR TAR REDUCTION

5.1. Effect of gasifier pressure and temperature

Tar measurements were carried out during the primary methods experimental campaign to investigate the tar production under different gasifier operating conditions. The effects of fluidized bed temperature and gasifier pressure on tar production are presented in this section. Several tar samples were collected using the solid phase adsorption method (described previously) after steady operation was achieved at each temperature and pressure condition. Samples were then prepared for analysis and analyzed using GC-FID, which provides a measure of the total tar content in a given sample and can also provide concentrations of specific tar species or classes of tars given the proper calibration standards.

5.1.1. Tar concentration

The effect of gasifier temperature and pressure on tar content in synthesis gas produced during fluidized bed gasification of biomass is presented in Figure 12. Concentrations are presented in terms of grams of tar per standard (normal) cubic meter of dry synthesis gas, which is a common representation of tar concentration. For the low-pressure cases (5 psig gasifier freeboard pressure), the tar concentration decreased by approximately 50% from the low (53 g/Nm^3)- to the high-bed-temperature case (26.7 g/Nm^3). For the medium-pressure cases (30 psig), the tar concentration decreased by approximately 43% from the low (25.5 g/Nm^3)- to the high-bed-temperature case (14.6 g/Nm^3). For the high-pressure cases (60

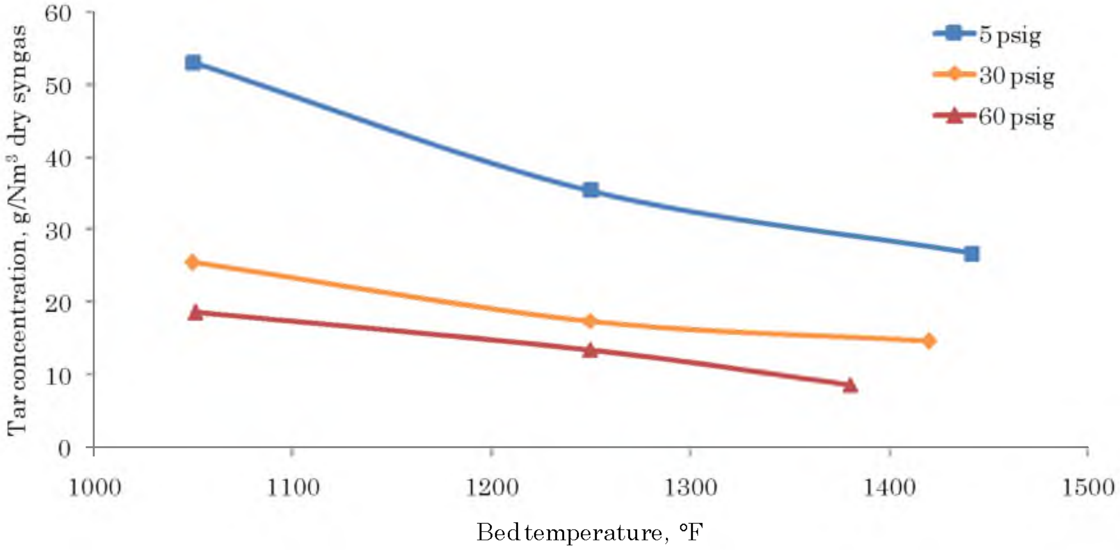

Figure 12. Synthesis gas tar concentration trends with bed temperature and freeboard pressure (g/Nm^3 dry synthesis gas).

psig), the tar concentration decreased by approximately 53% from the low (18.6 g/Nm^3)- to the high-bed-temperature case (8.7 g/Nm^3).

The decreasing tar content with increasing temperature is due in part to several factors. First, a higher temperature reactive environment provides a higher fuel particle heating rate, which plays a significant role in the type and quantity of products formed during fuel particle devolatilization. Devolatilization is the segment of the fuel conversion process in which tar species originate, and therefore has a significant impact on the initial tar content and composition. Second, following formation of the tar species during devolatilization, high reactor temperatures and ample amounts of reactant gas provide conditions for tar reforming reactions (R12) to progress, resulting in the formation of lighter tars, gaseous hydrocarbon species, and synthesis gas components. The magnitude of these reductions and the resulting tar concentrations are consistent with similar studies in literature under similar operating conditions, particularly for the low-pressure case where several previous experiments have been reported (*16*, *28*, *35*, *85*).

The gasifier operating pressure (as measured in the freeboard section) also had a significant impact on tar concentration. In general, tar concentrations were substantially lower at elevated pressure for these experiments. For the low-temperature cases (1050°F), the tar concentration decreased by approximately 65% from the low (53 g/Nm^3)- to the high-pressure case (18.6 g/Nm^3). For the medium-temperature cases (1250°F), the tar concentration decreased by approximately 62% from the low (35.4 g/Nm^3)- to the high-pressure case (13.5 g/Nm^3). For the high-temperature cases (1550°F), the tar concentration decreased by approximately 67% from the low (26.7 g/Nm^3)- to the high-pressure case (8.7 g/Nm^3).

There are several pressure-related factors that account for the lower tar concentrations at elevated pressure. First, the tar-reforming reactions, the rates of which increase with increasing temperature, are also affected by the pressure conditions in the reactor. Due to the volume decrease in the forward direction of the reaction, according to Le Chatelier's principle, the equilibrium of the reaction will shift in the direction in which fewer moles of product are formed. For example, for the methane-reforming reaction (R7), an increase in pressure causes a shift in equilibrium to the side of the reaction with fewer moles, the right side, thus increasing the yield of carbon monoxide and hydrogen. The same is true for larger hydrocarbon and tar-reforming reactions.

The second factor that likely contributes to reduced tar concentration is the higher concentration of steam relative to biomass feedstock at elevated pressure. In order to maintain adequate fluidization conditions in the bed, the velocity of steam flow through the bed is maintained between approximately 0.8 and 1.0 ft/s. This results in higher mass flows of steam at elevated pressure: for the high-pressure cases, approximately 2.8-2.9 times the amount of steam necessary for stoichiometric (SR=1) steam biomass gasification. As a result, Le Chatelier's principle again tells us that an increase in concentration of one species in a reaction causes a shift in equilibrium toward the opposite side of the reaction to counter the concentration increase. Therefore, an increase in steam concentration at high pressure causes a shift towards the forward product side in the steam-reforming reactions, resulting in a decrease in tar concentration.

Finally, due to the high mass flow rates of steam in high-pressure operation, which were 175% higher than in low-pressure operation, the rate of heat removal from the fluidized bed is higher at pressurized conditions. This results in higher rates of heat transfer to the upper sections of the gasifier and gasifier exit piping. Therefore, these sections of the gasifier maintained higher temperature during the elevated pressure tests. For example, the gasifier freeboard temperature during the high-temperature, high-pressure case maintained approximately 1400°F during steady operation in comparison to approximately 1200°F for the high-temperature, low-pressure case. The higher gasifier freeboard and exit temperatures allow for an in increase in effective reaction residence time for the products. Therefore, long-chain hydrocarbon species that exit the bed section can continue to reform through the freeboard section, producing a lower tar content product gas at high pressure.

In addition to tar concentration, it is informative to consider the tar yield with respect to the biomass feedrate (Figure 13). This is accomplished by normalizing the mass flow rate of total tar, as calculated using the concentration of tar in dry synthesis gas at standard conditions and the molecular weight of synthesis gas from the gas composition, with the biomass feedstock feedrate. The biomass feedrate was mostly constant for the primary methods experiments. However, the normalized tar mass flow rate provides an indication of the fraction of feedstock that is converted into total tar. For the primary methods experiments, normalized tar mass flow

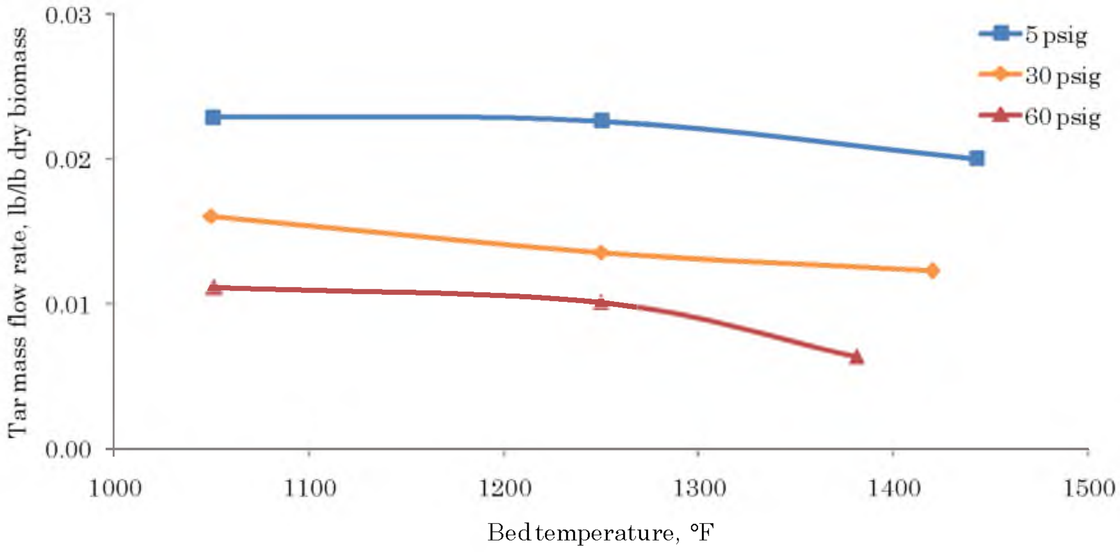

Figure 13. Tar mass flow rate trends with bed temperature and freeboard pressure (lb/lb dry biomass)

rate decreases with temperature and, more significantly, with pressure. In general, approximately 1-2% of the feedstock mass forms tars.

5.1.2. Tar composition

In addition to the concentration of total tar in the synthesis gas produced from biomass gasification, it is possible, with the use of a GC-FID or GC-MS, to identify particular tar species or classes of tar species that are formed under a given set of gasifier operating conditions. For this research, GC-FID was used to analyze the tar samples and compute the total tar concentration. Several characteristic FID chromatograms from tar samples are displayed in Figure 14-Figure 17. Typically, standard calibration mixtures would be used to calibrate the GC-FID in order to identify particular species in the tar sample. The chromatograms themselves are presented here without identification of individual species.

Figure 14 is a chromatogram for a tar sample that was extracted at steady operating conditions during test PM4 (low temperature, low pressure), which exhibited the highest overall tar concentration measured during the primary methods experimental campaign. The ordinate axis has been scaled to show the chromatogram details for the tar species detected. For this

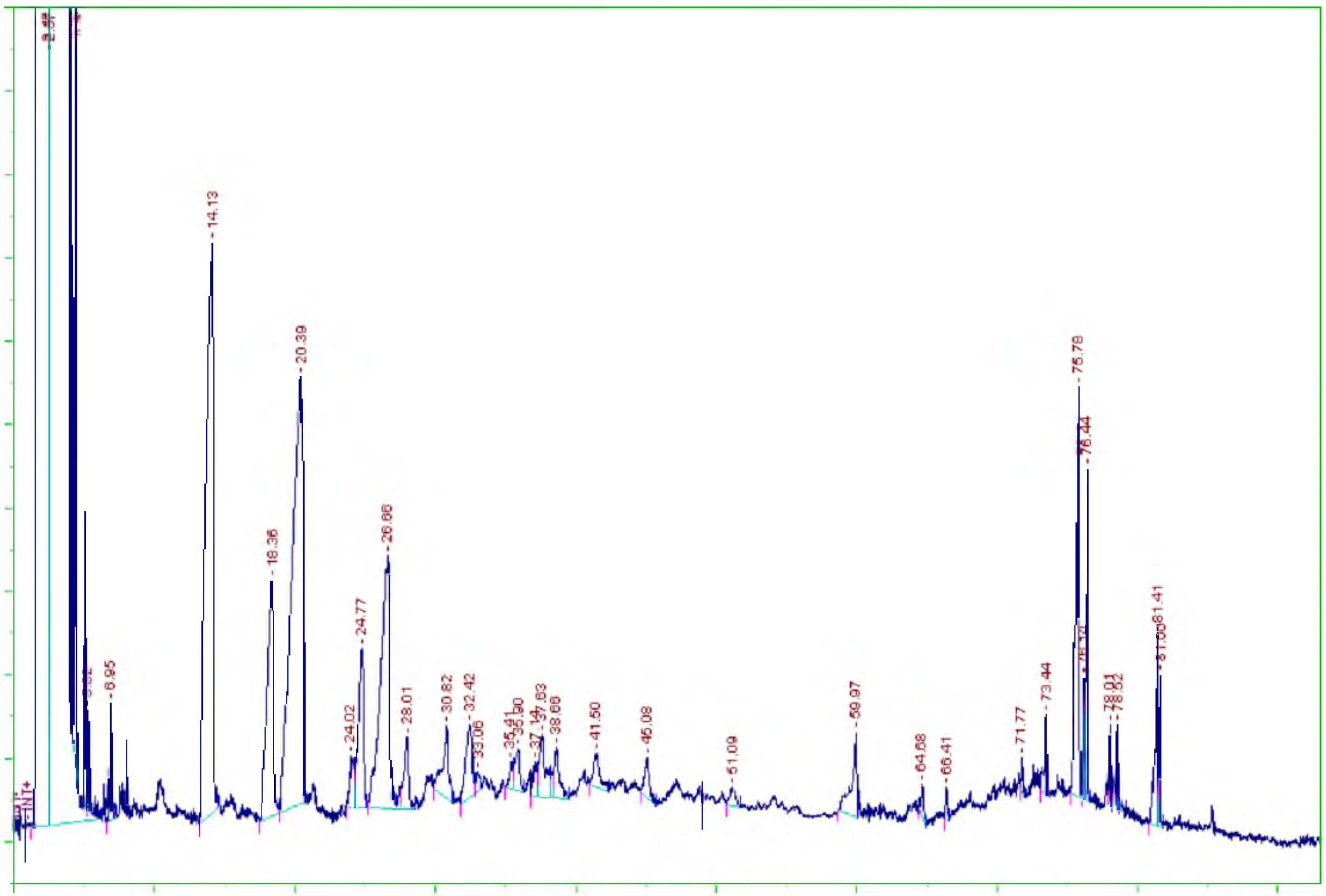

Figure 14. GC-FID chromatogram for tar sample extracted during test PM4 (tar concentration = 53.0 g/Nm^3). Abscissa is retention time (0-100 minutes) and ordinate is FID response intensity (0-2 millivolts).

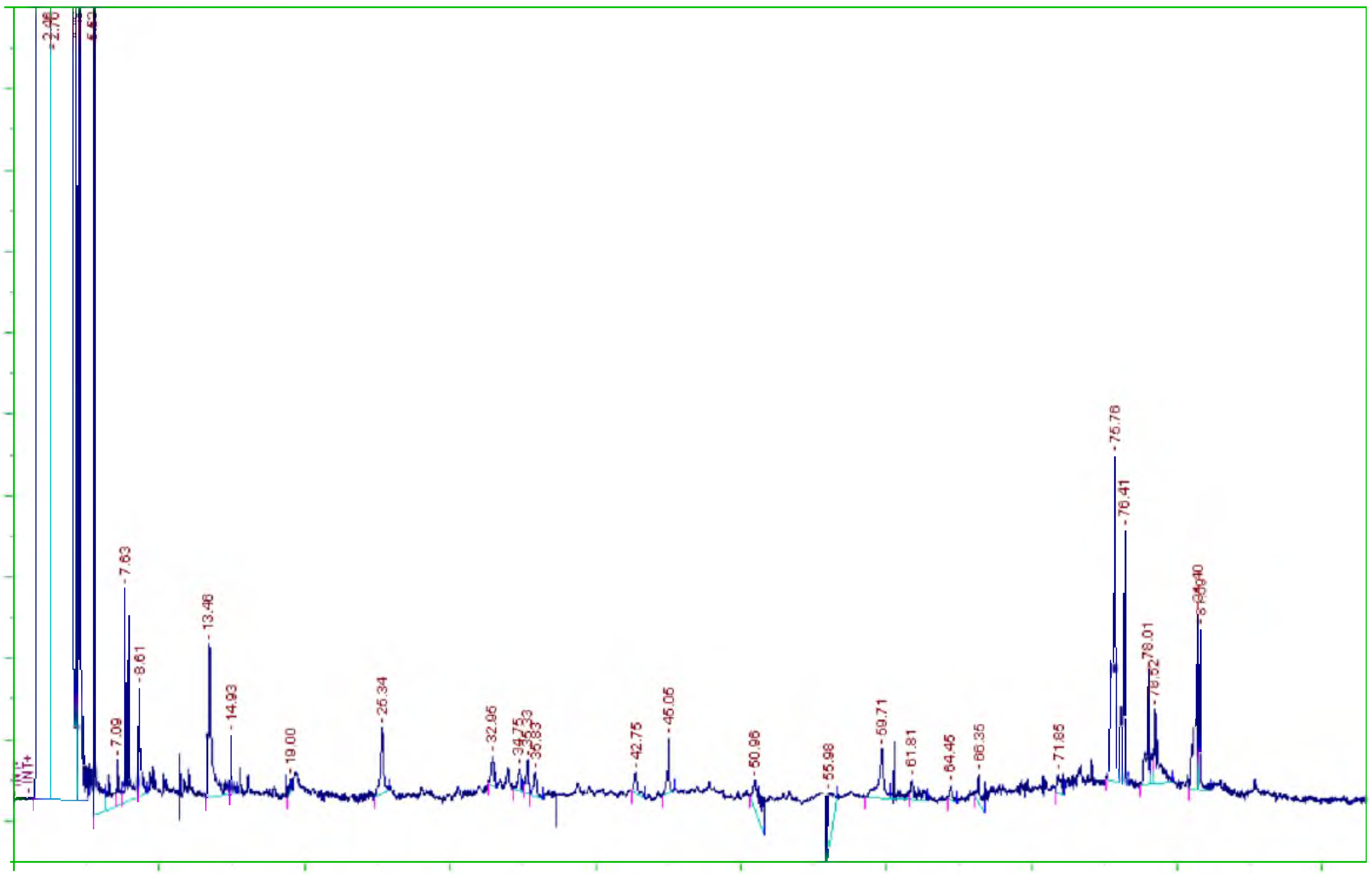

Figure 15. GC-FID chromatogram for tar sample extracted during test PM2 (tar concentration = 26.7 g/Nm^3). Abscissa is retention time (0-100 minutes) and ordinate is FID response intensity (0-2 millivolts).

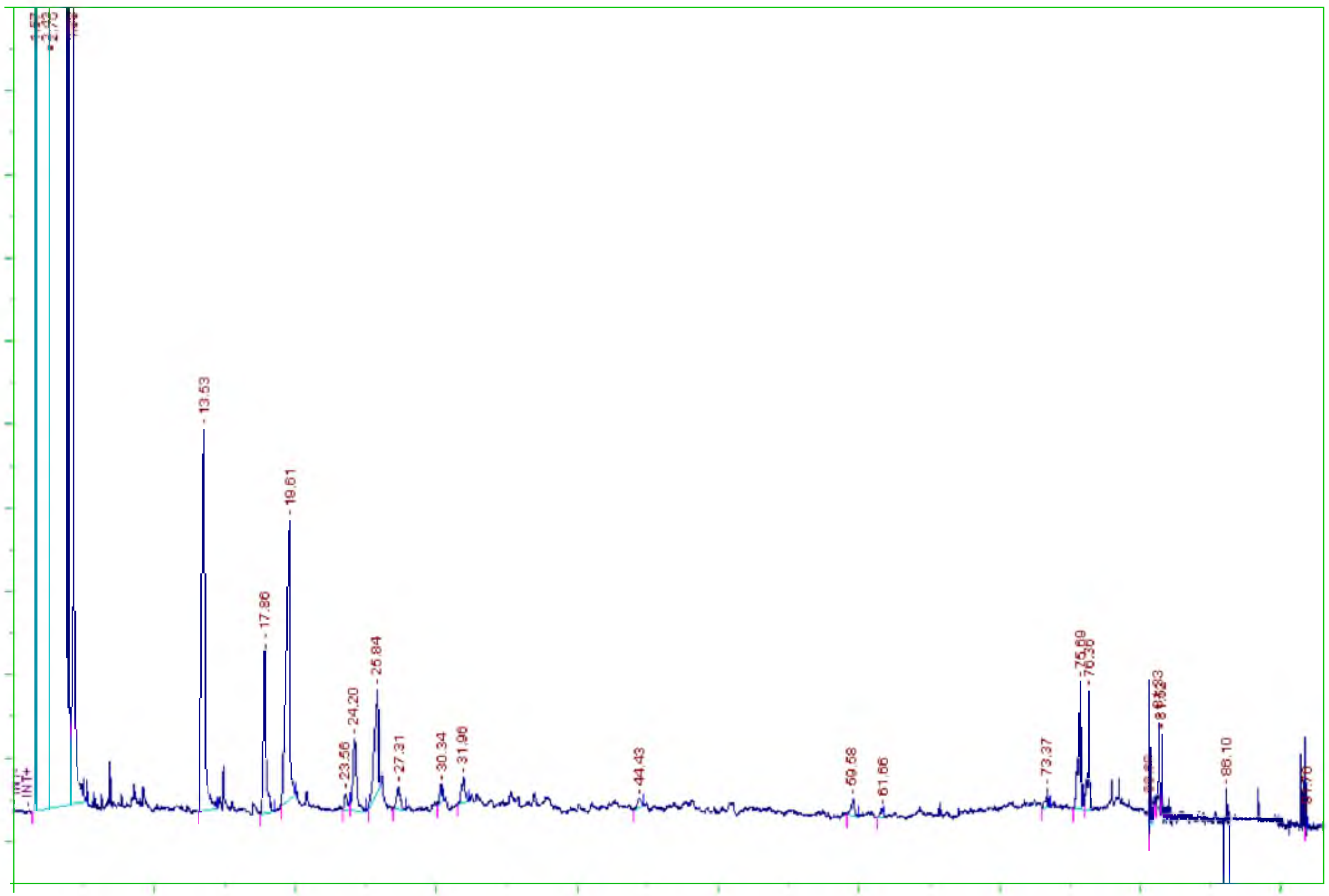

Figure 16. GC-FID chromatogram for tar sample extracted during test PM9 (tar concentration =18.6 g/Nm^3). Abscissa is retention time (0-100 minutes) and ordinate is FID response intensity (0-2 millivolts).

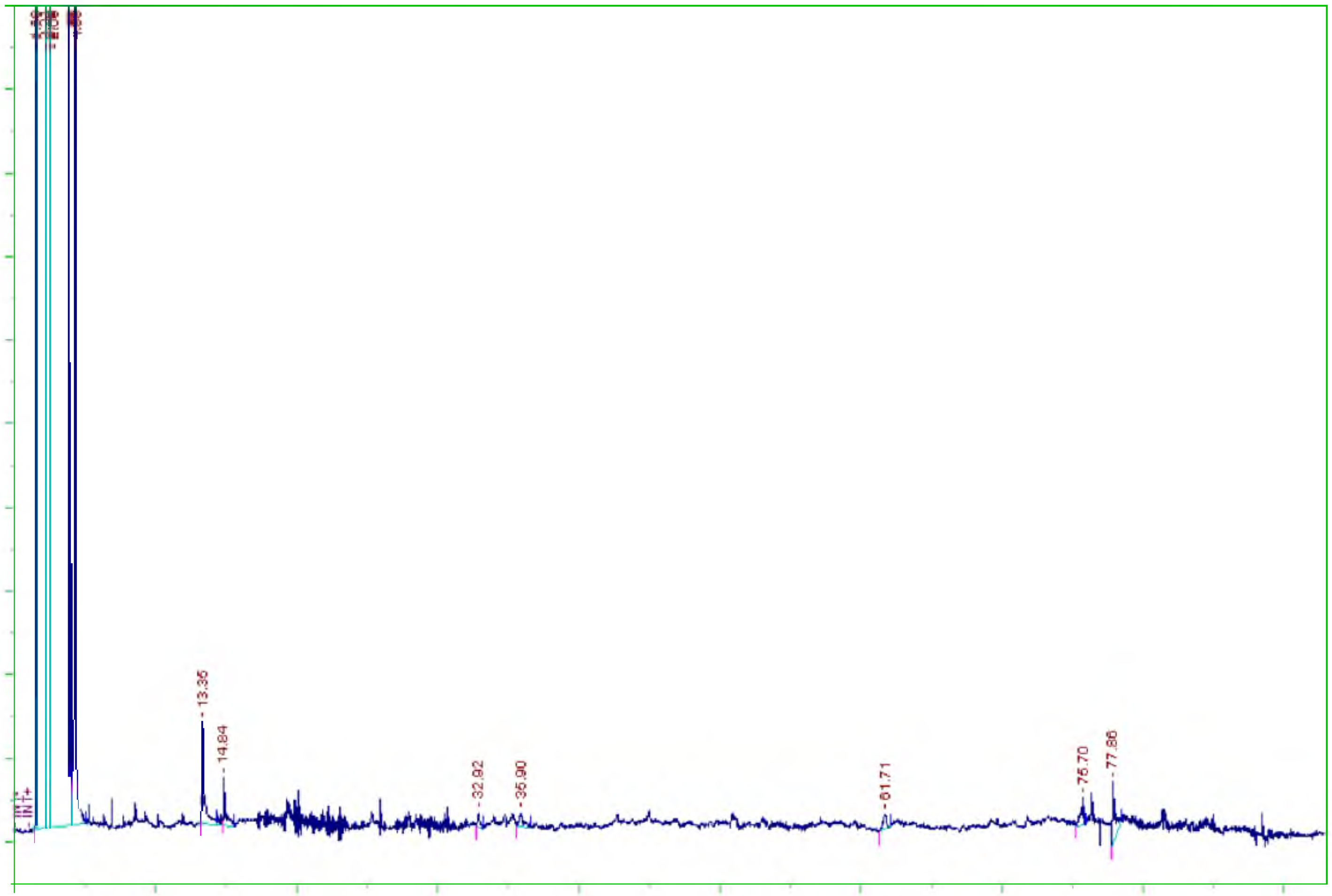

Figure 17. GC-FID chromatogram for tar sample extracted during test PM7 (tar concentration = 8.7 g/Nm^3). Abscissa is retention time (0-100 minutes) and ordinate is FID response intensity (0-2 millivolts).

operating condition, a wide range of tar species are detected with several relatively high intensity peaks at low retention time and a concentrated group of peaks at high retention time.

Figure 15 is a chromatogram for a tar sample extracted during steady operation for test PM2 (high temperature, low pressure). In comparison to the previous chromatogram for test PM4 (Figure 14), it is evident that the total tar concentration is significantly lower at this condition. While the number of peaks may be similar to that for test PM4, the relative magnitudes of individual peaks are much lower. The high magnitude peaks at shorter retention time seem to have largely disappeared. This indicates that these were likely primary tars, which are compounds formed during devolatilization that resemble the original fuel particle. The group of compounds with long retention times remain, but with smaller peak magnitude. These are likely secondary (phenolics and olefins) and tertiary tars (aromatics) that evolve from primary tars under more reactive conditions.

Figure 16 is a chromatogram for a tar sample that was extracted during steady operation for test PM9 (low temperature, high pressure). Overall, there appear to be fewer peaks in this sample, especially in the medium retention time region where peaks are nearly nonexistent. The primary products that were observed in the test PM4 chromatogram (Figure 14) are present again and are likely a characteristic of low temperature gasification. The tertiary products are also present but at lower magnitude and in lower quantities.

Figure 17 is a chromatogram for a tar sample extracted during test PM7 (high temperature, high pressure). Test PM7 exhibited the lowest tar concentration of all of the primary methods cases. The overall magnitude of all of the detected peaks is much lower than in the previous chromatograms presented. A few short peaks remain at short retention time and long retention time, which are likely secondary and tertiary tars as the majority of the primary tars have been reformed or polymerized to form larger tar species at temperatures above 1450°F(*20*).

5.2. Effect of biomass pretreatment

In addition to investigating reduction of tars at different gasifier operating conditions, an experimental campaign was performed to assess the effects of biomass feedstock pretreatment (torrefaction) on tar production. Tar samples were extracted during steady operation at each condition tested in the torrefied biomass experimental campaign (variables: torrefied feedstock type, feedrate, bed temperature). Results from the analysis of those tar samples, including concentration and composition, are presented in the following section.

5.2.1. Tar concentration

Tar concentrations, as determined by analysis of tar samples using GC-FID, for the torrefied biomass experimental campaign are displayed in Figure 18. The tar concentrations for raw biomass tests PM2 (high temperature, low pressure) and PM3 (medium temperature, low pressure) are also displayed for comparison. It should be noted that tar sampling during the torrefied biomass campaign was more challenging due to a breach that occurred in the particulate filter, which allowed significant amounts of char to flow through the filter. This resulted in char accumulation in many locations downstream of the filter, including the tar sample line. Efforts were made to keep the line clear but the samples were likely somewhat effected by this.

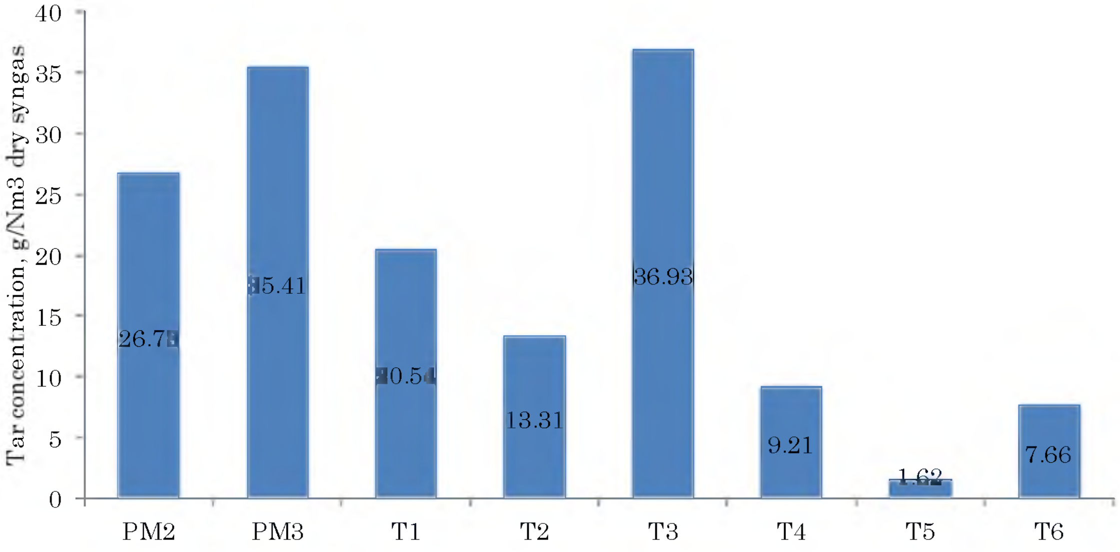

Figure 18. Synthesis gas tar concentrations for torrefied biomass gasification (g/Nm^3 dry synthesis gas).

First, in comparing the tar yields for raw biomass (PM2) and torrefied biomass (T1 and T4), the medium torrefied biomass (T1) produced 23% (by weight) less (20.5 g/Nm^3) and the dark torrefied material (T4) produced 66% less (9.2 g/Nm^3) tar than the raw biomass (26.7 g/Nm^3). This can likely be attributed to the decrease in feedstock volatile matter for torrefied material. Volatile matter is a precursor to tar species. Given the right conditions, a significant portion of the feedstock volatile content can go on to form tar species.

Comparison of the high (T1 and T4) and low feedrate (T2 and T5) conditions for the torrefied biomass shows a substantial decrease in tar content with decreasing feedrate. For the medium torrefied material, the low feedrate condition (T2) produced 35% less total tar than the high feedrate condition (T1). The reduction is even more significant for the dark torrefied material which exhibited an 82% decrease from high (T4) to low (T5) feedrate. Again, this can partially be attributed to the low total volatile feedrate entering the gasifier. Also, the lower feedrate results in a higher availability of steam for tar reforming.

The effect of decreased bed temperature also had a significant impact on tar yields (T2 vs. T3 and T5 vs. T6). A bed temperature reduction from 1450°F to 1250°F resulted in an increase in tar concentration by 64% for medium torrefied biomass and 79% for dark torrefied biomass. The tar concentration for test T3 (medium torrefied, low feedrate, low temperature) is particularly high (36.9 g/Nm^3), especially when compared to test PM3 (raw biomass, high feedrate, medium temperature, low pressure), which is also plotted in Figure 18 and produced a tar concentration of 35.4 g/Nm^3. From trends for raw and torrefied material at equivalent conditions, torrefied biomass produced significantly lower tar yields. Therefore, it is possible that the value reported for test T3 is flawed due to measurement error as result of particulate contamination in the sampling apparatus.

Representation of the tar yields on a lb/lb dry biomass basis for the torrefied experiments is displayed in Figure 19. Overall, these trends follow the tar concentration trends reported in Figure 18. It is interesting to

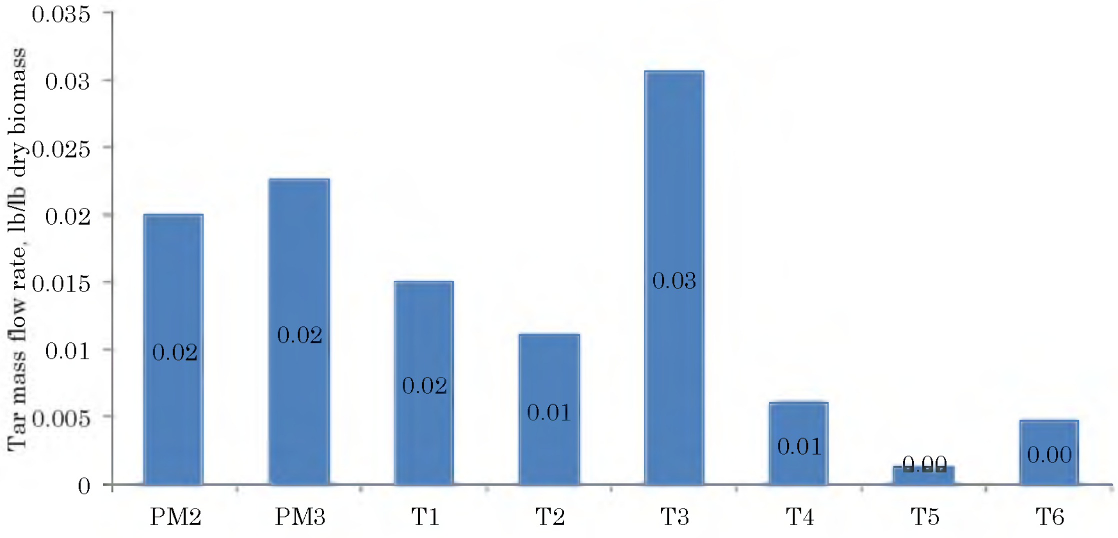

Figure 19. Tar mass flow rate for torrefied biomass gasification (lb/lb dry biomass).

consider that the best performing experiments with regard to tar production (dark torrefied tests, T4-T6) were converting less than 0.5% (by weight) of the biomass feedstock to tar species.

5.2.2. Tar composition

GC-FID chromatograms of two of the torrefied biomass tests are presented in Figure 20 and Figure 21 for qualitative comparison. The chromatogram for the worst performing torrefied biomass test with regards to tar production, test T3 (medium torrefied, low feedrate, low temperature), which yielded 35.4 g/Nm^3 of total tar, is displayed in Figure 20. The chromatogram for the best performing torrefied biomass test with regards to tar production, test T5 (dark torrefied, low feedrate, high temperature), which yielded 1.6 g/Nm^3 of total tar, is displayed in Figure 21. Comparison of these chromatograms with those of the raw biomass tar samples shows a higher proportion of heavy tars, which are detected at high retention times on the chromatogram, for torrefied biomass. This makes sense because torrefaction is a mild pyrolysis process in which light volatiles are driven off at relatively low temperatures, leaving a higher fraction of heavy volatile components. The test T5 tar sample produced very few tar species peaks but still shows a cluster of peaks at high retention time, which again indicates the presence of high boiling point, heavy tars.

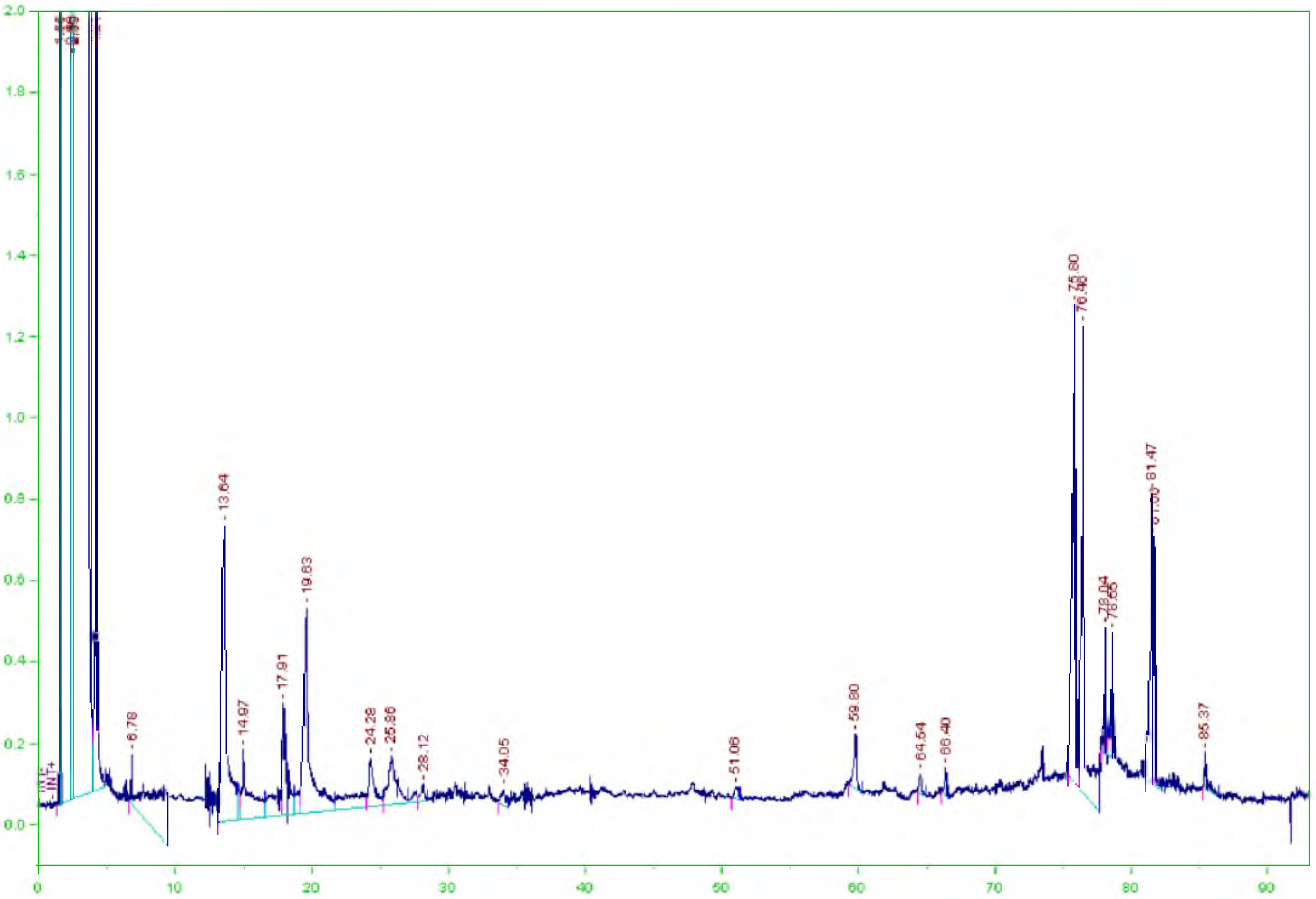

Figure 20. GC-FID chromatogram for tar sample extracted during test T3 (tar concentration = 36.9 g/Nm^3). Abscissa is retention time (0-100 minutes) and ordinate is FID response intensity (0-2 millivolts).

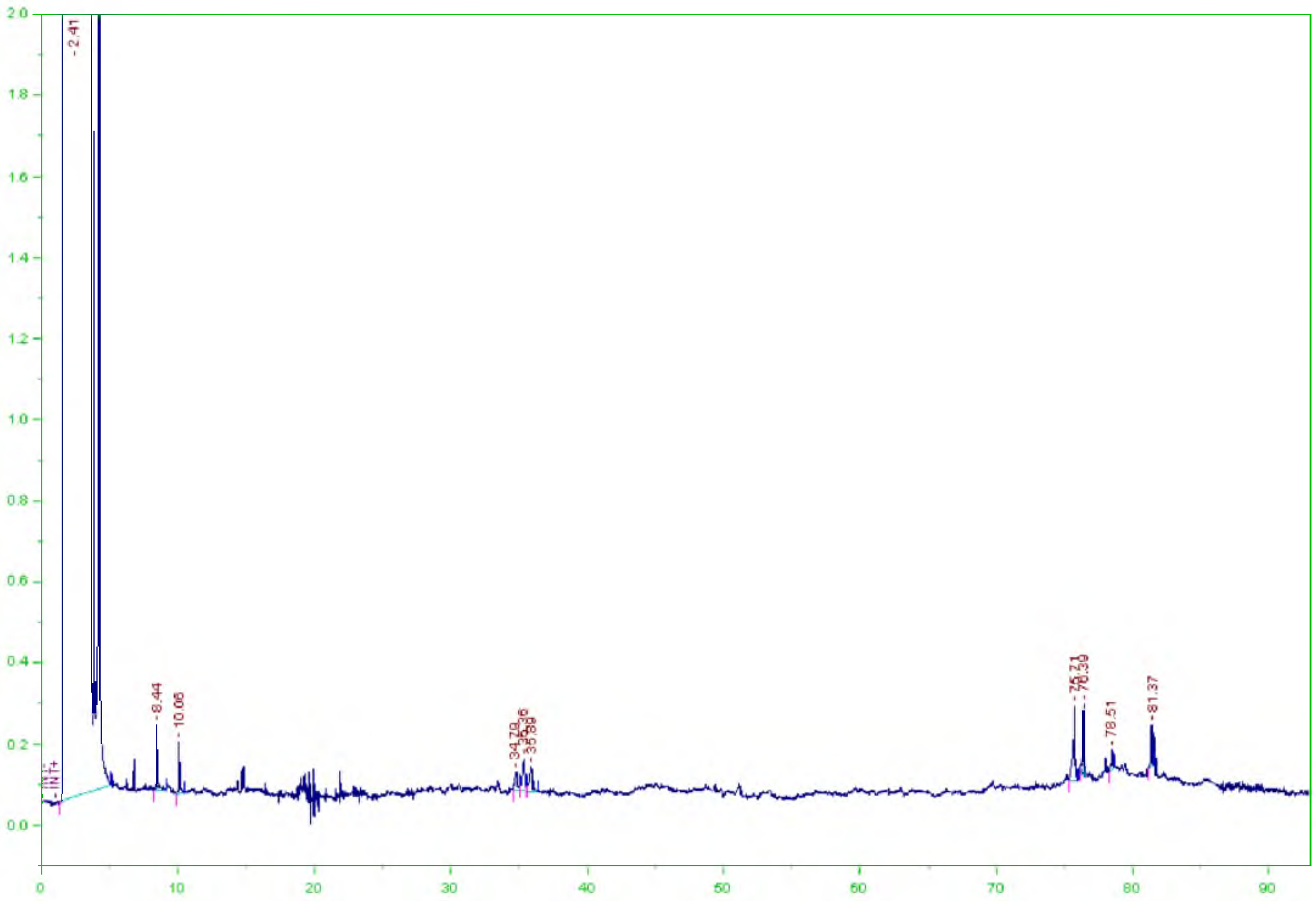

Figure 21. GC-FID chromatogram for tar sample extracted during test T5 (tar concentration = 1.6 g/Nm^3). Abscissa is retention time (0-100 minutes) and ordinate is FID response intensity (0-2 millivolts).

CHAPTER 6

RESULTS: GASIFIER OPERATION AND PERFORMANCE

Data presented in the preceding chapter demonstrates that implementation of primary methods, including elevated temperature, pressure, and feedstock preparation, results in an overall reduction of tar content in synthesis gas produced from gasification of woody biomass. However, from these data, it is clear that certain tar species, especially larger tertiary species, are more likely to resist cracking and can even mature, increasing in concentration, in more reactive conditions. Therefore, it is necessary to understand the effects of primary method implementation over a range of conditions so that the proper tar concentration and composition can be achieved in order to reduce downstream cleanup and meet the needs of end-use devices.

Furthermore, an in-depth understanding of the effects of primary method implementation on the operability and performance of the gasifier is necessary in order to assist in the selection of the desired gasifier operating conditions. The following sections will present results and discuss the outcomes of various gasifier operating conditions and feedstock pretreatment on the operability and efficiency, including mass and energy conversion, of the biomass gasification system.

6.1. Gasifier operation: qualitative evaluation

In order to establish a suitable understanding of the gasifier operation during a typical experiment, a description will be provided before providing operational details with regards to primary methods implementation. For this description, an experiment was selected from the primary methods campaign, which exhibited what can be considered "normal" operation of the gasifier. Deviations from normal operation at various other operating conditions will be discussed in the proceeding sections.

Monitoring of gasifier conditions during operation at elevated temperature and pressure is achieved by various methods of process measurement (e.g., temperature, pressure, flow). For the purpose of this description, several of the critical process measurements will be introduced and discussed, including system mass inputs, system energy inputs, gasifier internal monitoring, and system outputs. Primary methods test #2 (PM2) is selected as a standard case to demonstrate typical gasifier operation as it is within normal operating conditions and presented little operational difficulty in comparison with experiments performed at lower temperature or higher pressure. The target temperature and pressure for test PM2 are 1450°F (“high” condition) and 5 psig (“low” condition), respectively.

6.1.1. Normal high-temperature, low-pressure operation

6.1.1.1. Steam flow and SGV

The system mass inputs consist of superheated steam and woody biomass feedstock. The mass flow rate of saturated steam produced in the steam generator is measured using a v-cone flow measurement device and a K-type thermocouple for temperature measurement. For the primary methods experimental campaign, the steam flow rate was controlled in order to maintain a constant superficial gas velocity (SGV, ft/s), or fluidizing velocity, through the bed section of the gasifier. The SGV is typically maintained in the range of 0.8-1.2 ft/s in order to sustain adequate fluidizing conditions in the bed without large amounts of particle entrainment out of the reactor vessel. Depending on the bed material, a low SGV results in stagnation of the bed and poor mixing, and a high SGV results in channeling of steam through the bed and entrainment of bed particles with the exit gas. The SGV is calculated based on the temperature and pressure at the distributor plate, and the steam flow rate. For test PM2, a steam flow rate of approximately 40 lb/hr (Figure 22) was adequate to maintain an SGV of 1.0-1.2 ft/s (Figure 23). The steam flow rate typically fluctuates by approximately +/- 5 lb/hr due to cycling of the steam generator and lag in the steam flow PID control loop.

6.1.1.2. Gasification system pressure

One characteristic of the SGV is its dependence on the system pressure. In the case of test PM2, the pressure gradually increases throughout the test period due to the entrainment and accumulation of fine particulate (e.g., bed fines, char, ash) on the surface of the high-temperature candle filters (Figure 24). A sudden drop in pressure is observed in test PM2 at approximately 13:20 due to back-flushing of the filter using a high-pressure nitrogen pulse.

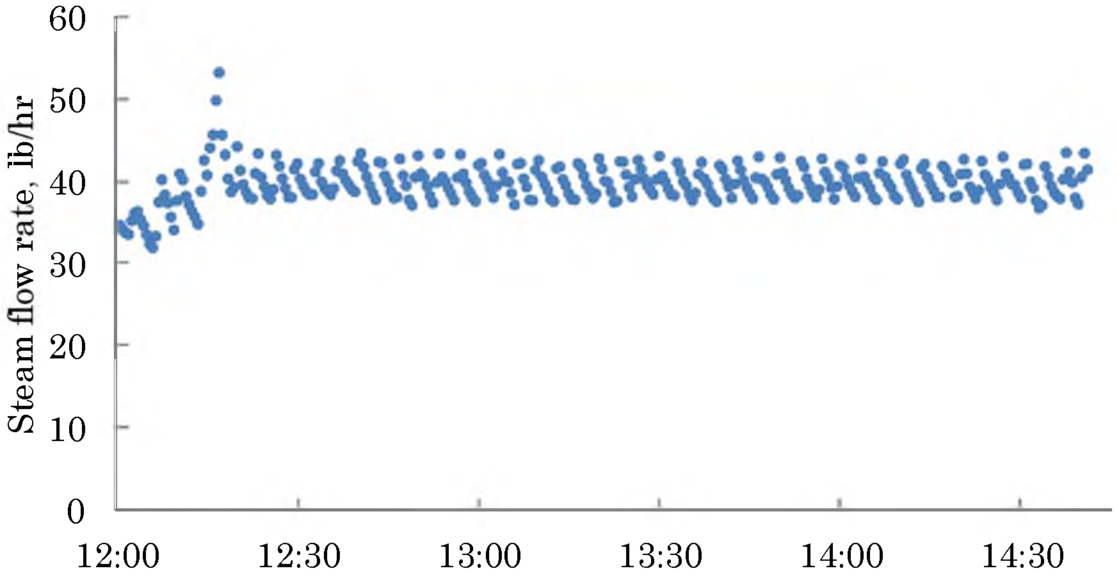

Figure 22. Test PM2 steam flow rate (lb/hr)

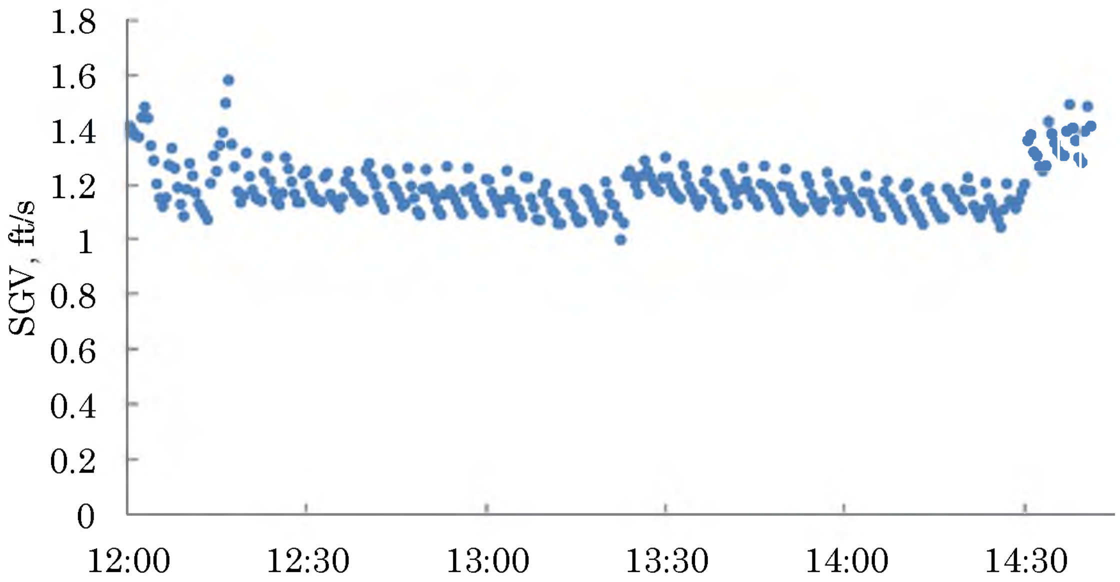

Figure 23. Test PM2 superficial gas velocity (ft/s)

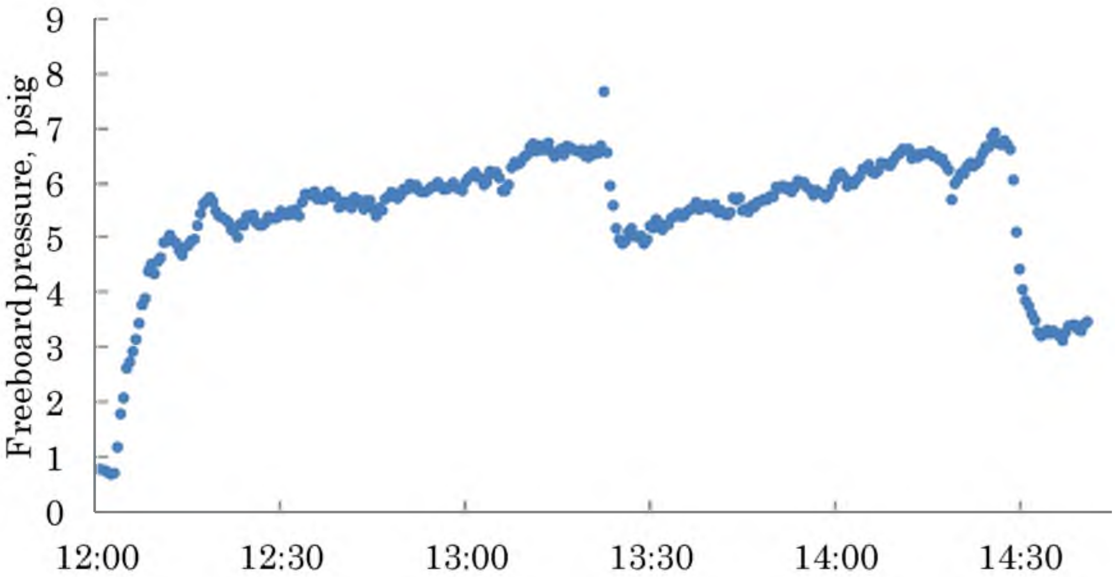

Figure 24. Test PM2 gasifier freeboard pressure (psig)

A second drop in the system pressure at 14:25 is due to reduction of product gas flow following the termination of biomass feed into the gasifier. Accordingly, the SGV gradually decreases throughout the test due to the compression of gas in the gasification system with increasing pressure.

6.1.1.3. Bed pressure drop

Several properties of the fluidized bed are critical in ensuring adequate performance of the gasifier. First, the bed pressure drop is measured between the solids drain pipe (high) and the freeboard (low). Nitrogen purge is supplied through the bed pressure drop transducer tubing to avoid accumulation of condensate and particulate. The bed pressure drop provides a relative estimate of the bed height for a given bed material type. The bed pressure drop trend during a gasification test can provide a qualitative valuation of the accumulation or reduction of bed material inventory. For example, conditions which do not favor conversion of char to gaseous species can result in an accumulation of char in the bed, in which case, the bed pressure drop would expectedly increase throughout a test. In the case of test PM2, conditions were sufficiently favorable for char conversion, resulting in very little bed pressure drop increase over the course of the test (Figure 25). In addition, no loss of bed inventory was observed during the test, indicating that the SGV was sufficiently low to avoid significant particle

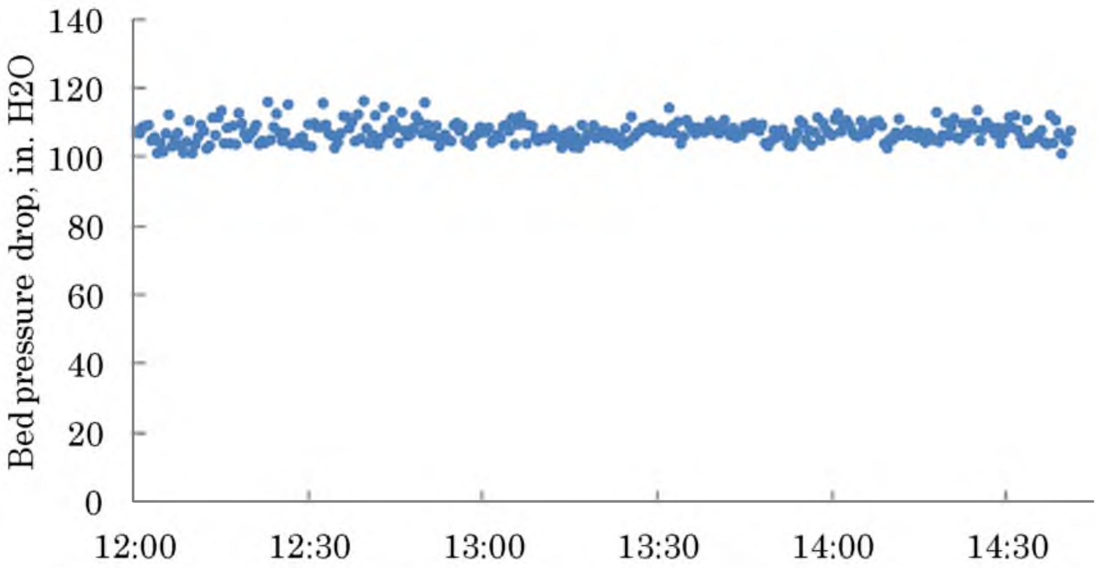

Figure 25. Test PM2 bed pressure drop (in. H_2O) trend

entrainment other than the char and ash that accumulated in the downstream particulate filter.

6.1.1.4. Particulate filter

In order to track the accumulation of particles entrained in the product gas in the downstream, high-temperature particulate filter, a wet-wet differential pressure transducer was added to measure the pressure drop across the filter. This addition was made following the primary methods tests and prior to the torrefied wood tests. For typical operation, the gas velocity through the gasifier was sufficient to entrain some amount of fine particulate from the gasifier. According to another work, the terminal velocity of 200 micron char particles is approximately 1.5 ft/s and below 1.0 ft/s for finer char particles (*86*). Therefore, the velocity through the gasifier was sufficient to entrain some amount of fine particles out of the gasifier despite having an internal cyclone to return entrained particles to the bed. This was especially true for the very fine (<50 micron) particles that are typically collected in and removed from the downstream particulate filter.

The filter pressure drop trend for test T1 (medium torrefied wood, high feedrate, high temperature, low pressure) is displayed in Figure 26. Gradual increase in the filter pressure drop is observed throughout the test. Sudden decreases in the filter pressure drop are due to filter back-flush using a high

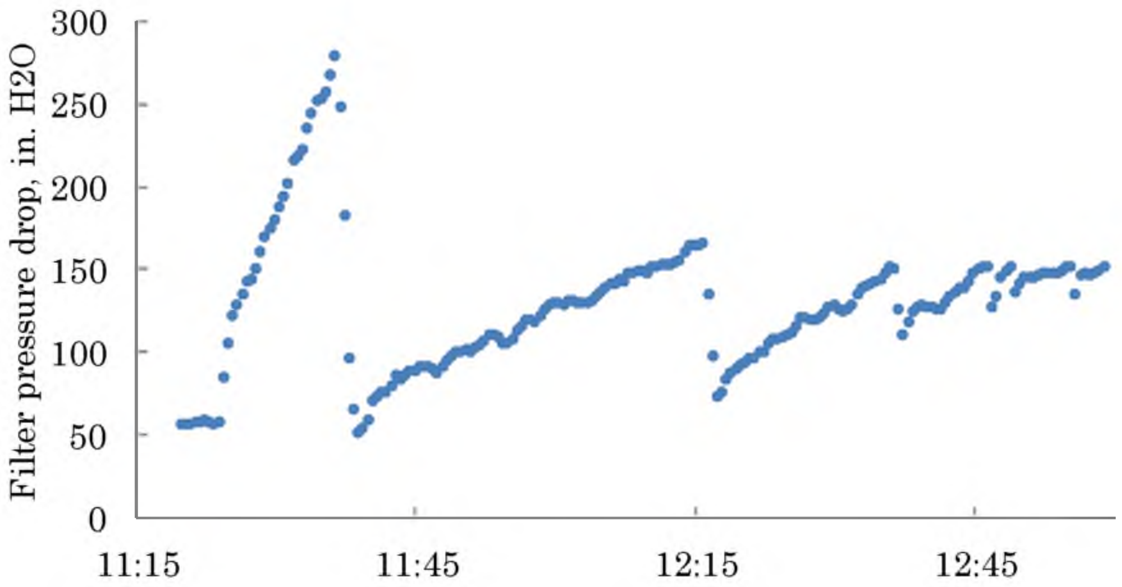

Figure 26. Test T1 particulate filter pressure drop trend (in. H_2O)

pressure nitrogen pulse. In addition to pulsing of the filter, a lock-hopper attached at the filter drain point allows for removal of the filter retentate during operation, which generally extends the amount of time between filter pulses.

6.1.1.5. Bed temperature

In order to ensure that the reactive conditions in the bed are sufficient for fuel conversion, the bed temperature is measured using six type-K thermocouples at various heights through the gasifier bed section. The bottommost thermocouple protrudes into the bed directly above the distributor plate, providing a measure of the bed motive fluid (steam) as it enters the bed. An additional thermocouple measures the bed temperature at the height of the feed injection point. Four thermocouples measure the bed temperature in the heater section, one above each bundle of electric bed heaters. Good mixing in the bed provides a relatively uniform temperature profile throughout the bed. During normal gasifier operation, the temperature disparity in the heater section of the bed is generally no more than approximately 10°F. The distributor plate temperature is generally less than 50°F cooler than the bed heater section.

Figure 27 displays the average bed temperature (blue), heater section temperature disparity (range of temperatures in the bed heater section) and

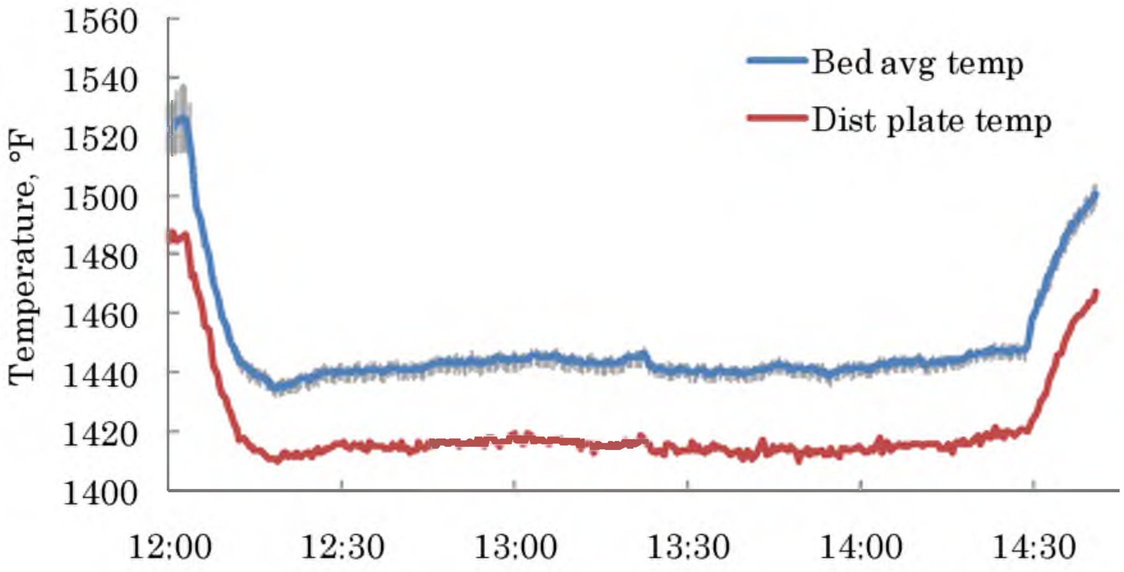

Figure 27. Test PM2 average bed temperature (blue) (grey shaded temperature disparity) and distributor plate temperature (red) trends (°F).

distributor plate temperature (red) for test PM2. Prior to initiation of biomass feed, the bed temperature is maintained at a relatively high temperature to avoid a significant temperature loss upon initiation of biomass feed. Caution is taken to avoid bed temperatures that approach the melting temperature of the ash content in the biomass feedstock. Ash melting in the bed can result in the fusing of the ash and bed particles and lead to agglomeration of the bed. For these experiments, the bed temperature was maintained below approximately 1550°F to avoid agglomeration according to past experience with this particular bed material (aluminum oxide) and biomass feedstock (raw pine wood chips). Steady bed temperature was achieved within approximately 45 minutes after the initiation of biomass feed with a heater section temperature disparity of approximately +/- 3°F, which would indicate good mixing conditions in the bed heater section. The bed temperature at the distributor plate was consistently 25-30°F cooler than the bed heater section during the thermally steady period. This temperature is quite high considering that the steam temperature at the plenum inlet (upstream of the distributor plate) was approximately 1070°F during test PM2. This indicates that heat from the heated section of the bed was transported to the bottom of the bed.

6.1.1.6. Bed heaters

Heat is supplied to the fluidized bed section via four electrical heater bundles totaling 32 kW_{th}. The electrical supply to each of the four bed heater bundles is controlled by a solid-state relay (SSR) which receives a 4-20 mA input signal from the distributed control system (DCS) based on the user-defined temperature bed average temperature set point. In general, the lower bed heaters operate at higher output than the upper bed heater bundles as heat generated in the lower bed is transported upward with the bed motive fluid. Prior to the initiation of biomass feed, the bed heaters generally operate well below their maximum rated output. In the case of test PM2, the bed average temperature was above 1500°F and increasing with a total bed heater output of approximately 12 kW_{th} (Figure 28). After initiation

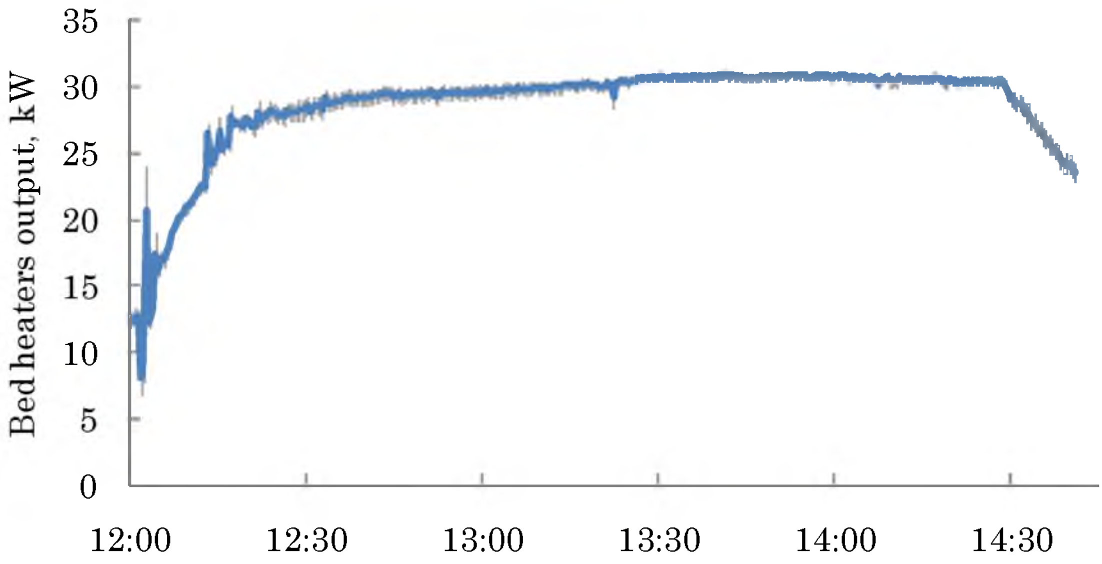

Figure 28. Test PM2 total bed heater output (blue) and bed individual bed heater output disparity (grey shaded) (kW_{th})

of biomass feed, at a rate of approximately 50 lb/hr (wet basis) in this case, the total bed heater output sharply increases in order to maintain the bed average temperature set point, 1450°F in this case. The total bed heater output remains relatively stable throughout the test, increasing slightly, which may be a result of the additional heat load on the bed due to increased purge gas flow as the system pressure increases (Figure 24). For test PM2, the bed heaters operated near maximum output for the duration of the test, which is common for high-temperature operation. Upon termination of biomass feed, the bed temperature immediately begins to increase, resulting in a decrease in the bed heater output.

6.1.1.7. Synthesis gas flow rate

The product gas output is measured using a v-cone mass flow meter device located downstream of the pressure control valve and upstream of the synthesis gas thermal oxidizer (a.k.a., afterburner). This flow rate measurement requires an assumed gas molecular weight; therefore, it cannot be used as an absolute mass flow measurement because the molecular weight of the product gas is not known in real-time. However, this measurement is useful in indicating the flow of product gas in addition to steam on a relative basis, for example, when determining steady gas flow conditions. In the case of test PM2, the initial synthesis gas flow rate measurement of approximately 40 lb/hr quickly increases upon initiation of biomass feed at 12:00 to a steady value of approximately 100 lb/hr within 20 minutes and after adjustment of the steam flow rate (Figure 29). During the primary methods experimental campaign, a synthesis gas molecular weight of 18 g/mol was assumed. For test PM2, the actual steady-state synthesis gas molecular weight was approximately 20.71 g/mol determined from GC measurement and not accounting for the steam content in the product.

6.1.1.8. Gas composition

The synthesis gas flow rate (Figure 29) provides a relative indicator of the amount of particulate free product exiting the gasifier. In order to further

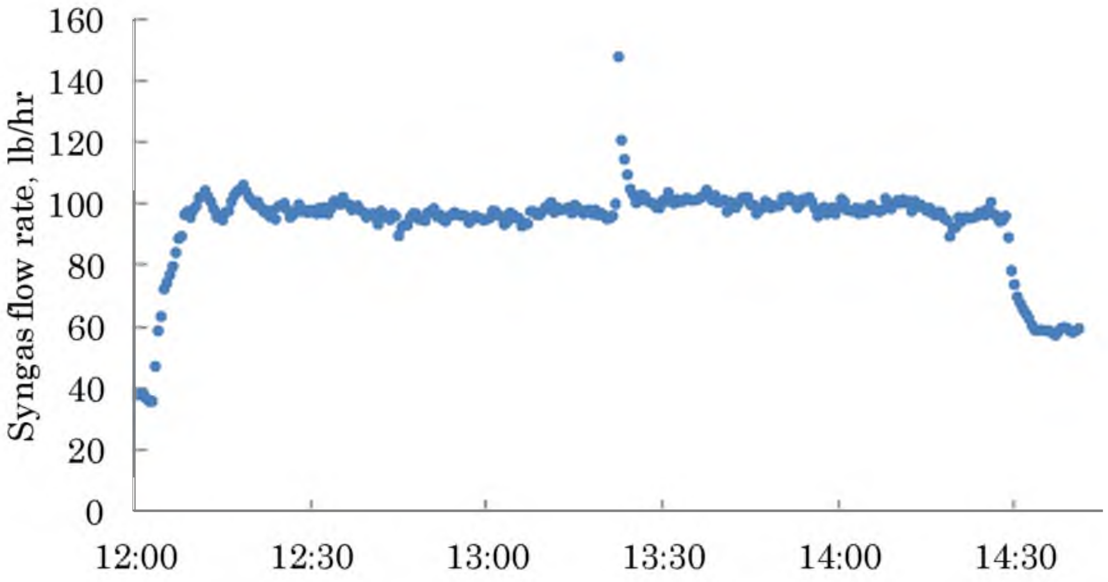

Figure 29. Test PM2 synthesis gas flow rate (lb/hr, including steam) using an assumed gas molecular weight of 18 g/mol

characterize the product gas, online measurement of the gas composition is carried out using micro-gas chromatography (micro-GC). A slipstream of product gas is pulled from the bulk gas stream downstream of the synthesis gas v-cone mass flow measurement device. The gas slipstream is first cooled in a continuous flow water impinger to remove fine particulate and condensable species. The sample gas is further conditioned by coalescing filtration and is cooled to remove moisture (as previously described). The micro-GC analyzes a gas sample approximately every 4 minutes and operates continuously throughout the test period. The 4-column micro-GC is calibrated to measure concentrations of 17 common gas species that are commonly produced during gasification. However, the bulk of the dry product gas consists of nitrogen (from fuel and purge), hydrogen, carbon monoxide, carbon dioxide, and methane. The product gas composition trend for test PM2 is displayed in Figure 30 and accounts for nitrogen; however, it is not displayed. Typically, the nitrogen concentration is approximately 10-20% (by volume). The production of synthesis gas is nearly instantaneous upon initiation of biomass feed into the gasifier, as can be seen by the sudden spike in synthesis gas concentration in the micro-GC trend. In general, relatively high concentrations of carbon monoxide and low concentrations of hydrogen and carbon monoxide are observed at the beginning of a test. As the gasifier reaches thermal equilibrium, within approximately the initial 45

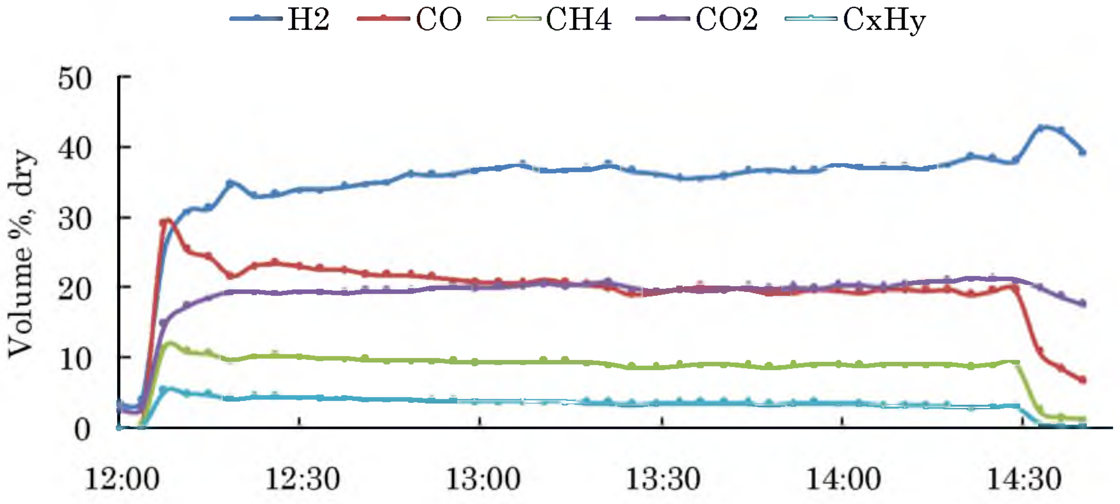

Figure 30. Test PM2 dry product gas composition trend from micro-GC (vol%, dry).

minutes of operation for test PM2, the carbon monoxide concentration sharply decreases and the hydrogen and carbon monoxide concentrations abruptly increase. Following these abrupt initial concentration trends, there is a continued gradual shift from carbon monoxide to hydrogen and carbon dioxide production, which indicates that the water-gas shift reaction rate, which is favored in steam reforming, is relatively slow. The accumulation and conversion of char requires long periods of time to reach equilibrium, on the order of tens of hours in a fluidized bed steam reformer (*87*). Therefore, achieving gas and solid phase chemical equilibrium takes a very long time and was not possible for this experimental campaign. The gas phase product composition generally achieved quasi-steady conditions during each test which was used as the characteristic gas composition for that condition. In the case of test PM2, quasi-steady gas composition was achieved approximately 1.5 hours after the initiation of biomass feed. The condition is typically maintained for 0.5-1.0 hours in order to produce an average gas composition for that condition. The average dry product gas composition for test PM2 is displayed in Table 6.

6.1.2. Reduced temperature operation

The preceding section provides a description of normal gasifier operation for the pilot-scale unit utilized for this research. The bed is maintained at a

Table 6. Test PM2 dry product gas average composition (with standard deviation) (vol%).

Component	Concentration, vol%, dry (std)
H_2	36.8 (0.9)
CO	19.4 (0.3)
CO_2	20.2 (0.6)
CH_4	8.9 (0.2)
C_xH_y	1.0 (0.2)

temperature safely below the melting temperature of ash in the fuel to avoid the risk of agglomeration, but high enough to provide conditions for adequate fuel and tar conversion. High-temperature operation does require more energy input in the form of indirect heat or oxygen addition compared to low-temperature operation. Therefore, energy savings from operation at low temperature should be considered and balanced with the reduction in fuel conversion and operational difficulties that low-temperature operation present. The following qualitative discussion will highlight operational difficulties and benefits from low-temperature operation compared to the baseline case described in the previous section. A discussion of the quantitative effects of reduced-temperature operation will be covered later.

6.1.2.1. Bed heaters

A significant benefit of low-temperature operation is the reduction in the energy requirement to maintain the bed temperature. While high-temperature operation requires the bed heaters to operate near full capacity (32 kW) during gasification conditions, primary methods tests carried out at low temperature (1050°F) require approximately 30% of full capacity output for the same woody biomass feedrate (Figure 31). This indicates that a significant amount of the energy input through the bed heaters is used to maintain the bed temperature and heat the motive superheated steam flow entering the bed.

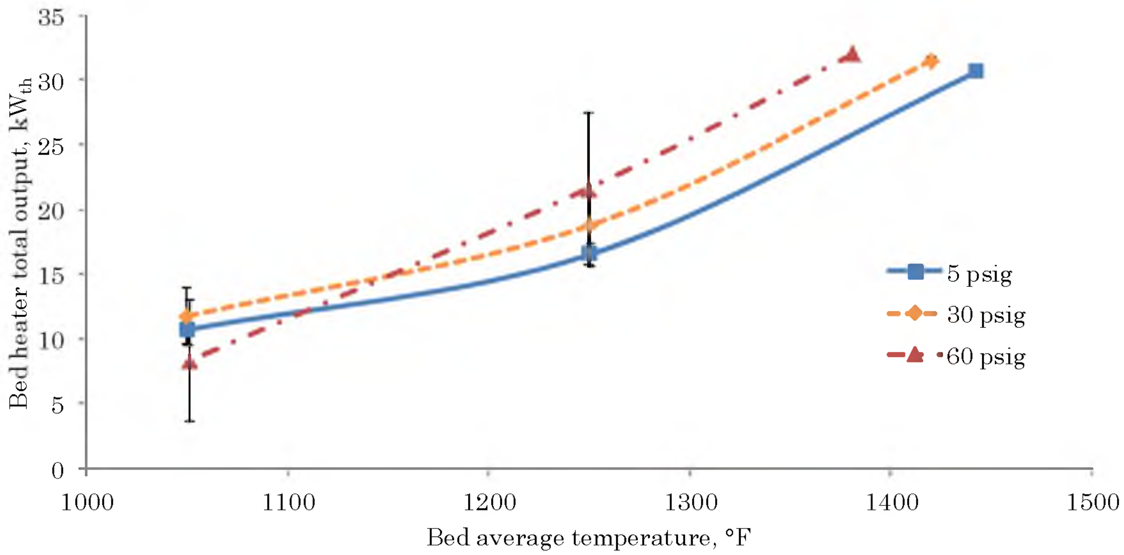

Figure 31. Bed heater total output for primary methods campaign (kW$_{th}$)

6.1.2.2. Char production

Due to the reduced fuel heating rate and char steam gasification reaction rate at lower temperature, it is expected that the char production and accumulation will be higher at low temperature. Operationally, this results in an accumulation of char in the bed, an accumulation of char in the downstream particulate filter, or both. The location in the system of char accumulation appears to depend mostly on the velocity of gas flow through the gasifier.

During low temperature operation, the fluidizing velocity can be compensated for by increasing the steam flow. However, at lower temperature, fuel conversion is inhibited, resulting in a lower synthesis gas yield and less total gas flow exiting the gasifier. In addition, the temperature at the exit of the gasifier is lower, which further reduces the gas velocity at the gasifier exit. These factors result in lower entrainment of fine particles, including char and ash, lower particulate loading in the particulate filter, and more accumulation of material in the bed. This was observed for all low-temperature cases (PM4, PM9, PM10 and T3) with the exception of T6 during which the bed pressure drop measurement was not functioning (Figure 32). The low amount of particle entrainment is verified by comparing the high- and low-temperature, medium-torrefied wood gasification tests (T2 and T3) (Figure 33). From this comparison, it is apparent that the entrainment of

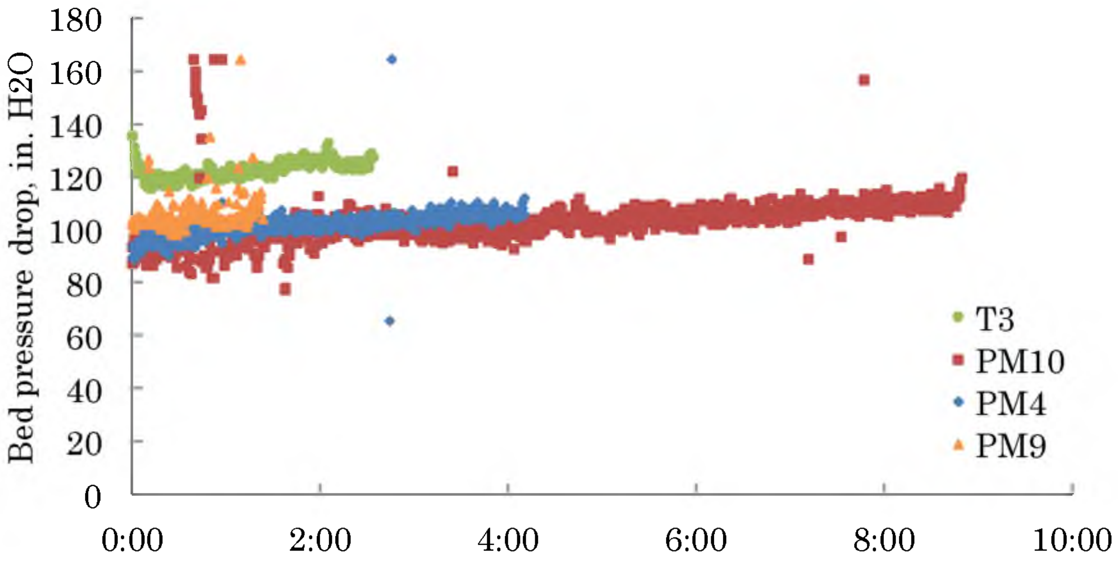

Figure 32. Bed pressure drop for low-temperature tests: PM4, PM9, PM10, and T3 (in. H_2O)

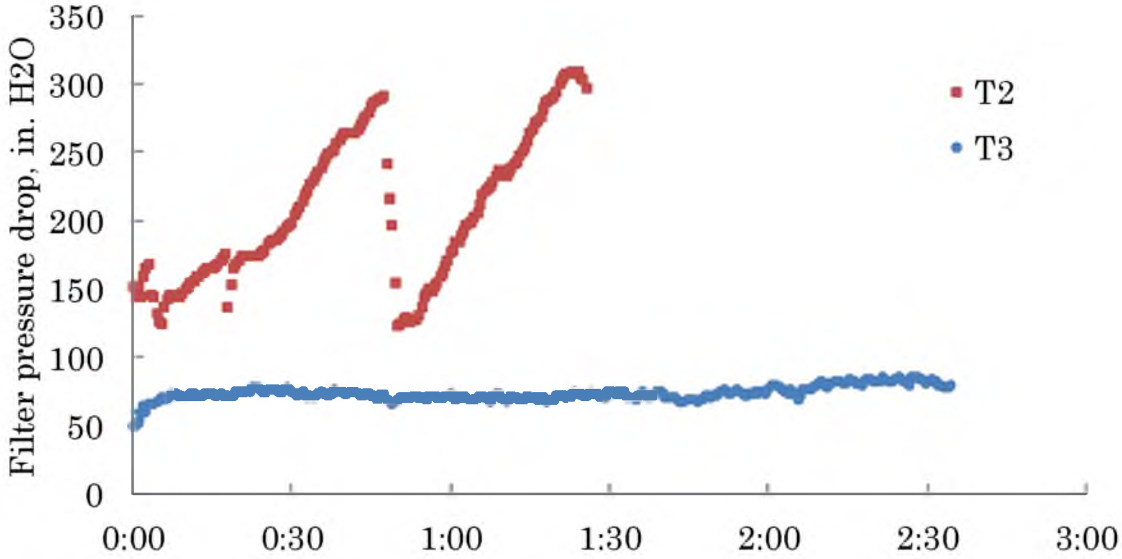

Figure 33. Filter pressure drop for high- and low-temperature, medium-torrefied wood gasification tests (T2 and T3) (in. H_2O)

particles from the gasifier is greater for high temperature operation despite the average steam fluidizing velocity being higher in the low-temperature test (0.99 ft/s in T3, 0.83 ft/s in T2). Operationally, it is desirable to retain unreacted fuel particles and char in the fluidized bed as it is more likely to react and form desirable products there than in cooler downstream locations. Particulate entrainment and loading in downstream equipment can cause product gas flow obstruction and uncontrolled gasifier pressure increases, and requires careful removal and disposal.

6.1.3. Elevated pressure operation

The gasifier pressure is maintained relatively low to avoid problems associated with high-pressure operation, including maintaining steady pressure conditions in the gasifier, difficulties in feeding at high pressure, and avoiding safety risks due to product gas leakage at elevated pressure. A number of advantages can be gained from gasification at high pressure. Methane formation from the methane-forming gasification reactions (R7) are favored at elevated pressure because formation of the products involves a decrease in volume. Increased methane content in the product gas increases the heating value of the product, which is desirable for direct heating applications such as steam generation or substitute natural gas production. In addition, several of the methane-forming reactions are exothermic, which results in decreased heating load and oxygen consumption. Operation at elevated pressure also allows for higher throughput of reactants for a given reactor volume and reduces or eliminates the need for downstream compression of the synthesis gas. The following qualitative description will highlight operational difficulties and benefits that were observed during the primary methods tests at elevated pressure. A discussion of the quantitative effects of elevated pressure gasification will be discussed later.

6.1.3.1. Biomass feeder

A significant effect of operation at elevated pressure for the pilot-scale gasification system used for this research was the difficulty experienced in maintaining biomass feed. While it is often an overlooked topic in academic literature, feeding of solid fuels at high pressure is a significant challenge and, in addition to tar and other contaminant removal from synthesis gas, presents a barrier in the commercialization of gasification technologies. Biomass, in particular, presents challenges in feeding and handling due to the heterogeneity of fuel particles size and shape, fibrous nature of many lignocellulosic feedstocks, and high moisture content (*30*, *88*). For the pilot-scale gasification system used in this research, the woody biomass feedstock requires careful preparation, including size reduction and screening to 3/8 in. or smaller and drying to less than 20% (by mass) moisture. Despite careful preparation of the feedstock, operation of the pressurized screw feeder can be challenging under high-pressure conditions. While nitrogen purge is minimized to prevent extra thermal loading of the hot bed and to reduce valueless nitrogen content in the product gas, inadequate purge through the feeder results in partial backflow of hot bed solids into the injector screw housing and subsequent jamming of the injector screw. Normal operation of the feeder lock-hopper causes small perturbations in the nitrogen purge flow into the feeder, which, at high pressure, can result in more substantial bed particle reflux into the injector screw and more frequent screw jamming. Some upgrades to the feeder have been made to ensure more consistent nitrogen purge flow to the feeder since the primary methods campaigns. However, occasional injector screw jamming was encountered during the primary methods campaigns. Figure 34 displays synthesis gas flow rate trends for primary methods tests PM3 and PM8. Test PM3 was run at low pressure (4.9 psig) while test PM8 was run at high pressure (61.8 psig). The synthesis gas flow rate trend for test PM3 is relatively smooth and consistent in comparison to that of test PM8 in which the gas flow rate fluctuates significantly throughout the test due to frequent screw jamming and as a result inconsistent synthesis gas production.

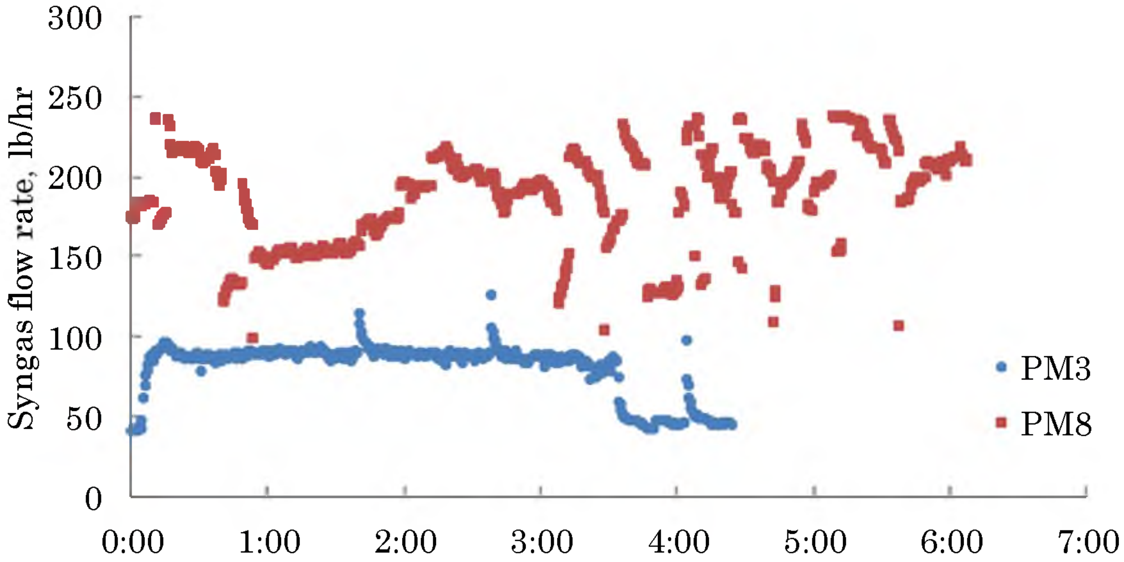

Figure 34. Synthesis gas flow rate for tests PM3 (low pressure, medium temperature) and PM8 (high pressure, medium temperature) (lb/hr).

6.1.3.2. Equipment limitations

The high-pressure condition (60 psig) for the primary methods experimental campaign was selected based on previous operating experience with the pilot-scale biomass gasification system and to provide a relatively wide range of conditions for evaluation of the pressure as a potential method for tar reduction and gasifier performance enhancement. In its current configuration, this condition represents the maximum pressure that the gasification system can support due to ancillary equipment limitations. For example, it was necessary to operate the steam generator at near maximum capacity, which caused more pronounced fluctuations in steam flow to the gasifier than for lower pressure operation (Figure 35). The fluctuations in

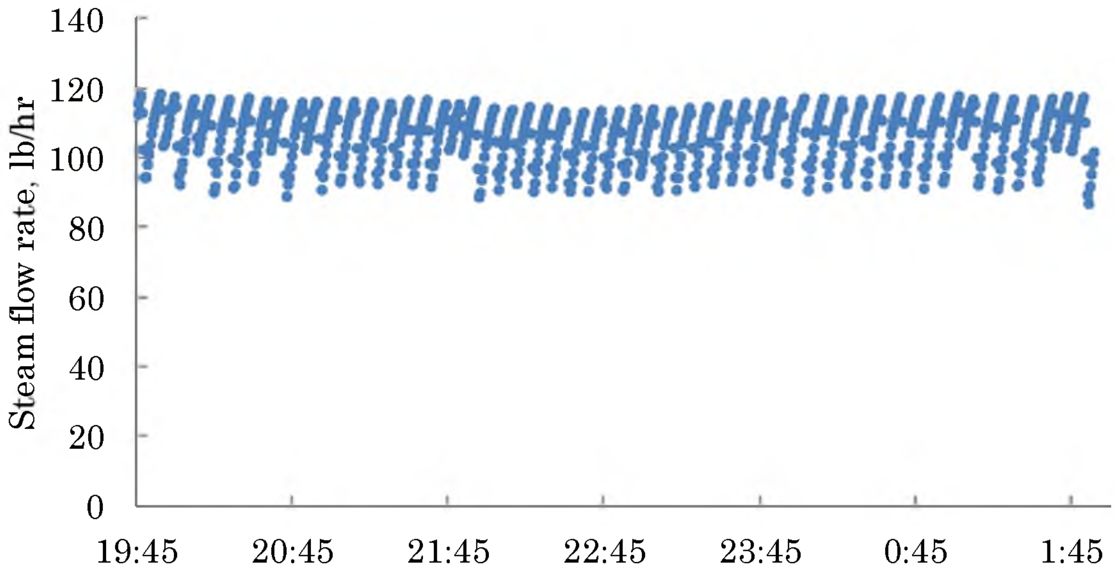

Figure 35. Test PM8 steam flow rate trend (lb/hr)

steam flow coupled with intermittent disturbances in the biomass feed supply led to various disturbances throughout the biomass gasification system. For test PM8 (high pressure, medium temperature), fluctuations in the steam SGV at the distributor plate ranged from 0.6 to 0.84 ft/s (Figure 36) and the freeboard pressure ranged from 55 to 68 psig (Figure 37). As a result of the system disturbances, the resulting synthesis gas composition trend contains large fluctuations (Figure 38) making accurate characterization of the high pressure operating conditions difficult. Despite the inconsistent operation experienced in the high-pressure tests, enough relatively stable operation was achieved in order to generate quasi-steady state averaged data for comparison with other operating conditions.

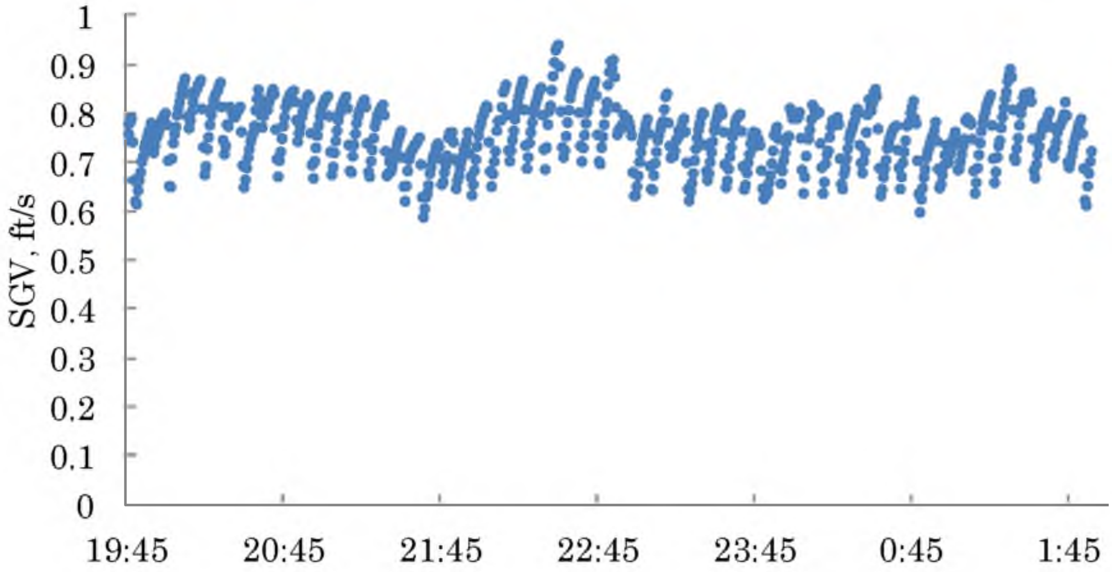

Figure 36. Test PM8 steam superficial gas velocity at the distributor plate (ft/s)

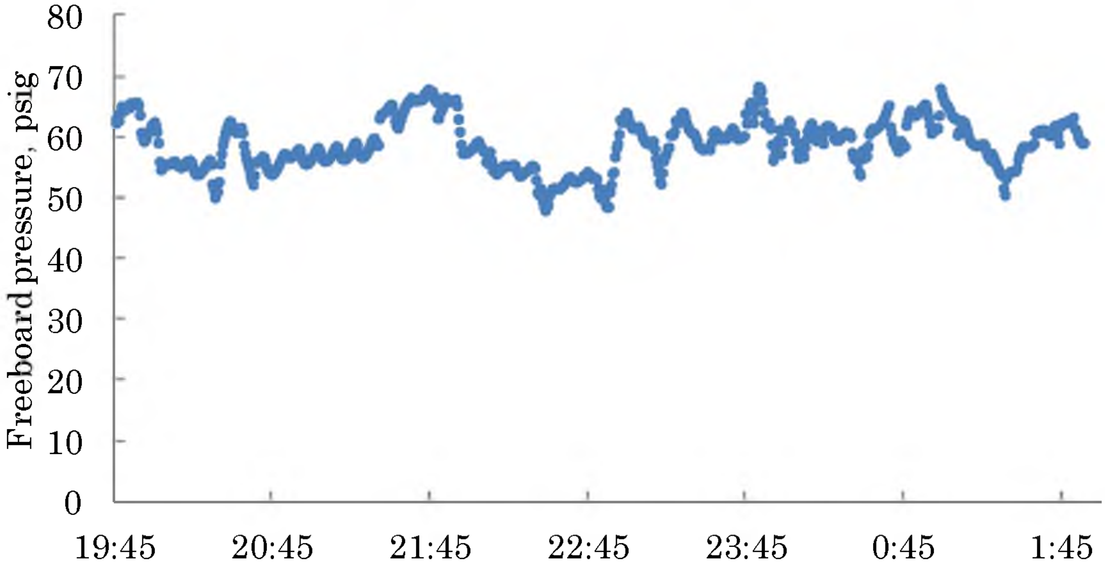

Figure 37. Test PM8 freeboard gauge pressure (psig)

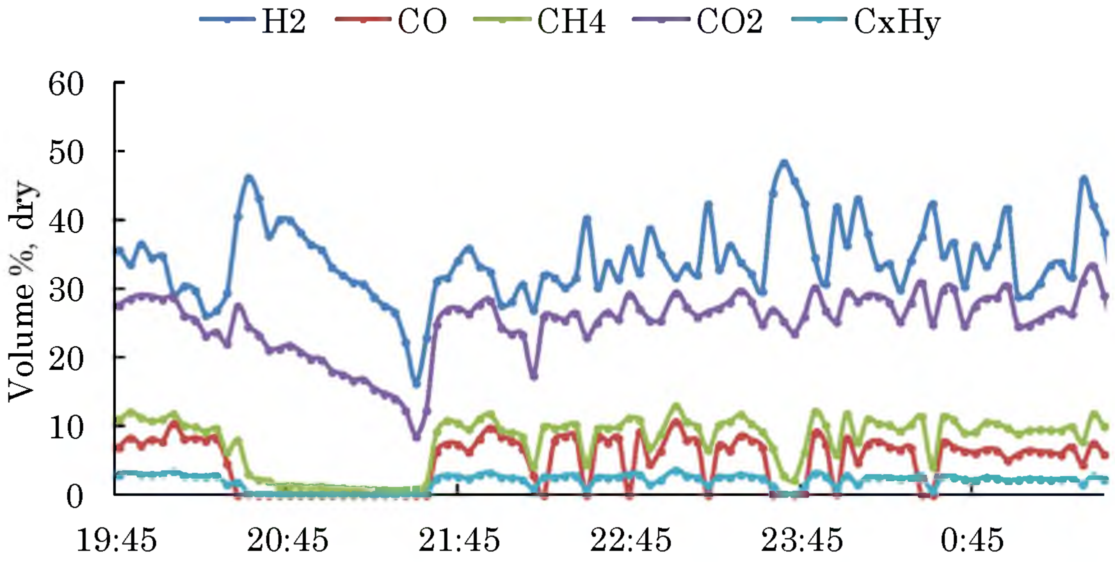

Figure 38. Test PM8 dry synthesis gas composition trend from micro-GC (vol%, dry)

6.1.4. Torrefied biomass operation

6.1.4.1. Char production

Due to the increased carbon content in the feedstock, torrefied material expectedly produces higher amounts of char than raw biomass material. Operationally, the production of char, the solid carbon product that remains after the initial drying and devolatilization of the fuel material, results in either an increase in the bed height as the char accumulates and slowly reacts to form synthesis gas, or entrains with the bulk gas flow out of the gasifier and accumulates in the downstream particulate filter. As was previously mentioned, the former tends to occur at lower temperatures in which the bulk gas flow and velocity is not adequate to entrain fine particulate, which tends to occur at high temperature resulting in the latter. Accurate estimates of filter retentate for the torrefied wood campaign were not possible due to a minor breach in a filter element gasket seat. In addition, none of the tests were run for long enough to allow equilibrium in the bed and bed samples were not obtained for each test. Therefore, it is difficult to estimate the amount of char production during the torrefied wood tests in comparison to the raw wood gasification tests. However, from carbon mass balance calculations, the char production rate for the torrefied biomass tests are nearly twice those of the raw wood tests. While increased char and particulate production can be problematic for downstream processes and equipment, char can be recycled to the gasifier for further conversion to synthesis gas or heat, or collected and used for other purposes such as an agricultural soil amendment (*89*).

6.1.4.2. Bed heaters

In addition to increased char production, it is observed that gasifier operation with torrefied wood required less energy input than operation with raw wood. For the same dry average biomass feedrate (approximately 44 lb/hr) and bed temperature (1450°F), conversion of torrefied biomass required about 13% less energy input from the bed heaters than raw biomass. This can partially be accounted for by the lower moisture content in the torrefied biomass (4-5%, by mass) compared to the raw biomass (14-15%, by mass). In addition, the medium and dark torrefied biomass feedstocks contain approximately 9 and 29% (by mass), respectively, less volatile matter than the raw biomass feedstock, which reduces the amount of mass devolatilized from the fuel particle upon entering the gasifier and thus the amount of energy required to devolatilize the feedstock.

6.2. Synthesis gas composition

As an initial indication of the quality of synthesis gas produced, the gas composition is measured using the micro-GC. Gas composition measurements are made approximately every 4 minutes and can be used as an online diagnostic tool for the gasification process. Different end-use applications of synthesis gas require different gas compositions. For example, a Fischer-Tropsch (FT) fuels synthesis process produces a mixture of alkanes comparable to diesel fuel through the reaction: $(2n + 1)H_2 + nCO \rightarrow C_nH_{2n+2} + nH_2O$. Therefore, a hydrogen-to-carbon monoxide ratio of approximately 2:1 is desirable for FT fuels synthesis (*90*). This can typically be achieved by adjusting the steam-to-biomass input ratio, the temperature of the gasifier, and the use of a catalyst to promote the water-gas shift reaction (R9) (*91*). Direct heating applications, such as steam generation in a gas fired boiler, would give preference to higher methane content, which provides a higher heating value fuel. Increased methane production can be achieved by operating the gasifier at lower temperature and higher pressure, which favors the methane-forming reactions. Synthesis gas composition is dependent on the type of gasifier, feedstock composition, reactive gas type, and gasifier operating conditions. Therefore, implementation of primary methods for tar reduction, including gasifier operating conditions and feedstock pretreatment, will no doubt affect the synthesis gas composition.

The following sections will describe the effects of gasifier temperature and pressure, and torrefaction on the synthesis gas composition. It is not within the scope of this research to identify the specific reaction mechanisms or kinetics that can account for the gas composition observations. However, discussion regarding general trends and the reaction phenomena that may be responsible for those will be included.

6.2.1. Effect of temperature and pressure

The effects of temperature and pressure have significant impacts on the equilibrium composition of many of the chemical reactions that are active during biomass gasification. The gas concentration trends with temperature and pressure for the major synthesis gas species are displayed in Figure 39 through Figure 43. In addition to the actual data, equilibrium model

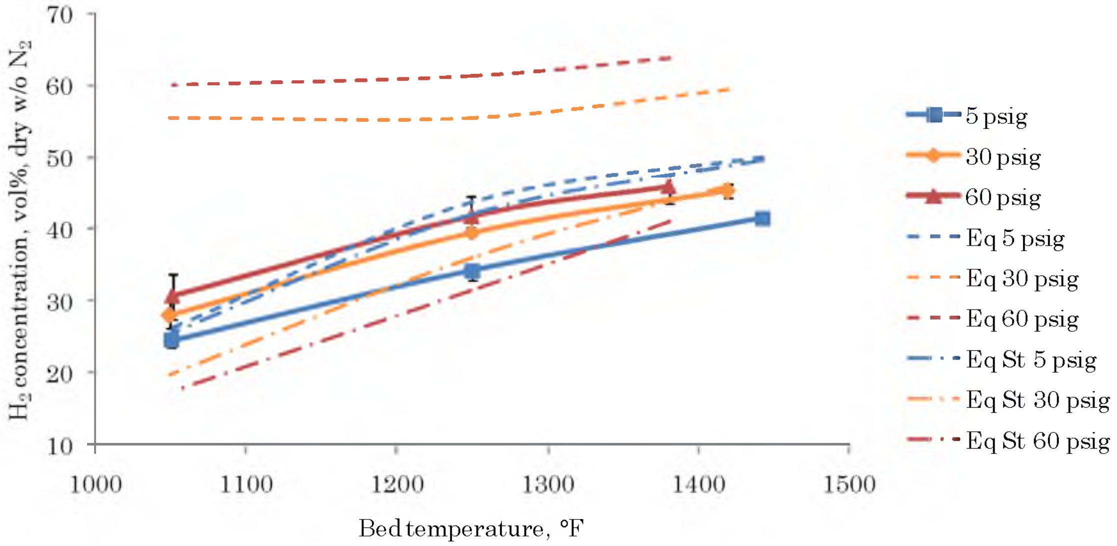

Figure 39. Actual hydrogen concentration (solid), equilibrium concentration (dash-dash), and equilibrium stoichiometric concentration (dash-dot) trends with bed temperature and freeboard pressure (vol%, dry, w/o N_2)

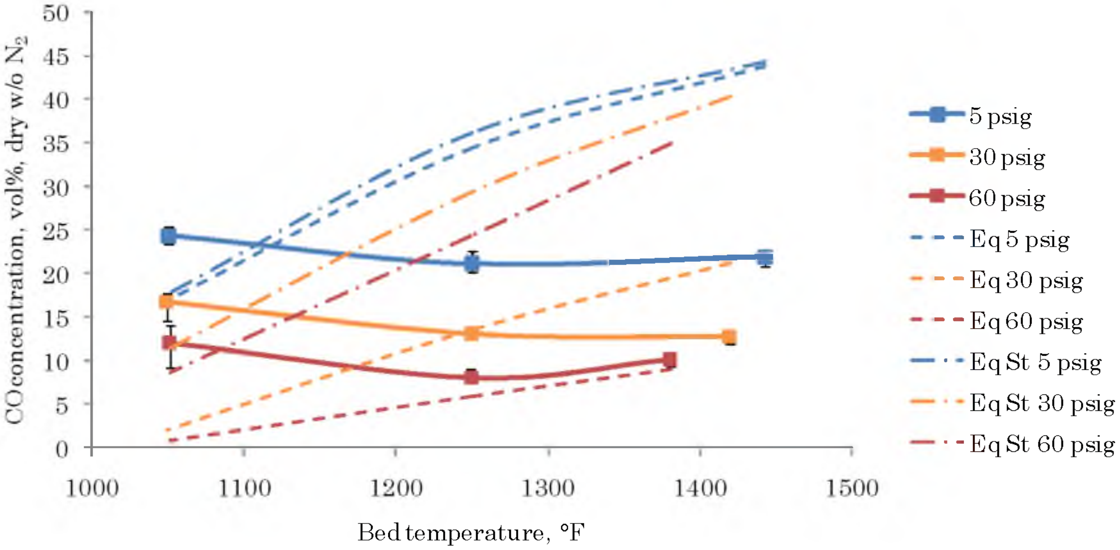

Figure 40. Actual carbon monoxide concentration (solid), equilibrium concentration (dash-dash), and equilibrium stoichiometric concentration (dash-dot) trends with bed temperature and freeboard pressure (vol%, dry, w/o N_2)

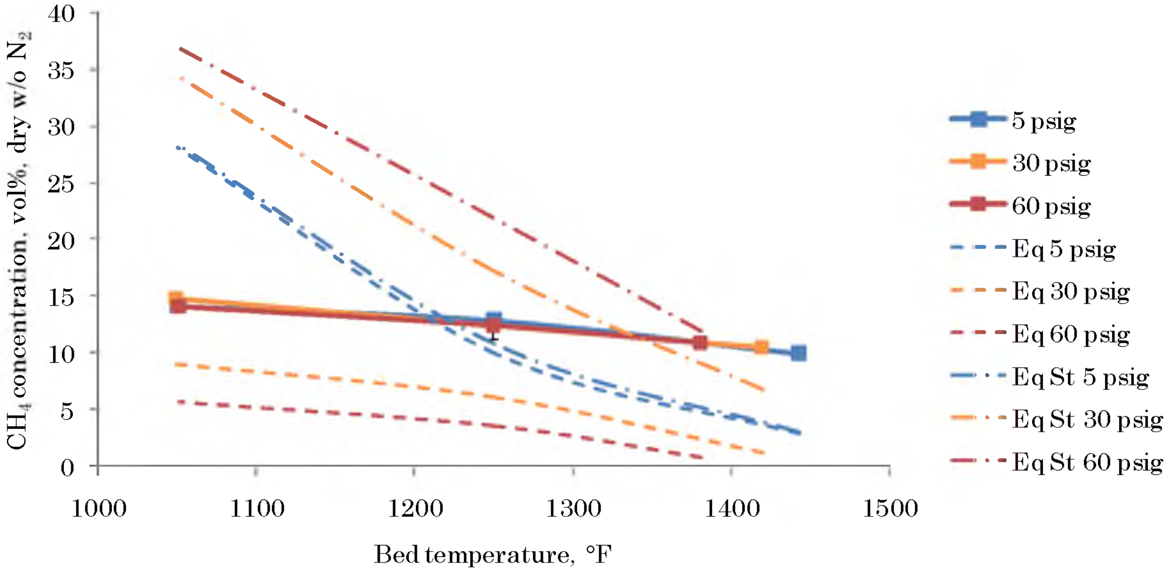

Figure 41. Actual methane concentration (solid), equilibrium concentration (dash-dash), and equilibrium stoichiometric concentration (dash-dot) trends trend with bed temperature and freeboard pressure (vol%, dry, w/o N_2)

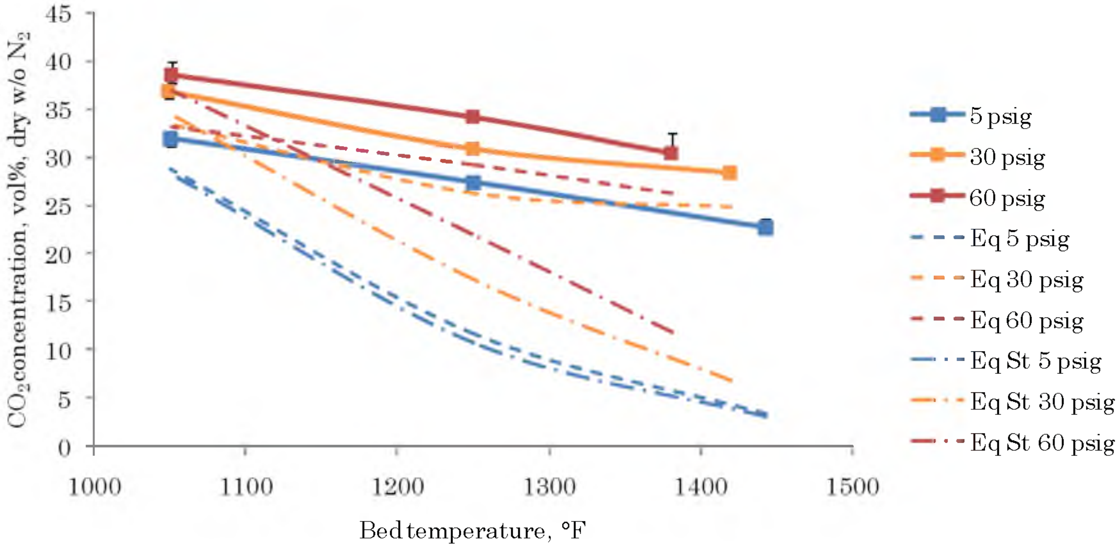

Figure 42. Actual carbon dioxide concentration (solid), equilibrium concentration (dash-dash), and equilibrium stoichiometric concentration (dash-dot) trends trend with bed temperature and freeboard pressure (vol%, dry, w/o N_2)

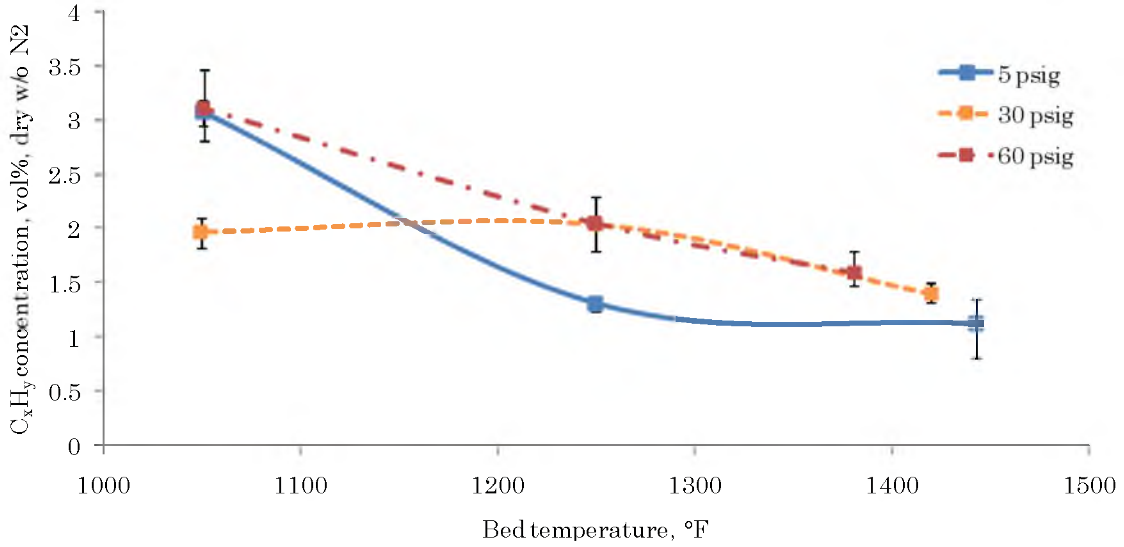

Figure 43. Hydrocarbons concentration trend with bed temperature and freeboard pressure (vol%, dry, w/o N_2)

predictions are based on minimization of the Gibb's free energy at stoichiometric conditions for steam gasification of biomass and at actual (non-stoichiometric) conditions. These trends are provided to assist in understanding the deviation in the actual gas composition results compared to theoretical predicted composition, assuming that chemical equilibrium is achieved.

The trends of hydrogen (H_2) concentration with bed temperature and freeboard pressure including error bars based on the maximum and minimum observed concentration during the quasi-steady test period are displayed in Figure 39. In addition, equilibrium modeling predictions are displayed for the actual reactant molar concentrations and stoichiometric molar concentrations based on steam gasification.

First, we will consider the equilibrium concentrations, which are indicated with a dash-dash line on the figures. Due to the excess steam in the system, especially at high pressures, the equilibrium model, with identical molar concentrations as the actual experiments, predicts large amounts of hydrogen and carbon dioxide production at the expense of carbon monoxide and methane at low temperatures. As temperature increases, hydrogen and carbon monoxide concentrations increase at the expense of methane and carbon dioxide due to enhanced methane reforming (R7) and decreased water-gas shift (R9) at high temperature. At the low-pressure condition, for which the reactive steam input was near the quantity required for stoichiometric water-gas reaction conditions, the product distribution is much more balanced, favoring methane and carbon dioxide formation at low temperature, and shifting to hydrogen and carbon monoxide formation at high temperature. The high-pressure stoichiometric predictions follow these same trends, but with high methane concentration at low temperature due to decreased methane reforming (R7), which is enhanced at higher temperature producing higher hydrogen and carbon monoxide concentrations and lower carbon dioxide concentrations due to reduced water-gas shift activity. Based on the trends observed from the equilibrium models, it can be concluded that the excess steam available at the actual experimental conditions vastly changes the synthesis gas equilibrium composition trends compared to stoichiometric water-gas reaction equilibrium trends.

The actual gas composition trends are quite different than the predictions of the equilibrium models. At low temperature and pressure, yield is shifted toward carbon monoxide and carbon dioxide production at the expense of methane. In addition, higher hydrocarbons, which are not produced in significant quantities in the equilibrium models, account for 2-3% (by volume) of the products (Figure 43). As temperature increases, all of the major synthesis gas components follow fairly consistent trends, with hydrogen increasing nearly linearly but consistently lower than equilibrium, carbon monoxide slightly decreasing, methane slightly decreasing linearly, carbon dioxide decreasing and consistently in higher concentration than the equilibrium values, and higher hydrocarbons decreasing.

There are several distinguishing characteristics of these trends with increasing temperature that should be discussed. First, hydrogen and carbon dioxide follow the equilibrium trends, but hydrogen equilibrium is consistently higher than the actual concentration and the carbon dioxide equilibrium values are consistently lower than actual. Based on this observation, it can be concluded that the water-gas shift reaction does not consistently account for the deviation from equilibrium. Second, the actual carbon monoxide concentration trend is opposite the equilibrium concentration trend with temperature. Third, the methane trend is consistent with equilibrium but the actual concentration is generally higher than equilibrium. Based on these two observations coupled with the high hydrogen concentration, it can be concluded that the methane and hydrocarbon-reforming reactions are inhibited in the gasifier. Therefore, methane and higher hydrocarbons produced during fuel devolatilization are not efficiently converted to synthesis gas.

In addition, it is possible that inadequate char conversion may account for the low concentrations for the low hydrogen and carbon monoxide concentrations. A significant amount of char was collected from the filter during most tests, especially those conducted at high temperature. The equilibrium models assume that the carbon in the char is available to fully react. However, char exiting the gasifier is not likely to further react significantly because temperatures downstream of the gasifier are much lower than the bed temperature (<1000°F), which greatly inhibits char conversion to carbon monoxide. In addition, oxygen in the steam that would normally be consumed through char gasification to form carbon monoxide, likely reacted with more of the synthesis gas species, producing carbon dioxide as a result of the lower availability of char in the bed at high temperature.

The effect of pressure is coupled with the effect of super-stoichiometric quantities of steam input for the pressurized tests in order to maintain a steam velocity through the bed adequate to maintain bubbling fluidization conditions. As a result, it is difficult to distinguish pressure-related effects that contribute to the deviation between actual and equilibrium gas composition, which assumes that all of the available steam is consumed in reactions, which form the major synthesis gas constituents.

As previously mentioned, the equilibrium model predicts large amounts of hydrogen production as a result of the excess hydrogen input via steam. In the actual experiments, a significant portion of the steam input remained unreacted in the gas exiting the gasifier. Therefore, the actual hydrogen concentrations were significantly lower (14-29%) than equilibrium predictions at high temperature. Rather, the stoichiometric equilibrium model values are closer to the actual hydrogen concentrations. For low-pressure operation, the equilibrium concentration is 1-8% higher than the actual hydrogen concentration. For the high-pressure conditions, the stoichiometric equilibrium concentrations were 5-13% lower than the actual hydrogen concentration. These two observations indicate that a portion of the steam input at the near-stoichiometric, low-pressure conditions was not consumed in gasification reactions, which is consistent with mass balance calculations. In addition, this indicates that the excess steam input at higher pressures allowed for increased hydrogen production to concentrations higher than those in which stoichiometric steam gasification would result. The latter point indicates that either the excess steam reacted to form the additional hydrogen, or a hydrogen-forming reaction was favored at high pressure. The latter is true for the methane-reforming reaction, which would also account for the low methane concentration at high pressure when compared to the stoichiometric yield.

A peculiar phenomenon that is observed in the actual concentration trends is that of carbon monoxide with both pressure and temperature. At low temperature, the pressure trend follows both the equilibrium trend at actual conditions and stoichiometric conditions, but is closer to the stoichiometric values, which underpredict by 3-7%. As the gasifier temperature increases, the low pressure (near-stoichiometric) concentration trend quickly drops below the equilibrium yield, finishing 22% lower than equilibrium. The medium-pressure conditions follow a similar trend, but intersect the equilibrium trend near the medium-temperature condition, finishing 8% lower than the actual equilibrium model value and 28% lower than the stoichiometric equilibrium value. For the high-pressure conditions, the actual trend begins near the stoichiometric equilibrium model value and finishes very close to the actual equilibrium model value.

The likely explanation for all of these observations is the loss of carbon from the reactor in the form of char, which is the major source of carbon monoxide production in biomass gasification. All of the carbon monoxide yields are far lower than the stoichiometric equilibrium values, especially at high temperature when more char loss was observed. The equilibrium yields at the actual conditions for the pressurized cases show much lower production of carbon monoxide due to the higher availability of steam which, with carbon monoxide, converts to hydrogen and carbon dioxide through the water-gas shift reaction.

A second peculiarity arises from the methane concentration trends, which exhibit almost no pressure dependence for any of the cases (Figure 41). This is peculiar because the methane-forming reactions are some of the most pressure- and temperature-dependent reactions that occur in gasification (*6*), which is evident from the equilibrium model values. In general, methane formation is favored at high-pressure and low-temperature conditions where the methane-reforming reaction is less active and the heterogeneous methanation reaction (R6) is more active due to the volume decrease in the forward direction. At low temperature and pressure, the actual methane concentration is significantly lower (14%) than the equilibrium concentration. At higher pressure, the stoichiometric equilibrium concentration increases while the actual concentration remains unchanged, in part due to the large presence of heavier hydrocarbons at low temperature, and in part due to increased methane reforming (R7) and oxidation (R8), which also accounts for the high hydrogen, carbon monoxide, and carbon dioxide concentrations. As temperature increases, the methane concentration slightly trends lower, but exceeds the equilibrium concentration. This is likely a result, again, of the apparent loss of carbon reactant due to unreacted char entrainment, which caused artificially low carbon monoxide concentration and high methane and carbon dioxide concentrations. Had more of the biomass char remained in the bed and reacted to form carbon monoxide, the methane and carbon dioxide concentrations would proportionally shift lower.

6.2.2. Effect of feedstock pretreatment

For this research, feedstock pretreatment was also considered as a potential primary method for tar reduction. In addition to having an appreciable effect on tar yield and general gasifier operation, torrefied wood gasification had a pronounced effect on the synthesis gas composition. For the torrefied wood tests, several factors were investigated to provide a general screening for the viability of torrefied woody biomass as a potential feedstock for biomass gasification. All cases were run at low pressure to reduce complications in gasifier operation that can arise during elevated pressure operation. It should be noted that all of the tests presented with respect to torrefied biomass gasification were carried out at near stoichiometric conditions for steam gasification of each feedstock. Therefore, effects of excess steam that may have been significant in pressurized tests are not in these tests.

To reiterate, first, torrefied wood prepared at two different conditions, referred to as “medium torrefied” (test T1) and “dark torrefied” (test T2) woody biomass, were compared to raw woody biomass (PM2) at the same gasifier operating conditions (high bed temperature, low pressure). Second, the effect of torrefied biomass feedrate was studied by gasifying both the medium (T1 and T2) and dark torrefied (T4 and T5) feedstocks at two different feedrates. Third, the effect of the gasifier temperature was studied by gasifying both the medium (T2 and T3) and dark torrefied feedstocks (T4 and T5) at two different bed temperatures (1450°F, 1250°F). The major synthesis gas species concentrations for each of these test cases are displayed in Figure 44-Figure 48. As with the primary methods gas composition results presented in the previous section, the objective of presenting this experimental data is not to formulate new or improve existing models for chemical species formation in biomass gasification, but rather to identify the effects of implementing methods for tar reduction on gasifier operation and the synthesis gas generated during fluidized bed biomass gasification. Actual concentration data are presented with error bars based on the maximum and

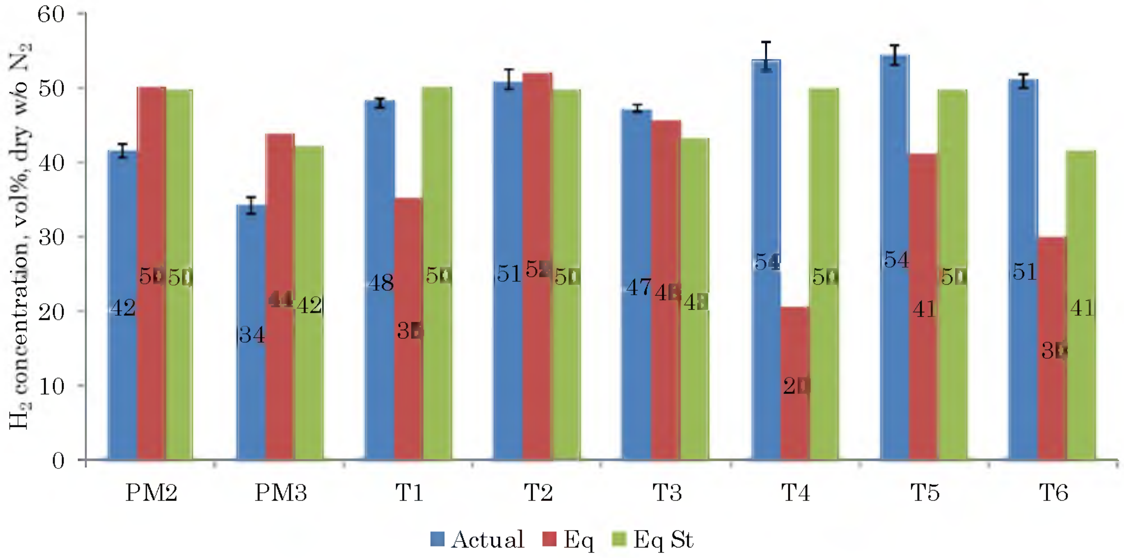

Figure 44. Actual hydrogen concentration (blue), equilibrium concentration (red), and equilibrium stoichiometric concentration (green) (vol%, dry, w/o N_2).

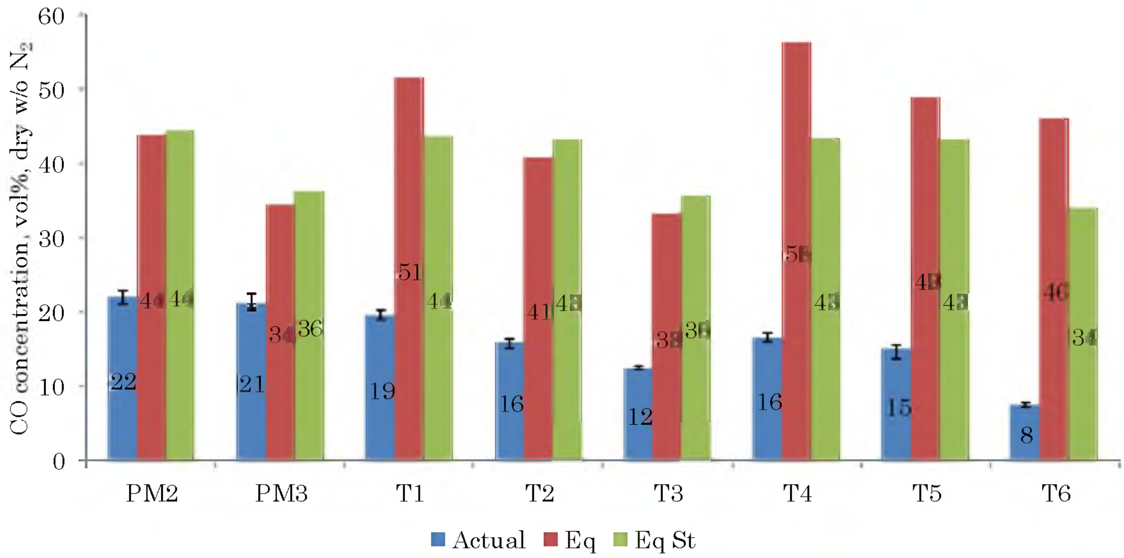

Figure 45. Actual carbon monoxide concentration (blue), equilibrium concentration (red), and equilibrium stoichiometric concentration (green) (vol%, dry, w/o N_2).

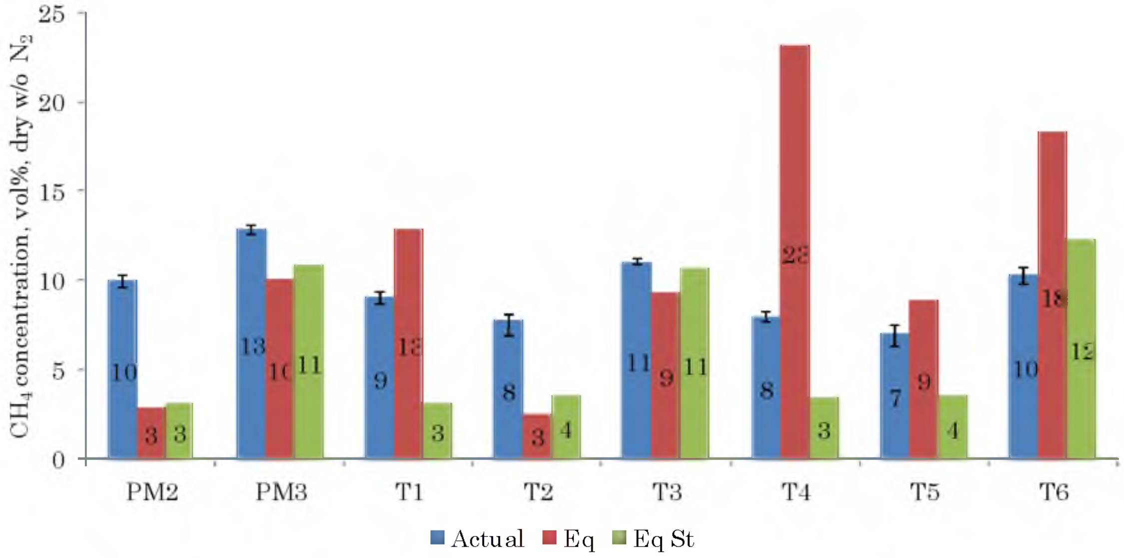

Figure 46. Actual methane concentration (blue), equilibrium concentration (red), and equilibrium stoichiometric concentration (green) (vol%, dry, w/o N_2).

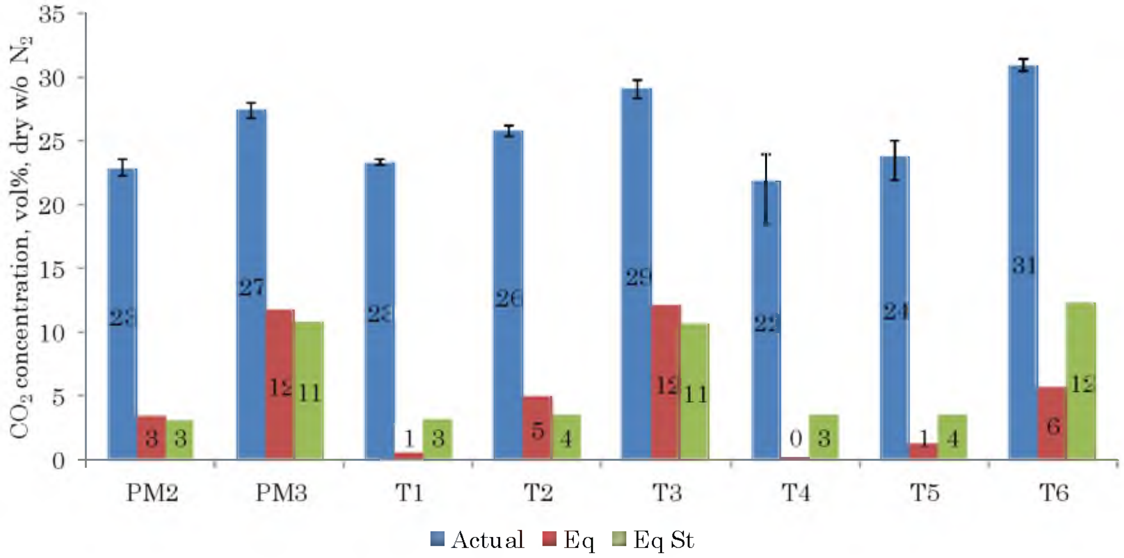

Figure 47. Actual carbon dioxide concentration (blue), equilibrium concentration (red), and equilibrium stoichiometric concentration (green) (vol%, dry, w/o N_2).

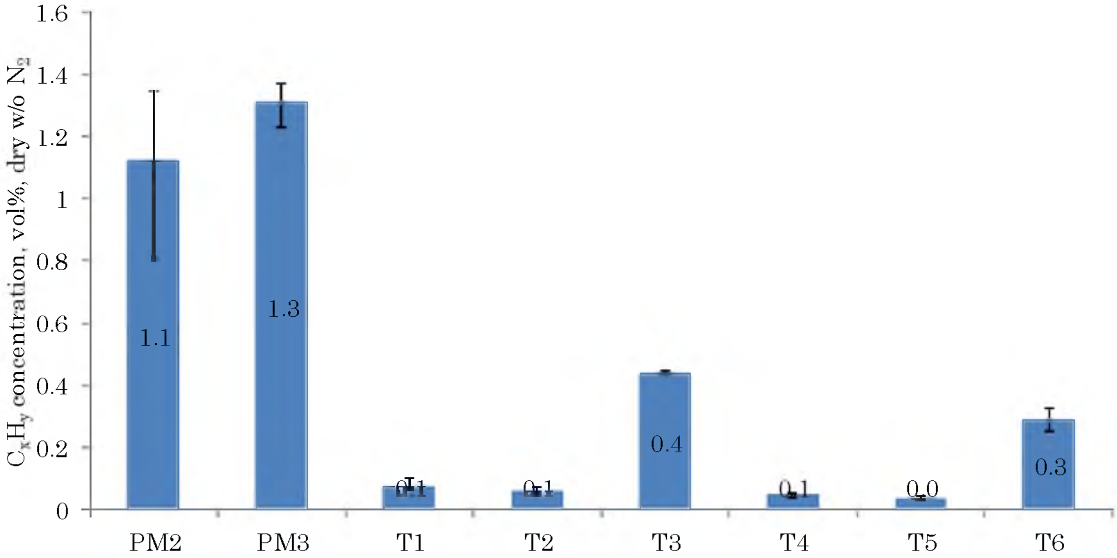

Figure 48. Actual hydrocarbons concentration (vol%, dry, w/o N_2).

minimum measured values from the micro-GC. Equilibrium concentration (red) and equilibrium concentration at stoichiometric steam gasification conditions (green) are displayed in addition to the actual measured gas concentration. It should be noted that there is an inconsistency in the concentrations presented for the sum of all higher hydrocarbon in Figure 48. Concentration presented from the primary methods (PM) experimental campaign (PM2 and PM3) was measured using a 4-column micro-GC, which was able to detect several hydrocarbon species that the 2-column micro-GC, utilized during the torrefied wood gasification experimental campaign (T1-T6), is not able to detect. Therefore, the hydrocarbon concentrations from the primary methods campaign are much higher than those from the torrefied wood campaign.

Several observations can be made with regard to synthesis gas produced from gasification of torrefied woody biomass in comparison to untreated woody biomass. First, gasification of torrefied biomass produces a higher hydrogen content product, generating 6-12% (by volume) more hydrogen than untreated biomass at similar gasifier operating conditions (Figure 44, PM2 vs. T1 and T4). Second, gasification of torrefied biomass produced lesser (3-6%, by volume) concentrations of carbon monoxide in comparison to raw biomass gasification (Figure 45, PM2 vs. T1 and T4). Third, torrefied wood and raw wood tests show similar concentrations of methane (Figure 46, PM2 vs. T1 and T4). Fourth, torrefied wood and raw wood show similar concentrations of carbon dioxide (Figure 47, PM2 vs. T1 and T4).

From these observations, it can likely be concluded that the water-gas reaction (R5) was more active for torrefied biomass operation due to the higher availability of carbon in the feedstock. In addition, the lower volatile matter (VM) content in the torrefied biomass (8.2% for medium torrefied and 24.7% for dark torrefied) permitted a lower steam demand for hydrocarbon reforming and higher steam availability for water-gas shift conversion of carbon monoxide to hydrogen and carbon dioxide (R9). As was the case in the primary methods campaign results presented in the preceding section, the loss of carbon by char elutriation accounts for the consistently lower concentrations of carbon monoxide in comparison to equilibrium concentrations.

Comparison of synthesis gas compositions for biomass feedstocks produced at two levels of torrefaction intensity, medium and dark “roast,” can also be made from the torrefied biomass campaign results. Comparison of the two feedstock compositions indicates that the medium torrefied material contains slightly more moisture content (+1.4%, by mass), more volatile matter (+16.5%), and lower carbon content (-8.5%) than the dark torrefied material. In summary, gasification of the medium torrefied material produced less hydrogen (3-6%, by volume), more carbon monoxide (1-4%), more methane (1%), more carbon dioxide (1-2%), and more heavy hydrocarbons (0.1%) than the dark torrefied material. Interestingly, several of these trends are not consistent with the concentrations from equilibrium modeling, which predict higher hydrogen, lower carbon monoxide, and lower methane concentration for medium compared to dark torrefied biomass gasification. One obvious explanation that is consistent with the deviances from equilibrium values in the primary methods campaign results is reactive carbon loss due to char elutriation, of which there was likely more during the dark torrefied biomass tests due to its higher carbon content. This results in lesser amounts of carbon dioxide and carbon monoxide, which are the major products of the char reactions. The steam used in converting carbon to synthesis gas in the medium torrefied biomass tests was available in higher quantities for the water-gas shift conversion to hydrogen, especially at low temperature, during the dark torrefied biomass tests. Methane and higher hydrocarbons content are likely to be higher in concentration for the medium torrefied biomass tests due to its higher volatile matter content.

In addition to comparison of untreated and treated biomass feedstocks, a two level comparative study on the effect of torrefied biomass feedrate was completed during the torrefied biomass gasification campaign. A high feedrate condition of approximately 45 lb/hr (dry) (T1 and T4) and a low feedrate condition of approximately 30 lb/hr (dry) (T2 and T5) were used with both medium (T1 and T2) and dark torrefied (T4 and T5) feedstocks at high bed temperature (approximately 1450°F). To summarize, the hydrogen concentration decreased (1-3%, by volume), the carbon monoxide concentration increased (1-3%), the methane concentration increased (1%), the carbon dioxide concentration decreased (2-3%), and the higher hydrocarbons concentration increased (0.1%) with increasing feedrate.

From these observations, it is clear that the water-gas shift reaction is more influential at low feedrate because lower quantities of steam are used in the water-gas and reforming reactions. In addition, with more total feedstock to convert at higher feedrate, the reforming reactions are less effective at converting hydrocarbons formed during devolatilization of the feedstock to simpler synthesis gas species.

Finally, the effect of gasifier temperature, which was studied during the primary methods experimental campaign, was also considered for the torrefied biomass experimental campaign. Both torrefied feedstocks were gasified at two bed temperature conditions, 1450°F (T2 and T4) and 1250°F (T3 and T5), both at low feedrate (30 lb/hr). In summary, hydrogen concentration increased (3-4%, by volume), carbon monoxide concentration increased (4-7%), methane concentration decreased (3%), carbon dioxide concentration decreased (3-7%), and heavy hydrocarbons decreased (0.3%) with increasing bed temperature. All of these trends are consistent with trends from the steam gasification equilibrium model. At high temperature, hydrogen and carbon monoxide production increases due to increased water-gas reaction activity. In addition, the large amount of carbon dioxide produced from char combustion reacts with char and steam available in the bed to form carbon monoxide and hydrogen. The methane- and hydrocarbon-reforming reactions are enhanced at high temperature and further increase hydrogen and carbon monoxide production.

6.3. Synthesis gas yield

While analysis of the synthesis gas composition is useful in identifying trends in product formation, dominant reactions responsible for production formation, and comparison to equilibrium gas composition, it is also important to consider the quantity of synthesis gas produced and the efficiency of different conditions at converting reactant mass to usable product mass. The following sections present and discuss synthesis gas yield results for each of the primary methods tests considered in this research.

6.3.1. Effect of temperature and pressure

The primary methods experimental campaign investigated the influence of the gasifier pressure and temperature on the various products from biomass gasification. In addition to the effects observed on synthesis gas composition, the temperature and pressure also show an effect on the yield of product gas. The dry, nitrogen-free synthesis gas yields for the primary methods campaign are displayed in Figure 49. As discussed previously, the total mass flow rate of gaseous products from the gasifier was calculated from a nitrogen mass balance on the system. The steam outflow from the gasifier was calculated from a hydrogen mass balance on the system. The synthesis gas yields presented in Figure 49 were calculated by summing the mass flow of all of the detectable product gas species from micro-GC measurement.

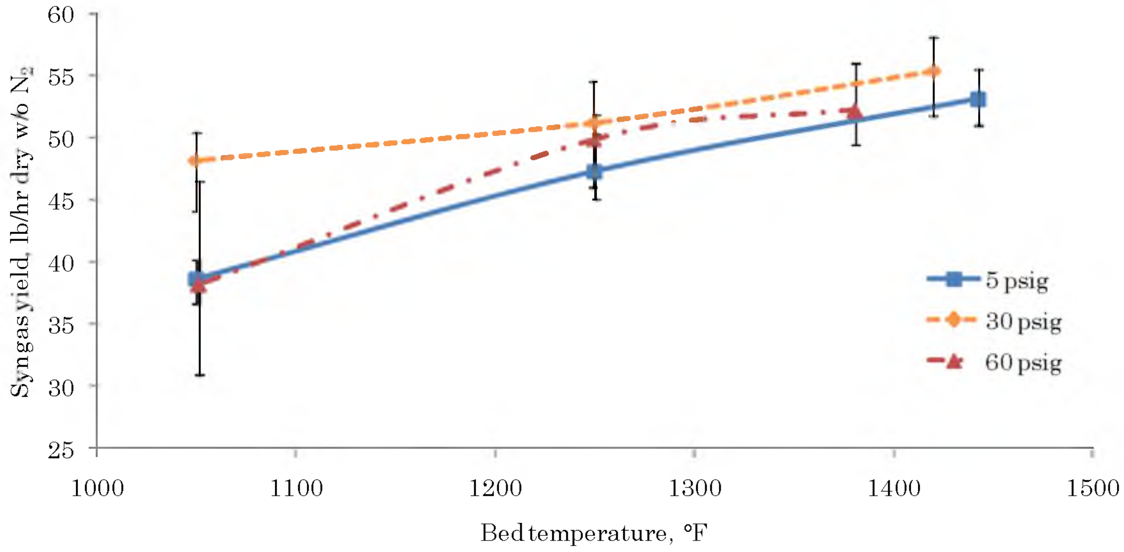

Figure 49. Dry, nitrogen-free synthesis gas yield trends with bed temperature and freeboard pressure (lb/hr, dry, w/o N_2).

As expected, the yield increases with increasing bed temperature due to the higher heating rate of the fuel, resulting in faster fuel devolatilization and higher synthesis gas-forming reaction rates at high temperature. High-temperature (1450°F) gasification results in a 13-38% increase in synthesis gas in comparison to low-temperature (1050°F) gasification. It is expected that the yields would be higher if not for the relatively high rates of char elutriation, especially at high gasifier temperature. The effect of pressurized gasification is less pronounced. However, synthesis gas production appears to be favored at high pressure conditions. Comparison of the low (5 psig)- and medium (30 psig)-freeboard-pressure cases show a 4-25% increase in synthesis gas production from low to medium pressure. Results are less conclusive for the high-pressure (60 psig) cases, which follow the overall temperature trend but show yields between those of the low- and medium-pressure cases. There are several potential explanations for this. One is the inconsistent gasifier operation during high pressure operation, which made achieving steady synthesis gas production challenging and likely caused an overall reduction in synthesis gas yield (Figure 38). This is consistent with the large amount of error Second, the steam velocity through the fluidized bed was generally lower for the high-pressure cases, averaging 0.75 ft/s compared to 1.08 ft/s for the low-pressure cases and 0.96 ft/s for the medium-pressure cases. Low fluidizing velocity has the potential to cause reduced fuel conversion due to poor fluidization, and thus lower synthesis gas yield.

Another method for representing product yield that is useful for comparing experiments run at different conditions is the dimensionless yield, in which the product yield is normalized by the feedstock input. The dimensionless yield representation also provides some insight on the overall reactant conversion efficiency of the process. For gasification, at a minimum, all of the feedstock mass should be converted to synthesis gas and normally some quantity of the reactant gas is typically converted. However, in reality, char and tar production can account for partial conversion of the feedstock.

The dimensionless yield trends for the primary methods campaign are displayed in Figure 50. On a dimensionless basis, the yields follow similar

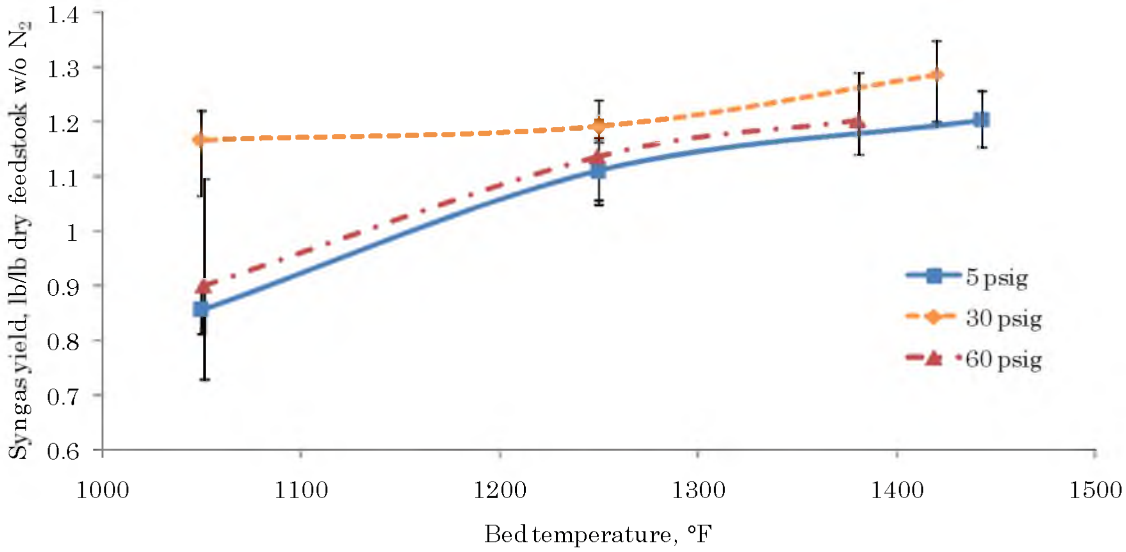

Figure 50. Dimensionless dry, nitrogen-free synthesis gas yield trends with bed temperature and freeboard pressure (lb/lb dry feedstock, w/o N_2)

trends compared to the dimensional basis. In general, the yield increases with increasing temperature, indicating better improved overall fuel conversion at higher temperature, which is consistent with trends in tar concentration. Interestingly, the medium-pressure case exhibits the best dimensionless product yield, producing 17-29% more synthesis gas mass than feedstock input mass. Again, the high-pressure conditions show slightly better feedstock conversion than the low-pressure conditions, but distinctly poorer conversion than the medium-pressure conditions. This, again, is likely attributable to the diminished operability of the gasification system at high pressure and resulting unsteady synthesis gas production.

6.3.2. Effect of feedstock pretreatment

Torrefied biomass gasification not only effects the synthesis gas composition but also the product yield. All of the variables screened during the torrefied biomass campaign exhibit unique yield characteristics. The synthesis gas yield results for the torrefied biomass gasification campaign are displayed in Figure 51.

First, comparing product outputs from gasification of raw (PM2) and torrefied biomass (T1 and T4) shows that raw biomass gasification produces slightly higher yields of synthesis gas at high temperature. This is likely due to the higher volatile and lower carbon content of raw, untreated biomass, which results in higher yields of hydrocarbons and reformed hydrocarbon

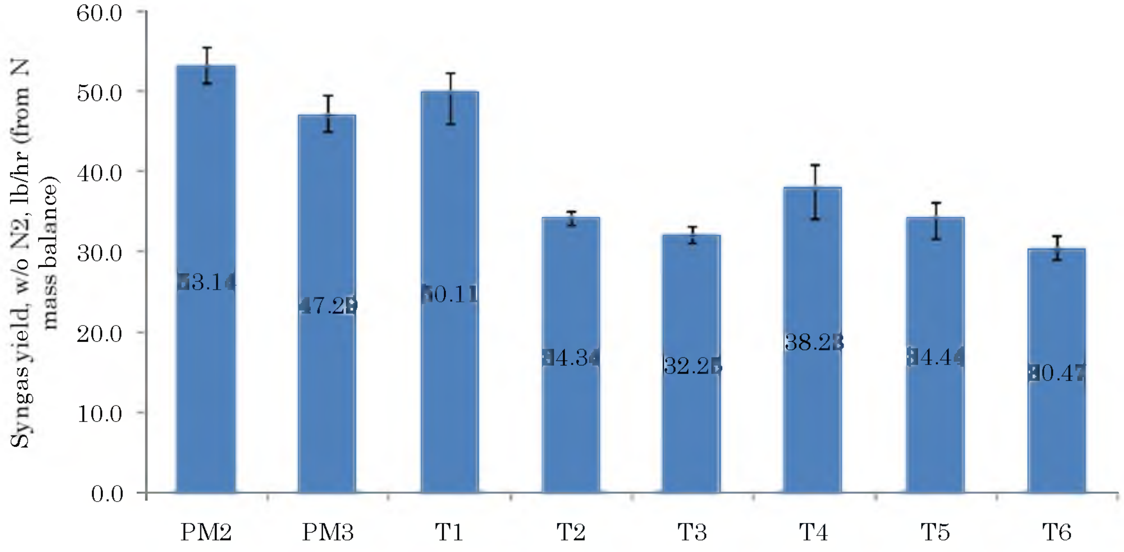

Figure 51. Dry, nitrogen-free synthesis gas yield trends for torrefied wood gasification (lb/hr, dry, w/o N_2).

products, and lower yields of solid residues (e.g., char and ash). Second, comparing gasification of medium (T1-T3) and dark torrefied biomass (T4-T6) shows that medium torrefied material generally produces higher quantities of synthesis gas for the same reason that untreated biomass conversion yields more synthesis gas than torrefied biomass conversion. Third, the effect of gasifier bed temperature indicates that a higher bed temperature (T2 and T5) tends to increase the product yield compared to a lower bed temperature (T3 and T6). However, this increase is less pronounced than for untreated biomass gasification (Figure 49). Finally, the effect of torrefied biomass feedrate shows that an increase in feedrate results in an increase in synthesis gas production (T1 vs. T2, T4 vs. T5) and that this increase is more pronounced for medium-torrefied material. Many of these trends are linked to the low volatile and high carbon content of the dark-torrefied material, which results in reduced conversion, especially from slower reactions such as char gasification.

Similar to the primary methods results in the previous section, the synthesis gas yield results for torrefied biomass gasification are displayed in dimensionless form in Figure 52. Comparison of the yield per unit feedstock input for untreated biomass and torrefied biomass are consistent with the previous observation with the untreated feedstock producing 7-25% more synthesis gas than the torrefied cases. The temperature and torrefaction

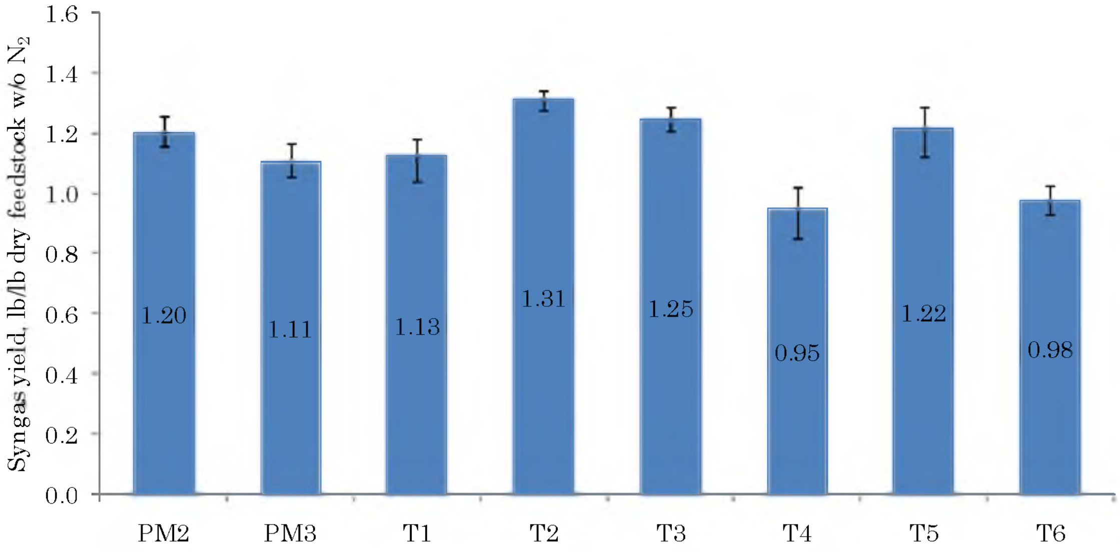

Figure 52. Dimensionless dry, nitrogen-free synthesis gas yield trends for torrefied biomass gasification (lb/lb dry feedstock, w/o N_2)

degree trends are also consistent with previous observations. The most interesting result from the dimensionless yield data is the trend with torrefied biomass feedrate (T1 vs. T2 and T4 vs. T5). These data show a significant increase in reactant utilization for synthesis gas production at low biomass feedrate. Yield improves by 18% at low feedrate for the medium torrefied material, and 27% for the dark torrefied material. Less feedstock input for the same amount of reactant steam results in improved feedstock conversion. This is consistent with observations in the synthesis gas composition, which shows that hydrogen and carbon dioxide content increases at lower feedrate, indicating that enough steam is present to first gasify carbon forming carbon monoxide, followed by water-gas shift to form additional hydrogen and carbon dioxide.

6.4. Carbon conversion efficiency

In addition to representing biomass yield in a nondimensional form, which allows for comparison between experiments run under different conditions and at different scales, it is common to express fuel conversion in terms of fuel carbon to synthesis gas carbon. The fate of carbon in biomass gasification can take on several forms, from desirable species in synthesis gas such as carbon monoxide, to higher gaseous hydrocarbons such as ethane or pentane, to condensable hydrocarbon tar species, to solid carbon residues such as char or soot. The carbon conversion efficiency accounts for the conversion of reactant carbon to gaseous product carbon. For this research, reactant carbon content was determined by feedstock ultimate analysis and product gas carbon content was determined from micro-GC gas composition measurement and nitrogen mass balance. A carbon conversion efficiency value of 1.0 (100%) indicates that the entirety of the feedstock carbon is converted to gaseous product carbon. A carbon conversion efficiency of 0 (0%) indicates that none of the fuel carbon is converted to gaseous carbon product.

6.4.1. Effect of temperature and pressure

The carbon conversion efficiency trends for the primary methods tests are displayed in Figure 53. These trends follow fairly closely with the gas yield trends in the previous section with a general increase in carbon efficiency with increasing temperature. In addition, the medium-pressure condition exhibits the most efficient fuel conversion of the three pressure conditions. Conversions at the high-pressure condition are markedly lower than the low- and medium-pressure conditions. Again, this is likely due to discontinuities in the gasifier operation and high rates of char elutriation for these tests. However, reduced conversion of feedstock to hydrogen and carbon monoxide at high temperature is consistent with equilibrium predictions presented in

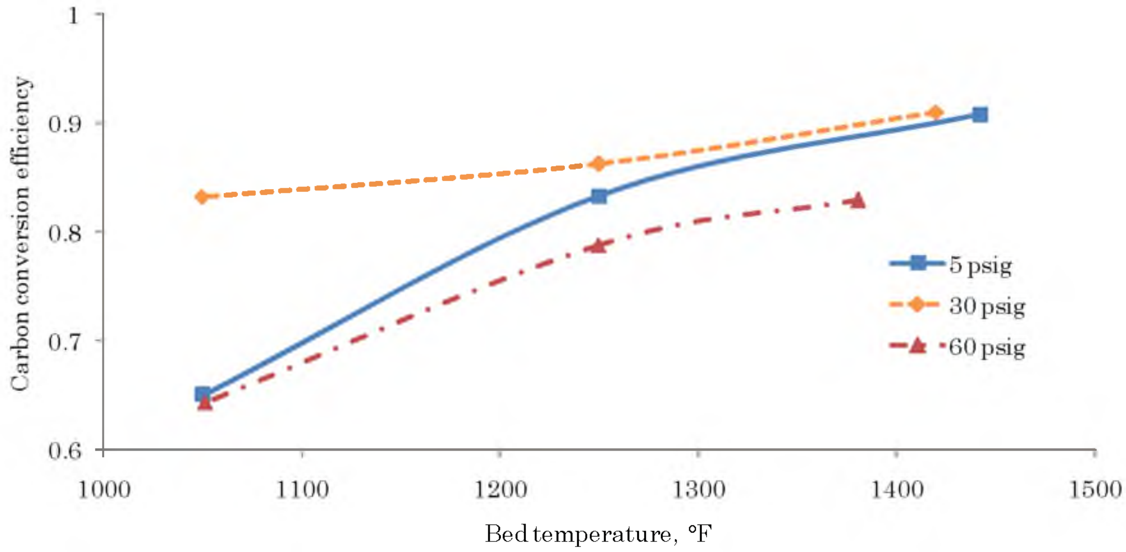

Figure 53. Carbon conversion efficiency trends with bed temperature and freeboard pressure

literature for pressurized gasification (*5*). The low-temperature condition for the high- and low-pressure cases exhibit considerably lower conversion, which can be explained by accumulation of slow reacting char in the bed, indicated by a consistently increasing bed pressure drop and accumulation of solids in the downstream filter, which are not likely to react further as indicated by the consistently increasing filter pressure drop during those tests. Conversely, particulate elutriation appears to be much lower for the low-temperature, medium-pressure condition, which resulted in some bed height growth but better conversion, which may be attributed to adequate fluidizing velocity, relatively smooth operation, and excess steam availability.

6.4.2. Effect of feedstock pretreatment

The carbon conversion efficiency trends for the torrefied biomass gasification tests are displayed in Figure 54. Many of the trends in carbon conversion for the torrefied gasification are dictated by the relatively high fixed carbon content in the torrefied biomass feedstock. It is assumed that higher fixed carbon content results in higher char production, which, under many of the operating conditions discussed, resulted in some amount of carbon loss from the system due to particulate elutriation. Comparison of the carbon conversion of the raw biomass and torrefied biomass (PM2 vs. T1 and T4) indicates substantially lower carbon conversion (23-42%) for the torrefied

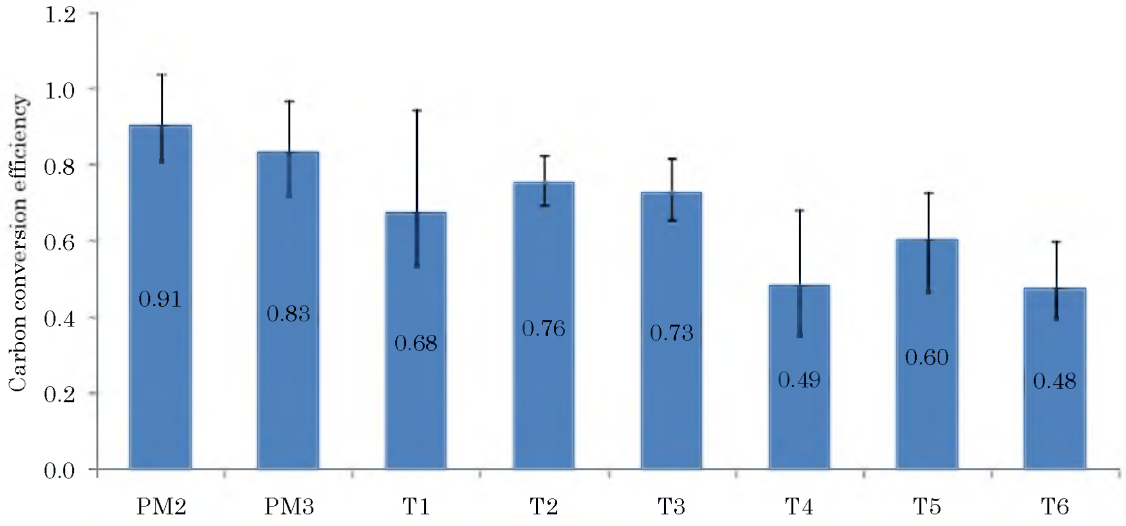

Figure 54. Carbon conversion efficiency for torrefied biomass gasification

biomass, which is likely due to the large difference in feedstock carbon and volatile content. In following with this trend, the medium-torrefied material (T1-T3) exhibited better conversion (68-76%) in the gasifier compared to the dark-torrefied material (T4-T6) (48-60%). Similar to the normalized synthesis gas mass flow rate, the carbon conversion efficiency improves at lower feedrate (T1 vs. T2, T4 vs. T5) by 8-11%, which indicates that the super-stoichiometric quantities of steam for steam gasification at the low-feedrate conditions (SR_{T1}=0.79, SR_{T2}=1.33, SR_{T4}=0.87, SR_{T5}=1.24) allow for improved mass conversion. Finally, the effect of gasifier temperature on carbon conversion is consistent with previous trends with a slight increase (3%) in medium-torrefied biomass carbon conversion with a temperature increase from 1250 to 1450°F, and a 12% increase in conversion efficiency for dark-torrefied material. The better improvement in conversion with temperature for the dark-torrefied material is likely due to the stronger dependence of char conversion on reactor temperature in comparison to volatile conversion.

6.5. Cold and hot gas efficiencies

In addition to assessing the efficiency of the gasification process at converting fuel mass to synthesis gas mass, it is useful to analyze the process in terms of energy conversion. As a first step, the cold (CGE) and hot gas efficiencies (HGE) provide useful indication of the feedstock energy conversion efficiency accounting for the lower heating value (LHV) of the synthesis gas in the case of the cold gas efficiency and the LHV plus the sensible heat of the synthesis gas and thermal energy inputs in the case of the hot gas efficiency.

6.5.1. Effect of temperature and pressure

The cold and hot gas efficiency trends for the primary methods campaign are displayed in Figure 55. Both efficiency trends increase with increasing temperature, which is consistent with the conversion efficiency trends presented in the preceding section, i.e. a higher degree of fuel conversion generally results in a higher energy content product gas. However, low-

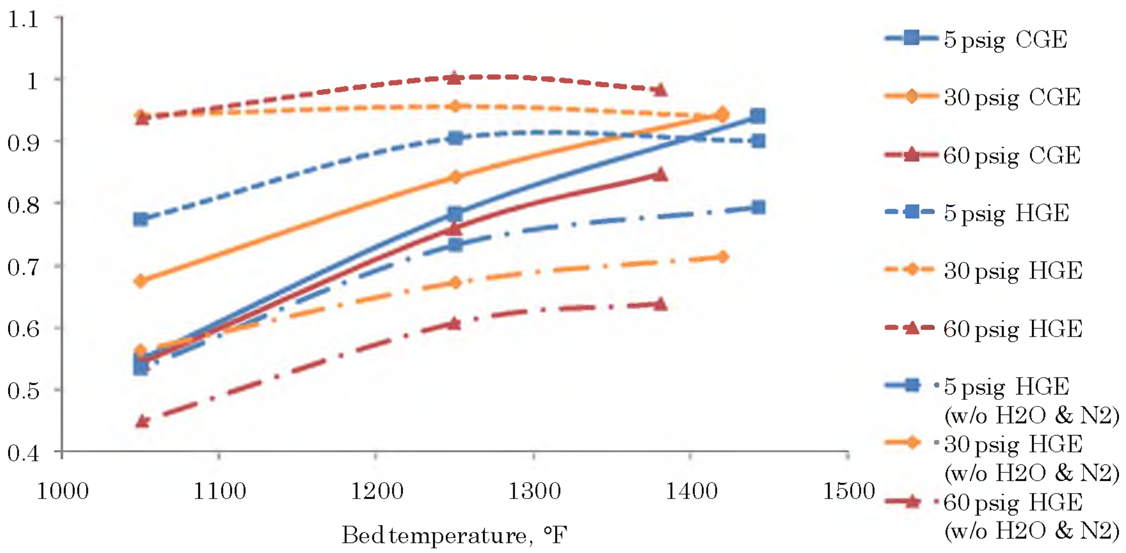

Figure 55. Cold (CGE) (solid line) and hot gas efficiency (HGE) (w/ steam and N_2- dash-dash; w/o steam and N_2- dash-dot) trends with bed temperature and freeboard pressure

temperature, high-pressure gasification generally produces lower yields of synthesis gas but higher concentrations of methane and other hydrocarbon species, which are more energy dense than hydrogen and carbon monoxide, producing a higher energy content product. For these cases, the methane content for low-temperature operation was relatively low compared to the predicted methane concentration from chemical equilibrium modeling. It is expected that higher methane content would increase the cold gas efficiency at low temperature, but likely not greater than the high temperature efficiencies due to better overall mass conversion at high temperature. Gasification equilibrium modeling from literature indicates that the heating value of product gas generally increases with increasing pressure and decreases slightly with increasing temperature (*5*). Again, the primary methods results are not consistent with equilibrium models due to excess steam at elevated pressure, carbon losses due to char elutriation, and operability difficulties at high pressure.

The hot gas efficiency (HGE) trends (dash-dash) indicate that there is a balance between the sensible energy in the product gas and the energy input to the reactor (steam and electrical). At low temperature, the HGE ranges from 78 (low pressure) to 94% (high pressure) compared to the CGE, which ranges from 54 (low and high pressure) to 68% (medium pressure). The large increase in HGE under pressurized conditions indicates that the sensible heat content of the product gas is high compared to the additional energy input required to produce and superheat the additional reagent steam. As the bed temperature increases to the medium temperature condition (1250°F), both the CGE and HGE increase due to the improved fuel conversion at relatively low energy input cost. Further increase in bed temperature results in an increase in CGE and a decrease in HGE. The increase in CGE is a result of improved fuel conversion at high temperature. The decrease in the HGE is due to the significant increase in electrical energy consumption to maintain high temperature in the bed. In addition, high temperature operation likely results in the highest amount of heat loss from the reactor vessel. The maximum at the medium-temperature condition at all reactor pressures indicates that a balance between fuel conversion and reactor energy input exists, with the optimum occurring somewhere between the low- and high-temperature conditions.

To emphasize the effect of excess steam in the product gas at elevated pressure, HGE trends (dash-dot) not including the sensible heat in steam and nitrogen products are also displayed in Figure 55. The HGE is significantly lower (up to 16%) for the elevated pressure cases than for the low pressure cases. Comparison of these trends with the HGE that include steam- and nitrogen-sensible heat indicates that the output steam-sensible energy contribution is large. Since there is not chemical energy value in the steam exiting the gasifier, energy recovery by cooling the product gas would result in increased HGE.

6.5.2. Effect of feedstock pretreatment

The cold and hot gas efficiencies for the torrefied biomass gasification campaign are displayed in Figure 56. Similar to the primary methods campaign, the torrefied biomass experimental campaign exhibits results that are not in good agreement with the equilibrium model predictions. This is mostly due to the influence of excess steam and reactant carbon loss during the biomass gasification tests. The equilibrium models show that the carbon

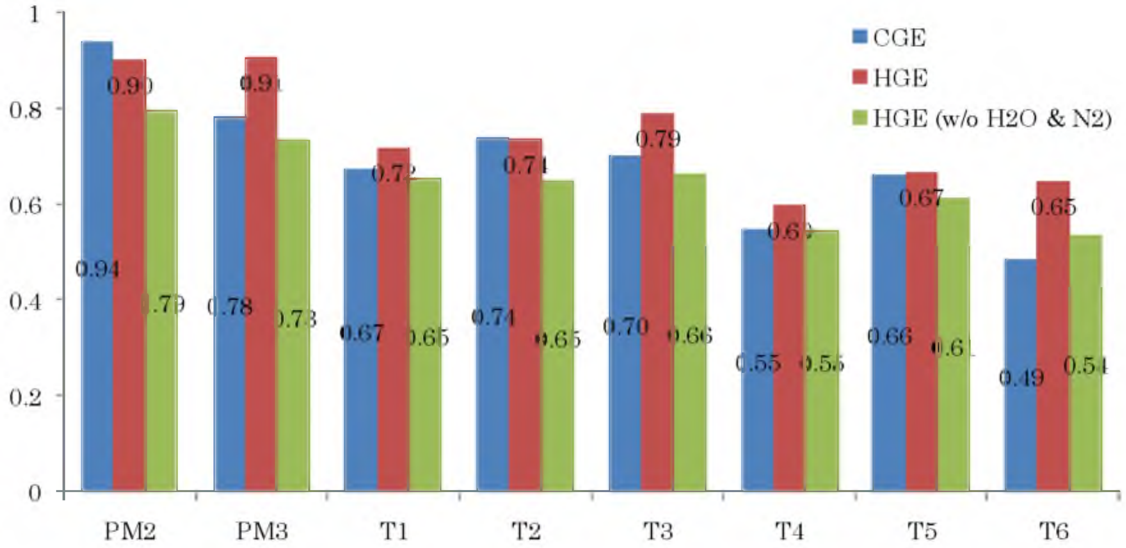

Figure 56. Cold (CGE) and hot gas efficiency (HGE) for torrefied biomass gasification

monoxide and methane gas concentrations are higher for torrefied biomass gasification, but the experimental results show that the opposite was true. Therefore, it is expected that the heating value per unit volume of the synthesis gas produced from torrefied biomass gasification will be lower in comparison to gas produced from raw biomass gasification. This, in addition to the higher fixed carbon content in torrefied biomass, a portion of which will not contribute to synthesis gas production, likely explains the lower CGE and HGE in comparison to raw biomass. The same rationale can be used to explain the lower CGE and HGE for dark in comparison to medium-torrefied biomass conversion. Lower biomass feedrate and higher gasifier temperature improves both the CGE and HGE, but more so for dark-torrefied material, which is consistent with the mass conversion trends. This indicates that the conversion of energy in fuel carbon, in comparison to volatile matter, is more dependent on the concentration of reactant gas and gasifier conditions. This is consistent with equilibrium constant trends for heterogeneous carbon gasification reactions, which are highly temperature and pressure dependent (*92*).

6.6. Net gasification effectiveness

Up to this point, the efficiency of fuel mass and energy conversion has been quantified using the carbon conversion efficiency and hot and cold gas efficiencies. However, these measures do not encompass other important inputs and outputs of a gasification process, including indirect heat addition, steam generation, and residue recovery. Therefore, the net gasification effectiveness (NGE) is computed to account for all energy inputs and outputs to and from the gasifier. Several definitions of the NGE have been adopted for the purpose of considering different potential gasifier operation scenarios. The mathematic definitions for these are discussed in the "Materials and Methods" section of this dissertation. All of the NGE forms follow the "energy output to energy input" form with various definitions of the inputs and outputs. In short, "NGE1" accounts for the consumption of the direct energy inputs to the reactor (steam production, steam superheating, and bed heating) and the chemical and sensible energy content in the synthesis gas. “NGE2” is similar to the HGE but considers recovery of gasification residues (char and tar) as energy inputs. “NGE3” is similar to NGE1 but accounts for the chemical energy in the gasification residue (char and tar) outputs.

6.6.1. Effect of temperature and pressure

6.6.1.1. NGE1

NGE1, which accounts for the thermal energy input to the gasification system compared to the thermal and chemical energy in the synthesis gas, is displayed in Figure 57 (solid line) for the primary methods tests. According

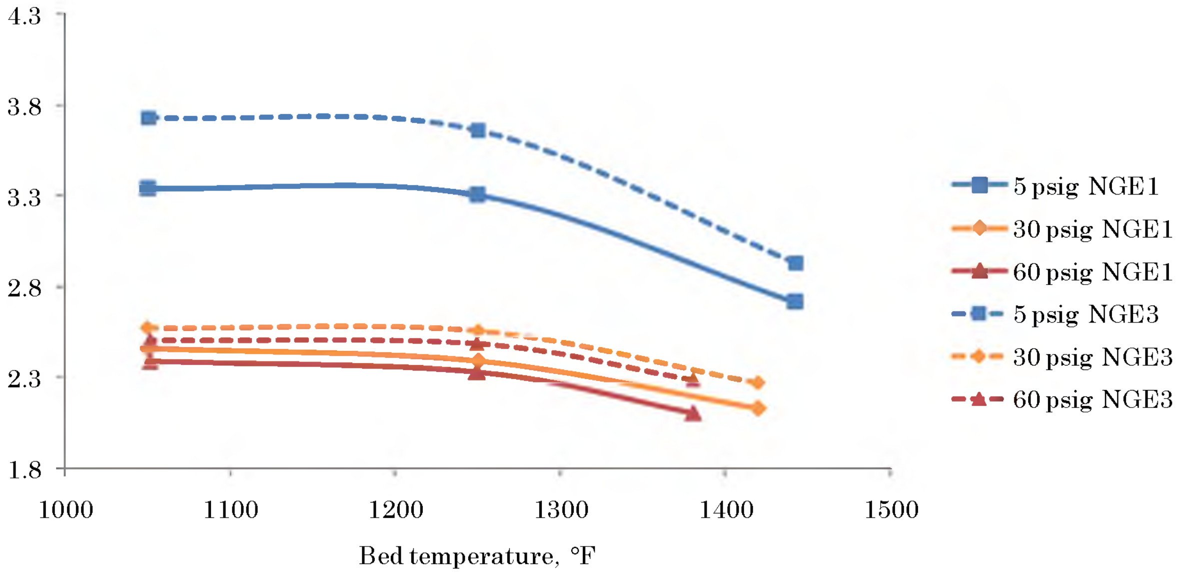

Figure 57. Net gasification effectiveness NGE1 and NGE3 trends with bed temperature and freeboard pressure

to NGE1, the gas exiting the gasifier contains 2.1-3.3 times the amount of energy that is required to operate the gasification system, save auxiliary power loads (e.g., motors, pumps). Unlike previous representations of the energy conversion efficiency of the system, the low-pressure, low-temperature case exhibits the best efficiency according to NGE1. As the bed temperature increases, NGE1 remains relatively constant to the medium-temperature condition and then decreases to the high-temperature condition. This is due to a sizable increase in the bed heater power output to maintain the bed at the high-temperature set point (1450°F) without a proportional increase in synthesis gas chemical or thermal energy content. The medium- and high-pressure cases exhibit similar characteristics but at a much lower magnitude than the low-pressure cases. NGE1 for the pressurized cases is markedly lower than for the low-pressure case due in large part to the greater amount of steam requiring heat addition, which is not compensated for by a similar increase in synthesis gas yield or energy content.

6.6.1.2. NGE2

NGE2, which is similar to the HGE but accounts for additional fuel input from recovered char and tar, is displayed in Figure 58. With the significant rates of char production during these experiments, which is typical for fluidized bed gasification at moderate temperature, and a portion of that char

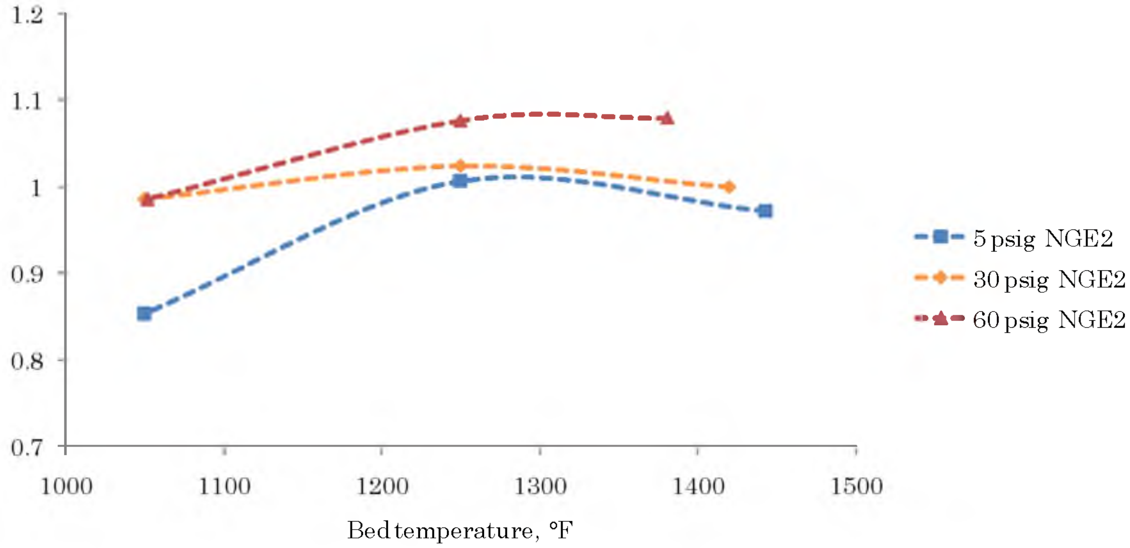

Figure 58. Net gasification effectiveness NGE2 trends with bed temperature and freeboard pressure

collecting in the downstream particulate filter, the potential for utilizing that char for energy recovery is substantial. Char, which is generally 85% (by mass) or more carbon content, has a heating value of approximately 32 MJ/kg (7) compared to the untreated, dry biomass, which has a heating value of approximately 18 MJ/kg (Table 3). In addition, biomass char particles are physically very fine and dry, similar to pulverized coal, which makes char suitable for immediate use in fuel applications. Due to its high production rates, the contribution to energy recovery from char was much higher than for tar (2-10 times on an energy basis). Residue recovery for energy use results in a 13-36% increase in net effectiveness at low temperature and a 6-9% increase at high temperature. While the relative magnitude of net effectiveness gains for the low- and medium-pressure cases is larger than the high-pressure cases with addition of residue recovery, the net effectiveness of the high-pressure case is substantially higher than the other cases. This is due to the fact that the decrease in input energy with the addition of residue recovery is relatively low in comparison to the increase in synthesis gas chemical and thermal (including steam) energy content.

6.6.1.3. NGE3

NGE3, which is similar to NGE1 (which does not account for the feedstock energy input) but accounts for the heating value of the gasification residues (char and tar) as energy outputs, is displayed in Figure 57. For all cases, the addition of residue energy content increases the net effectiveness of the gasification process, with the low-temperature, low-pressure case having the highest net effectiveness (373%) and the medium- and high-pressure, high-temperature cases having the lowest net effectiveness (227% and 229%). With less external energy input to the system for steam generation and heating, along with the relatively high tar production rates, the low-temperature cases remain the most energetically effective when not considering the biomass feedstock energy input. For the low-pressure cases, the relatively low amount of sensible heat in the product gas compared to the pressurized cases results in substantial energy increases when residues are recovered. In addition, the low-pressure conditions produced the highest concentration of tar, and with similar synthesis gas yields for most of the cases, the tar energy contribution for the low-pressure cases were larger. Overall, the NGE3 net effectiveness represents the maximum obtainable energy gain. Of course, inefficiencies (e.g., heat loss), additional process costs (e.g., separation, pumping), and feedstock costs will ultimately reduce the net effectiveness.

6.6.2. Effect of biomass pretreatment

6.6.2.1. NGE1

The NGE1 effectiveness, which accounts for the synthesis gas chemical (LHV) and thermal energy (enthalpy), for the torrefied biomass experiments are displayed in Figure 59 (blue bars). Comparison of the net effectiveness for raw biomass and the two torrefied biomass feedstocks (medium- and dark-roast) at similar gasifier operating conditions (PM2 vs. T1 and T4) shows a slight disadvantage to gasification of dark-torrefied biomass, which is likely due to the reduced synthesis gas production at the expense of high char production rates. Gasification of dark-torrefied material at low temperature and feedrate (T6) resulted in the highest NGE1 net effectiveness of all the torrefied biomass tests (293%). This is likely due to the substantially lower heat input to the bed for this case despite the relatively low synthesis gas

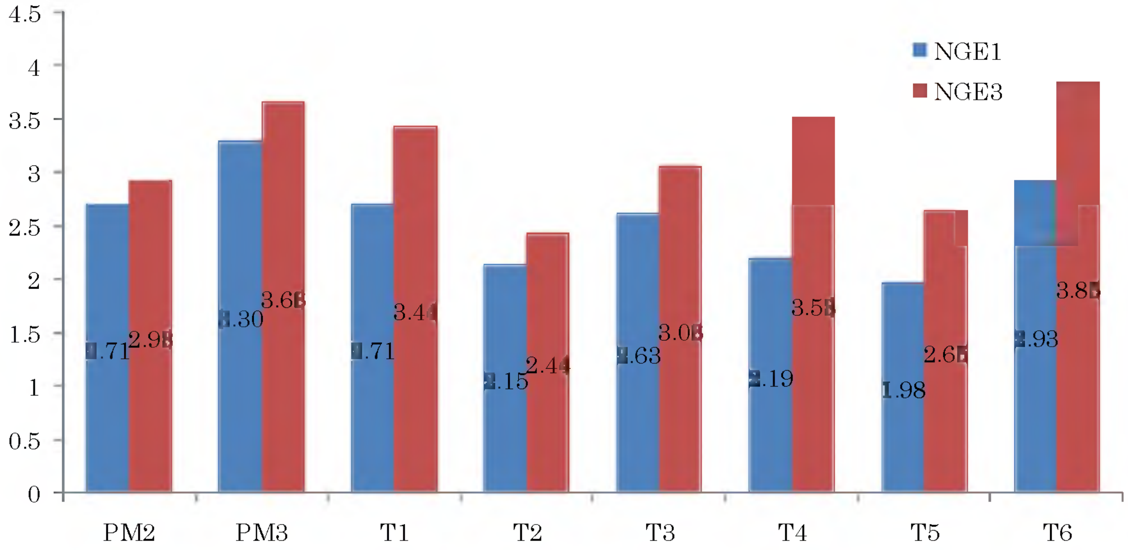

Figure 59. Net gasification effectiveness NGE1 and NGE3 for torrefied biomass gasification

yield. For both the medium- and dark-torrefied feedstocks, the lowest net effectiveness was recorded for the low-feedrate, high-temperature condition (T2 and T5), which is due to the high bed heat input and low synthesis gas yield despite the high mass conversion efficiency (Figure 54).

6.6.2.2. NGE2

The NGE2 net effectiveness, which is similar to the HGE but includes recycling of residues as energy inputs (e.g., char combustion to provide bed heat), is displayed in Figure 60. For this net effectiveness definition, gasification of the raw biomass feedstock (PM2) resulted in the highest efficiency (97%) despite the lower amount of char recovery in comparison to

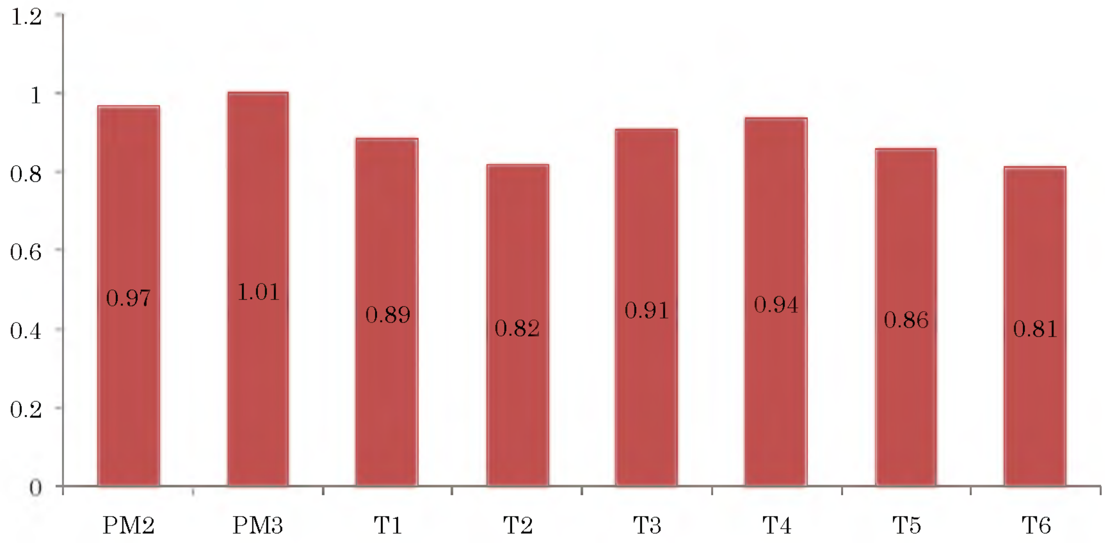

Figure 60. Net gasification effectiveness NGE2 for torrefied biomass gasification

torrefied biomass gasification at high temperature (T1 and T4). This is likely due to the significantly higher synthesis gas energy content. Between the two torrefied biomass feedstocks, the dark-torrefied biomass (T4 and T5) exhibited higher net effectiveness than the medium-torrefied biomass (T1 and T2) due to the substantially higher char production (2-3 times) in these cases.

6.6.2.3. NGE3

The NGE3 net effectiveness, which is similar to NGE1 but includes gasification residues as a desirable energy outputs from the system, is displayed in Figure 59 (red bars). For the NGE3 net effectiveness, the torrefied feedstocks (T1 and T4) perform much better than the raw biomass feedstock due in large part to the high char residue production. For that same reason, the dark-torrefied material (T4-T6) exhibits higher net effectiveness than the medium-torrefied material (T1-T3) under all conditions, with the highest net effectivness (457%) occurring at the low-temperature, low-feedrate condition (T6). This condition exhibits similar product gas energy content (83 kW), but 10% lower reactor energy input and 80% more residue production than the equivalent medium torrefied case (T3). The higher feedrate conditions (T1 and T4) also produced significantly higher quantities of residues and synthesis gas than the equivalent low-feedrate conditions (T2 and T5), which result in much higher net effectiveness. In addition, the lower bed temperature condition for both torrefied feedstocks resulted in higher net effectiveness, which can be partially attributed to the low energy input to the system, but also to the high residue production rate.

CHAPTER 7

RESULTS: FLUIDIZED BED DIAGNOSTICS FROM PRESSURE FLUCTUATION MEASUREMENT

Data presented in the preceding section focus on evaluation of the biomass gasification system operation with respect to general monitoring and measurement in the system, and conversion of mass and energy inputs to desirable outputs. In addition to those performance evaluations, an advanced method for fluidized bed diagnostics is proposed in this section.

7.1. Cold-flow fluidized bed

The measurement of pressure fluctuations at a single, wall-flush point in a gas-solid fluidized bed is widely reported on in literature. This research aims to demonstrate this fluidized bed diagnostic technique in a high-temperature fluidized bed reactor. Initial studies were carried out using a scaled, cold-flow model of the pilot-scale fluidized bed reactor. Several screening studies were performed to ensure proper functionality of the pressure measurement devise. A brief discussion of results from a single cold-flow test is discussed for the purpose of demonstrating the measurement method. Discussion of the dynamics of the fluidized bed reactor is discussed in the proceeding section.

7.1.1. Raw pressure signal

A typical bed-pressure data set is displayed in Figure 61. For this test condition, the superficial gas velocity was maintained at approximately 1.0 ft/s. A continuous 6-minute measurement period is divided into three, 2-minute ensemble sets. Statistical and spectral analysis is performed on each ensemble dataset and the three are averaged to provide averaged quantities

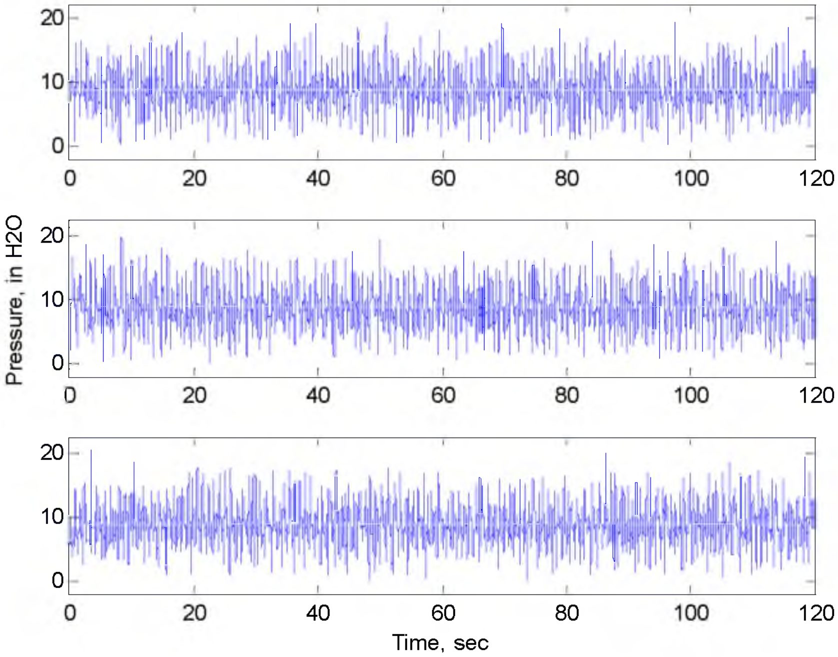

Figure 61. Raw pressure ensemble signals for test CF10 (SGV=1 ft/s) (in. H_2O)

for a single experiment.

From visual inspection, the signal appears to be highly chaotic with no apparent cyclic patterns or structure. The signal appears to be relatively stationary, with little fluctuation of the mean pressure and relatively little change in the magnitude of fluctuations from the mean pressure. The fluctuating component of the pressure signal, which is computed by subtracting the ensemble mean pressure from the raw ensemble dataset, is displayed in Figure 62.

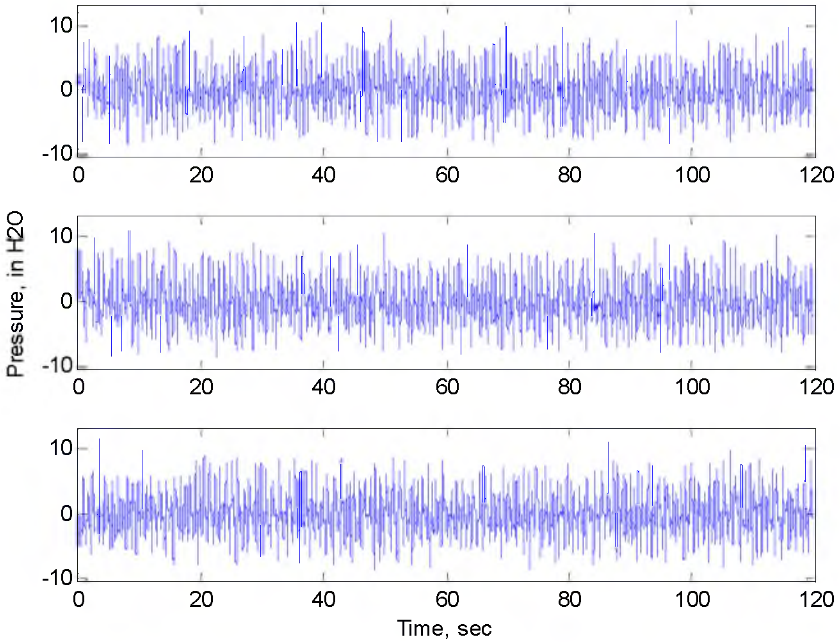

Figure 62. Raw pressure fluctuation ensemble signals for test CF10 (SGV=1 ft/s) (in. H_2O)

7.1.2. Central moments and PDF

The relevant and important statistical quantities for this flow condition are displayed in Table 7. The central moments of the signal describe the probability distribution of the signal, which is portrayed in normalized form as the probability density function (PDF) (Figure 63). The ensemble averaged PDF of the signal is displayed with a polynomial curve fit using least square regression and the equivalent (identical mean and variance) normalized Gaussian distribution.

From the PDF and the associated statistical quantities that describe it, several observations can be made with regard to the pressure conditions in the cold-flow fluidized bed. First, there appears to be some asymmetry in the distribution with more data points spread to the right of the mean fluctuation

Table 7. Bed pressure signal characteristics for cold-flow fluidized bed test data (1ft/s).

SGV, m/s	0.30
Mean pressure, in. H_2O	8.79
Pressure fluctuation standard deviation, in. H_2O	2.91
Pressure fluctuation variance	8.46
Pressure fluctuation skewness	0.28
Pressure fluctuation kurtosis	3.41

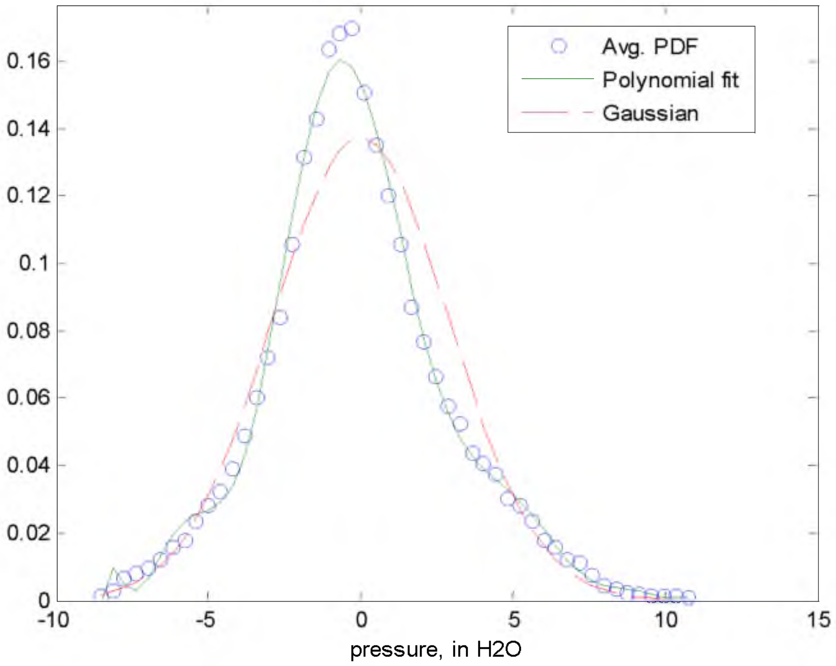

Figure 63. Normalized, ensemble average probability density function (blue circles), polynomial fit (green line), and equivalent Gaussian distribution (red dash line) for test CF10 (SGV=1 ft/s).

(zero). The third central moment, the skewness, which indicates the amount and direction of asymmetry in a distribution, has a value of 0.28. The Gaussian distribution has a skewness of zero. A positive skewness indicates that the data are biased in the positive direction, right of the mean. Physically, this indicates that the pressure is more likely to exhibit large positive fluctuations than negative fluctuations. This is likely due to the intermittency of bubble passage near the pressure probe as opposed to the more continuous but smaller fluctuations due to circulation of solids from the top of the bed.

The fourth central moment of the distribution, or kurtosis, provides an indication of the probability of a pressure fluctuation event to occur in the tails of the distribution. The kurtosis for this distribution is 3.41, compared to the kurtosis of the Gaussian distribution, which is 3. A kurtosis greater than 3 indicates that high-magnitude fluctuations, which appear in the tails of the distribution, are more likely to occur than for a signal following the random, Gaussian distribution.

7.1.3. Power spectral density

The covariance power spectral density (PSD) of the pressure fluctuation signal, as estimated by an auto-regression model (n=100), is displayed in Figure 64. The PSD is a representation of the signal in frequency space in which the signal power corresponding to the frequency of motion in the flow is plotted. The PSD is useful in identifying dominant frequencies in the flow. In this case, the dominant frequency occurs at about 1.5 Hz, with several minor peaks from 3-8 Hz. Scale analysis can be utilized to estimate characteristic length and time scales associated with the dominant frequencies. In many cases, dominant frequencies in the flow field can be attributed to physical (e.g., geometric) constraints. In this case, the dominant frequency corresponds to a characteristic length scale of about 2 inches. While this length scale cannot be linked to a geometric constraint in the bed,

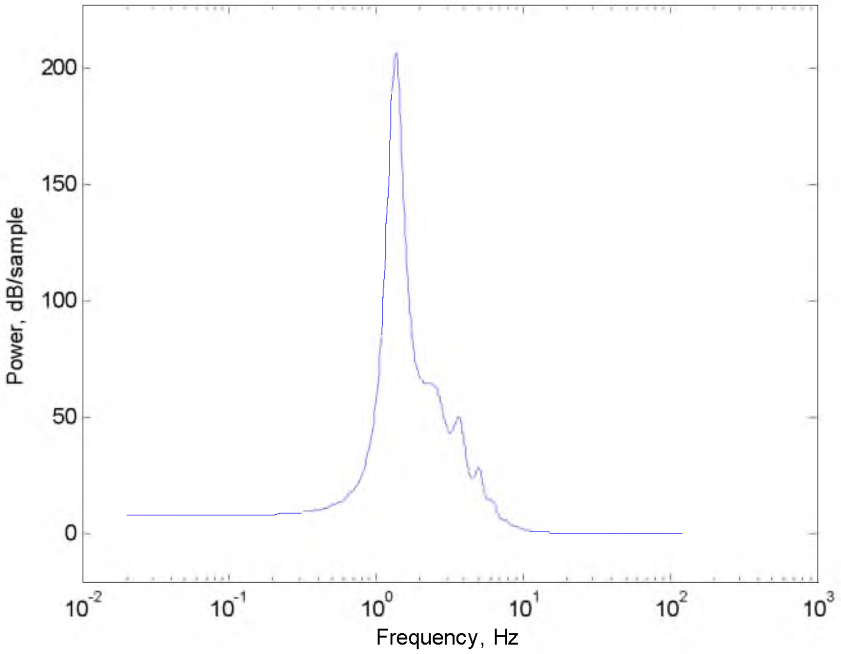

Figure 64. Pressure fluctuation covariance power spectral density (semi-log) for test CF10 (SGV=1 ft/s)

the dominant length scales in a fluidized bed have been shown to be related to bubble passage and pressure wave propagation through the bed (*56*). In addition, the drop-off of the power spectrum provides some indication as to whether there is any order retained from the integral scales at small length and time scales. In this case, the linear drop-off indicates that little order is retained and energy dissipation is random at small length scales (*62*).

Plotting the PSD on a log-log scale produces some additional information in the high-frequency region of the spectrum (Figure 65). The near linear drop-off of the spectrum at high frequency indicates that energy decay in this region can be described by a power-law relationship. Power-law decay

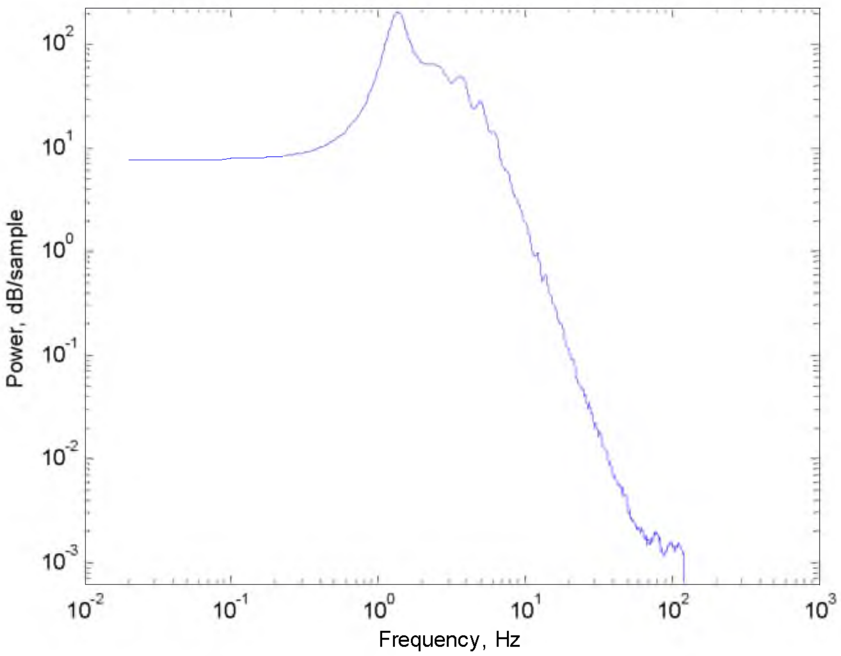

Figure 65. Pressure fluctuation covariance power spectral density (log-log) for test CF10 (SGV=1 ft/s)

generally indicates that the process is stochastic, as in turbulent flow. In this case, it is likely that the power-law decay is likely due to the power-law tails of bubble size distributions for bubbling fluidized beds (*66*). However, this region does provide some insight regarding the degradation of ordered, integral scale bubble motion to smaller bubbles and granular motion.

7.1.4. Autocorrelation function

The normalized autocorrelation function of the pressure fluctuation signal is displayed in Figure 66. The autocorrelation function provides an indication of how well-correlated a signal is with itself in time. The

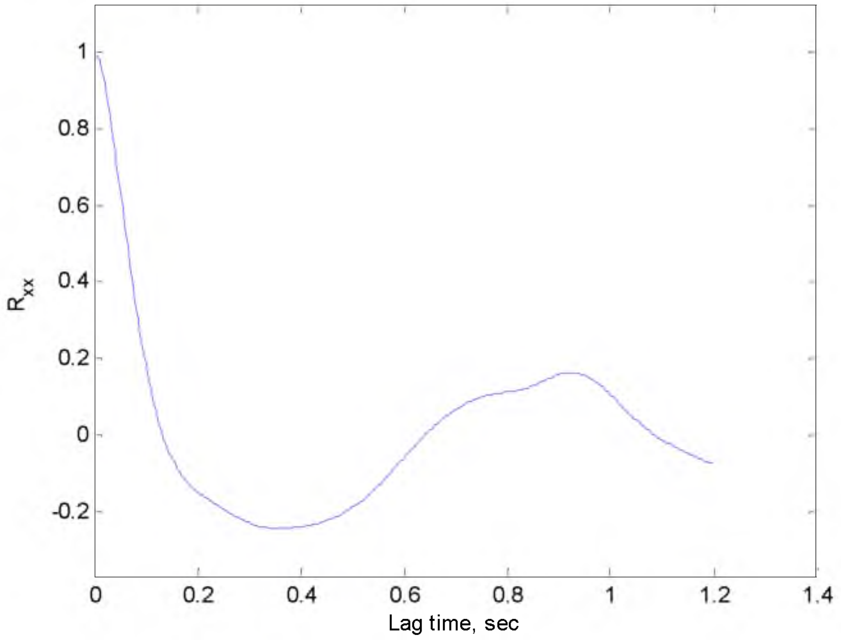

Figure 66. Autocorrelation function for test CF10 (SGV=1 ft/s)

autocorrelation function provides some spatial information from a single point, time-series signal. In this case, the autocorrelation function drops relatively slowly to zero and appears to exhibit the beginning of a cyclic fluctuation based on the limited lag time length for this case. This indicates that the signal is somewhat correlated with itself within the period of time shown. It also indicates that there is likely some large-scale cyclic motion present in the flow field, such as periodic slugging or bed expansion. Finally, the initial drop-off of the autocorrelation function provides an estimate of the characteristic integral length scale for the flow field. Integrating under the initial drop-off section of the autocorrelation function and using scale analysis, the estimated integral length scale is approximately 1 inch, which is on the order of the flow holes in the distributor plate of the fluidized bed (0.5625 in.). In addition, what appears to be a periodic oscillation in the autocorrelation function profile indicates that there is a deterministic quality to the flow.

7.2. Fluidized bed gasifier

Following testing of the measurement method on the cold-flow fluidized bed apparatus, the high-frequency pressure measurement device was installed in the pilot-scale fluidized bed reactor for testing under reactive conditions. Despite some initial difficulties in preventing bed material from back-flowing into the pressure probe, continuous pressure measurement through many of the primary methods and torrefied biomass gasification tests was achieved. The following is a description of determining an adequate sample length and pressure fluctuation signal characteristics for various reactor operating conditions.

7.2.1. Effect of time-series sample length

A 6-minute time series was used for pressure fluctuation measurement tests in the cold-flow apparatus. However, in a system that is less controlled, with many different dynamics such as the larger scale fluidized bed reactor, it is necessary to reassess the sample length. While a short sample is more likely to remain stationary, which is a concern for the reactor due to sudden changes in downstream pressure drop, a longer sample length can average out many of these erratic disparities. However, longer sample lengths can also average out features of the signal that may be of interest.

A relatively steady period of gasifier operation (steady conditions during PM11- high-temperature, medium-pressure duplicate test) was selected to evaluate sample length effects and the resulting signal characteristics. This period of operation did however exhibit erratic qualities that are inherent in normal operation of the gasifier (e.g., pressure bumps due to downstream valve adjustment, steam flow fluctuations). Sample lengths of 6, 12, 18, 24, and 30 minutes were analyzed. The ensemble pressure datasets for the 6- and 30-minute sample lengths are displayed in Figure 67.

Relatively little change was observed in the statistical descriptors of the signal over the course of the entire sample length test (Figure 68). The most pronounced is a near 10% decrease in the pressure fluctuation variance from the 6-minute to the 12-minute test. This was fairly consistent when tested over other periods of the PM11 gasification experiment. Therefore, 12-minute sample lengths were utilized for bed pressure sampling in the fluidized bed gasifier.

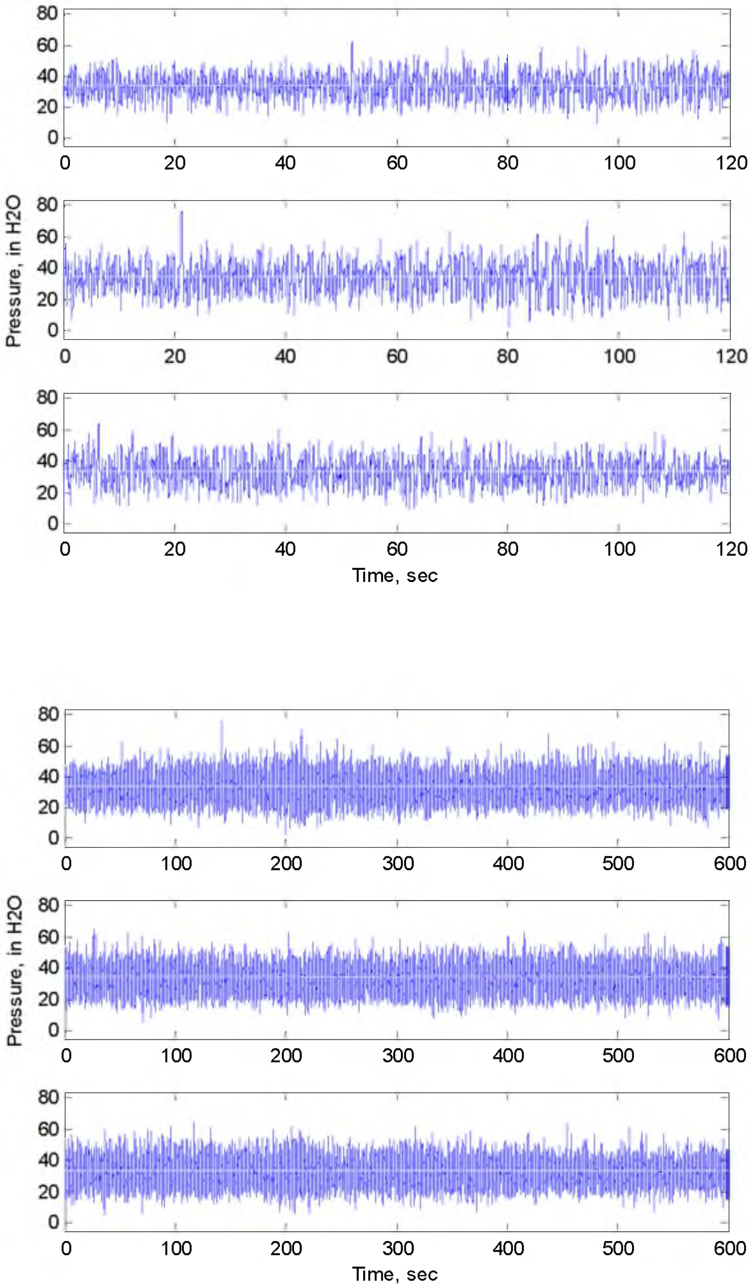

Figure 67. Raw pressure ensemble data for a 6-minute (top) and 30-minute sample length (bottom) during test PM11

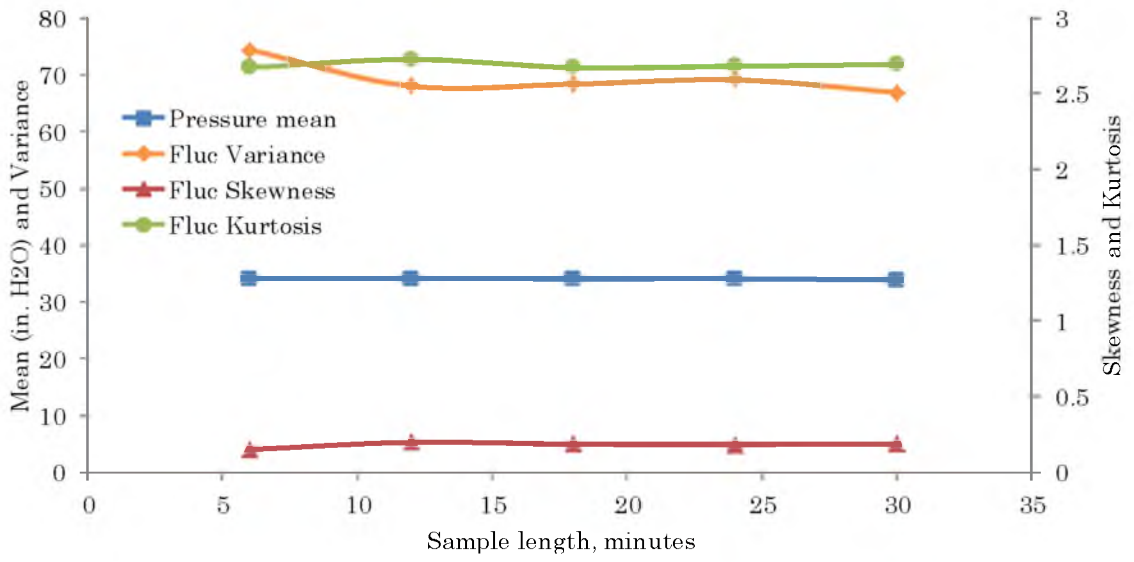

Figure 68. Statistical quantity trends with sample length for the pressure signal during test PM11

7.2.2. Effect of reactive conditions

Prior to installing the high-frequency pressure transducer in the fluidized bed reactor, the only method for assessing bed conditions was with a series of five thermocouples located at various locations along the bed height. A uniform temperature distribution (+/- 5-10°F in the heater section) along the bed height defines a well-fluidized bed. This method of bed fluidization monitoring is adequate for identifying when conditions are “good” or “not good” but provides little insight as to why. With the ability to detect the dynamics (e.g., bubble passage, agglomeration, bed growth) of the bed, local bed pressure fluctuation measurement has the potential to be a useful tool.

7.2.2.1. Test conditions

For demonstration of the pressure fluctuation signal and the various signal characteristics, pressure measurements made during the dark torrefied biomass tests will be used. This series of consecutive gasifier runs consists of:

- T4: high temperature (1450°F) and high feedrate (45 lb/hr dry biomass), 14:45-17:30
- T5: high temperature (1450°F) and low feedrate (30 lb/hr dry biomass), 17:30-19:00
- T5: low temperature (1250°F) and low feedrate (30 lb/hr dry biomass), 19:00-20:10

7.2.2.2. Temperature trends

The average bed temperature and distributor plate temperature profile over the course of the three tests is displayed in Figure 69. Temperature profiles of the individual tests are displayed in Figure 70. According to these profiles, the bed exhibits fairly good temperature distribution during steady operation with bed temperature disparities of 10-30°F. Transient conditions are observed prior to the start of test T4 which will be discussed later. Transitions between each test do not appear to show any significant changes in fluidization conditions. The low-temperature test (T6) appears to exhibit

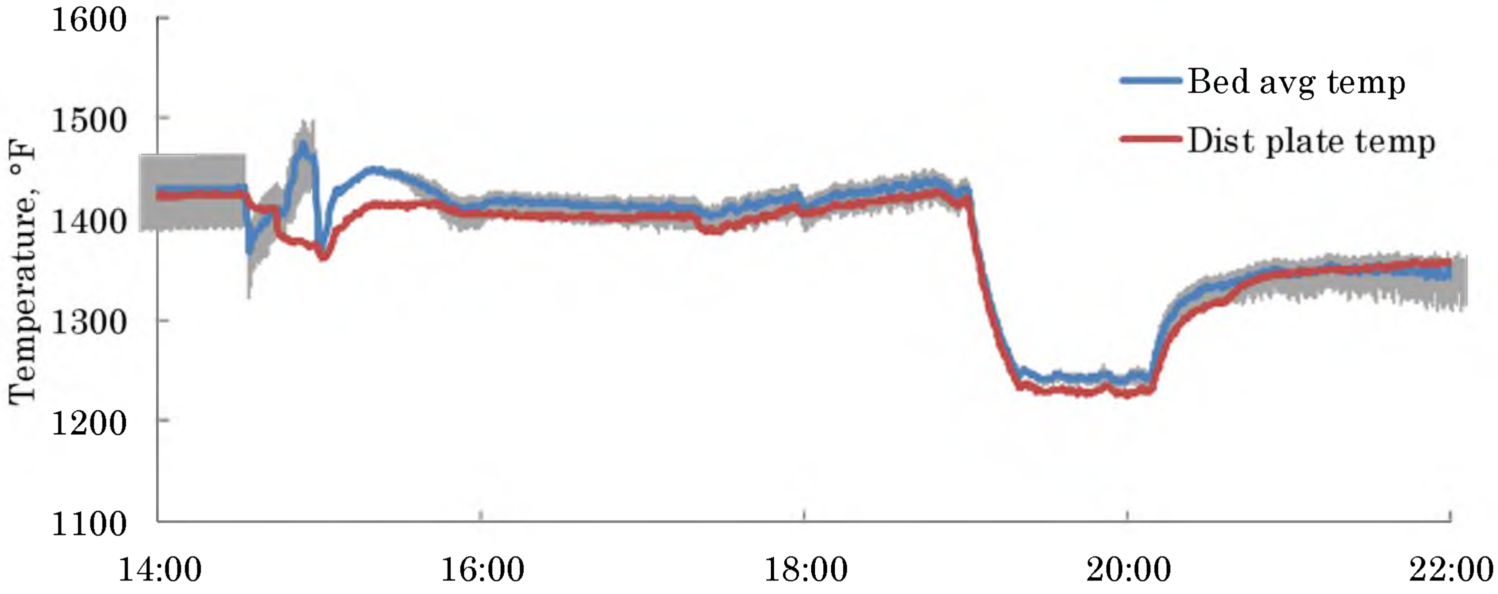

Figure 69. Bed average temperature (blue) (with temperature disparity, grey shading) and distributor plate temperature trend (red) during dark torrefied biomass experiments T4-T6 (°F)

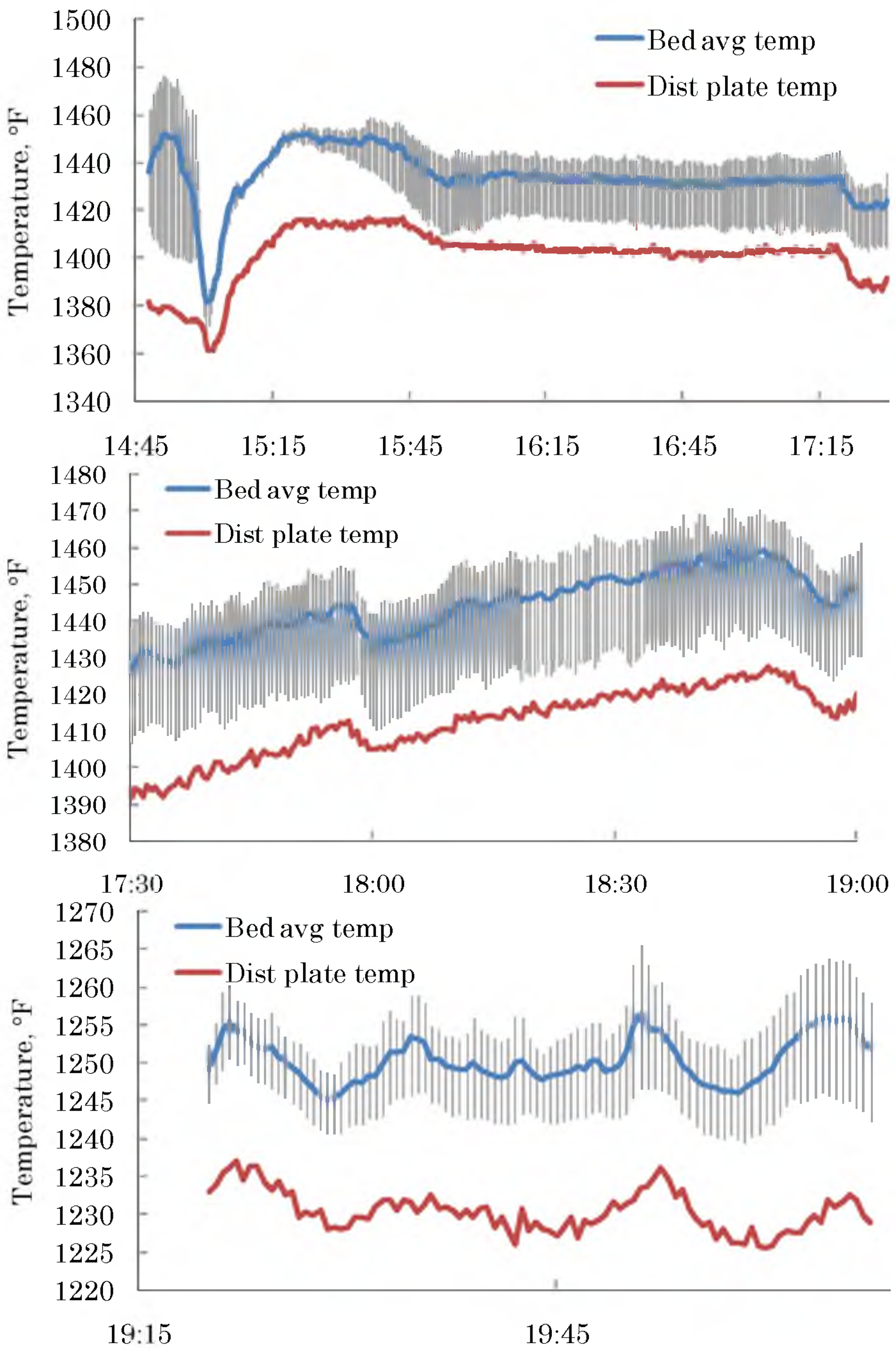

Figure 70. Bed average temperature (blue) (with temperature disparity, grey shading) and distributor plate temperature (red) trend during dark torrefied biomass experiments T4 (high temperature, high feedrate) (top), T5 (high temperature, low feedrate) (middle) and T6 (low temperature, low feedrate) (bottom) (°F).

the best fluidizing conditions based on the bed temperature profile, with 5-10°F between the high and low temperatures in the bed heater section and the distributor plate temperature within 30°F of the heater section.

7.2.2.3. Raw pressure data

The raw data set for this day of testing is displayed in Figure 71. This data set consists of 18,516,100 data points over the course of 25 hours and 43 minutes. The data file was logged using National Instruments (NI) Labview

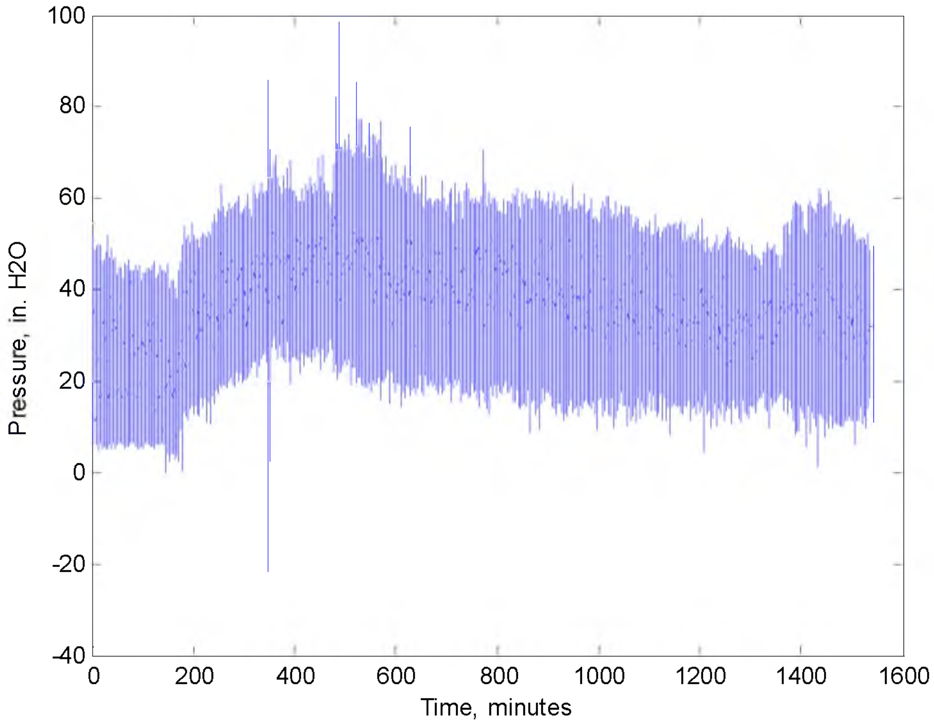

Figure 71. Raw pressure signal before, during, and after T4-T6 dark torrefied biomass tests (in. H_2O). 0=12:07, T4 start @ 160 minutes, T6 end @ 479 minutes

data acquisition software. The NI Labview data file was then imported to Matlab using a custom written script. Conversion of the NI .tdms files to .mat files took as long as 30 minutes for each file. This data set shows continuous logging of what appears to be real pressure measurements. Several of the datasets had some discontinuities due to pressure line plugging.

7.2.2.4. Measurement sample

Samples of the raw dataset were selected to be analyzed using the pressure fluctuation measurement techniques previously described. One sample was selected from the period prior to starting the first dark torrefied biomass gasification test (T4). A sample was selected at the onset of feeding at the start of test T4. Three samples were analyzed during steady state operation during all three dark torrefied biomass tests. Finally, one sample was analyzed 1 hour following the end of the final test.

7.2.2.5. Signal characteristics

The statistical descriptors for each test are displayed in Table 8. These correspond to analysis results that are presented in Figure 72-Figure 75.

Table 8. Average statistical quantities for each pressure fluctuation measurement sample during the dark torrefied biomass gasification campaign

	Pre T4	Feed start T4	Steady T4	Steady T5	Steady T6	Post T6
Mean pressure, in. H_2O	33.88	20.67	38.47	45.30	45.23	47.15
Pressure fluctuation standard deviation, in. H_2O	8.18	5.65	5.20	4.87	4.20	5.33
Pressure fluctuation variance	66.92	31.93	27.07	23.79	17.69	28.73
Pressure fluctuation skewness	0.19	0.15	0.04	-0.15	-0.24	-0.02
Pressure fluctuation kurtosis	2.69	2.57	2.75	3.08	3.30	3.76

7.2.2.6. Observations

In following the progression of the samples chronologically, there are many distinct differences between pregasifying and gasifying bed conditions. The first pressure fluctuation sample shows a bimodal probability distribution (Figure 72a), the negative peak being the larger of the two. The power spectra in the initial sample show a single, high-magnitude peak near4 Hz that encompasses a large portion of the total energy in the flow field (Figure 73a). The autocorrelation function shows some correlation in the sample with periodic fluctuations about zero that dissipate after a few

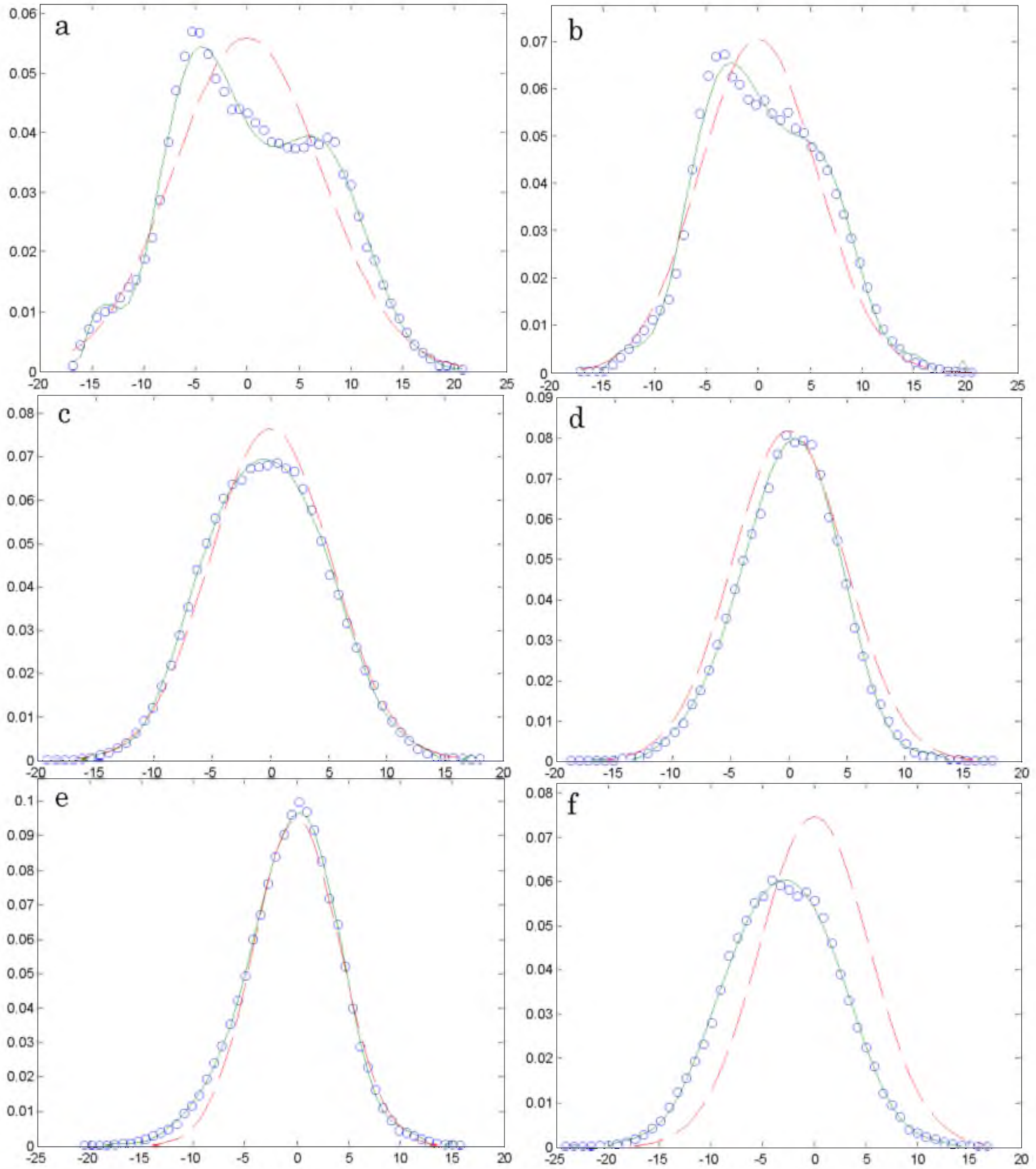

Figure 72. Pressure fluctuation probability density function for a) 1 hour before T4, b) initiation of feed for T4, c) steady T4, d) steady T5, e) steady T6, f) 1 hour after T6. Abscissa is pressure fluctuation (in. H_2O) and ordinate is normalized probability. Blue circles are actual probability density values, solid green line is a polynomial fit the actual values, and the dashed red line is an equivalent Gaussian distribution.

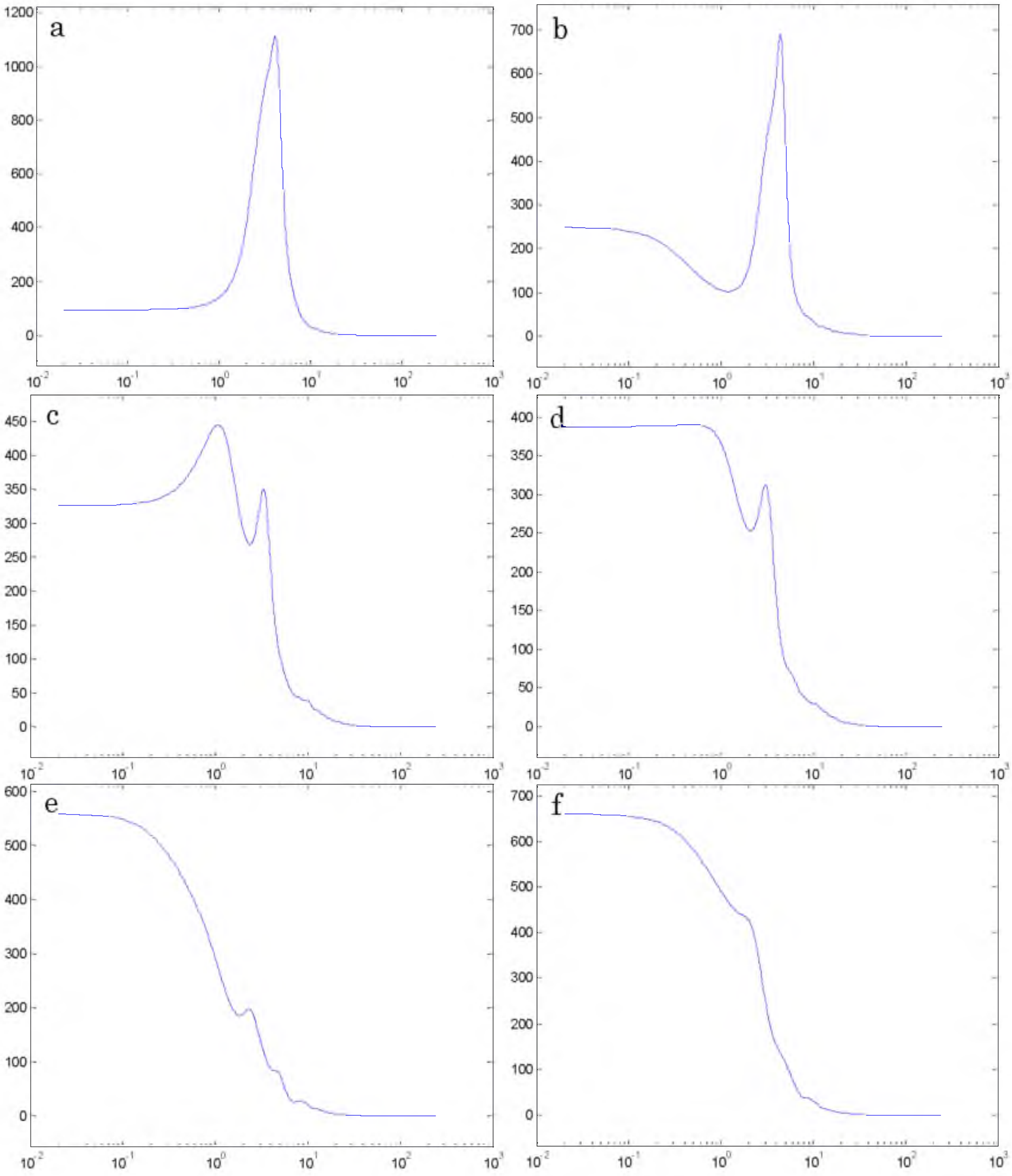

Figure 73. Autocovariance power spectral density (semi-log) for a) 1 hour before T4, b) initiation of fee for T4, c) steady T4, d) steady T5, e) steady T6, f) 1 hour after T6. Abscissa is frequency (Hz) and ordinate is signal power (dB/sample).

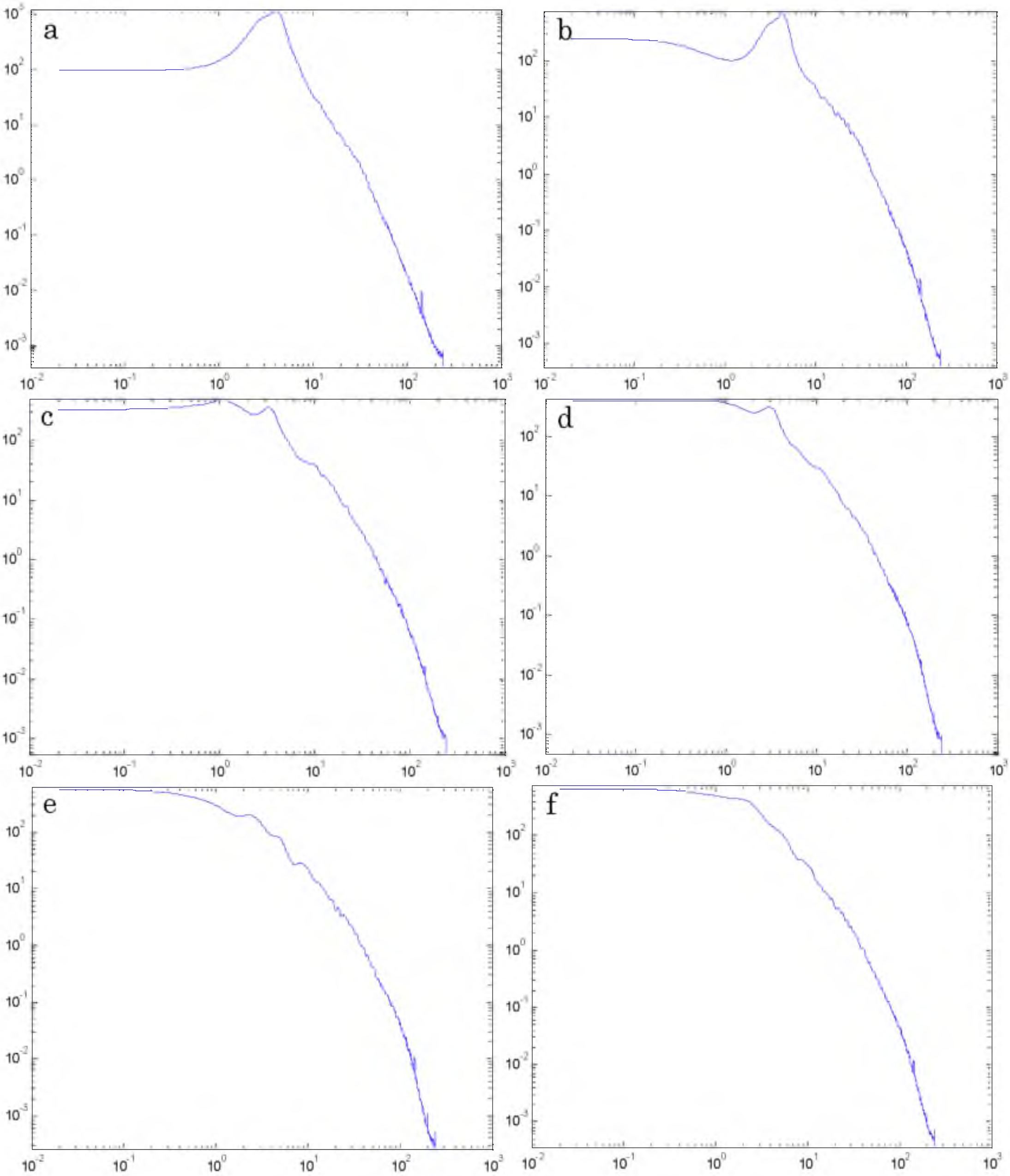

Figure 74. Autocovariance power spectral density (log-log) for a) 1 hour before T4, b) initiation of fee for T4, c) steady T4, d) steady T5, e) steady T6, f) 1 hour after T6. Abscissa is frequency (Hz) and ordinate is signal power (dB/sample).

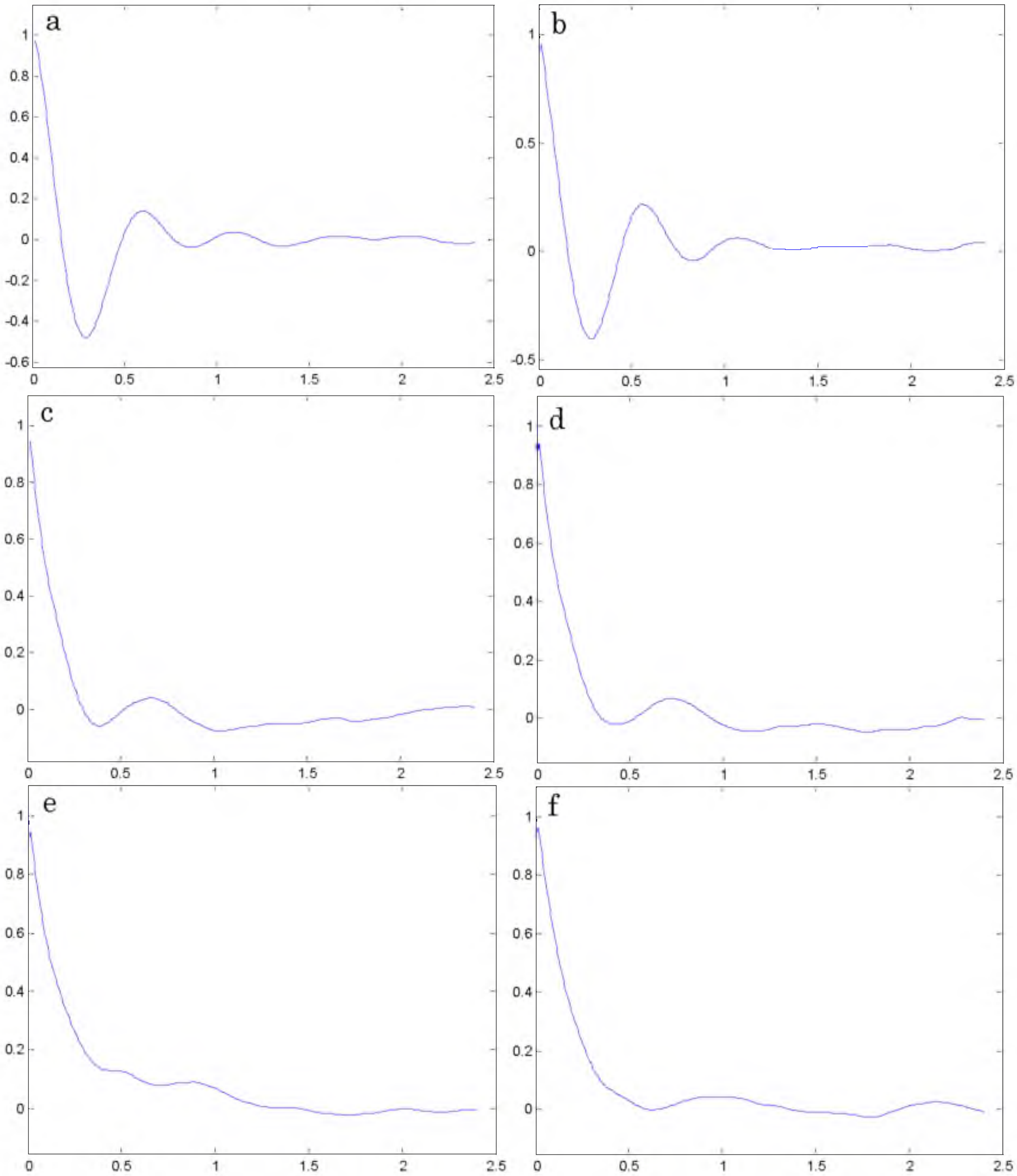

Figure 75. Normalized autocorrelation function for a) 1 hour before T4, b) initiation of feed for T4, c) steady T4, d) steady T5, e) steady T6, f) 1 hour after T6. Abscissa is lag time (seconds) and ordinate is the normalized correlation coefficient.

seconds (Figure 75a).

As feeding begins in the second measurement sample in the series and into steady gasifier operation in the third sample set, the bimodal distribution transitions to a negative skew unimodal distribution upon reaching steady gasifier operating conditions during test T4 (Figure 72c). The single dominant peak in the power spectrum gives way to a more distributed spectrum, still containing the original peak, but with more energy contained in lower frequencies (Figure 73c). The higher frequency (20-100 Hz) spectrum fall-off transitions from linear to exponential decay with the progression of the tests (Figure 74c). By the T4 steady operation sample set, the autocorrelation in the signal and decaying periodic behavior have given way to a less correlated profile with a slightly larger integral length scale.

Several trends and transitions occur in the statistical descriptors as the gasification tests continue (Table 8). First, the variance of the pressure fluctuations continues to decrease until the end of the dark torrefied biomass testing. The skewness transitions to a negative value and the kurtosis transitions to a value greater than three during steady operation at condition T5. The decrease in variance indicates that probability distribution is becoming narrower with fewer extreme fluctuations. The transition to a negative skewness indicates that the distribution of fluctuations is more heavily distributed in the positive direction with a larger tail in the negative direction. This is opposite to the distribution shape that was typically observed in the cold-flow tests and in the fluidized bed reactor when not under gasifying conditions. The increasing kurtosis value indicates that the distribution is becoming more peaky with fatter tails, suggesting that more of the pressure fluctuations are close to the mean.

As the final dark torrefied biomass test (T6) achieves steady conditions, the PDF has become more peaky and negative skewed. The single peak that previously dominated the power spectrum has nearly disappeared, giving way to a near continues exponential decay profile. Also, the autocorrelation function no longer immediately drops to zero but more gradually drops, indicating that the integral length scale may have increased. All of these indicate that under gasifying conditions, there are fewer signs of distinct features such as bubbles, slugs, or pressure waves in the flow field. Instead, the bed appears to be more uniformly chaotic, with energy at large scales quickly dissipating to granular scales.

After the completion of the dark torrefied biomass tests, many of the statistical quantities revert back in the direction of their values prior to the start of the gasification experiments. The pressure fluctuation variance and skewness sharply increase. Interestingly, the kurtosis continues in an upwards trend. Also, the dominant peak at 4 Hz and linear fall-off at higher frequencies appear to be reemerging. From the autocorrelation function, the integral length scale appears to decrease with a sharper drop to zero and some periodicity in the signal is reappearing.

7.2.2.7. Conclusions

While it is difficult to connect all of these observations and generate a cohesive explanation for the hydrodynamic conditions in the bed, it is apparent that there are distinct characteristics of the bed during gasification conditions and during standby operation. The gasification conditions appear to be characterized by high rates of energy dissipation from large to small scales. This is likely due to one, or both, of two features. First, the amount of gas flow through the bed is presumably higher during gasification conditions due to synthesis gas production from the feedstock. This additional gas, if well distributed in the bed, may enhance distribution of bed solids, gas, and fuel particles through better mixing as opposed to large scale transport like bubbles gas slugs. The accumulation of bed char and ash also likely plays a role in the change in hydrodynamic conditions in the bed. Previous research has found that the addition of fine particles to the bed assists in fluidization, acting as a lubricant for larger particles in the bed. This viscous nature of the fine particles would account for the high energy dissipation rate and lower variance in the pressure fluctuation signal.

7.2.3. Formation of a bimodal pressure distribution: A case study

A brief mention was made in the previous section regarding the bimodal probability distribution of pressure fluctuations detected prior to the dark torrefied biomass experiments. This section will investigate the origins of this event in an attempt to understand how the bimodal distribution came to be.

7.2.3.1. Case description

Following the first day of torrefied biomass gasification experiments (T1-T3) using medium torrefied material, the gasifier was left overnight operating at a moderate bed temperature (1350-1400°F) with approximately 30 lb/hr of steam flow through the bed to maintain a fluidizing velocity of approximately 1.0 ft/s. These standby operating conditions are standard procedure during an experimental campaign, which can last for several weeks, and rarely requires continuous gasification conditions through the night. By all accounts, the gasifier maintained normal standby operation through the night except for a peculiar and subtle event that drew out over the course of the night. Slightly after 2:00, the temperature of the lower bed and distributor plate remained constant while the bed heaters section, in the upper portion of the bed, steadily increased in temperature (Figure 76). In

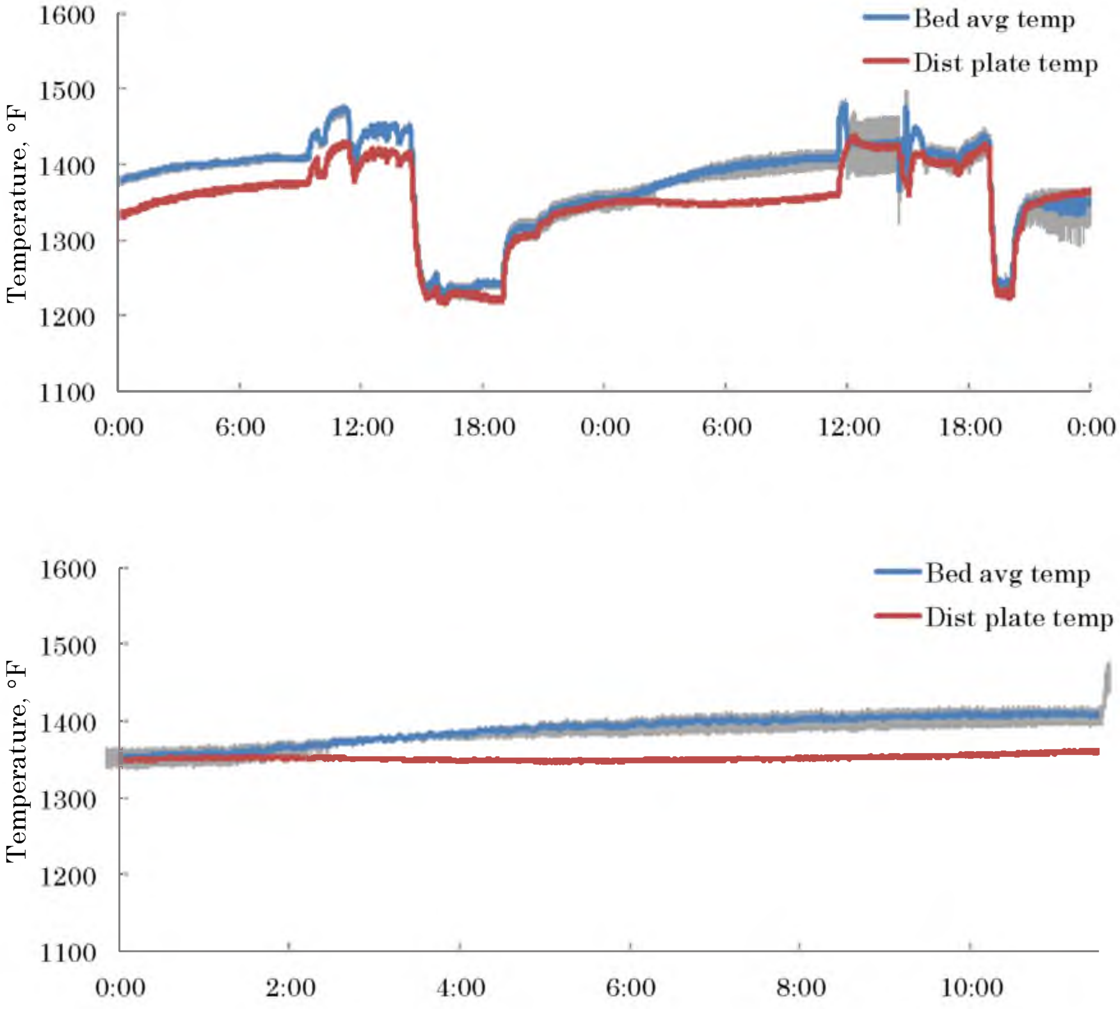

Figure 76. Overnight bed average temperature (with temperature disparity, shaded grey) and distributor plate temperature over all torrefied biomass tests (top) and between torrefied biomass tests T3 and T4 (bottom) (°F)

addition, the temperature disparity of the bed heaters section (grey shaded area) increased, indicating that the temperature distribution in the bed was becoming less uniform. Review of the gasifier control system data logs revealed no significant changes in the system (e.g., pressure, steam flow, nitrogen purge, bed pressure drop) that might account for the temperature disparity.

Luckily, the high-frequency bed pressure transducer was functioning during this event (Figure 77), which allows for a deeper view into this case. Several bed pressure sample sets were analyzed from periods over the course of the night. A summary of the relevant statistical quantities for several of these sample sets is displayed in Table 9. The corresponding analysis results are displayed in Figure 78-Figure 81.

7.2.3.2. Observations

Again, following the progression of the samples chronologically, the conditions in the bed appear similar to the conditions in the bed following the dark torrefied biomass experiments discussed in the preceding section. The variance is relatively low, the skewness is slightly negative, and the kurtosis is relatively high, generating a long left-tailed, peaky pressure fluctuation distribution (Figure 78a). Following the prior gasification test, the single dominant peak is well-developed at just under 3 Hz with a steep drop-off

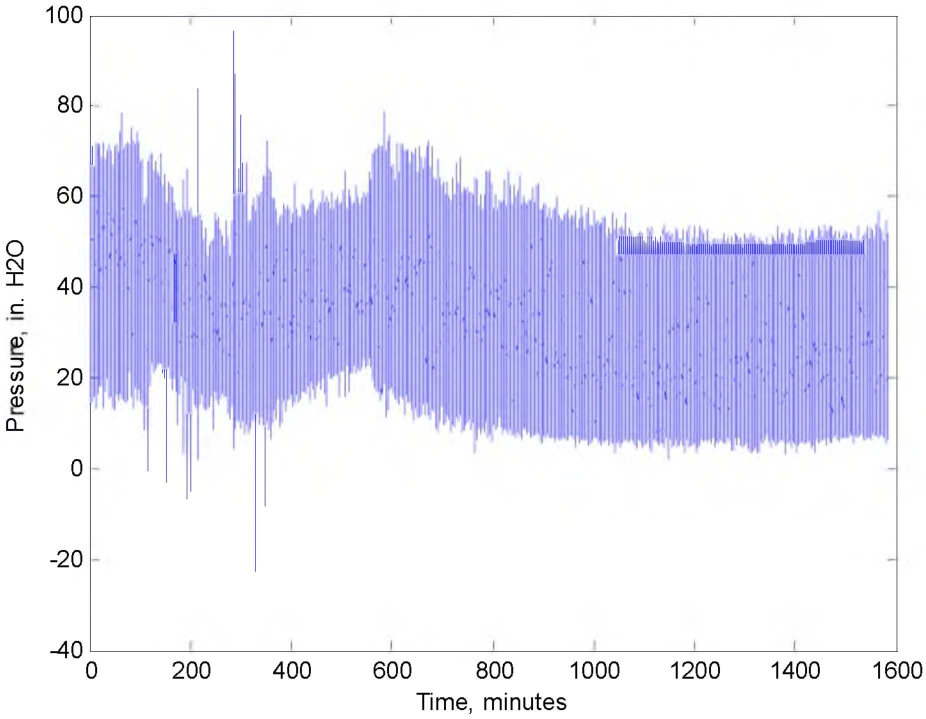

Figure 77. Raw pressure signal before, during, and after T1-T3 dark torrefied biomass tests (in. H_2O). 0=9:42, T1 start @ 98 minutes, T3 end @ 392 minutes, disturbance @ 978 minutes

Table 9. Average statistical quantities for each pressure fluctuation measurement sample during the overnight standby period

Sample time	20:00	0:00	2:00	4:00	8:00	12:00	14:48
Mean pressure, in. H_2O	40.65	33.66	28.87	25.87	25.50	23.25	33.88
Pressure fluctuation standard deviation, in. H_2O	4.78	8.22	8.84	8.73	8.61	7.13	8.18
Pressure fluctuation variance	22.85	67.55	78.16	76.20	74.07	50.79	66.92
Pressure fluctuation skewness	-0.10	0.06	0.15	0.19	0.13	0.10	0.19
Pressure fluctuation kurtosis	3.57	2.58	2.38	2.23	2.24	2.28	2.69

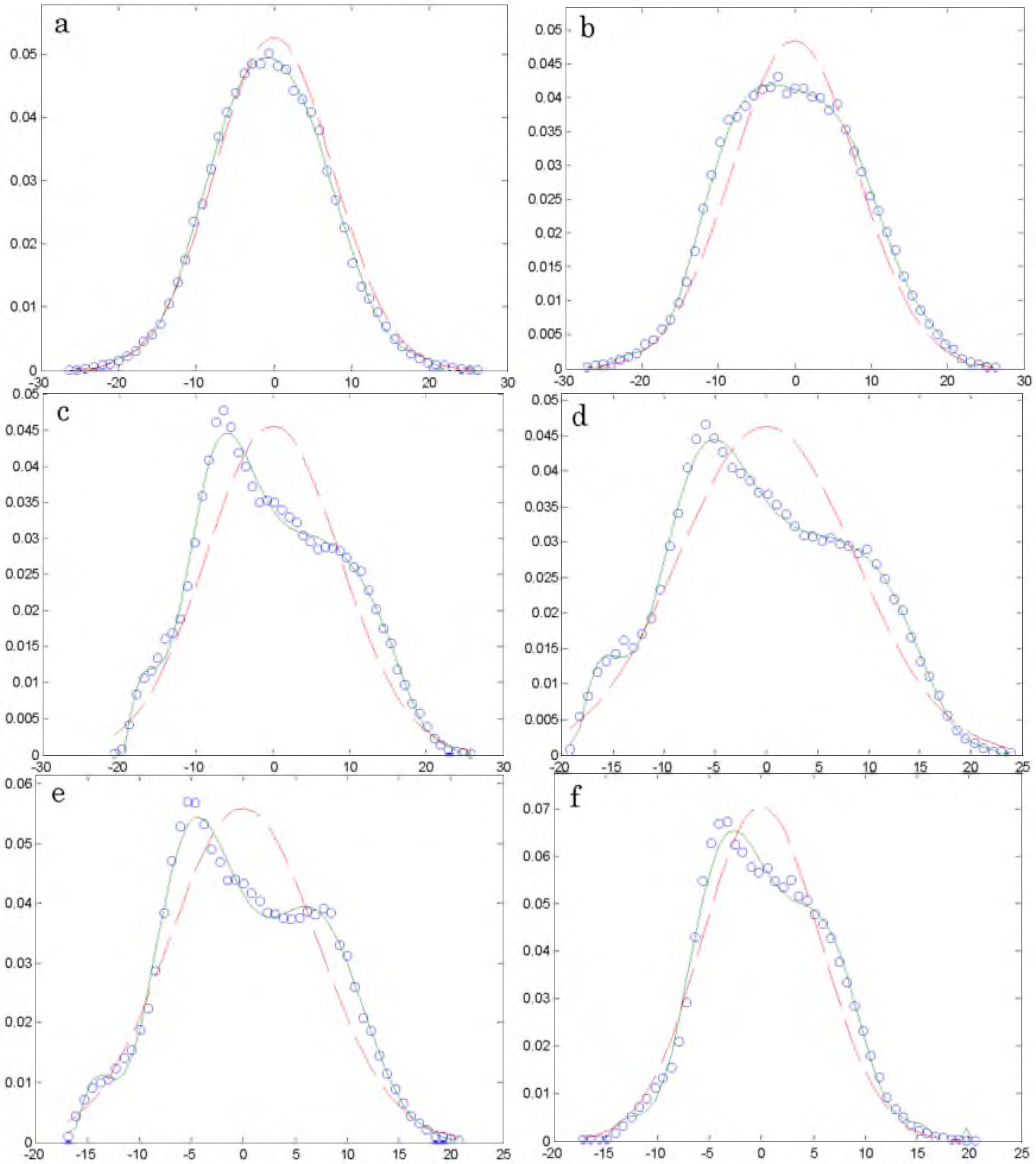

Figure 78. Pressure fluctuation probability density function overnight between tests T3 and T4 at a) 20:00, b) 0:00, c) 4:00, d) 8:00, e) 12:00, f) start of T4 (14:48). Abscissa is pressure fluctuation (in. H_2O) and ordinate is normalized probability. Blue circles are actual probability density values, solid green line is a polynomial fit the actual values, and the dashed red line is an equivalent Gaussian distribution.

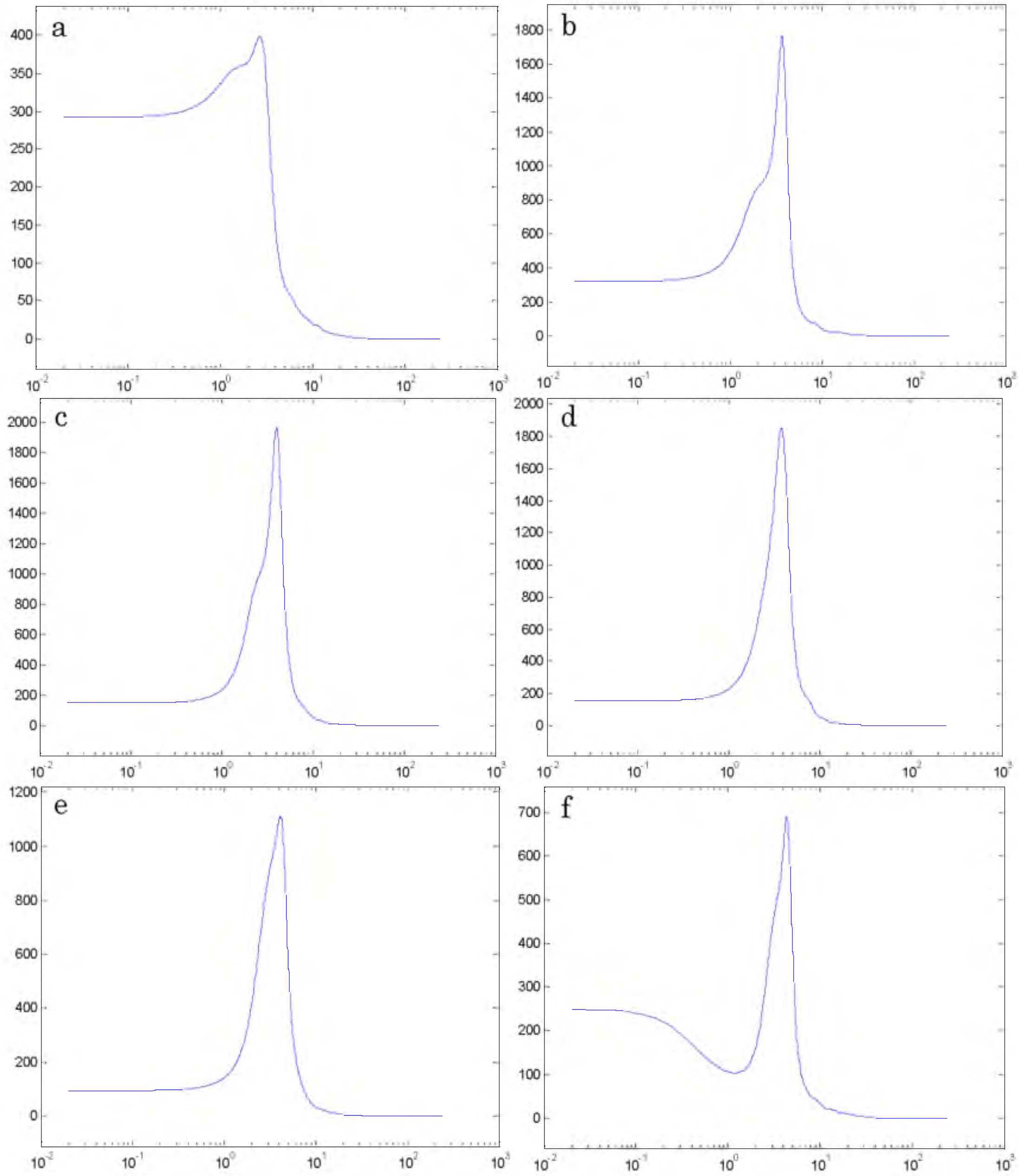

Figure 79. Pressure fluctuation autocovariance power spectral density (semi-log) overnight between tests T3 and T4 at a) 20:00, b) 0:00, c) 4:00, d) 8:00, e) 12:00, f) start of T4 (14:48). Abscissa is frequency (Hz) and ordinate is signal power (dB/sample).

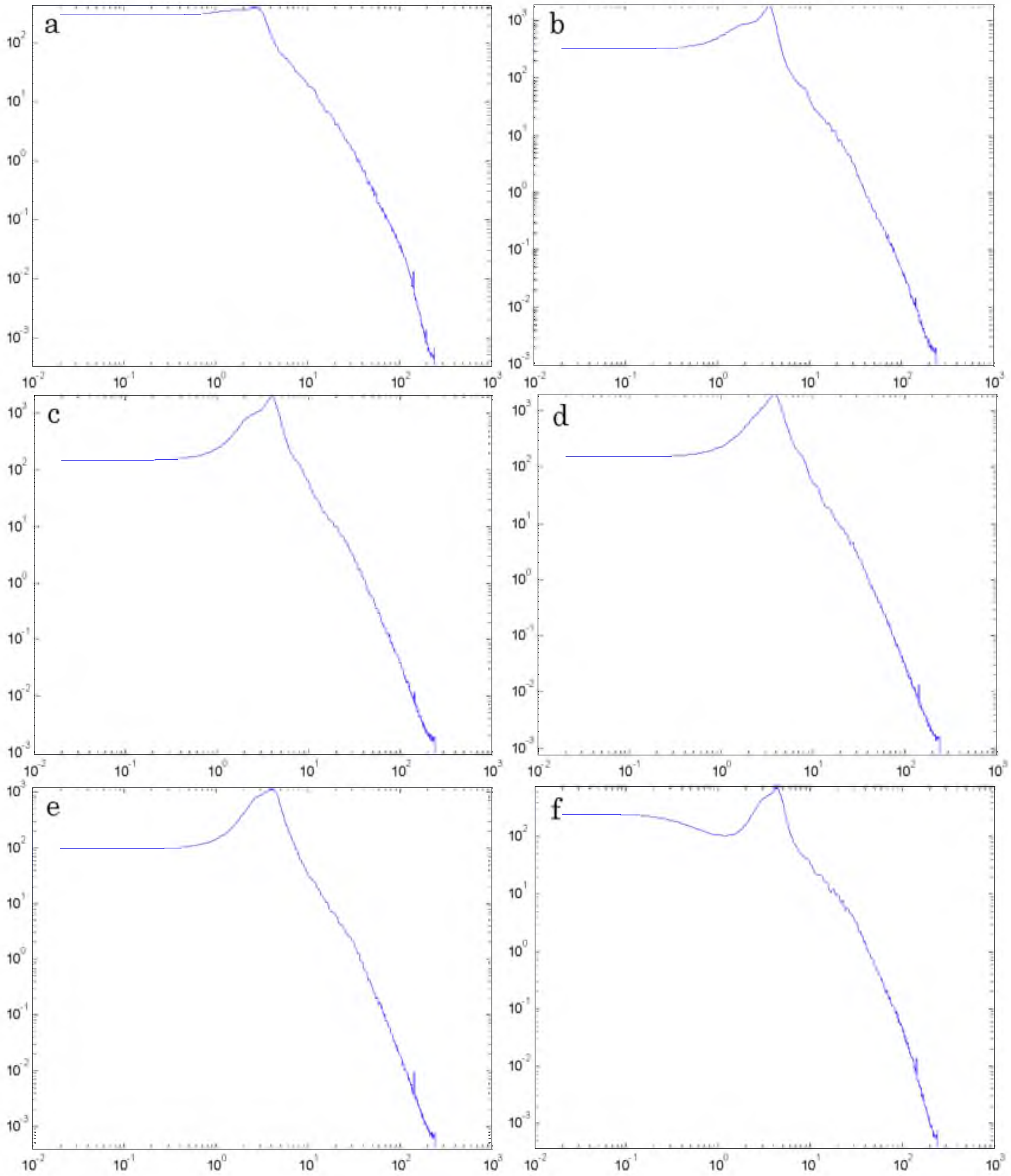

Figure 80. Pressure fluctuation autocovariance power spectral density (log-log) overnight between tests T3 and T4 at a) 20:00, b) 0:00, c) 4:00, d) 8:00, e) 12:00, f) start of T4 (14:48). Abscissa is frequency (Hz) and ordinate is signal power (dB/sample).

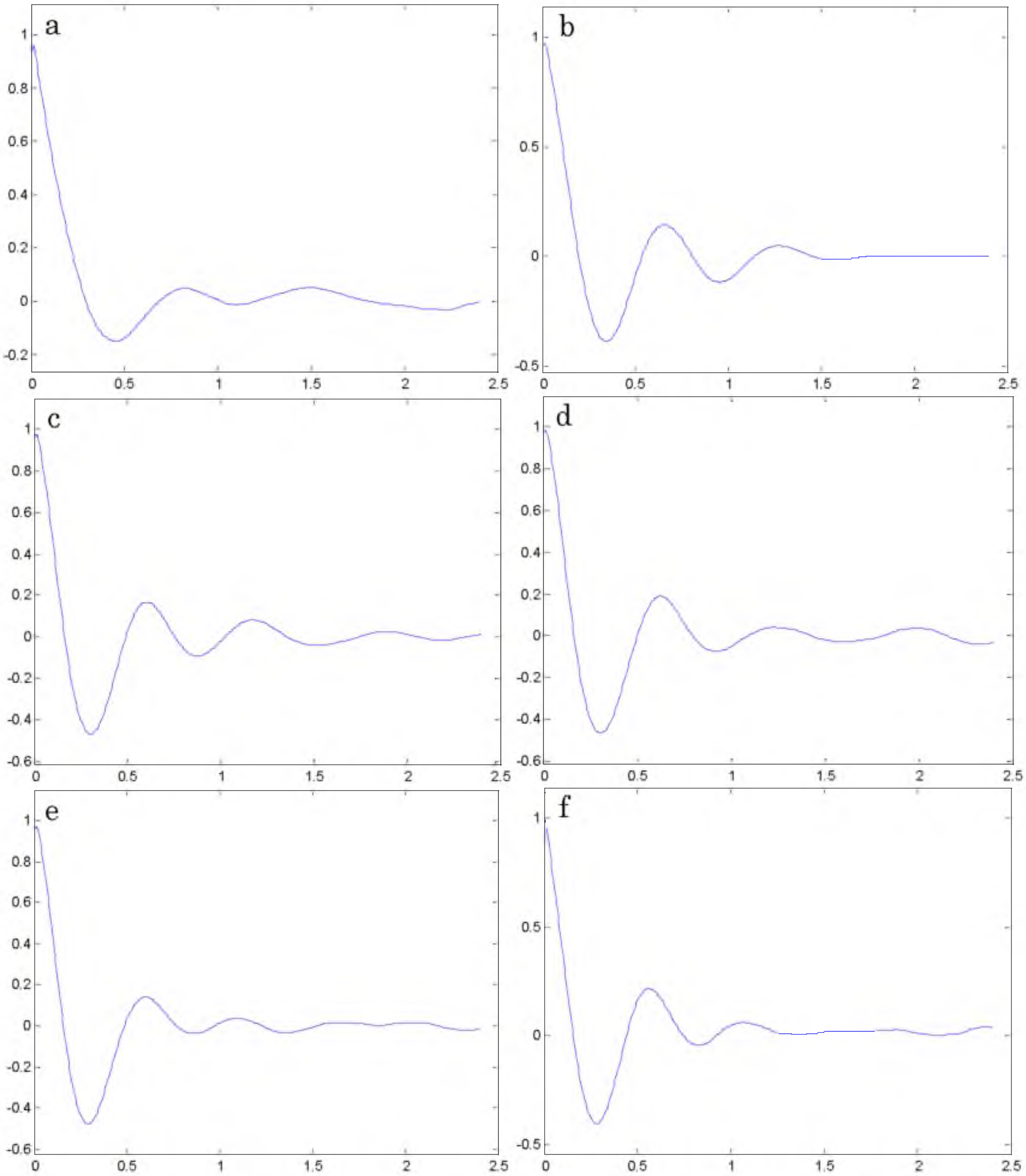

Figure 81. Pressure fluctuation normalized autocorrelation function overnight between tests T3 and T4 at a) 20:00, b) 0:00, c) 4:00, d) 8:00, e) 12:00, f) start of T4 (14:48). Abscissa is lag time (seconds) and ordinate is normalized correlation coefficient.

followed by linear decay to higher frequencies (Figure 79a). The autocorrelation function displays some decaying periodicity and a relatively moderate initial decrease (Figure 81a).

Two hours later (0:00), significant changes have occurred that are reflected in the statistical and spectral analyses of the pressure fluctuations, but are not evident in the bed temperature profile. The variance is nearly triple its previous value, the skewness has transitioned to slightly positive, and the kurtosis has transitioned to a value less than 3, which is the kurtosis of a normal distribution. Visual inspection of the PDF of the pressure fluctuations reveals that the second mode is appearing, which has shifted the combined peak in the positive direction and flattened it substantially (Figure 78b). Also, the extent to which the tails extend in both positive and negative directions has increased. The dominant peak in the PSD is at slightly above 3 Hz (Figure 79b). However, a secondary peak is showing near the 2 Hz frequency. The fall-off on the power spectrum is even steeper than the previous, and the linear decay region has extended to lower frequencies (60-120 Hz) (Figure 80b). The autocorrelation function exhibits a high magnitude (>0.4) oscillation that decays quickly.

As the temperature departure occurs, the pressure fluctuation variance goes through a maximum while the skewness continues an upward trend and the kurtosis drops sharply. The pressure fluctuation variance and kurtosis then stabilize until about 8:00 with the variance at a relatively high value (74-76) and the kurtosis a relatively low value (2.24). By 12:00, the pressure fluctuation variance falls off sharply to 51, skewness slowly approaches zero, and the kurtosis remains stable at 2.24-2.28. Throughout the event, the variance remains relatively high, indicating a large amount of spread in the pressure fluctuation probability distribution. The skewness remains slightly positive, which is likely due to the influence of the second mode in the distribution. The kurtosis remains relatively low, favoring a distribution with more weight in the tails.

By approximately 8:00, the bimodal distribution is very pronounced and it appears that a third feature in the PDF could be appearing near the negative tail. At 12:00, both modes are well defined and appear to be the combination of two independent modes for the first time. The dominant peak in the power spectrum continues to narrow until 8:00 and then begins to widen and reduce magnitude by 12:00. Very little change is observed in the autocorrelation function, with only a slight increase in the dampening of the periodic oscillation as in the 12:00 sample.

After 12:00, as measures are taken to remedy the situation by increasing bed heater outputs and the steam flow rate to increase the SGV, the temperature disparity in the bed begins to decrease and fluidizing conditions are brought back to a sufficient state to start gasification testing again. The bimodal distribution took some time to return to a unimodal distribution, not fully dissolving until the start of test P4 at approximately 15:00. By the start of test T4, the 3 Hz peak in the power spectrum is decreasing in magnitude and appears that it will soon be overpowered by an increase in low frequency transport. The autocorrelation function is further dampened by the start of test T4 but still shows relatively strong, but short lived, oscillation.

7.2.3.3. Conclusions

Again, it is difficult to pinpoint what caused the formation of the bimodal probability distribution in the pressure fluctuation signal. What can be inferred from the pressure signal analysis is that disturbance generated a physical change in the transport mechanisms in the lower bed. Normally, bimodal distribution in a fluidized bed can be attributed to the use of two different bed materials of different particle size. Given that, it is possible that some agglomerate formed and caused a disturbance in transport in the bed that became evident by the poor temperature distribution. However, given the sudden nature of the temperature departure, and the large quantities of solid residues that were produced during the previous day's torrefied biomass experiments, it is more likely that a section of the bed was blocked or obstructed by a buildup of material that eventually eroded away. A blockage of steam flow could have produced an uneven distribution of flow through the bed, causing high-magnitude pressure fluctuations and flow structures that showed a different signature than the typical bed standby signature that had previously been observed.

More important than what caused the disturbance is the fact that the pressure signal showed signs of a disturbance several hours before it was realized in the bed temperature profile. With online measurement and analysis of the bed pressure, problems related to poor hydrodynamic conditions in fluidized beds could be anticipated sooner and remedied. This case is an example of the potential that this method could have for fluidized bed reactor diagnostics.

CHAPTER 8

CONCLUSIONS

8.1. Conclusions from this research

The influence of gasifier operating conditions on gasifier performance, and tar yield and composition was studied using a pilot-scale, pressurized, steam-blown, woody biomass gasifier. While there is not an ideal operating condition for all of the performance indicators, general trends and recommended windows of operation were identified.

As expected, gasification at higher temperatures produced an overall cleaner gas, with up to a 53% decrease in tar production for an increase in the bed temperature from 1050 to 1450°F. The resulting effect on the net gasification efficiency (NGE1, p. 66) was a decrease from 271 to 211%. Higher temperature operation generally provided higher quality synthesis gas with hydrogen and carbon monoxide (H_2 + CO) concentration increasing from 43% at low temperature (1050°F) to 63% at high temperature (1450°F). Temperature had the most significant impact on synthesis gas yield, improving carbon conversion from 65 to 91% from low to high temperature.

Operation at increased temperature resulted in high rates of char elutriation with rates as low as 0.8 lb/hr at low temperature to rates as high as 4 lb/hr at high temperature. Operationally, high temperature conditions did not present any significant challenges other than the increased char elutriation due to higher velocities through the gasifier.

Pressure also exhibited a strong influence on tar production with yields as high as 53 g/Nm^3 at low pressure (5 psig) decreasing to 8.7 g/Nm^3 at high pressure (60 psig) due to super-stoichiometric quantities of steam and increased gasifier freeboard temperatures. The effect of elevated pressure resulted in slightly lower quality synthesis gas with approximately 6% lower hydrogen and carbon monoxide content at high compared to low pressure due to increased carbon dioxide production. Elevated pressure improved synthesis gas yield but not as significantly as temperature, improving yield an average of 4% from low to high pressure for a given gasifier temperature. Pressurized operation exhibited significantly lower NGE1 net effectiveness due to the high heating load on the bed, with an average of 228% at high pressure compared to 312% at low pressure for a given bed temperature. However, the hot gas efficiency increased substantially at elevated pressure due to the increased sensible heat content from the excess steam in the synthesis gas. On an operational level, pressurized gasification presents additional challenges in comparison to low pressure gasification. This is mostly due to equipment limitations, which can be addressed but generally require additional capital cost.

The use of torrefied biomass improved tar levels with a low yield of 1.62g/Nm^3, the lowest recorded on the fluidized bed gasifier, for the dark torrefied biomass at low feedrate (30 lb/hr) and high temperature (1450°F). The quality of the synthesis gas also improved, with torrefied biomass exhibiting 68-70% of hydrogen and carbon monoxide in the product compared to 64% at the equivalent raw biomass condition. As expected, the synthesis gas yield was lower and char production was higher for torrefied biomass with a carbon conversion efficiency of 49% (dark torrefied) to 68% (medium torrefied) compared to 91% for raw biomass. The NGE1 net effectiveness decreased slightly for torrefied biomass due to the decreased synthesis gas yield and increased heating load. However, when accounting for residue recovery (NGE3), the torrefied biomass (344-353%) outperformed raw biomass (293%), due mostly to char recovery. Operationally, torrefied biomass exhibited some benefits and some drawbacks. The material is very easy to feed and handle. However, the low volatile content resulted in a higher load on the bed heaters and the high carbon content resulted in increased char production and elutriation (2-15 lb/hr).

Finally, the use of a high-frequency differential pressure transducer for point measurement in the fluidized bed was demonstrated as a potential fluidization diagnostic and monitoring method. Operationally, this method was mostly successful, only experiencing a few minor problems with probe blockage during the gasification experiments. Analysis of the pressure signal reveals unique characteristics for different modes of gasifier operation and insight into the dominant transport features in the gasifier. A case was presented in which the pressure fluctuation signal detected a growing disturbance in the bed that eventually resulted in poor fluidization.

Overall, this research demonstrates the value of experimental research at large scale. It is difficult, or impossible, for simulation and small-scale experiment to anticipate challenges that are encountered in large scale experimentation. For this research, these included difficulties in operation at pressurized conditions, feeding various types of biomass solids, handling large rates of particulate loss from the gasifier, and fluidization disturbances. Understanding these challenges and devising solutions to remedy or prevent them is one of the benefits of large-scale research facilities.

8.2. Recommendations for future research

This research has provided a base level understanding of the effects of gasifier operating conditions on the various aspects of gasifier performance. A significant portion of the effort required to perform such research is constructing a functional experimental apparatus. This has largely been completed, which allows for future work to continue without significant delay.

With the foundation in primary methods research that this work has laid, a vast amount of research can be carried out investigating various other primary methods for tar reduction, including catalytic bed materials. In addition, the system is capable of operating on various solid feedstocks, including agricultural residues and other waste materials (e.g., municipal solid waste), which will provide valuable data for the research field in general, for technology developers, and policy makers.

Due to the unique experimental capabilities at The University of Utah, several key findings were identified in this research, which have not been identified in previous research. These include the influence of excess steam at elevated pressure on biomass gasification product distribution and occurrence of char elutriation during high-temperature fluidized bed gasification. It is recommended that well-controlled, fundamental laboratory-scale experimental and analytical techniques be utilized to investigate these findings in more depth. Investigation of product formation under pressurized steam gasification conditions using thermogravimetric analysis (TGA) would be useful in identifying the kinetics of thermal decomposition of biomass. An explanation for the greater char elutriation rates at high temperature as opposed to low temperature may be possible differences in the physical or chemical characteristics of char produced during high- and low-temperature steam gasification. Char produced at these conditions and collected from the downstream particulate filter could be analyzed using scanning electron microscopy (SEM) and Brunauer, Emmett, Teller (BET) analysis to indicate physical differences in char structure.

The use of pressure fluctuations for fluidized bed diagnostics could yield real benefits. During the various experimental campaigns that were completed for this work, the fluidized bed tended to have a mind of its own. On certain days, it seemed to perform well, and on others it was somewhat uncooperative. From conversations with industry engineers, this seems to be a common sentiment. On one occasion, I was told that “a better set of eyes would be nice.” A simple solution like pressure fluctuation measurement could provide that improved vision. Future work should focus on a better understanding of the fundamental transport processes in the fluidized bed as interpreted by pressure fluctuations and extensive real measurement experience to validate the concept. A major focus of this work should focus on accumulating pressure fluctuation datasets from well-controlled cold-flow fluidized bed experiments. These experiments should attempt to characterize the pressure fluctuation signal and associated signal characteristics under “well-fluidized” and “poorly fluidized” conditions. Well-fluidized conditions can be generated by using a uniformly sized, engineered bed material at an adequate bed height in the cold-flow apparatus. Poorly fluidized conditions can be established using a number of methods, including blocking off holes in the distributor plate to induce uneven gas distribution into the bed and increasing the bed height to induce slugging gas flow through the bed. In addition, the effect of fine- and/or low-density particle accumulation in the bed should be investigated to understand how char and ash accumulation in the gasifier affect hydrodynamic conditions.

APPENDIX A

TIME-SERIES SIGNAL ANALYSIS BACKGROUND

The following is a discussion of the theory and application of statistical and spectral methods for analyzing time-series data that was used to analyze pressure fluctuation data in this research. Much of the theoretical description in the following sections is adapted from textbooks and other material on turbulent flows, specifically Tennekes and Lumley (1972), Pope (2000), and Stull (1988), and notes from the course “Turbulence” taught by Professor Patrick McMurty at the University of Utah.

Probability density function

For analysis of a time-series signal, it is often useful to interpret the measured signal by the statistical quantities that describe it. Random quantities can only be specified with a certain probability. Therefore, the complete statistical description of a random variable can be given by its probability distribution at n points in space-time. The single point *probability density function* (PDF), $p_\phi(x)$, of a quantity, ϕ, provides the complete statistical description of ϕ. Therefore:

$$p_\phi(x)dx = \text{probability that } \phi \text{ has a value between } x \text{ and } x + dx$$

As a result, the resulting expression must be true of the probability density function:

$$\int_{-\infty}^{\infty} p_\phi(x)dx = 1$$

From the PDF, useful statistical quantities can be calculated, including the *cumulative distribution function* (CDF), and the central moments of the distribution (e.g., mean, variance, etc.) given by the following expression where μ_k is the kth central moment of the distribution:

$$\mu_k = \int_{-\infty}^{\infty} (\phi - \mu)^k p_\phi(x)dx$$

The second central moment (μ_2), known as the *variance*, provides information related to the spread of the probability distribution. The third central moment (μ_3), known as the *skewness*, provides information related to the symmetry of the probability distribution. Perfectly symmetric distributions have a skewness of zero. Asymmetry in the distribution that favors events in the positive direction will have a positive skewness while asymmetry favoring events in the negative direction will have a negative skewness. The fourth central moment (μ_4), known as the *kurtosis*, provides information related to the degree of flatness of a distribution. More flat distributions are referred to as *platykurtic* while less flat distributions are referred to as *leptokurtic*.

Statistical moments of a discrete signal

While the statistical quantities known as the central moments can be computed from the PDF of a signal, it is more common to compute these quantities based on knowledge of the arithmetic mean value of the measured signal in time-series analysis. The arithmetic, or ensemble mean, μ, for a discrete set of quantity ϕ is given by the expression:

$$\mu = \frac{1}{n}\sum_{i=1}^{n} \phi_i$$

Or for the mean for a discrete time-series signal $\phi(t)$ measured over time period T:

$$\mu = \frac{1}{T}\sum_{t=1}^{T}\phi(t)$$

Subsequently, the higher order statistical moments of the measured signal can be discretely calculated in dimensionless form using the expression:

$$\mu_k = \frac{1}{n\mu_2^{k/2}}\sum_{i=1}^{n}(\phi_i - \mu)^k$$

The *standard deviation*, σ, of a time-series signal $\phi(t)$, is calculated from the square root of the second central moment (variance):

$$\sigma = \left[\frac{1}{n-1}\sum_{i=1}^{n}(\phi_i - \mu)^2\right]^{1/2}$$

Signal decomposition

In fluid mechanics, complex transport associated with short length and time scales can be described by separating a quantity, ϕ, into its mean component, $\bar{\phi}$, and fluctuating component, ϕ'. This process is referred to as signal decomposition. In other words, a quantity measured continuously over a period of time can be represented by its mean and fluctuating components:

$$\phi(t) = \bar{\phi}(t) + \phi'(t)$$

Following decomposition of a measured signal, the original signal and its fluctuating component can be analyzed independently to extract useful information about phenomena occurring in the process. For example, the PDF of the fluctuating component of a signal provides information related to the probability of a deviation from the mean being near or far from the mean and less than or greater than the mean, which can give insight to physical processes occurring. Additionally, the following methods can be used to analyze fluctuating components of time-series signals.

Autocorrelation function

The statistical moments described in previous sections are single-point moments, meaning that they contain information about a signal at a single point in space. In many cases, it is useful to have a measure of spatial information, for example, to determine information related to length scales in a flow field. In order to obtain such information, two-point statistics are necessary. However, spatial measurement variation is not always possible, in which case the *autocovariance* provides a useful method for obtaining spatial information from a single-point measurement. The autocovariance of a time-series quantity is the correlation between the measured quantity $\phi(t)$ and itself at time $t + \tau$, given by:

$$R(\tau) = \overline{\phi(t)\phi(t + \tau)}$$

Or normalized by the variance, giving the *autocorrelation function*:

$$\rho(\tau) = \frac{\overline{\phi(t)\phi(t + \tau)}}{\overline{\phi^2}}$$

The autocorrelation function is essentially the correlation of the process at time t and at time $t + \tau$. As a result, the autocorrelation has the properties $\rho(0) = 1$: and $|\rho(\tau)| \leq 1$.

For processes in which the correlation diminishes relatively rapidly (e.g., turbulent flows and most real-world time-series signals), the integral of the autocorrelation function from $\tau = 0$ to $\tau = \infty$ will converge and yield the *integral timescale*, $\bar{\tau}$, of the process given by:

$$\bar{\tau} = \int_0^\infty \rho(t)dt$$

Calculation of the integral timescale from the autocorrelation function provides an estimation of the longest timescales (which can be related to length-scales for a given characteristic velocity) in a physical process.

Spectral analysis

Spectral analysis is applied a signal to obtain information regarding the "power" in the process of interest and the frequencies that dominate the process. For example, for turbulent flow, the "power" in a flow field is distributed through a range of time-scales, or corresponding frequencies, and length-scales, or corresponding wavenumbers, with specific ranges of frequencies and wavenumbers containing more energy than others. The complete profile of frequencies or wavenumbers and corresponding power contained in the process for those frequencies or wavenumbers is called the *power spectrum* of the process. The remainder of the discussion regarding spectral analysis will be in terms of the frequency domain rather than wavenumber domain as time-series signal analysis does not typically contain sufficient spatial data for wavenumber transforms.

In order to generate a power spectrum for a particular signal, the original signal needs to be converted to frequency space by calculating the Fourier transform of the signal. In general, for a continuous function $f(t)$ the Fourier transform, $g(\omega)$, is:

$$g(\omega) = \mathcal{F}\{f(t)\} = \int_{-\infty}^{\infty} f(t)e^{-\iota\omega t}dt$$

And inverse transform to transform the function $g(\omega)$ into time-space:

$$f(t) = 2\pi \int_{-\infty}^{\infty} g(\omega)e^{\iota\omega t}d\omega$$

The *power spectral density* (PSD) of a signal is a function that describes the relative power contributions of a signal as a function of frequency. The PSD, $S(\omega)$, can be obtained mathematically by computing the Fourier transform of the signal autocovariance, $R(\tau)$:

$$S(\omega) = \mathcal{F}\{R(\tau)\} = \int_{-\infty}^{\infty} \overline{\phi(t)\phi(t+\tau)}e^{-\iota\omega t}dt$$

APPENDIX B

MATLAB PRESSURE SIGNAL ANALYSIS SCRIPT

The following is a Matlab script used for analyzing raw pressure fluctuation sample periods. The input file is a signal file (“sig1.mat”) consisting of time data in the first column and the pressure data in the second column. An additional file named “name.mat” is used for labeling an Excel sheet that is generated containing important quantities calculated in the script. Material, geometry, and flow properties defined on the first page of the script are used to calculate dimensionless numbers relevant to fluidized bed dynamics.

```
clear
close all

% load pressure signal file formatted with time (seconds) in column 1
and
% the pressure signal in column 2
load sig1.mat
load name.mat

% define the number of ensemble sets
sets = 3;
t = sig1(:,1);          % time vector
```

```
pr = sig1(:,2);          % pressure vector
sl = floor(length(pr)/sets);        % set length

% sample frequency (Hz)
freq = 200;

% pdf calculation parameters
nbins = 50;      % number of sample bins for pdf
pdfdeg = 12;     % INPUT average pdf curvefit polynomial degree

% autocorrelation paramaters
laglength = sl*0.01;

%power spectral density paramaters
peakval = nan(sets,1);

% particle/bed characteristics
d_p = 192.5e-6;   % average particle size, [m]
rho_s = 1108;       % particle bulk density, [kg/m^3]
h_bed = 16 /12*0.3048;   % static bed height, [m]
d_bed = 6.46 /12*0.3048; % bed diameter, [m]

% flow characteristics (@ 80 deg F, 1 atm)
sgv = 1.25*0.3048;     % INPUT superficial gas velocity [m/s]
Cp = 1.0049;     % specific heat, [kJ/kg-K]
kcp = 1.4;       % ratio of specific heats, (Cp/Cv)
mu = 1.846e-5;   % dynamic viscosity, [kg/m-s]
nu = 1.568e-5;   % kinematic viscosity, [m^2/s]
rho_g = 1.177;     % density, [kg/m^3]
g = 9.81;        % gravitational acceleration, [m/s^2]

Re_p = d_p*sgv*rho_g/mu;     % particle Reynolds number
Re_h = d_bed*sgv*rho_g/mu;   % hydraulic Reynolds number
r_rho = rho_s/rho_g;         % solid-gas density ratio
r_hd = h_bed/d_p;            % bed height/particle size ratio
r_dd = d_bed/d_p;            % bed diameter/particle size ratio
Fr_p = sgv/(g*d_p)^0.5;      % bed particle Froude number
Fr_b = sgv/(g*d_bed)^0.5;    % hydraulic Froude number
Ar = d_p^3*(rho_s-rho_g)*g/mu^2;    % Archmedes number

for i = 1:sets
% pressure signal stastics
prs(i,:) = pr((i-1)*sl+1:i*sl);
prsrange(i) = max(prs(i,:))-min(prs(i,:));
prsmean(i) = mean(prs(i,:));
prsmeanvec(:,i) = prsmean(i)*ones(length(prs(i,:)),1);
prsstd(i) = std(prs(i,:));
prsvar(i) = var(prs(i,:));
prsskew(i) = skewness(prs(i,:));
prskurt(i) = kurtosis(prs(i,:));

% fluctuating pressure component:
```

```
fprs(i,:) = prs(i,:)-prsmean(i);
fprsrange(i) = max(fprs(i,:))-min(fprs(i,:));
fprsmax(i) = max(abs(fprs(i,:)));
fprsmean(i) = mean(fprs(i,:));
fprsstd(i) = std(fprs(i,:));
fprsvar(i) = var(fprs(i,:));
fprsskew(i) = skewness(fprs(i,:));
fprskurt(i) = kurtosis(fprs(i,:));

% norm.autocorrelation function of the pressure and pressure
fluctuation
% signals
prsxcorr(i,:) = xcorr(prs(i,:),'coeff');
fprsxcorr(i,:) = xcorr(fprs(i,:),'coeff');
% integral length scale calculation

% covariance power spectral density (psd) for each ensemble set
n = length(prs(i,:));
k(i,:) = n/200*linspace(0,1,n/4+1);
psd(i,:) = pcov(fprs(i,:),200,n/2);
% psd peak locations:
peakthresh =
mean(psd(i,5:length(psd(i,:))))+2*std(psd(i,5:length(psd(i,:))));
[peakh,peakloc] = findpeaks(psd(i,:),'minpeakheight',peakthresh);

% define variable peakval as nan if no peaks are detected in first set
PSD
if i == 1 && length(peakh) == 0
peakval(i,1) = nan;
end

% add NaN values if the number of peaks in the current (i) ensemble is
larger
% than the number of peaks in the i-1 ensemble
if i > 1 && length(peakh) < length(peakval(i-1,:))
for m = length(peakh)+1:length(peakval(i-1,:))
peakval(i,m) = nan;
peakfreq(i,m) = nan;
end
end
if i > 1 && length(peakh) > length(peakval(i-1,:))
for l = length(peakval(i-1,:))+1:length(peakh)
peakval(i-1,l) = nan;
peakfreq(i-1,l) = nan;
end
end

if length(peakh) > 0
peakval(i,1:length(peakh)) = peakh;
for j = 1:length(peakloc)
peakfreq(i,j) = k(i,peakloc(j));
end
end
```

```
% probability density function for each ensemble set
prshist(i,:) = hist(prs(i,:),nbins);
fprshist(i,:) = hist(fprs(i,:),nbins);
% normalize pdfs by integrating histograms
prsbins(i,:) = linspace(min(prs(i,:)),max(prs(i,:)),nbins);
binwidth = prsbins(i,2)-prsbins(i,1);
int1 = prshist(i,:).*binwidth;
int2 = sum(int1);
int3 = int1./int2;
prspdf(i,:) = int3./binwidth;

fprsbins(i,:) = linspace(min(fprs(i,:)),max(fprs(i,:)),nbins);
binwidth = fprsbins(i,2)-fprsbins(i,1);
int1 = fprshist(i,:).*binwidth;
int2 = sum(int1);
int3 = int1./int2;
fprspdf(i,:) = int3./binwidth;
end

fpr = pr-mean(pr);

% x-axis time values for signal plots
time = 0:1/freq:(sl-1)/freq;
% x-axis time values for signal plots:
lagtime = 0:1/freq:(laglength)/freq;

%% Data averaging and averaged data calculations

% average pressure signal statistics
prmax = max(pr);
prmin = min(pr);
prrange = mean(prsrange);
prmean = mean(prsmean);
prstd = mean(prsstd);
prvar = mean(prsvar);
prskew = mean(prsskew);
prkurt = mean(prskurt);

% average pressure fluctuation signal statistics
fprmax = max(fpr);
fprmin = min(fpr);
fprrange = mean(fprsrange);
fprmean = mean(fprsmean);
fprstd = mean(fprsstd);
fprvar = mean(fprsvar);
fprskew = mean(fprsskew);
fprkurt = mean(fprskurt);

% non-dimensional root mean square pressure fluctuation "Euler" number
Eu = fprstd*249.09/(0.5*rho_g*sgv^2);
```

```
% average ensemble autocorrelation sets
avprxcorr = mean(prsxcorr);
avfprxcorr = mean(fprsxcorr);

% average power spectral density sets
avpsd = mean(psd);
[avpeakh,avpeakloc] = findpeaks(avpsd,'minpeakheight',peakthresh);
avpeakfreq = k(1,avpeakloc);

% length scales associated with PSD peaks
avpsdlength = sgv./avpeakfreq;  % dominant length scales according to
PSD [m]

% Strouhal number for largest dominant frequency (maybe greater than 1
Hz?)
St = avpeakfreq(find(max(avpeakh)))*d_bed/sgv;
% if avpeakfreq(find(max(avpeakh))) < 1

% average pdf sets
avprspdf = mean(prspdf);
avfprspdf = mean(fprspdf);

% average pdf curvefit algorithm (polynomial degree defined above)
avpdfpfit = polyfit(fprsbins(1,:),avfprspdf,pdfdeg);
avpdfpval = polyval(avpdfpfit,fprsbins(1,:));
avpdfpfitcc = corrcoef(avfprspdf,avpdfpval);
avpdfpfitcc = avpdfpfitcc(2);

% average pdf Gaussian distribution and correlation coefficient
avpdfgauss = pdf('Normal',fprsbins(1,:),mean(fprs(1,:)),fprstd);
avpdfgausscc = corrcoef(avfprspdf,avpdfgauss);
avpdfgausscc = avpdfgausscc(2);

% compute integral time-scale by integrating average autocorrelation
% function up to first x-axis intersection
% find first x-intersection:
int1 = avfprxcorr(length(avfprxcorr)/2:length(avfprxcorr)-1);
int2 = avfprxcorr(length(avfprxcorr)/2+1:length(avfprxcorr));
int3 = int1.*int2;
int4 = find(int3<0);
% use trapezoidal integration to solve for integral time-scale
inttime =
trapz(lagtime(1:int4(1)),avfprxcorr(length(avfprxcorr)/2:length(avfprxc
orr)/2+int4(1)-1));    % [sec]
% convert integral time to integral length scale using sgv as
% characteristic velocity:
intlength = inttime*sgv;    % [in]

% populate moments data matrix for export to excel spreadsheet
moments = {name,name;'SGV [m/s]',sgv;'Press max [in H2O]',prmax;...
'Press min [in H2O]',prmin;'Press range [in H2O]',prrange;...
```

```
'Press mean [in H2O]',prmean;'Pressure std',prstd;'Press
var',prvar;'Press skew',prskew;...
'Press kurt',prkurt;'Fluc max [in H2O]',fprmax;'Fluc min [in
H2O]',fprmin;...
'Fluc range [in H2O]',fprrange;'Fluc mean [in H2O]',fprmean;'Fluc
std',fprstd;...
'Fluc var',fprvar;'Fluc skew',fprskew;'Fluc kurt',fprkurt;'Particle
size',...
    d_p;'Particle bulk density',rho_s;'Bed height [m]',h_bed;'Bed
diameter [m]',...
    d_bed;'Specific heat [kJ/kg-K]',Cp;'Ratio of specific
heats',kcp;...
'Dynamic viscosity [kg/m-s]',mu;'kinematic viscosity [m^2/s]',nu;'gas
density [kg/m^3]',...
    rho_g;'Particle Reynolds number',Re_p;'Hydraulic Reynolds
number',Re_h;...
'Solid-gas density ratio',r_rho;'Bed height-particle ratio',r_hd;...
'Bed diameter-particle size ratio',r_dd;'Bed particle Froude
number',Fr_p;...
'Hydraulic Froude number',Fr_b;'Archimedes number',Ar;...
'Euler number (pressure RMS)',Eu;'Strouhal number (peak freq)',St;...
'Integral length scale (xcorr) [m]',intlength;'Integral time scale
(xcorr) [s]',inttime};

% save moments data matrix to stats.mat file in current directory
savemoments.matmoments

% save averaged profiles to stats.mat file
savestats.matavfprxcorrlagtimeavpsdkavfprspdfpeakvalpeakfreqinttimeintl
engthavpeakhavpeakfreqavpdfpfit...
avpdfpfitccavpdfgaussccavpsdlength

%% write dataset statistics to Excel spreadsheet titled stats.xls
xls = xlswrite('C:\Users\Sween\Documents\RESEARCH\Cold Flow FBG
project\TRI March 2011\stats.xls',moments,name);
localxls = xlswrite('moments.xls',moments,name);

%% Plot preparation
% plot raw pressure signal for each ensemble set
figure
for i = 1:sets
subplot(sets,1,i)
plot(time,prs(i,:))
if i == 1
title('Raw pressure signal')
end
if i == ceil(sets/2)
ylabel('Pressure, in H2O')
end
holdon
plot(time,prsmeanvec(:,i),'w')
holdoff
ylim([min(min(prs))-max(prsrange)*0.1 max(max(prs))+max(prsrange)*0.1])
```

```
end
xlabel('Time, sec')
print('-f1','-dpng','pressfig.png')

% plot pressure fluctuation for each ensemble set
figure
for i = 1:sets
subplot(sets,1,i)
plot(time,fprs(i,:))
if i == 1
title('Pressure fluctuation')
end
if i == ceil(sets/2)
ylabel('Pressure, in H2O')
end
ylim([min(min(fprs))-max(range(fprs))*0.1
max(max(fprs))+max(range(fprs))*0.1])
end
xlabel('Time, sec')
print('-f2','-dpng','prflucfig.png')

% % plot norm.autocorrelation functions for ensemble average pressure
% % fluctuation
% figure
% plot(fprxcorr)
% title('Norm. autocorrelation function for fluctuating pressure
component')
% ylabel('R_x_x')

% plot norm.autocorrelation functions for ensemble average pressure
% fluctuation
figure
for i = 1:sets
subplot(sets,1,i)
plot(lagtime,fprsxcorr(i,length(prsxcorr)/2:(length(prsxcorr)/2+lagleng
th)))
if i == 1
title('Norm. autocorrelation function for pressure fluctuation')
end
if i == ceil(sets/2)
ylabel('R_x_x')
end
ylim([min(min(fprsxcorr))-max(range(fprsxcorr))*0.1
max(max(fprsxcorr))+max(range(fprsxcorr))*0.1])
end
xlabel('Lag time, sec')
print('-f3','-dpng','xcorrfig.png')

% plot covariance power spectral density for each ensemble set
% figure
% for i = 1:sets
% subplot(sets,1,i)
% plot(k(i,:),psd(i,:))
```

```
% if i == 1
%     title('Power spectral density (covariance)')
% end
% if i == ceil(sets/2)
%     ylabel('Power, ?')
% end
% ylim([min(min(psd))-max(range(psd))*0.1
max(max(psd))+max(range(psd))*0.1])
% end
% %print('-f2','-dpng','psdfig.png')

% plot log-log covariance power spectral density for each ensemble set
figure
for i = 1:sets
loglog(k(i,:),psd(i,:),'Color',[0 (i-1)/sets 0])
if i == 1
title('Power spectral density (covariance)')
end
if i == ceil(sets/2)
ylabel('Power, dB/sample')
end
ylim([min(min(psd))-max(range(psd))*0.1
max(max(psd))+max(range(psd))*0.1])
holdon
end
xlabel('Frequency, Hz')
print('-f4','-dpng','psdfiglglg.png')
holdoff

% plot semilog covariance power spectral density for each ensemble set
figure
for i = 1:sets
semilogx(k(i,:),psd(i,:),'Color',[0 (i-1)/sets 0])
if i == 1
title('Power spectral density (covariance)')
end
if i == ceil(sets/2)
ylabel('Power, dB/sample')
end
ylim([min(min(psd))-max(range(psd))*0.1
max(max(psd))+max(range(psd))*0.1])
holdon
end
xlabel('Frequency, Hz')
print('-f5','-dpng','psdfigsmlg.png')
holdoff

% plot normalized pdf for pressure signal ensemble sets
figure
for i = 1:sets
plot(prsbins(i,:),prspdf(i,:),'Color',[0 (i-1)/sets 0])
if i == 1
title('Norm. PDF - Pressure')
```

```
end
if i == ceil(sets/2)
ylabel('')
end
ylim([0 max(max(prspdf))+max(range(prspdf))*0.1])
holdon
end
xlabel('pressure, in H2O')
print('-f6','-dpng','prpdffig.png')
holdoff

% plot normalized pdf for pressure fluctuation signal ensemble sets
figure
for i = 1:sets
plot(fprsbins(i,:),fprspdf(i,:),'Color',[0 (i-1)/sets 0])
if i == 1
title('Norm. PDF - Pressure fluctuation')
end
if i == ceil(sets/2)
ylabel('')
end
ylim([0 max(max(fprspdf))+max(range(fprspdf))*0.1])
holdon
end
xlabel('pressure, in H2O')
print('-f7','-dpng','pfpdffig.png')
holdoff

%% Averaged data plots

% plot averaged norm. autocorrelation functions for pressure
% fluctuation
figure
plot(lagtime,avfprxcorr(length(avfprxcorr)/2:(length(avfprxcorr)/2+lagl
ength)))
title('Norm. autocorrelation function for pressure fluctuation')
ylabel('R_x_x')
ylim([min(min(avfprxcorr))-max(range(avfprxcorr))*0.1
max(max(avfprxcorr))+max(range(avfprxcorr))*0.1])
xlabel('Lag time, sec')
print('-f8','-dpng','avxcorrfig.png')

% plot averaged log-log covariance power spectral density
figure
loglog(k(1,:),avpsd)
title('Power spectral density (covariance)')
ylabel('Power, dB/sample')
ylim([min(min(avpsd))-max(range(avpsd))*0.1
max(max(avpsd))+max(range(avpsd))*0.1])
xlabel('Frequency, Hz')
print('-f9','-dpng','avpsdfiglglg.png')

% plot average semilog covariance power spectral density
```

```
figure
semilogx(k(1,:),avpsd)
title('Power spectral density (covariance)')
ylabel('Power, dB/sample')
ylim([min(min(avpsd))-max(range(avpsd))*0.1
max(max(avpsd))+max(range(avpsd))*0.1])
xlabel('Frequency, Hz')
print('-f10','-dpng','avpsdfigsmlg.png')

% plot average normalized pdf for pressure fluctuation signal
figure
plot(fprsbins(1,:),avfprspdf)
title('Norm. PDF - Pressure fluctuation')
ylim([0 max(max(avfprspdf))+max(range(avfprspdf))*0.1])
xlabel('pressure, in H2O')
print('-f11','-dpng','avpfpdffig.png')

% plot average normalized pdf for pressure fluctuation signal with
% polynomial curvefit of degree "pdfdeg"
figure
plot(fprsbins(1,:),avfprspdf,'o',fprsbins(1,:),avpdfpval,'-
',fprsbins(1,:),avpdfgauss,'--')
title('Norm. PDF - Pressure fluctuation w/polynomial curvefit &
Gaussian dist')
ylim([0 max([max(avpdfgauss) max(avpdfpval)])+max([max(avpdfgauss)
max(avpdfpval)])*0.1])
xlabel('pressure, in H2O')
legend('Avg. PDF','Polynomial fit','Gaussian','Location','best')
print('-f12','-dpng','avpfpdfcurvefitfig.png')
```

APPENDIX C

SUPPLEMENTAL EXPERIMENTAL TEST MATRIX

The tests matrix on the following page is intended to be removed and used as a reference while reading the results section of this thesis. The author apologizes for inconveniences due to the test number codes used.

Test #	Description	Target temp., °F	Target pressure, psig	Biomass type	Target biomass feedrate (lb/hr)
PM1	Low press shakedown	-	5	Raw wood	45
PM2	High temp, low press	1450	5	Raw wood	45
PM3	Med temp, low press	1250	5	Raw wood	45
PM4	Low temp, low press	1050	5	Raw wood	45
PM5	High temp, med press	1450	30	Raw wood	45
PM6	Med temp, med press	1250	30	Raw wood	45
PM7	High temp, high press	1450	60	Raw wood	45
PM8	Med temp, high press	1250	60	Raw wood	45
PM9	Low temp, high press	1050	60	Raw wood	45
PM10	Low temp, Med press	1050	30	Raw wood	45
PM11	Duplicate: High temp, med press	1450	30	Raw wood	45
T1	Med torr, high temp, high feed	1450	5	Med torr	45
T2	Med torr, high temp, low feed	1450	5	Med torr	30
T3	Med torr, med temp, low feed	1250	5	Med torr	30
T4	Dark torr, high temp, high feed	1450	5	Dark torr	45
T5	Dark torr, high temp, low feed	1450	5	Dark torr	30
T6	Dark torr, med temp, low feed	1250	5	Dark torr	30

REFERENCES

(1) *International Energy Annual 2003*; 2005.

(2) Perlack, R. D.; Stokes, B. J. U.S Billion-Ton Update: Biomass Supply for a Bioenergy and Bioproducts Industry **2011**, 227.

(3) Faaij, A. Potential Contribution of Bioenergy to the World's Future Energy Demand **2007**, 1-11.

(4) Raman, P.; Walawender, W. P.; Fan, L. T.; Chang, C. C. Mathematical model for the fluid-bed gasification of biomass materials. *Ind. Eng. Chem. Process Des. Dev.* **1981**, *20*, 686-692.

(5) Higman, C.; van der Burgt, M. *Gasification*; 2nd ed.; Gulf Professional Publishing: Burlington, MA, 2008.

(6) Basu, P. *Biomass Gasification and Pyrolysis Practical Design*; 1st ed.; Academic Press: Burlington, MA, 2010.

(7) Rezaiyan, J.; Cheremisinoff, N. P. *Gasification technologies: a primer for engineers and scientists*; CRC Press, 2005; Vol. 105.

(8) Li, C.; Suzuki, K. Tar property, analysis, reforming mechanism and model for biomass gasification—An overview. *Renewable and Sustainable Energy Reviews* **2009**, *13,* 594-604.

(9) IEA Thermal Gasification of Biomass Task: Meeting on tar measurement protocol **1998**.

(10) Stevens, D. *Hot gas conditioning: recent progress with larger-scale biomass gasification systems*; Golden, CO, 2001; pp. 1-89.

(11) Arena, U.; Zaccariello, L.; Mastellone, M. L. Tar removal during the fluidized bed gasification of plastic waste. *Waste Management* **2009**, *29*, 783-791.

(12) Bergman, P. C. A.; van Paasen, S. V. B.; Boerrigter, H. The novel " OLGA " technology for complete tar removal from biomass producer gas. In *Pyrolysis and Gasification of Biomass and Waste Expert Meeting*; Strasbourg, France, 2002.

(13) Smoot, L. D.; Smith, P. J. *Coal Combustion and Gasification*; Plenum Press: New York, 1985; p. 443.

(14) Corella, J.; Aznar, M. P.; Delgado, J.; Aldea, E. Steam gasification of cellulosic wastes in a fluidized bed with downstream vessels. *Ind. Eng. Chem. Res.* **1991**, *30*, 2252-2262.

(15) Gil, J.; Corella, J.; Aznar, M. P.; Caballero, M. A. Biomass gasification in atmospheric and bubbling fluidized bed: Effect of the type of gasifying agent on the product distribution. *Biomass and Bioenergy* **1999**, *17*, 389-403.

(16) Narvaez, I.; Orio, A.; Aznar, M. P.; Corella, J. Biomass gasification with air in an atmospheric bubbling fluidized bed. Effect of six operational variables on the quality of the produced raw gas. *Industrial & Engineering Chemistry Research* **1996**, *35*, 2110-2120.

(17) Lin, C.-L.; Wey, M.-Y. Statistical and power spectral analysis of quality of fluidization for different particle size distributions at high temperature. *Advanced Powder Technology* **2004**, *15*, 79-96.

(18) Fagbemi, L.; Khezami, L.; Capart, R. Pyrolysis products from different biomasses□: application to the thermal cracking of tar. *Applied Energy* **2001**, *69*, 293-306.

(19) Gil, J.; Aznar, M. P.; Caballero, M. a.; Francés, E.; Corella, J. Biomass Gasification in Fluidized Bed at Pilot Scale with Steam−Oxygen Mixtures. Product Distribution for Very Different Operating Conditions. *Energy & Fuels* **1997**, *11*, 1109-1118.

(20) Evans, R. J.; Milne, T. A. Chemistry of tar formation and maturation in the thermochemical conversion of biomass. *Fuel and Energy Abstracts* **1998**, *39*, 197-198.

(21) Simell, P.; Kurkela, E.; Stahlberg, P. Formation and Catalytic Decomposition of Tars from Fluidized-Bed Gasification. In *Advances in*

Thermochemical Biomass Conversion; Bridgwater, A. V., Ed.; Blackie Academic & Professional, 1993; pp. 265-279.

(22) Mayerhofer, M.; Mitsakis, P.; Meng, X.; de Jong, W.; Spliethoff, H.; Gaderer, M. Influence of pressure, temperature and steam on tar and gas in allothermal fluidized bed gasification. *Fuel* **2012**, *99*, 204-209.

(23) Milne, T. A.; Evans, R. J.; Abatzoglou, N. *Biomass Gasifier " Tars ": Their Nature , Formation , and Conversion*; Golden, CO, 1998.

(24) Good, J.; Ventress, L.; Knoef, H.; Group, B. T.; Zielke, U.; Hansen, P. L.; Wild, P. D.; Coda, B.; Paasen, S. V.; Kiel, J.; Liliedahl, T. Sampling and analysis of tar and particles in biomass producer gases. *Measurement* **2005**, 1-44.

(25) Milne, T. A.; Evans, R. J. *An atlas to pyrolysis-mass spectrograms for selected pyrolysis oils*; Golden, 1987.

(26) Knight, R. A. Experience with raw gas analysis from pressurized gasification of biomass. *Biomass and Bioenergy* **2000**, *18*, 67-77.

(27) Brage, C.; Yu, Q.; Sjostrom, K. Characterization of tars from coal-biomass gasification. In *3rd International Symposium on Coal Combustion*; Beijing, 1995; pp. 45-52.

(28) Kinoshita, C. M.; Turn, S. Q.; Overend, R. P.; Bain, R. L. Power generation potential of biomass gasification systems. *Journal of Energy Engineering* **1997**, *123*, 88-99.

(29) Herguido, J.; Corella, J.; Gonzalez-Saiz, J. Steam Gasification of Lignocellulosic Residues in a Fluidized Bed at a Small Pilot Scale . Effect of the Type of Feedstock. *Ind. Eng. Chem. Res.* **1992**, *31*, 1274-1282.

(30) Bridgwater, A. V. The technical and economic feasibility of biomass gasif ication for power generation. *Fuel* **1995**, *74*, 631-653.

(31) Lv, P. M.; Xiong, Z. H.; Chang, J.; Wu, C. Z.; Chen, Y.; Zhu, J. X. An experimental study on biomass air-steam gasification in a fluidized bed. *Bioresource technology* **2004**, *95*, 95-101.

(32) Kosstrin, H. Direct formation of pyrolysis oil from biomass. In *Proceedings Specialists Workshop on Fast Pyrolysis of Biomass*; 1980.

(33) Hanaoka, T.; Inoue, S.; Uno, S.; Ogi, T.; Minowa, T. Effect of woody biomass components on air-steam gasification. *Biomass and Bioenergy* **2005**, *28*, 69-76.

(34) Sadakata, M.; Takahashi, K.; Saito, M.; Sakai, T. Production of fuel gas and char from wood, lignin and holocellulose by carbonization. *Fuel* **1987**, *66*, 1667–1671.

(35) van Paasen, S. V. B.; Kiel, J. H. A. Tar formation in a fluidised-bed gasifier: Impact of fuel properties and operating conditions **2004**, 58.

(36) Couhert, C.; Salvador, S.; Commandré, J.-M. Impact of torrefaction on syngas production from wood. *Fuel* **2009**, *88*, 2286-2290.

(37) Qin, K.; Lin, W.; Jensen, P. A.; Jensen, A. D. High-temperature entrained flow gasification of biomass. *Fuel* **2012**, *93*, 589-600.

(38) Prins, M. J.; Ptasinski, K. J.; Janssen, F. J. J. G. More efficient biomass gasification via torrefaction. *Energy* **2006**, *31*, 3458-3470.

(39) van der Stelt, M. J. C.; Gerhauser, H.; Kiel, J. H. a.; Ptasinski, K. J. Biomass upgrading by torrefaction for the production of biofuels: A review. *Biomass and Bioenergy* **2011**, *35*, 3748-3762.

(40) Chen, Q.; Zhou, J.; Liu, B.; Mei, Q.; Luo, Z. Influence of torrefaction pretreatment on biomass gasification technology. *Chinese Science Bulletin* **2011**, *56*, 1449-1456.

(41) Beenackers, A. A. C. .; Maniatis, K. Gasification technologies for heat and power from biomass. *Fuel and Energy Abstracts* **1998**, *39*, 36.

(42) Corella, J.; Aznar, M.-P.; Gil, J.; Caballero, M. a. Biomass Gasification in Fluidized Bed: Where To Locate the Dolomite To Improve Gasification? *Energy & Fuels* **1999**, *13*, 1122-1127.

(43) Hu, G.; Xu, S.; Li, S.; Xiao, C.; Liu, S. Steam gasification of apricot stones with olivine and dolomite as downstream catalysts. *Fuel Processing Technology* **2006**, *87*, 375-382.

(44) Delgado, J.; Aznar, M. P. Biomass gasification with steam in fluidized bed: Effectiveness of CaO, MgO, and CaO-MgO for hot raw gas cleaning. *Ind. Eng. Chem. Res.* **1997**, *36*, 1535-1543.

(45) Aznar, M.-P.; Delgado, J.; Corella, J.; Lahoz, J. Steam gasification of biomass in a fluidized bed with a secondary catalytic bed. II. Tar cracking with dolomites in the secondary reactor. *Pyrolysis and Gasification* **1989**.

(46) El-Rub, Z. A.; Bramer, E. A.; Brem, G. Review of Catalysts for Tar Elimination in Biomass Gasification. *Ind. Eng. Chem. Res.* **2004**, *43*, 6911-6919.

(47) Narvaez, I.; Corella, J.; Orio, A. Fresh tar (from a biomass gasifier) elimination over a commercial steam-reforming catalyst. Kinetics and effect of different variables of operation. *Industrial & Engineering Chemistry Research* **1997**, *36*, 317-327.

(48) Zhang, R.; Brown, R. C.; Suby, A.; Cummer, K. Catalytic destruction of tar in biomass derived producer gas. *Energy Conversion and Management* **2004**, *45*, 995-1014.

(49) Dayton, D. A Review of the Literature on Catalytic Biomass Tar Destruction Milestone Completion Report **2002**, 27.

(50) Devi, L.; Craje, M.; Thüne, P.; Ptasinski, K. J.; Janssen, F. J. J. G. Olivine as tar removal catalyst for biomass gasifiers: Catalyst characterization. *Applied Catalysis A: General* **2005**, *294*, 68-79.

(51) Han, J.; Kim, H. The reduction and control technology of tar during biomass gasification/pyrolysis: An overview. *Renewable and Sustainable Energy Reviews* **2008**, *12*, 397-416.

(52) Teislev, B. *Harboore - woodchips updraft gasifier and 1500 kW gas-engines operating at 32% power efficiency in CHP configuration*; Kolding, Denmark, 1996; pp. 4-6.

(53) Lefebvre, A. H. *Gas Turbine Combustion*; 2nd ed.; Taylor & Francis, 1999; p. 400.

(54) Gupta, C. K.; Sathiyamoorthy, D. *Fluid Bed Technology in Materials Processing*; CRC Press, 1999.

(55) Ghasemi, F.; Ruud van Ommen, J.; Sahimi, M. Analysis of pressure fluctuations in fluidized beds. I. Similarities with turbulent flow. *Chemical Engineering Science* **2011**, *66*, 2627-2636.

(56) van Ommen, J. R.; Sasic, S.; van der Schaaf, J.; Gheorghiu, S.; Johnsson, F.; Coppens, M.-O. Time-series analysis of pressure fluctuations in gas–solid fluidized beds – A review. *International Journal of Multiphase Flow* **2011**, *37*, 403-428.

(57) Johnsson, F.; Zijerveld, R. C.; Schouten, J. C.; van den Bleek, C. M. Characterization of fluidization regimes by time-series analysis of pressure fluctuations. *International Journal of Multiphase Flow* **2000**, *26*, 663-715.

(58) Yerushami, J.; Ayidan, A. A. High Velocity Fluidization. In *Fluidization*; Davidson, J. F.; Keairns, D. L., Eds.; CUP Archive: Cambridge, England, 1978; p. 407.

(59) Bi, H.; Fan, L. S. Existence of turbulent regime in gas-solid fluidization. *AIChE J.* **1992**, *38*, 297-301.

(60) Bi, H. T.; Ellis, N.; Abba, I. A.; Grace, J. R. A state-of-the-art review of gas-solid turbulent fluidization. *Chemical Engineering Science* **2000**, *55*, 4789-4825.

(61) Andreux, R.; Gauthier, T.; Chaouki, J.; Simonin, O. New description of fluidization regimes. *AIChE Journal* **2005**, *51*, 1125-1130.

(62) Gheorghiu, S.; van Ommen, J.; Coppens, M.-O. Power-law distribution of pressure fluctuations in multiphase flow. *Physical Review E* **2003**, *67*, 1-7.

(63) Kage, H.; Iwasaki, N.; Yamaguchi, H.; Matsuno, Y. Frequency analysis of pressure fluctuation in fluidized bed plenum. *Journal of Chemical Engineering of Japan* **1991**, *24*, 76-81.

(64) van Ommen, J. R.; van der Schaaf, J.; Schouten, J. C.; van Wachem, B. G. M.; Coppens, M.-O.; van den Bleek, C. M. Optimal placement of probes for dynamic pressure measurements in large-scale fluidized beds. *Powder Technology* **2004**, *139*, 264-276.

(65) Parise, M. R.; Kurka, P. R. G.; Taranto, O. P. The Gaussian spectral pressure distribution applied to a fluidized bed. *Chemical Engineering and Processing: Process Intensification* **2009**, *48*, 120-125.

(66) Bai, B.; Gheorghiu, S.; van Ommen, J. R.; Nijenhuis, J.; Coppens, M.-O. Characterization of the void size distribution in fluidized beds using statistics of pressure fluctuations. *Powder Technology* **2005**, *160*, 81-92.

(67) van Ommen, J. R.; de Korte, R.-J.; van den Bleek, C. M. Rapid detection of defluidization using the standard deviation of pressure fluctuations. *Chemical Engineering and Processing: Process Intensification* **2004**, *43*, 1329-1335.

(68) Gheorghiu, S.; van Ommen, J. R.; Coppens, M.-O. Monitoring fluidized bed hydrodynamics using power-law statistics of pressure fluctuations. In *Fluidization XI*; 2004; pp. 403-410.

(69) Lin, C.-L.; Wey, M.-Y.; Cheng, H.-T. Relationship between pressure fluctuations and generation of organic pollutants with different particle size distributions in a fluidized bed incinerator. *Chemosphere* **2004**, *56*, 911-22.

(70) Brown, R. C.; Brue, E.; Schroeder, J. R.; De La Cruz, R. *Pressure fluctuations as a diagnostic tool for fluidized beds*; Ames, IA, 1998.

(71) Brue, E. Pressure fluctuations as a diagnostic tool for fluidized beds, Iowa State University, 1996.

(72) Simell, P.; Ståhlberg, P.; Kurkela, E.; Albrecht, J.; Deutsch, S.; Sjöström, K. Provisional protocol for the sampling and anlaysis of tar and particulates in the gas from large-scale biomass gasifiers. Version 1998. *Biomass and Bioenergy* **2000**, *18*, 19–38.

(73) Rubiano, C. Characterization of tar from a fluidized bed steam reformer of black liquor, The University of Utah, 2006.

(74) Brage, C.; Yu, Q.; Chen, G.; Sjbstrm, K. Use of amino phase adsorbent for biomass tar sampling and separation. *Fuel* **1997**, *76*, 137-142.

(75) Corella, J.; Caballero, M. A.; Aznar, M.-P.; Brage, C. Two Advanced Models for the Kinetics of the Variation of the Tar Composition in Its

Catalytic Elimination in Biomass Gasification. *Ind. Eng. Chem. Res.* **2003**, *42*, 3001-3011.

(76) Gil, J.; Caballero, M. A.; Martı, J. A.; Aznar, M.-P.; Corella, J. Biomass Gasification with Air in a Fluidized Bed : Effect of the In-Bed Use of Dolomite under Different Operation Conditions. *Ind. Eng. Chem. Res.* **1999**, *38*, 4226-4235.

(77) Simeone, E.; Holsken, E.; Nacken, M.; Heidenreich, S.; De Jong, W. Study of the Behaviour of a Catalytic Ceramic Candle Filter in a Lab-Scale Unit at High Temperatures Filter in a Lab-Scale Unit at High Temperatures. *International Journal of Chemical Reactor Engineering* **2010**, *8*, 1-16.

(78) Ponzio, A.; Kalisz, S.; Blasiak, W. Effect of operating conditions on tar and gas composition in high temperature air/steam gasification (HTAG) of plastic containing waste. *Fuel Processing Technology* **2006**, *87*, 223-233.

(79) Siedlecki, M.; de Jong, W. Biomass gasification as the first hot step in clean syngas production process – gas quality optimization and primary tar reduction measures in a 100 kW thermal input steam–oxygen blown CFB gasifier. *Biomass and Bioenergy* **2011**, *35*, S40-S62.

(80) Standard Practice for Ultimate Analysis of Coal and Coke. In *ASTM D3176 - 09*; ASTM International.

(81) Zhou, J.; Masutani, S. M.; Ishimura, D. M.; Turn, S. Q.; Kinoshita, C. M. Release of Fuel-Bound Nitrogen during Biomass Gasification. *Industrial & Engineering Chemistry Research* **2000**, *39*, 626-634.

(82) Basu, P. *Combustion And Gasification in Fluidized Beds*; CRC Press, 2006; p. 473.

(83) Bi, H. T. A critical review of the complex pressure fluctuation phenomenon in gas–solids fluidized beds. *Chemical Engineering Science* **2007**, *62*, 3473-3493.

(84) Siddoway, M. Measurement of bubble behavior and heat transfer in a fluidized bed having horizontal heat exchange tubes, The University of Utah, 2006, p. 100.

(85) Yu, Q.; Brage, C.; Chen, G.; Sjöström, K. Temperature impact on the formation of tar from biomass pyrolysis in a free-fall reactor. *Journal of Analytical and Applied Pyrolysis* **1997**, *40-41*, 481-489.

(86) Gerhauser, H.; Generalis, S. C.; Hague, R. A.; Bridgwater, A. V. CFD for the Modelling of Entrainment in Fluidised Bed Fast Pyrolysis of Biomass. In *Progress in Thermochemical Biomass Conversion*; Bridgwater, A. V., Ed.; Blackwell Science Ltd, 2001; pp. 1281-1295.

(87) Kunii, D.; Levenspiel, O. *Fluidizatoin Engineering*; 2nd ed.; Elsevier, 1991; p. 491.

(88) Cummer, K. R.; Brown, R. C. Ancillary equipment for biomass gasification. *Biomass and Bioenergy* **2002**, *23*, 113–128.

(89) Brewer, C. E.; Unger, R.; Schmidt-Rohr, K.; Brown, R. C. Criteria to Select Biochars for Field Studies based on Biochar Chemical Properties. *Bioenergy Research* **2011**, *4*, 312-323.

(90) Hamelinck, C. N.; Faaij, A.; den Uil, H.; Boerrigter, H. Production of FT transportation fuels from biomass: technical options, process analysis and optimisation, and development potential. *Energy* **2004**, *29*, 1743-1771.

(91) Littlewood, K. Gasification- Theory and application. *Progress in Energy and Combustion Science1* **1977**, *3*, 35-71.

(92) Probstein, R. F.; Hicks, R. E. *Synthetic fuels*; Courier Dover Publications, 2006.